UNIVERSITY OF CALIFORNIA SAN DIEGO

Molecular and Circuit Organization of Amygdalostriatal Circuits Controlling Valence Behaviors

A dissertation submitted in partial satisfaction of the requirements for the degree Doctor of Philosophy

in

Neurosciences with a Specialization in Computational Neurosciences

by

James Robinson Howe

Committee in charge:

Professor Cory Root, Chair
Professor Edward Callaway
Professor Byungkook Lim
Professor Eran Mukamel
Professor Kay Tye

2024

The dissertation of James Robinson Howe is approved, and it is acceptable in quality and form for publication on microfilm and electronically.

University of California San Diego

2024

DEDICATION

To my father,

the giant whose shoulders I've always stood on.

EPIGRAPH

The truth is we don't know what we don't know.
We don't even know the questions we need to ask in order to find out,
but when we learn one tiny little thing,
a dim light comes on in a dark hallway,
and suddenly a new question appears.
We spend decades, centuries, millennia,
trying to answer that one question
so that another dim light will come on.

Yaa Gyasi

TABLE OF CONTENTS

LIST OF SUPPLEMENTAL VIDEOS

Supplemental Video 1: Howe – ASt Neural Trajectories Video.mp4

Supplemental Video 2: Howe – TS Neural Trajectories Video.mp4

Supplemental Video 3: Howe – CeA Neural Trajectories Video.mp4

LIST OF FIGURES

ACKNOWLEDGMENTS

Throughout the work compiled in this dissertation, I have received a truly incredible amount of support, guidance, and assistance from many people too numerous to name across every sphere of my life. Any acknowledgments that I make would be incomplete without noting all the diffuse contributions, great and small, crucial to my work's creation and completion.

I would first like to thank my mentor, Cory Root. Ever since the very beginning of graduate school, he has always supported me, and he believed in me when no one else did. He gave me all the freedom I needed to try my ideas, while providing extremely useful direction to try to keep me on track. None of this would have been possible without him.

I would also like to thank my other, less official mentor, Kay Tye, along with the rest of my committee, who provided such valuable advice and direction along the way. You have been such a crucial source of feedback and support, and your thoughts have so helpful in developing my work and my outlook on science. Without your help, my growth as a scientist would certainly have been far slower and far lower than at present.

I would next like to acknowledge my collaborators within the laboratory and without, chief among them Fergil Mills, K-Dan Lee, and Marlon Blanquart. Your strengths have all complemented my own, and I hope mine have done the same for yours. You have all been so accommodating, and I have learned so much from all of you.

In addition, I would also like to thank my family: my mother, Denise, my father, Jim, and my sister, Julia. You have been a limitless source of support and strength for me over the years, and I could always speak with you at any time, knowing you would either have some sort of advice for me, or even just a willing ear for me to vent at. I could not have kept my sanity without your continual patience and love.

Finally, I would like to thank all my friends, both the ones I brought here with me and the ones that I made along the way. I would like to specifically mention Sam, Josh, Alex, Fred, Sue, Brian, Ronak, and Jamie, who have been of particular importance in my life over the past six years. You are the collective lights of my life, have been with me every step of the way on this long, long path, and are the chief distractions from my work, in the best way possible.

Chapter 2, in full, is a reprint of the material as it was submitted for publication to Cell. Mills, F., Lee, C.R., Howe, J.R., Li, H., Shao, S., Keisler, M.N., Lemieux, M.E., Taschbach, F.H., Keyes, L.R., Borio, M.R., Chen, H.S., Patel, R.R., Gross, A.L., Delahanty, J., Cazares, C., Maree, L., Wichmann, R., Pereira, T.D., Benna, M.K., Root, C.M., Tye, K.M. Amygdalostriatal transition zone neurons encode sustained valence to direct conditioned behaviors. Cell, in revision. The dissertation author was one of the primary investigators and a co-first author on the paper, responsible for all matters pertaining to single-nucleus RNA sequencing.

Chapter 3, in full, is a reprint of the material as it was prepared for simultaneous submission to Cell and Neuron. Howe, J.R., Chan, C.L., Blanquart, M., Lemieux, M.E., Mills, F., Tye, K.M., Root, C.M. Control of innate olfactory valence by segregated cortical amygdala circuits. In preparation. The dissertation author was the primary investigator and the first author on the paper.

VITA

2017 Bachelor of Arts, Dartmouth College
2024 Doctor of Philosophy, University of California San Diego

PUBLICATIONS

Howe, J.R., Chan, C.L., Blanquart, M., Lemieux, M.E., Mills, F., Tye, K.M., Root, C.M. Control of innate olfactory valence by segregated cortical amygdala circuits. In preparation.

Dunton, K.L., Hedrick, N.G., Meamardoost, S., Ren, C., Howe, J.R., Wang, J., Root, C.M. Gunawan, R., Komiyama, T., Zhang, Y., Hwang, E.U. (2024). Experience-dependent dfferentiation of glutamatergic cortical neurons into transcriptomically defined subtypes. Journal of Neuroscience, in press.

Mills, F.*, Lee C.R.*, Howe, J.R.*, Li, H.*, Shan, S., Keisler, M.N., Lemieux, M.E., Taschbach, F.H., Keyes, L.R., Borio, M.R., Chen, H.S., Patel, R.R., Gross, A.L., Delahanty, J., Cazares, C., Maree, L., Wichmann, R., Pereira, T.D., Benna, M.K., Root, C.M., Tye, K.M. (2024). Amygdalostriatal transition zone neurons encode sustained valence to direct conditioned behaviors. Cell, in revision. (preprint, bioRxiv).

Getz, S.A., Tariq, K., Marchand, D.H., Dickson, C.R., Howe VI, J.R., Skelton, P.D., Wang, W. Li, M., Barry, J.M., Hong, J., Luikart, B.W. (2022). PTEN regulates dendritic arborization by decreasing microtubule polymerization rate. Journal of Neuroscience. 42(10): 1945-1957.

Howe VI, J.R., Bear, M.F., Golshani, P., Klann, E., Mucke, L., Sahin, M., Lipton, S.A., Silva, A.J. (2018). The mouse as a model for neuropsychiatric drug development. Current Biology. 28(17): R909-914.

Howe VI, J.R., Li, E.S., Streeter, S.E., Rahme, G.J., Chipumuro, E., Russo, G.B., Litsky, J.F., Hills, L.B., Rodgers, K.R., Skelton, P.D., Luikart, B.W. (2017). MiR-338-3p regulates neuronal maturation and suppresses glioblastoma proliferation. PLoS ONE, 12(5): e0177661.

Howe VI, J.R., Dahdaleh, F.S., Carr, J.C., Wang, D., Sherman, S.K., Howe, J.R. (2013). BMPR1A mutations in juvenile polyposis affect cellular localization. Journal of Surgical Research, 184(2): 739-745.

Dahdaleh, F.S., Carr, J.C., Calva, D., Howe VI, J.R., Howe, J.R. (2011). SP1 regulates the transcription of BMPR1A. Journal of Surgical Research, 171(1): e15-20.

FIELDS OF STUDY

Major Field: Neuroscience

Studies in Valence Processing and Extended Amygdala Circuits
Professor Cory Root

Major Field: Neuroscience

Studies in Neuronal Development and Glioblastoma
Professor Bryan Luikart

ABSTRACT OF THE DISSERTATION

Molecular and Circuit Organization of Amygdalostriatal Circuits Controlling Valence Behaviors

by

James Robinson Howe

Doctor of Philosophy in Neurosciences with a Specialization in Computational Neurosciences

University of California San Diego, 2024

Professor Cory Root, Chair

This dissertation characterizes the composition and functional relevance of selected extended amygdala transition regions involved in valence behaviors. Chapter 1 introduces the basis of innately valenced behaviors and its relationship to the cortical amygdala and explores possible implications of observed innate valence behaviors. Chapter 2 uses electrophysiology, calcium imaging, optogenetics, and single-nucleus RNA-sequencing to characterize the molecular and electrophysiological composition of the amygdalostriatal transition region and the

adjacent central amygdala and striatal regions and identify distinct features of each in either domain. These approaches find that the amygdalostriatal transition area is enriched for *Drd2*-expressing MSNs compared to surrounding regions, and the activity of the region's *Drd2*+ neurons, which is necessary for conditioned fear responses, encodes learned negative valence for stimuli, identifying a critical role for the amygdalostriatal transition area in motivated behaviors, especially with regard to negative valence. Chapter 3 uses optogenetics, chemogenetics, single-nucleus RNA-sequencing, and long-range projection tracing to identify a functional topography for valence in the posterolateral cortical amygdala, characterize its molecular cell types and downstream outputs, and examine the relationship between these three modalities. This work shows that plCoA contains dissociable, topographically biased pathways projecting to either the medial amygdala or the nucleus accumbens, and these circuits respectively control innate olfactory attraction and aversion. Overall, these findings add to our understanding of the composition of these extended amygdala subregions, their function, and the unique features of each necessary to exert their behavioral effects.

Chapter 1: Introduction

1.1. Phobias: A class of diseases of innate valence

Early in his career, the esteemed psychologist Martin Seligman wrote the seminal paper "Phobias and Preparedness", objecting to the then-current behaviorist paradigm, where most, if not all, valence and emotion were considered the result of various conditioning processes (Seligman, 1971). He identified four incongruences undermining their account, especially regarding specific phobias, one of the most common non-generalized anxiety disorders. First, phobias seem to be highly selective. Pavlov's original account of fear conditioning stated that "any natural phenomenon chosen at will may be converted into a conditioned stimulus," wherein any stimulus may elicit a fear response if associated with trauma (Pavlov, 1928). However, phobias tend towards a few highly stereotyped stimuli, such as heights, darkness, or animals, but not mundane objects or plants, even though they are also likely to be present during any given traumatic episode. Second, phobias are much more resistant to extinction than conditioned fears. Though exposure therapy is the most common treatment for phobias, the number of presentations required for successful exposure therapy far exceeds those required for successful extinction of a conditioned stimulus in a laboratory setting. Third, these phobias tend to be irrational. Many times, phobias are not associated with a specific traumatic episode for the individual, defying the traditional account of fear conditioning: for example, most people with a fear of heights were never seriously injured in a high fall and never witnessed a person seriously harmed by a fall. Fourth, many phobias can be acquired following a single event. Most fear conditioning relies upon repeated CS-UCS co-presentations, unless fear of imminent death is involved, whereupon a single presentation is sufficient. However, these single-trial presentations are better models of posttraumatic stress disorder (PTSD) or acute shock disorder, not phobias, where a much less

emotionally salient episode can have a similar effect or can occur independent of an episode, as stated in the third objection.

In response, Seligman developed the "preparedness theory of phobias": phobias are highly prepared to be learned by humans, and, like other highly prepared relationships, they are selective and resistant to extinction, learned even with degraded input, and probably are non-cognitive (Seligman, 1971). He proposed that evolutionary processes may have 'prepared' certain stimuli of phylogenetic importance, such as ancestral predators or common sources of disease, to easily induce strong fear responses compared to other stimuli, like household objects. The preparedness theory had a massive immediate impact and touched off an explosion of research; results were positive but mixed, and while the theory clearly had merit, it would require further modification and refinement before it the field could fully accept it (McNally, 2016).

Thirty years after Seligman's original proposal, two groups made separate but overlapping contributions explaining these deficiencies. The first was the concept of innate, non-associative fear in humans (Poulton and Menzies, 2002a; 2002b). They proposed that a subset of possible fear associations could be acquired without any aversive associative episode of if and only if: the stimulus represents a long-standing danger to the species, a fearful response increases reproductive success in nature, and this response is at least partially under genetic control. The second was the evolved fear module (Öhman and Mineka, 2001a). They proposed this module, originating from a dedicated neural pathway, would be preferentially activated by evolutionarily relevant threats in an automatic, noncognitive manner. Synthesis of these two ideas yields a theoretical fear pathway in humans that responds automatically and relatively uncontrollably to an innate set of stimuli defined by Darwinian selection processes.

Since Seligman's original paper, snakes and spiders have been considered the model innate fearful stimuli in humans, for many reasons. Around 5% of children and adults have clinical phobias of these animals, while 20-30% report some degree of fear, despite neither posing any realistic threat to the average person today (Fredrikson et al., 1996; Muris et al., 1997). Snakes were one of primates' first and most lethal predators, and many anthropologists believe unique aspects of the primate visual system (i.e. trichromacy, high visual acuity, and enhanced depth perception) to be resultant adaptations; such profound alterations to one part of the nervous system imply profound changes to others as well (Isbell, 2006). Similarly, widow spiders have populated Africa since tens of millions of years before the emergence of hominids, and possess a highly lethal neurotoxin that, when not outright fatal, can incapacitate an adult for weeks (New and German, 2015).

Measures of attentional bias and arousal are most used to test such hypotheses, as they are both increased in response to threats. Adults display enhanced attentional bias towards spiders and snakes compared to fear-irrelevant animals and other stimuli of negative valence (New and German, 2015; Öhman et al., 2001b). Both young children and infants also attend much more readily to snakes than other images, implying this bias is heritable and innate instead of a result of social/experiential conditioning. (LoBue and DeLoache, 2008; 2010). Similarly, adults more easily acquire fearful associations to spiders and snakes, which also take much longer to extinguish than associations to less-"prepared" stimuli (Öhman et al. 2001a). However, this result carries over to infants as well, who display greater degrees of arousal in response to presentation of images of spiders or snakes compared to neutral images, confirming infant attentional bias is not neutrally-valenced (Hoehl et al. 2017). These results clearly indicate that humans possess some automatic innate fear response selective to certain ancestral predators from

infancy that can last through adulthood, just as predicted by Seligman's model. While this response is best studied and understood in humans, we are not the only species likely to possess an evolved fear module. Indeed, given that such a module is likely both heritable and non-cognitive, it would not likely arise *de novo* in hominids, and is likely present in other animals very phylogenetically distant from humans. Interestingly, lab-reared, snake-naïve rhesus and squirrel monkeys do selectively acquire fear when observing another wild-reared primate respond fearfully to snakes compared to neutral stimuli from infancy onward, (though they do not display an clear intrinsic fear response to snakes), partially supporting the existence of a snake-selective evolved fear module in non-human primates (Cook and Mineka, 1990; Murray and King, 1973; Mineka et al., 1980; Mineka et al., 1984; Weiner and Levine, 1992).

Rodents are even more distant than non-human primates, and they have one of the best-characterized innate fear pathways in the entire animal kingdom, further attesting to the phenomenon's conservation. This pathway is olfactory, instead of visual, and generally serves to detect predator secretions in the wild, but interestingly, rodents retain innate fear responses despite hundreds, if not thousands, of generations of breeding in laboratory conditions without ever encountering the predator species of interest (Stowers and Kuo, 2015). Cats serve as the model predator for rats, and rats serve as the model predator for mice, though mice also display a predator response to cats as well (Blanchard and Blanchard, 1971; Blanchard et al., 2003). Cat odor alone is sufficient to induce a fear response in mice and rats, and rats will display this from infancy (Chan et al., 2011; de Oliveira Crisanto, 2015). In fact, this innate aversion has been isolated to a single compound, 2-phenethylamine (PEA), where it alone can produce an aversive response, and either its depletion from cat urine or deletion of the olfactory receptors it binds is sufficient to prevent innate aversion in mice (Ferrero et al., 2011; Dewan et al., 2013). There are

a far greater number of innately aversive odorant compounds, however, most notably the fox anal gland secretion compound trimethylthiazoline (TMT), the most used innately aversive odorant in the mouse literature, though its actual naturalistic relevance is currently disputed (Vernet-Maury et al., 1968; Root et al. 2014; Saraiva et al., 2016; Rampin et al., 2018).

Ample evidence exists within the literature to support an innate, evolved fear response independent of associative experiences. These innate fear responses do not necessarily fit the current threat profile of the stimulus, but instead reflect its importance across nearly innumerable past generations. These responses can thus become the basis for specific phobias when maladaptive, despite these responses being largely vestigial in humans at baseline under modern conditions. This response is highly conserved in mammals, present from rodents up to humans, and not limited to a single specific sensory modality. It manifests in a relatively unaltered form throughout all stages of life, from infancy through adulthood. Finally, it is content-specific: highly selective for the threats specific to that species, making use of that species' sensory modalities best suited for threat detection.

1.2 The neurobiology of innate sensory valence

The existence of this predicted innate evolved fear response leads immediately to another question: what is the evolved fear module, and how does it arise? Further, is this evolved fear module specific to just fear alone, or is it one specific instance of a larger, more general innate valence system? Such a system, independent of modality, would likely require the following qualities: it must establish some form of content selectivity, arise relatively early in neural development, form in a heritable manner independent of any of the individual's associative/learning processes, and provide some theoretical functional or fitness benefit.

Neurobiological evidence for content selectivity in innate fear can be found in both primates and in rodents. Primate snake specificity can be difficult to establish due to the complexities of visual sensation (e.g. many separate factors, continuous inputs, high variability), but some links have been made to the pulvinar nucleus of the thalamus. The pulvinar nucleus is a thalamic region involved in visual processing and strongly connected to the amygdala that is necessary for visual attention and fast processing of threatening images, and its lateral nucleus is unique to primates (Romanski et al., 1997; Ward et al., 2005; Van Le et al., 2013). The macaque pulvinar responds most strongly and most quickly to images of snakes compared to any other images, and even preferentially responded to snakes in threatening postures compared to non-threatening postures (Van Le et al., 2013; 2014). Further, images of snakes elicit large increases in strength of gamma oscillations, which mediate visual attention and feedforward visual processing, faster than other salient visual stimuli (Van Le et al., 2016). Thus, innate visual snake selectivity in primates likely involves highly coherent responses by primate-specific pulvinar neurons, but the exact identity of these neurons, their properties, their connectivity, the snake-specific properties they respond to, and how they recognize these remains unknown.

Rodent content selectivity can be established in a more straightforward manner. Odorants are highly discrete, and detection is limited to whether the odorant is present, unlike visual stimuli, which are considerably more multivariate and require a much higher degree of processing to extract or collate to produce a response. Thus, content selectivity can and indeed does begin at initial sensation by the odorant receptor. The TAAR4 olfactory receptor binds PEA at ultrasensitive levels, and it does so non-redundantly (Ferrero et al., 2011; Dewan et al., 2013; Zhang et al., 2013). TAAR-expressing olfactory sensory neurons (OSNs) project to a distinct class of glomeruli in the dorsal main olfactory bulb (OB), which is required for innate aversive

responses (Kobayakawa et al., 2007; Johnson et al., 2012; Pacifico et al., 2012). *Taar4* deletion completely prevents the aversive response to PEA and multiple forms of cat urine, while retaining the innate aversive response to other pungent amines and 2,3,5-trimethyl-3-thiazoline (TMT), the active aversive compound in fox odor (Dewan et al., 2013). The olfactory receptor for TMT has also been discovered, as well, in the olfactory receptor Olfr1019, which is both sufficient and necessary for mice to manifest innate fear behavior to TMT (Saito et al., 2017).

Interestingly, the human and rodent olfactory systems serve as a potent model system to investigate the other potential necessary features of an innate valence system. First, innate olfactory responses are not just fearful in nature. Innate olfactory responses can also be positive or neutral in rodents, representing stimuli that could be neutral in a natural context or positive, like food or heterospecifics, driving approach behaviors instead (Root et al., 2014; Li and Liberles, 2015; Stowers et al., 2015). In both species, these odors comprise a small subset of perceptible chemical space, and the detection of specific odorants is both species-specific and under genetic control (Hayden et al., 2010; Ibarra-Soria et al., 2017; Saraiva et al., 2019). There is evidence that even humans display innate olfactory responses: the valence of specific odors is constant across cultures, and the perceptual features of novel odors are predictable *in silico* from structural features alone, revealing that olfactory responses are highly stereotyped and independent of individual experience (Keller et al., 2017; Arshamian et al., 2022; Lee et al., 2023). Odor intensity and valence for a wide range of odors are strongly modulated by individual genotype and human olfactory receptor expression is biased to recognize key food odorants, which points to an underlying genetic origin for these olfactory perceptual features (Keller et al., 2007; Menashe et al., 2007; McRae et al., 2012; Jaeger et al., 2013; Mainland et al., 2014; Saraiva et al., 2019; Trimmer et al., 2019; Li et al., 2022).

Further, all sensory systems have their own dedicated pathways for processing specific innately meaningful information. Gustation and somatosensation have low dimensional stimulus spaces, where nearly all information is innately relevant and discrete, with specific sensory receptors encoding specific innately relevant features of the stimulus. These sensory systems broadly follow a "labeled lines" paradigm, where qualities are generally established by receptor features of sensory neurons and maintained upstream in the circuit, though some integration and processing does occur early in the circuit. In gustation, these qualities (e.g. sweet, bitter) are detected in the taste buds and maintained along segregated taste-specific pathways up through the brainstem and gustatory thalamus to the gustatory cortex to diverge into separate generalized valence circuits in the amygdala; in somatosensation, features like pressure, pain, temperature, and pleasurable touch among others are detected by lineage-defined receptor populations, and subsequently segregated by location and modality in the dorsal horn, brainstem nuclei, and somatosensory cortex (Yarmolinsky et al., 2009; Todd, 2010; Abraira and Ginty, 2013; Ohla et al., 2019; Elias et al., 2023). On the other hand, vision and audition are extremely complex, continuous, high-dimensional, and represented by population codes; the vast majority of information is not innately relevant, where the small innately relevant subset of stimulus space is routed through the colliculi (Recanzone and Sutter, 2008; Gruters and Groh, 2012; Tanabe, 2013; Ito and Feldheim, 2018).

Given how widespread dedicated innate divisions of sensory systems are, it is highly likely that they are highly beneficial to neural function or to the overall reproductive fitness of the organism. On a theoretical level, innate systems can be represented as a transfer learning model like those in use in artificial neural networks (ANNs), where a general model is first trained on a more general large dataset and then trained in a task-specific manner on a smaller,

more curated dataset. In biological terms, the larger training dataset can be represented as the experiences across the organism's ancestry, with each generation akin to an epoch trying to maximize fitness. When possible, transfer learning from a large model is a far superior approach to fully training the model *de novo* on the curated dataset, avoiding overfitting, requiring far less training data and far fewer epochs to reach plateau, with significantly better performance both initially and once trained to plateau (Pan and Yang, 2010; Koulakov et al., 2022). Despite theoretical gains, this account still leaves the biological implementation unexplained.

The greatest issue with importing a pre-trained across generations is the "genomic bottleneck" problem, where a precise synaptic map of the human brain would require 5-6 orders of magnitude more information than can be possibly encoded within the entire genome at perfect efficiency, meaning that the precise connectivity on neuronal circuits is generally not explicitly specified in the genome (Zador, 2019). Instead, neuronal connectivity must be specified in a necessarily lossy manner, and the function of such circuits must be implemented in a robust manner. To permit the specification of such networks, the genome instead encodes simple, general rules with duplicated, modular structures, reducing the number of parameters to specify circuits and allowing their specification via scale-free mechanisms (Itzkovitz et al., 2008). These rules tend to govern neuronal development by controlling neuronal behavior throughout development spatially and/or molecularly (e.g. transcription factor gradients, axon guidance markers). These rules do not necessarily limit performance compared to more precisely specified networks, as ANNs trained using genomic bottleneck-compliant simple wiring principles either match or outperform traditional transfer learning networks, especially when the model must learn to perform tasks mimicking those faced by animals in naturalistic settings (Koulakov et al., 2022;

Barábasi et al., 2023). As a result, understanding the organization and processing rules of an innate sensory system may dovetail with understanding its molecular and spatial features.

1.3. Spatiomolecular organization of the main olfactory sytem

The relationship between odor content and neural architecture is visible from the very beginning of olfactory processing. This process starts with initial olfactory sensation, where an odorant molecule binds to one or more olfactory receptors in the olfactory epithelium (OE), with a general rule of one receptor per OSN, projecting to spatially stereotyped glomeruli in the olfactory bulb (OB). Olfactory sensory neurons sharing receptor identity display highly stereotyped spatial organization even within the olfactory epithelium, segregating continuously within and between five restricted zones (Ressler et al., 1993; Vassar et al., 1993; Miyamichi et al., Zhang et al., 2005; Tan et al., 2018). Interestingly, this only applies to spatiomolecular features of OE, as population encoding of olfactory features and identity is paradoxically performed in an extremely diffuse manner, with each odor being represented by ensembles of OSNs with multiple receptor identities across all five described zones (Malnic et al., 1999; Nara et al., 2011).

This spatial patterning continues one level deeper into the OB, where neurons expressing any given olfactory receptor converge on two spatially invariant glomeruli each, controlled by topographically variable spatial gradients of axon guidance molecules during development, helping establish specific wiring patterns between the two regions (Takeuchi et al., 2010). These glomeruli themselves localize to distinct, stereotyped topographies within broad regions in OB based on its upstream OSNs' receptor expression (Mombaerts et al., 1996; Soucy et al, 2009; Matsumoto et al, 2010; Nishizumi et al, 2019). The regional topography of both axonal wiring

patterns of specific types of upstream olfactory sensory neurons into MOB and MOB itself are themselves determined based on gene expression (Gogos et al., 2000; Kobayakawa et al., 2007; Bozza et al., 2009; Johnson et al., 2012; Wang et al., 2023). One of these regions, the dorsal OB, is enriched for glomeruli processing aversive odorants, and region-specific ablation of the dorsal zone as specified by gene expression is sufficient to ablate innate olfactory aversion, establishing a behavioral/functional relevance for regionalization within OB (Kobayakawa et al., 2007; Johnson et al., 2012; Pacifico et al., 2012; Dewan et al., 2013). Like the OE, however, such regionalization is not reflected in population encoding and activity, where it is similarly sparse, diffuse, and unrelated to behavioral phenotypes (Soucy et al., 2009; Ma et al., 2012; Chae et al., 2019).

Mitral and tufted cells within OB then synapse with OSNs at olfactory glomeruli and afferently transmit information to five different third-order regions involved in olfactory processing, the olfactory tubercle, piriform cortex, anterior olfactory nucleus, tenia tecta, and posterolateral cortical amygdala (plCoA), where these projections synapse in a topographically stereotyped pattern (Price, 1973; Buonviso et al., 1991; Sosulski et al., 2011; Imamura et al., 2020; Chen et al., 2022). For the first four regions listed, few spatiomolecular gradients can be identified, and all of them represent information in the same sparse, diffuse, identity-centric manner observed in the OE and the OB upstream in processing (Stettler and Axel, 2009; Payton et al., 2012; Iurilli and Datta, 2017; Roland et al., 2017; Tsuji et al., 2019; Cousens 2020; Lee et al., 2023). The one exception to this rule is the plCoA, which retains some evidence for spatial organization, primarily along the anteroposterior axis. First, plCoA inputs from OB are distributed from all over but biased dorsally, which contains these olfactory glomuruli responsive to innate aversive odors (Miyamichi et al., 2011). Second, though the entire plCoA responds to

aversive odors, the anterior cortical amygdala and the anterior portion of the posterolateral cortical amygdala responds almost exclusively to innately aversive odors, and the posterior plCoA responds to both appetitive and aversive odors, though there is some debate on the extensiveness and specificity of these response properties (Staples et al., 2008; Root et al., 2014; Govic and Paolini, 2015). Third, the inputs from OB to plCoA are extremely spatially compact and stereotyped, depending on the identity of the glomerulus, while inputs elsewhere are far more diffuse and homogenous (Sosulski et al., 2011). Finally, plCoA histology varies along its anteroposterior axis, where the anterior domain is bilaminar, bordered by the anterior cortical amygdala medially, and located on the ventral surface of the temporal cortex, while the posterior domain is trilaminar, bordered by the posteromedial cortical amygdala medially, and located on the ventrolateral transition of the temporal cortex.

In contrast to other third-order olfactory processing regions, the plCoA is much more specialized towards innate olfactory valence. Comparatively little has been published on its function, but the plCoA has been shown to be sufficient and necessary for both positive and negative innate olfactory valence behaviors (Root et al., 2014). Given the greater predominance of spatial patterning in plCoA compared to other third-order olfactory processing regions, it stands to reason that the plCoA's spatial organization could be related to how it organizes and controls these innate olfactory valence responses, especially given spatiomolecular patterning in other brain regions to overcome constraints imposed by genetic bottlenecking.

The current state of the literature on the innate olfactory system strongly supports a few key inferences about the nature of plCoA. First, differences do exist between aplCoA and pplCoA, given divergent histology in the two subregions, as well as their spatially segregated inputs. Second, plCoA broadly mediate innate olfactory valence, and has at least some degree of

segregation based on the direction of the odor's valence. Third, given the prior two inferences, it is highly likely that there is some stable feature of plCoA related to odor processing, that could correlate with its structure features as well.

In this work, I aim to determine a few key phenomena about the plCoA that could shed further light on the nature of this enigmatic region and how it controls and organizes innate olfactory valence. Before answering this question, however, I also examine the molecular organization of the ASt, a similarly situated transition region bordering the central amygdala and the tail of the striatum. By performing this molecular characterization, I was able to prepare to answer many of the later main questions of my thesis. Initially, I would like to understand the direct relationship between plCoA topography and innate olfactory valence behavior. If there is indeed a difference, I would like to then characterize the divergent features underlying these two subregions. I would then like to leverage these divergent features to affect these behaviors directly, drawing a line from the features organizing plCoA to behavior directly, moving past broad topographies. Finally, I would then like to determine why these features specifically induce their divergent behaviors. Through these successive lines of evidence, I can then identify what links specific odorants to their respective innate valences, assigning valence to stimuli based on their structural and molecular features alone in the absence of prior experience.

1.4. References

Abraira, V.E., Ginty, D.D. (2013). The Sensory Neurons of Touch. Neuron *79*.

Arshamian, A., Gerkin, R.C., Kruspe, N., Wnuk, E., Floyd, S., O'Meara, C., Garrido Rodriguez, G., Lundström, J.N., Mainland, J.D., Majid, A. (2022). The perception of odor pleasantness is shared across cultures. Curr. Biol. *32*, 2061-2066.e3.

Barabási, D.L., Beynon, T., Katona, Á., and Perez-Nieves, N. (2023). Complex computation from developmental priors. Nat. Commun. *14*, 2226.

Blanchard, D.C., Griebel, G., Blanchard, R.J. (2003). The mouse defense test battery: Pharmacological and behavioral assays for fear and anxiety. Eur. J. Pharmacol. *463*: 97-116.

Blanchard, R.J., Blanchard, D.C. (1971). Defensive reactions in the albino rat. Learn. Motiv. *2*: 351-362.

Bozza, T., Vassalli, A., Fuss, S., Zhang, J.-J., Weiland, B., Pacifico, R., Feinstein, P., Mombaerts, P. (2009). Mapping of class I and class II odorant receptors to glomerular domains by two distinct types of olfactory sensory neurons in the mouse. Neuron *61*, 220-233.

Buonviso, N., Revial, M. F. & Jourdan, F. (1991). The projections of mitral cells from small local regions of the olfactory bulb-an anterograde tracing study using PHA-L (Phaeseolus-Vulgaris Leukoagglutinin). Eur. J. Neurosci. *3*, 493-500.

Chan, T., Kyere, K., Davis, B.R., Shemyakin, A., Kabitzke, P.A., Shair, H.N., Barr, G.A., Wiedenmayer, C.P. (2011). The role of the medial prefrontal cortex in innate fear regulation in infants, juveniles, and adolescents. J. Neurosci. *31*: 4991-4999.

Chen, Y., Chen, X., Baserdem, B., Zhan, H., Li, Y., Davis, M.B., Kebschull, J.M., Zador, A.M., Koulakov, A.A., Albeanu, D.F. (2022). High-throughput sequencing of single neuron projections reveals spatial organization in the olfactory cortex. Cell *185*: 4117-4134.

Cook, M., Mineka, S. (1990). Selective associations in the observational conditioning of fear in rhesus monkeys. J. Exp. Psychol. Learn. Mem. Cogn. *16*: 372-389.

Cousens, G.A. (2020). Characterization of odor-evoked neural activity in the olfactory peduncle. IBRO Rep. *9*, 157–163.

de Oliveira Crisanto, K., de Andrade, W.M.G., de Azevedo Silva, K.D., Lima, R.H., de Oliveira Costa, M.S.M., Cavalcante, J.d-S., de Lima, R.R.M., do Nascimiento Jr., E.S., Cavalcante, J.C. (2015). The differential mice response to cat and snake odor. Physiol. Behav. *152*: 272-279.

Dewan, A., Pacifico, R., Zhan, R., Rinberg, D., Bozza, T. (2013). Non-redundant coding of aversive odors in the main olfactory pathway. Nature. *497*: 486-490.

Elias, L.J., Succi, I.K., Schaffler, M.D., Foster, W., Gradwell, M.A., Bohic, M., Fushiki, A., Upadhyay, A., Ejoh, L.L., Schwark, R., Frazer, R., Bistis, B., Burke, J.E., Saltz, V., Boyce, J.E., Jhumka, A., Costa, R.M., Abraira, V.E., Abdus-Saboor, I. (2023). Touch neurons underlying dopaminergic pleasurable touch and sexual receptivity. Cell *186*, 577-590.e16.

Ferrero, D.M., Lemon, J.K., Fluegge, D., Pashkovski, S.L., Korzan, W.J., Datta, S.R., Spehr, M., Fendt, M., Liberles, S.D. (2011). Detection and avoidance of a carnivore odor by prey. Proc. Natl. Acad. Sci. U.S.A. *108*: 11235-11240.

Fredrikson, M., Annas, P., Fischer, H., Wik, G. (1996). Gender and age differences in the prevalence of specific fears and phobias. Behav. Res. Ther. *34*: 33-39.

Gogos, J. A., Osborne, J., Nemes, A., Mendelsohn, M., Axel, R. (2000). Genetic ablation and restoration of the olfactory topographic map. Cell *103*, 609-620.

Govic, A. & Paolini, A.G. (2015). *In vivo* electrophysiological recordings in amygdala subnuclei reveal selective and distinct responses to a behaviorally identified predator odor. J. Neurophysiol. *113*, 1423-1436.

Gruters, K., Groh, J. (2012). Sounds and beyond: multisensory and other non-auditory signals in the inferior colliculus. Front. Neural Circuits *6*.

Hayden, S., Bekaert, M., Crider, T.A., Mariani, S., Murphy, W.J., and Teeling, E.C. (2010). Ecological adaptation determines functional mammalian olfactory subgenomes. Genome Res. *20*, 1–9.

Hoehl, S., Hellmer, K., Johansson, M., Gredebäck, G. (2017). Itsy bitsy spider…: Infants react with increased arousal to spiders and snakes. Front. Psychol. *8:* 1710.

Ibarra-Soria, X., Nakahara, T.S., Lilue, J., Jiang, Y., Trimmer, C., Souza, M.A., Netto, P.H., Ikegami, K., Murphy, N.R., Kusma, M., Kirton, A., Saraiva, L.R., Keane, T.M., Matsunami, H., Mainland, J., Papes, F., Logan, D.W. (2017). Variation in olfactory neuron repertoires is genetically controlled and environmentally modulated. eLife *6*, e21476.

Imamura, F., Ito, A., LaFever, B.J. (2020). Subpopulations of Projection Neurons in the Olfactory Bulb. Front. Neural Circuits *14*.

Isbell, L.A. (2006). Snakes as agents of evolutionary change in primate brains. J. Hum. Evol. *51*: 1-35.

Ito, S., Feldheim, D.A. (2018). The Mouse Superior Colliculus: An Emerging Model for Studying Circuit Formation and Function. Front. Neural Circuits *12*, 10.

Itzkovitz, S., Baruch, L., Shapiro, E., Segal, E. (2008). Geometric constraints on neuronal connectivity facilitate a concise synaptic adhesive code. Proc. Natl. Acad. Sci. U.S.A., *105*: 9278–9283.

Iurilli, G., and Datta, S.R. (2017). Population coding in an innately relevant olfactory area. Neuron *93*, 1180-1197.

Jaeger, S.R., McRae, J.F., Bava, C.M., Beresford, M.K., Hunter, D., Jia, Y., Chheang, S.L., Jin, D., Peng, M., Gamble, J.C., Atkinson, K.R., Axten, L.G., Paisley, A.G., Tooman, L., Pineau, B., Rouse, S.A., Newcomb, R.D. (2013). A mendelian trait for olfactory sensitivity affects odor experience and food selection. Curr. Biol. *23*, 1601–1605.

Johnson, M.A., Tsai, L., Roy, D.S., Valenzuela, D.H., Mosley, C., Magklara, A., Lomvardas, S., Liberles, S.D., Barnea, G. (2012). Neurons expressing trace amine-associated receptors project to discrete glomeruli and constitute a distinct olfactory subsystem. Proc. Natl. Acad. Sci. U.S.A. *109:* 13410-13415.

Keller, A., Gerkin, R.C., Guan, Y., Dhurandhar, A., Turu, G., Szalai, B., Mainland, J.D., Ihara, Y., Yu, C.W., Wolfinger, R., Vens, C., Scheitgat, L., de Grave, K., Norel, R., DREAM Olfaction Prediction Consortium, Stolovitzky, G., Cecchi, G., Vosshall, L.B., Meyer, P. (2017). Predicting human olfactory perception from chemical features of odor molecules. Science *355*, 820–826.

Keller, A., Zhuang, H., Chi, Q., Vosshall, L.B., and Matsunami, H. (2007). Genetic variation in a human odorant receptor alters odour perception. Nature *449*, 468–472.

Kobayakawa, K., Kobayakawa, R., Matsumoto, H., Oka, Y., Imai, T., Ikawa, M., Okabe, M., Ikeda, T., Itohara, S., Kikusui, T., Mori, K., Sakano, H. (2007). Innate versus learned odour processing in the mouse olfactory bulb. Nature. *450:* 503-510.

Koulakov, A., Shuvaev, S., Lachi, D., Zador, A. (2022). Encoding innate ability through a genomic bottleneck. bioRxiv.

Lee, B.K., Mayhew, E.J., Sanchez-Lengeling, B., Wei, J.N., Qian, W.W., Little, K.A., Andres, M., Nguyen, B.B., Moloy, T., Yasonik, J., Parker, J.K., Gerken, R.C., Mainland, J.D., Wiltschko, A.B. (2023). A principal odor map unifies diverse tasks in olfactory perception. Science *381*, 999–1006.

Lee, D., Liu, L., and Root, C.M. (2023). Transformation of value signaling in a striatopallidal circuit. eLife *12*.

Li, B., Kamarck, M.L., Peng, Q., Lim, F.-L., Keller, A., Smeets, M.A.M., Mainland, J.D., and Wang, S. (2022). From musk to body odor: Decoding olfaction through genetic variation. PLoS Genet. *18*, e1009564.

Li, Q., and Liberles, S.D. (2015). Aversion and Attraction through Olfaction. Curr. Biol. 25, R120–R129.

LoBue, V., DeLoache, J.S. (2008). Detecting the snake in the grass: Attention to fear-relevant stimuli by adults and small children. Psychol. Sci. *19:* 284-289.

LoBue, V, DeLoache, J.S. (2010). Superior detection of threat-relevant stimuli in infancy. Dev. Sci. *13:* 221-228.

Ma, L., Qiu, Q., Gradwohl, S., Scott, A., Yu, E.Q., Alexander, R., Wiegraebe, W., Yu, C.R. (2012). Distributed representation of chemical features and tunotopic organization of glomeruli in the mouse olfactory bulb. Proc. Natl. Acad. Sci. U.S.A. *109*, 5481–5486.

Mainland, J.D., Keller, A., Li, Y.R., Zhou, T., Trimmer, C., Snyder, L.L., Moberly, A.H., Adipietro, K.A., Liu, W.L.L., Zhuang, H., Zhan, S., Lee, S.S., Lin, A., Matsunami, H. (2014). The missense of smell: Functional variability in the human odorant receptor repertoire. Nat. Neurosci. *17*, 114–120.

Malnic, B., Hirono, J., Sato, T., Buck, L.B. (1999). Combinatorial Receptor Codes for Odors. Cell *96*, 713–723.

Matsumoto, H., Kobayakawa, K., Kobayakawa, R., Tashiro, T., Kenji, M., Sakano, H., Kensaku, M. (2010). Spatial arrangement of glomerular molecular-feature clusters in the odorant-receptor class domains of the mouse olfactory bulb. J Neurophysiol *103*, 3490–3500.

McNally, R.J. (2016). The legacy of Seligman's "Phobias and Preparedness" (1971). Behav. Ther. *47:* 585-594.

McRae, J.F., Mainland, J.D., Jaeger, S.R., Adipietro, K.A., Matsunami, H., Newcomb, R.D. (2012). Genetic variation in the odorant receptor OR2J3 is associated with the ability to detect the "grassy" smelling odor, cis-3-hexen-1-ol. Chem. Senses *37*, 585–593.

Menashe, I., Abaffy, T., Hasin, Y., Goshen, S., Yahalom, V., Luetje, C.W., Lancet, D. (2007). Genetic elucidation of human hyperosmia to isovaleric acid. PLOS Biol. 5, e284.

Mineka, S., Keir, R., Price, V. (1980). Fear of snakes in wild- and laboratory-reared rhesus monkeys (*Macaca mulatta*). Learn. Behav. *8*: 653-663.

Mineka, S., Davidson, M., Cook, M., Keir, R. (1984). Observational conditioning of snake fear in rhesus monkeys. J. Abnorm. Psychol. *93*: 355-372.

Miyamichi, K., Serizawa, S., Kimura, H. M. & Sakano, H. (2005). Continuous and overlapping expression domains of odorant receptor genes in the olfactory epithelium determine the dorsal/ventral positioning of glomeruli in the olfactory bulb. J. Neurosci. *25*, 3586.

Mombaerts, P., Wang, F., Dulac, C., Chao, S.K., Nemes, A., Mendelsohn, M., Edmondson, J. (1996). Visualizing an olfactory sensory map. Cell *87*, 675–686.

Muris, P., Merckelbach, H., Collaris, R. (1997). Common childhood fears and their origins. Behav. Res. Ther. *35:* 929-937.

Murray, S.G., King, J.E. (1973). Snake avoidance in feral and laboratory reared squirrel monkeys. Behaviour. *18:* 281-288.

Nara, K., Saraiva, L.R., Ye, X., Buck, L.B. (2011). A large-scale analysis of odor coding in the olfactory epithelium. J. Neurosci. *31*, 9179–9191.

New, J.J., German, T.C. (2015). Spiders at the cocktail party: an ancestral threat that surmounts inattentional blindness. Evol. Hum. Behav. *36:* 165-173.

Nishizumi, H., Miyashita, A., Inoue, N., Inokuchi, K., Aoki, M., Sakano, H. (2019). Primary dendrites of mitral cells synapse unto neighboring glomeruli independent of their odorant receptor identity. Commun. Biol. *2*, 1-12.

Ohla, K., Yoshida, R., Roper, S.D., Di Lorenzo, P.M., Victor, J.D., Boughter, J.D., Fletcher, M., Katz, D.B., Chaudhari, N. (2019). Recognizing Taste: Coding Patterns Along the Neural Axis in Mammals. Chem. Senses *44*, 237–247.

Öhman, A., Mineka, S. (2001a). Fears, phobias, and preparedness: Toward an evolved model of fear and fear learning. Psychol. Rev. *108*: 483-522.

Öhman, A., Flykt, A., Esteves, F. (2001b). Emotion drives attention: Detecting the snake in the grass. J. Exp. Psychol. Gen. *130:* 466-478.

Pacifico, R., Dewan, A., Cawley, D., Guo, C., Bozza, T. (2012). An olfactory subsystem that mediates high-sensitivity detection of volatile amines. Cell Rep. *2*: 76-88.

Pavlov, I.P. (1928). Lectures on conditioned reflexes. New York: International Publishers.

Pan, S. J., Yang, Q. (2010). A survey on transfer learning. IEEE Trans. Knowl. data Eng. *22*, 1345-1359.

Payton, C.A., Wilson, D.A., and Wesson, D.W. (2012). Parallel odor processing by two anatomically distinct olfactory bulb target structures. PloS One *7*, e34926.

Poulton, R., Menzies, R.G. (2002a). Non-associative fear acquisition: a review of the evidence from retrospective and longitudinal research. Behav. Res. Ther. *40:* 127-149.

Poulton, R., Menzies, R.G. (2002b). Fears born *and* bred: toward a more inclusive theory of fear acquisition. Behav. Res. Ther. *40:* 197-208.

Price, J. L. (1973). An autoradiographic study of complementary laminar patterns of termination of afferent fibers to the olfactory cortex. J. Comp. Neurol. *150*, 87–108.

Rampin, O., Jerome, N., Saint-Albin, A., Ouali, C., Boué, F., Meunier, N., Nielsen, L.B. (2018). Where is the TMT? GC-MS analyses of fox feces and behavioral responses of rats to fear-inducing odors. Chem. Senses *43*:105-115.

Recanzone, G.H., Sutter, M.L. (2008). The Biological Basis of Audition. Annu. Rev. Psychol. *59*, 10.

Ressler, K. J., Sullivan, S. L., Buck, L. B. (1993). A zonal organization of odorant receptor gene expression in the olfactory epithelium. Cell *73*, 597–609.

Roland, B., Deneux, T., Franks, K.M., Bathellier, B., and Fleischmann, A. (2017). Odor identity coding by distributed ensembles of neurons in the mouse olfactory cortex. eLife *6*, e26337.

Romanski, L.M., Giguere, M., Bates, J.F., Goldman-Rakic, P.S. (1997). Topographic organizations of medial pulvinar connections with the prefrontal cortex in the rhesus monkey. J. Comp. Neurol. 379: 313-332.

Root, C.M., Denny, C.A., Hen, R., Axel, R. (2014). The participation of cortical amygdala in innate, odour-driven behavior. Nature. *515*: 269-275.

Saito, H., Nishizumi, H., Suzuki, S., Matsumoto, H., Ieki, N., Abe, T., Kiyonari, H., Morita, M., Yokota, H., Hirayama, N., Yamazaki, T., Kikusui, T., Mori, K., Sakano, H. (2017). Immobility responses are induced by photoactivation of single glomerular species responsive to fox odour TMT. Nat. Commun. *8*: 16011.

Saraiva, L.R., Kondoh, K., Ye, X., Yoon, K.H., Hernandez, M., Buck, L.B. (2016). Combinatorial effects of odorants on mouse behavior. Proc. Natl. Acad. Sci. U.S.A. *113*: E3300-E3306.

Saraiva, L.R., Riveros-McKay, F., Mezzavilla, M., Abou-Moussa, E.H., Arayata, C.J., Makhlouf, M., Trimmer, C., Ibarra-Soria, X., Khan, M., Van Gerven, L., Jorissen, M., Gibbs, M., O'Flynn, C., McGrane, S., Mombaerts, P., Marioni, J.C., Mainland, J.D., Logan, D.W. (2019). A transcriptomic atlas of mammalian olfactory mucosae reveals an evolutionary influence on food odor detection in humans. Sci. Adv. *5*, eaax0396.

Seligman, M.E.P. (1971). Phobias and preparedness. Behav. Ther*. 2:* 307-320.

Sosulski, D.L., Lissitsyna Bloom, M., Cutforth, T., Axel, R., Datta, S.R. (2011). Distinct representations of olfactory information in different cortical centres. Nature *472*, 213–219.

Soucy, E. R., Albeanu, D. F., Fantana, A. L., Murthy, V. N., Meister, M. (2009). Precision and diversity in an odor map on the olfactory bulb. Nat Neurosci *12*, 210–220.

Staples, L.G., McGregor, I.S., Apfelbach, R. & Hunt, G.E. (2008). Cat odor, but not trimethylthiazoline (fox odor), activates accessory olfactory and defense-related brain regions in rats. Neuroscience *151*, 937-947.

Stettler, D.D., and Axel, R. (2009). Representations of odor in the piriform cortex. Neuron *63*, 854-864.

Stowers, L., Cameron, P., and Keller, J.A. (2013). Ominous Odors: olfactory control of instinctive fear and aggression in mice. Curr. Opin. Neurobiol. *23*: 339–345.

Stowers, L., and Kuo, T.-H. (2015). Mammalian pheromones; emerging properties and mechanisms of detection. Curr. Opin. Neurobiol. *34*: 103–109.

Takeuchi, H., Inokuchi, K., Aoki, M., Suto, F.. Tsuboi, A., Matsuda, I., Suzuki, M., Aiba, A., Serizawa, S., Yoshihara, Y., Fujisawa, H., Sakano, H. (2010). Sequential arrival and graded secretion of Sema3F by olfactory neuron axons specify map topography at the bulb. Cell *141*: P1056-P1067.

Tanabe, S. (2013). Population codes in the visual cortex. Neurosci. Res. *76*, 101–105.

Todd, A.J. (2010). Neuronal circuitry for pain processing in the dorsal horn. Nat. Rev. Neurosci. *11*, 823–836.

Trimmer, C., Keller, A., Murphy, N.R., Snyder, L.L., Willer, J.R., Nagai, M.H., Katsanis, N., Vosshall, L.B., Matsunami, H., and Mainland, J.D. (2019). Genetic variation across the human olfactory receptor repertoire alters odor perception. Proc. Natl. Acad. Sci. U.S.A. *116*, 9475–9480.

Van Le, Q., Isbell, L.A., Matsumoto, J., Nguyen, M., Hori, E., Maior, R.S., Tomaz, C., Tran, A.H., Ono, T., Nishijo, H. (2013). Pulvinar neurons reveal neurobiological evidence of past selection for rapid detection of snakes. Proc. Natl. Acad. Sci. U.S.A. *110*: 19000-19005.

Van Le, Q., Isbell, L.A., Matsumoto, J., Le, V.Q., Hori, E., Tran, A.H., Maior, R.S., Tomaz, C., Ono, T., Nishijo, H. (2014). Monkey pulvinar neurons fire differentially to snake postures. PLoS ONE. *9*: e114258.

Van Le, Q., Isbell, L.A., Matsumoto, J., Le, V.Q., Nishimaru, H., Etsuro, H., Maior, R.S., Tomaz, C., Ono, T., Nishijo, H. (2016). Snakes elicit earlier, and monkey faces, later, gamma oscillations in macaque pulvinar neurons. Sci. Rep. *6*: 20595.

Vassar, R., Ngai, J., Axel, R. (1993). Spatial segregation of odorant receptor expression in the mammalian olfactory epithelium. Cell *74*, 309–318.

Vernet-Maury E, Le Magnen J, Chanel J. (1968). Comportement émotif chez le rat; influence de l'odeur d'un prédateur et d'un non-prédateur. C R Acad Sci Hebd Seances Acad Sci D. *267*:331–334.

Ward, R., Danziger, S., Bamford, S. (2005). Response to visual threat following damage to the pulvinar. Curr. Biol. *15*: 571-573.

Wang, I.-H., Murray, E., Andrews, G., Jiang, H.-C., Park, S.J., Donnard, E., Durán-Laforet, V., Bear, D.M., Faust, T.E., Garber, M., Baer, C.E., Schafer, D.P., Weng, Z., Chen, F., Macosko,

E.Z. (2022). Spatial transcriptomic reconstruction of the mouse olfactory glomerular map suggests principles of odor processing. Nat. Neurosci. *25*, 484-492.

Yarmolinsky, D.A., Zuker, C.S., Ryba, N.J.P. (2009). Common Sense about Taste: From Mammals to Insects. Cell *139*, 234–244.

Zador, A.M. (2019). A critique of pure learning and what artificial neural networks can learn from animal brains. Nat. Commun. *10*, 3770.

Zhang, J., Pacifico, R., Cawley, D., Feinstein, P., Bozza, T. (2013). Ultrasensitive detection of amines by a trace amine-associated receptor. J. Neurosci. *33:* 3228-3239.

Zhang, X., Rogers, M., Tian, H., Zhang, X., Zou, D.-J., Liu, J., Ma, M., Shepherd, G.M., Firestein, S.J. (2004). High-throughput microarray detection of olfactory receptor gene expression in the mouse. Proc. Natl. Acad. Sci. U.S.A. *101*, 14168.

Chapter 2: Amygdalostriatal transition zone neurons encode sustained valence to direct conditioned behaviors

2.1 Abstract

In order to respond appropriately to threats in the environment, the brain must rapidly determine whether a stimulus is important and whether it is positive or negative, and then use that information to direct behavioral responses. Neurons in the amygdala have long been implicated in valence encoding and in fear responses to threatening stimuli, but show transient firing responses in response to these stimuli that do not match the timescales of associated behavioral responses. For decades, there has been a logical gap in how behavioral responses could be mediated without an ensemble representation of the internal state of valence that has rapid onset, high signal-to-noise, and is sustained for the duration of the behavioral state. Here, we present the amygdalostriatal transition zone (ASt) as a missing piece of this highly conserved process that is of paramount importance for survival, which does exactly this: represents an internal state (e.g. fear) that can be expressed in multiple motor outputs (e.g. freezing or escape). The ASt is anatomically positioned as a "shortcut" to connect the corticolimbic system (important for evaluation) with the basal ganglia (important for action selection) with the inputs of the amygdala and the outputs of the striatum – ideally poised for evaluating and responding to environmental threats. From in vivo cellular resolution recordings that include both electrophysiology and calcium imaging, we find that ASt neurons are unique in that they are sparse coding, extremely high signal-to-noise, and also maintain a sustained response for negative valence stimuli for the duration of the defensive behavior – a rare but essential combination. We further show that photostimulation of the ASt is sufficient to drive freezing and avoidance behaviors. Using single-nucleus RNA sequencing and *in situ* RNA labelling we

generate a comprehensive profile of cell types and gene expression in the ASt, and find the ASt is genetically distinct from adjacent striatal and amygdalar structures. We also find that the ASt has a greater proportion of neurons expressing Drd2 than neurons expressing Drd1a, a unique feature compared to other regions of the striatum. Using in vivo calcium imaging, we show that that this *Drd2+* population robustly encodes stimuli of negative valence, and in loss-of-function experiments find that optogenetic inhibition of *Drd2+* ASt neurons causes a striking reduction in cue-conditioned fear responses. Together, our findings identify the ASt as a previously unappreciated critical missing link for encoding learned associations and directing ongoing behavior.

2.2 Introduction

Associative learning is critical for survival and is necessary to direct appropriate behavioral responses to environmental stimuli that predict rewards or punishments. However, appetitive and aversive behaviors are inherently distinct. Appetitive behaviors such as hunting, foraging, and mating are generally self-initiated motor sequences that may or may not be time-locked to the presentation of a reward-predictive stimulus. In contrast, for effective defensive and escape behaviors environmental stimuli must trigger an immediate response; to respond appropriately, we need to select important information, assign valence, select an action, and execute that action for the duration of the threat.

For decades, the amygdala has been studied as a key structure for orchestrating defensive fear responses, and shown to be a critical site for encoding learned associations of both positive and negative valence (Gallagher and Holland, 1994; Jennings et al., 2013; Josselyn et al., 2015; Kim et al., 2016; Kong and Zweifel, 2021; LeDoux, 1992; Marcinkiewcz et al., 2016; Maren,

2005; Piantadosi et al., 2022; Quirk et al., 1995; Tye, 2018; Weiskrantz, 1956). In particular, the central nucleus of the amygdala (CeA) and its outputs play a key role in conditioned fear responses and mediate freezing and escape behaviors (Ciocchi et al., 2010; Fadok et al., 2017; Haubensak et al., 2010; Keifer et al., 2015; LeDoux et al., 1988; Tovote et al., 2016).

However, an unresolved mystery in current models of amygdala function is the discrepancy in timescales between the activity of amygdala complex neurons and the conditioned behaviors that they drive. Neurons in the amygdala exhibit increased responses to a conditioned stimulus (CS), but these are often only transient, lasting less than a second from the onset of a sensory stimulus (Goosens and Maren, 2004; Li et al., 2022; Quirk et al., 1995, 1995; Tye et al., 2008; Whittle et al., 2021). This does not match the behaviors that can be elicited by these stimuli, which include defensive responses expressed for the full duration of the threat presentation that would be essential to survive or evade threats in the real world. Mediating these behaviors would ideally require a neural substrate which is connected to circuits for learning and valence processing, can rapidly respond to stimuli, and is upstream of circuits able to direct appropriate behaviors.

A structure which is well-situated to play a role in these processes is the woefully understudied amygdalostriatal transition zone (ASt). The function of the ASt in encoding valence and directing behavior is currently unknown and represents a major gap in our understanding of circuits mediating motivated behaviors. However, the limited data collected of ASt neuron activity shows that the ASt receives the necessary information to encode learned associations. For instance, single-unit recordings indicate that ASt neurons respond to auditory, visual and somatosensory stimuli, including painful stimuli such as foot shocks (Romanski et al., 1993; Uwano et al., 1995). ASt responses to stimuli are fast, with lower latency than responses in the

basolateral amygdala (BLA) or CeA, and of similar latency to responses in the lateral amygdala (LA) (Bordi et al., 1993; Quirk et al., 1995; Uwano et al., 1995). Indeed, like the LA, the ASt receives converging inputs from thalamic and cortical pathways, including calretinin-expressing thalamic neurons that are known to relay sensory information critical for learned associations (Barsy et al., 2020). There also exists a robust direct projection from the LA to the ASt (Jolkkonen et al., 2001; Wang et al., 2002). The LA is known to be a key site for emotional memory formation (Blair et al., 2001; Fanselow and LeDoux, 1999; Maren, 2005; Maren and Quirk, 2004; Sah et al., 2008), and the existence of this direct LA input to the ASt is intriguing as propagation of signals from the LA to ASt is even more rapid than from the LA to the BLA (Wang et al., 2002). This suggests that information about learned associations encoded in the LA may be rapidly routed to the ASt to mediate components of conditioned responses to stimuli.

Together, these studies show that the ASt can rapidly respond to stimuli and is connected with known amygdala circuits for emotional learning and valence processing. However, the outputs of the ASt diverge significantly from the amygdala complex, and are integrated with striatal pathways known to control action selection and execution. ASt neurons project to the globus pallidus and substantia nigra pars lateralis (Jolkkonen et al., 2001; Shammah-Lagnado et al., 1999), which are both major target structures of the 'direct' and 'indirect' striatal pathways characterized by the respective expression of dopamine receptor 1 (Drd1a) and dopamine receptor 2 (Drd2) in striatal medium spiny neurons (MSNs) (Gerfen et al., 1990; Nelson and Kreitzer, 2014). The direct and indirect pathways have been shown to mediate opposing and complementary effects on action selection and motor output (Cui et al., 2013; Kravitz et al., 2012, 2010; Markowitz et al., 2018; Nelson and Kreitzer, 2014; Tai et al., 2012). Thus, the outputs of the ASt are well-situated to mediate the selection and expression of specific

behaviors guided by learned valence assignment. This positions the ASt at a crucial intersection of systems in the brain, bridging corticolimbic circuits involved in the recognition and learning of threats with basal ganglia circuits responsible for selection and execution of actions.

To establish the ASt's unique functional role and to distinguish it from other well-studied structures of complementary function, we perform a systematic comparison spanning systems (large-scale ensemble dynamics), circuit (cell-type specific dynamics and manipulations), and molecular (transcriptomic profiling) levels of investigation across three neighboring regions of similar composition. We perform high-density electrophysiological recordings in the ASt and the adjacent CeA and tail of striatum (TS), and find that ASt neurons show robust sustained responses to cues of negative valence across behaviorally-relevant time scales, and that activation of ASt neurons is sufficient to drive robust freezing and avoidance behaviors. We also characterize the cell types and gene expression in the ASt and surrounding structures using single-nucleus RNA sequencing, and find that the ASt is a genetically distinct region with a significantly greater proportion of Drd2+ neurons than other regions of the striatum. Finally, we show that Drd2+ ASt neurons encode stimuli of negative valence and are critical for expression of cue-conditioned fear responses, but not reward responses or contextual fear. Together, these findings identify the ASt as a novel structure of interest for associative learning and as a critical missing piece of the neural mechanisms for expression of motivated behaviors.

2.3 Results

2.3.1. The ASt encodes conditioned stimuli

The ASt is extensively interconnected with circuits known to be involved in associative learning (Figure 2.1A), and we first sought to determine whether ASt neurons were involved in the

encoding of conditioned responses to stimuli of positive and negative valence. We began by recording the endogenous activity of ASt neurons in freely-moving mice using chronically implanted probes for in vivo electrophysiology (Figure 2.1B, S2.1A-C). ASt neuron activity was examined in a two-tone discrimination task, where a pair of distinct pure tones (20s in length, 3.5 kHz and 20 kHz, counterbalanced for each conditioned stimulus (CS) type within all groups) predicted either an aversive footshock (100 ms, 0.7 mA) or delivery of a reward (7.5 μL chocolate Ensure™) to a reward port in the test apparatus. Mice were trained on this task until they showed robust defensive behaviors in response to CS-shock and port entry responses to CS-reward (Figure S2.1D-F). The behavioral discrimination between the two tones indicated the mice had successfully learned the contingencies of each CS-type, allowing us to examine their neural activity for encoding of the learned associations and conditioned behaviors. To distinguish between responses of neurons to sensory stimuli and conditioned responses driven by associative learning, we also examined neural responses to stimuli in 'unpaired' control group mice, who received the same tone and US presentations but in randomized order and explicitly unpaired so the tones had no predictive significance.

Our recording probes targeting the ASt also recorded neuronal responses from the adjacent regions, the tail of the striatum (TS) and central nucleus of the amygdala (CeA), both predominantly GABAergic regions which lie immediately dorsal and ventral, respectively, to the ASt (Figure 2.1A). This allowed us to record conditioned responses to CS-shock and CS-reward in these structures simultaneously during the same task, and compare them to those of the ASt. We began by examining recorded neurons from all regions together, using hierarchical clustering to group neurons based on their response profiles to each CS type (Figure 2.1D). Neurons from the ASt, TS and CeA showed considerable heterogeneity in responses to stimuli of positive and

Figure 2.1. ASt neurons have distinct responses to stimuli of positive and negative valence.

(A) The amygdalostriatal transition zone (ASt), surrounding regions, and major inputs and outputs of the ASt.

(B) Representative image of Neuropixels recording probe targeting the ASt and adjacent regions.

(C) Two-tone discrimination task design for in vivo electrophysiology recordings.

(D) Hierarchical clustering of ASt, tail of striatum (TS) and central nucleus of the amygdala (CeA) neurons based on responses to CS-shock and CS-reward. Dendrogram shows clustering of neurons based on responses to cues of positive and negative valence. Heatmap rows show the mean Z-score PSTH for each individual neuron's responses to both CS-shock and CS-reward in paired group mice (N=15 mice, 222 neurons ASt, 5 mice 280 neurons TS, 2 mice 25 neurons CeA).

(E) Z-score average responses to CS-shock and CS-reward in each identified functional cluster. Inset pie charts show the proportion of neurons from each region in that cluster, normalized by number of neurons recorded from each region.

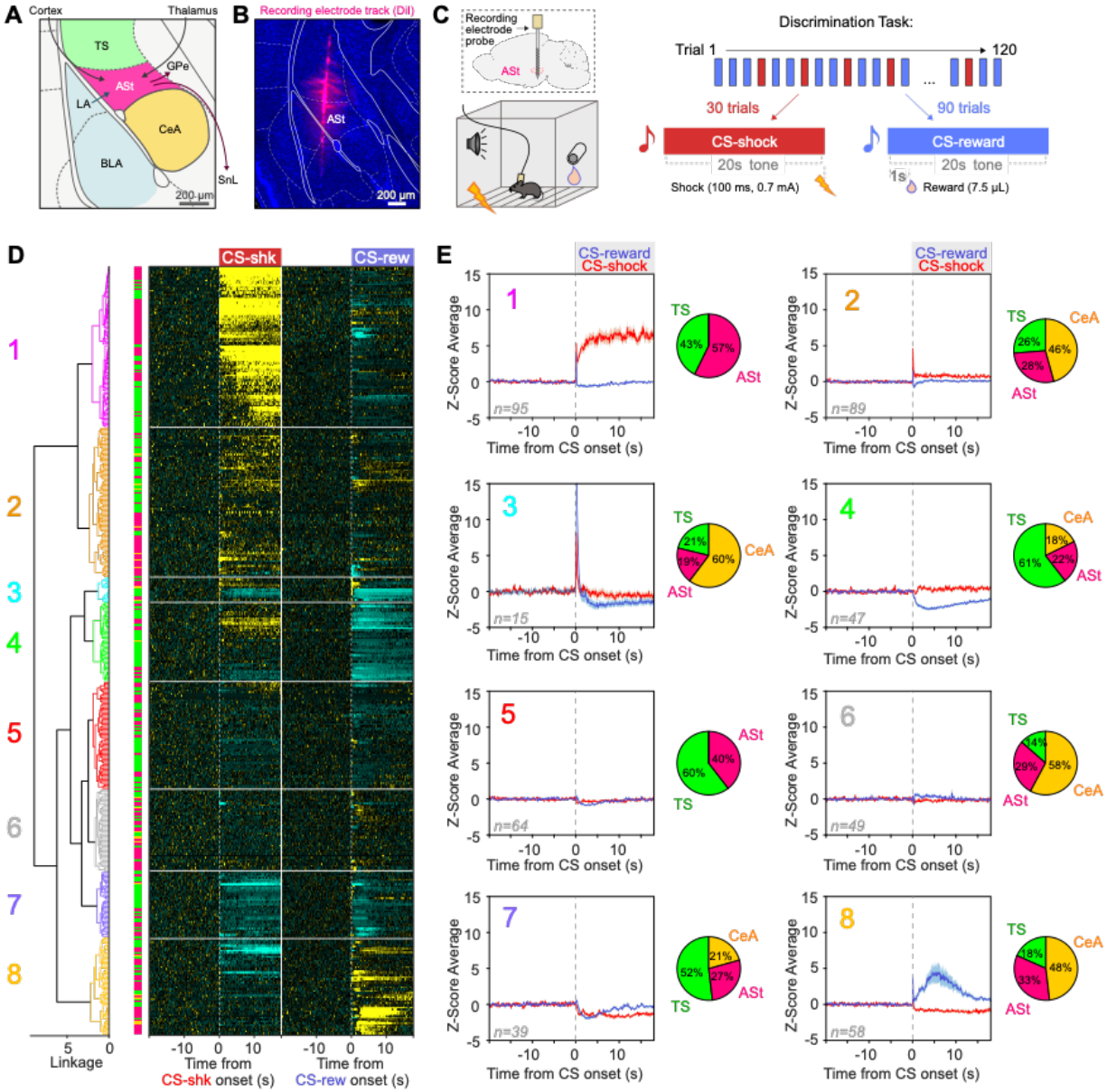
A
Cortex
Thalamus
TS
GPe
ASt
LA
CeA
BLA
SnL
200 μm
B
Recording electrode track (DiI)
ASt
200 μm
C
Recording electrode probe
ASt
Discrimination Task:
Trial 1
120
30 trials
90 trials
CS-shock
20s tone
Shock (100 ms, 0.7 mA)
CS-reward
20s tone
1s
Reward (7.5 μL)
D
CS-shk
CS-rew
Linkage
Time from CS-shk onset (s)
Time from CS-rew onset (s)
E
CS-reward
CS-shock
Z-Score Average
Time from CS onset (s)
n=95
n=89
n=15
n=47
n=64
n=49
n=39
n=58
TS
CeA
ASt
43%
57%
26%
46%
28%
21%
19%
60%
18%
61%
22%
40%
60%
14%
29%
58%
21%
52%
27%
18%
33%
48%

negative valence, and we examined the average responses and the representation of neurons from each region within each functional cluster (Figure 2.1E). Neurons from the CeA and ASt formed a relatively greater proportion of neurons which had transient responses to CS-shock and CS-reward (Cluster 3), while neurons from the TS were the greatest relative proportion of neurons which showed inhibitory responses to CS reward (Clusters 2 and 9). However, ASt neurons were the dominant representative in one of the most highly responsive clusters (Cluster 1), a functional cluster of neurons which showed minimal responses to CS-reward, but robust and sustained responses to CS-shock.

We then examined each individual region's overall neural responses to stimuli of positive and negative valence (Figure 2.2A-C). Our recordings revealed that ASt neurons, on a population level, showed conditioned responses to CS-shock and CS-reward cues, a previously unknown role for this structure (Figure 2.2A). To further characterize encoding of these cues across regions, we examined trial-averaged trajectories of neuron population activity in the ASt, TS and CeA during presentation of each CS (Figure 2.2D-F, Supplementary Video 1-3) (Allsop et al., 2018; Cunningham and Yu, 2014; Glaser et al., 2020; Padilla-Coreano et al., 2022). In paired group mice, ASt neuron trajectories during CS-shock and CS-reward moved in orthogonal directions from the time of cue onset, with CS-shock trajectories maintaining distance from the baseline position throughout the entire CS. The divergent paths of the trajectories indicate that, even during the transient period where ASt neurons respond to both CS-shock and CS-reward, the population distinctly encoded the two stimuli of opposing valences despite the apparent similarity in the perievent time histograms (Figure 2.2A). To quantify the responses in each region, we examined phasic (1-100 ms) and sustained (100 ms – 18s) response windows after cue onset to both CS-shock and CS-reward in the ASt, TS and CeA, and compared responses

Figure 2.2. ASt neurons encode sustained conditioned responses to stimuli of negative valence.

(A-C) Heat maps and group average of z-score changes in neural firing rate in response to CS-shock and CS-reward in ASt (A), TS (B), and CeA (C). Heatmap rows represent average Z-score PSTH for individual neurons. Arrowheads show average peak z-score during phasic window (0-100 ms). Insets show zoom of mean Z-score at +/-1s at onset of each CS type.

(D-F) Neural trajectories of neuron firing rates in ASt (A), TS (B), and CeA (C) in response to conditioned cues of opposing valence. Inset shows that euclidean distance between CS-shock and CS-reward trajectories in paired group mice.

(G) ASt neurons show significantly greater phasic responses to CS-shock (Two-tailed t-test, $t = 4.228$, $df = 310$, *** $p = 0.0000310$), sustained responses to CS-shock (Two-tailed t-test, $t = 3.232$, $df = 310$, ** $p = 0.00136$) and phasic responses to CS-reward (Two-tailed t-test, $t = 3.810$, $df = 310$, *** $p = 0.000167$) in paired group mice compared to unpaired controls.

(H) TS neurons showed overall little phasic responses to CS-shock (Two-tailed t-test, $t = 2.410$, $df = 539$, $p = 0.1805$), small but significant sustained responses to CS-shock (Two-tailed t-test, $t = 3.266$, $df = 539$, ** $p = 0.001160$), phasic responses to CS-reward (Two-tailed t-test, $t = 2.061$, $df = 539$, * $p = 0.0398$), and sustained inhibitory responses to CS-reward (Two-tailed t-test, $t = -5.244$, $df = 539$, *** $p = 0.000002251$) in paired group mice compared to unpaired controls.

(I) CeA neurons showed robust phasic responses to CS-shock (Two-tailed t-test, $t = 2.9397$, $df = 88$, ** = $p = 0.00419$), but no significant sustained responses to CS-shock (Two-tailed t-test, $t = -1.529$, $df = 88$, $p = 0.129$), and phasic responses to CS-reward (Two-tailed t-test, $t = 3.127$, $df = 88$, ** $p = 0.00239$), and a trend towards sustained responses to CS reward (Two-tailed t-test, $t = 1.7442$, $df = 88$, $p = 0.0846$) in paired group mice compared to unpaired controls.

(J) Average Z-score responses to CS-shock and CS-reward in paired group mice neurons recorded in tail of striatum (TS), amygdalostriatal transition zone (ASt) and central nucleus of the amygdala.

(K) ASt neurons show significantly greater sustained responses to CS-shock than neurons in adjacent TS or CeA regions in paired group mice (One-way ANOVA, * $p < 0.05$, ** $p < 0.01$, *** $p < 0.001$, Tukey's multiple comparison test. N=15 mice paired, 4 mice unpaired ASt, 5 mice paired, 4 mice unpaired TS, 2 mice paired, 2 mice unpaired CeA).

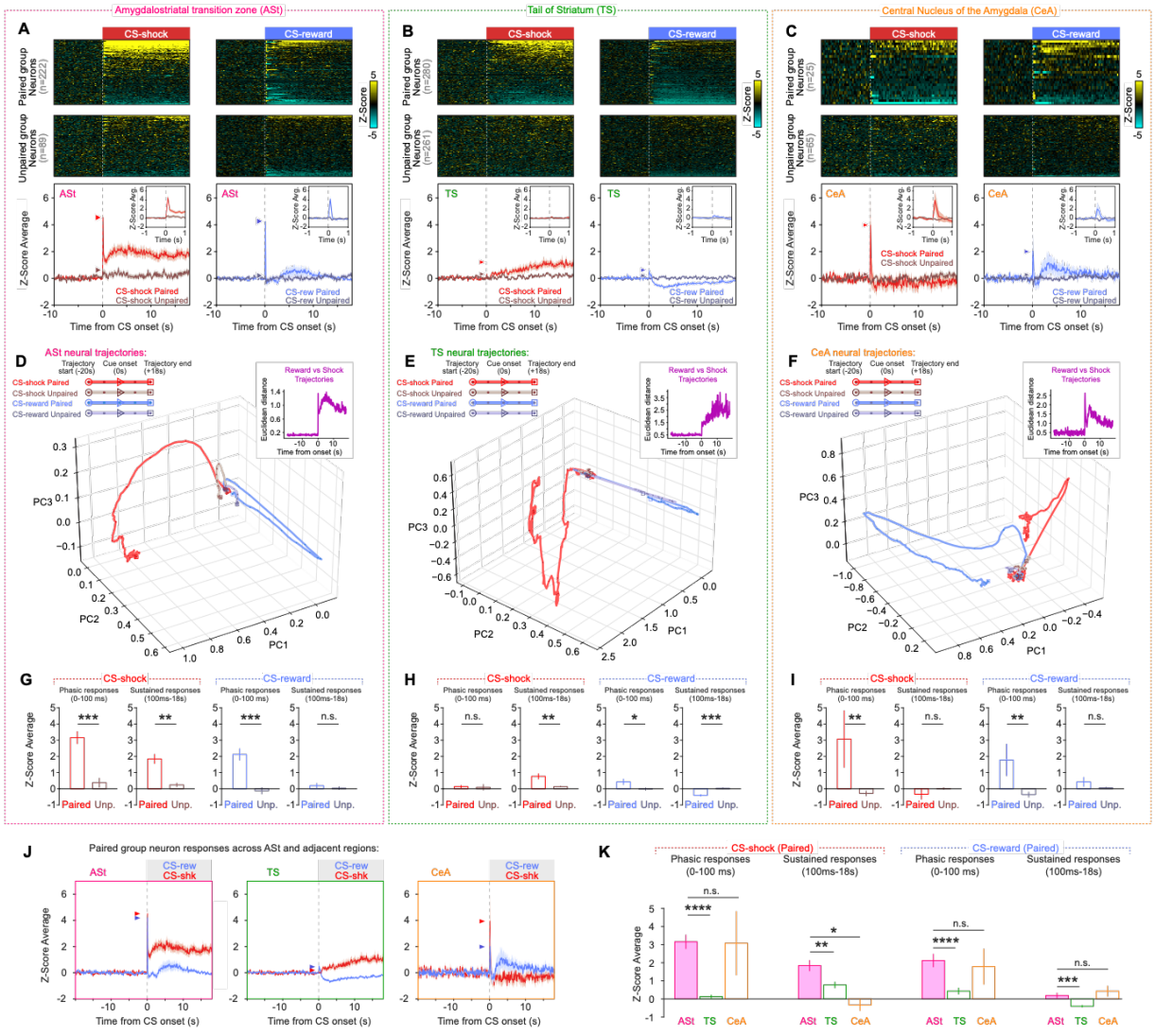
Amygdalostriatal transition zone (ASt)
Tail of Striatum (TS)
Central Nucleus of the Amygdala (CeA)
A
B
C
CS-shock
CS-reward
Paired group Neurons (n=422)
Unpaired group Neurons (n=95)
Z-Score
Z-Score Average
ASt
TS
CeA
CS-shock Paired
CS-shock Unpaired
CS-rew Paired
CS-rew Unpaired
Time from CS onset (s)
D
E
F
AST neural trajectories:
TS neural trajectories:
CeA neural trajectories:
Trajectory start (-20s)
Cue onset (0s)
Trajectory end (+18s)
Reward vs Shock Trajectories
Euclidean distance
Time from onset (s)
PC1
PC2
PC3
G
H
I
CS-shock
CS-reward
Phasic responses (0-100 ms)
Sustained responses (100ms-18s)
Paired
Unp.
n.s.
J
Paired group neuron responses across ASt and adjacent regions:
CS-rew
CS-shk
K
CS-shock (Paired)
CS-reward (Paired)

during these time periods between paired and unpaired group mice (Figure 2.2G-I). We found that the ASt had robust phasic responses to stimuli of positive and negative valence and sustained responses to CS-shock, all of which were only seen in paired group mice and absent in unpaired controls (Figure 2.2G). TS neurons showed no significant phasic responses to CS-shock, but some gradually increasing sustained responses, and phasic excitatory responses to CS-reward, but inhibitory responses during the sustained period (Figure 2.2H). In contrast, the CeA had robust phasic responses to both CS types but no significant sustained responses. Finally, we directly compared the magnitude of conditioned responses in paired group mice from neurons in each region (Figure 2.2J). ASt neurons showed robust phasic responses to both CS-shock and CS-reward that were of comparable magnitude to responses in the CeA but significantly greater than phasic responses in the TS (Figure 2.2K). However, ASt neurons showed significantly greater magnitude of sustained responses to CS-shock than either the TS or CeA. Thus, while each examined region had a unique pattern of response profiles to each CS type, the sustained responses to negative-valence stimuli was a major feature differentiating neural responses in the ASt from adjacent structures.

2.3.2 ASt neuron activity is sufficient to drive freezing and avoidance behavior

Given that ASt neurons respond to stimuli predicting shocks and rewards, we then sought to determine what behaviors might be driven by activation of ASt neurons. To investigate this, we targeted expression of channelrhodopsin-2 (ChR2) to the ASt using a Cre-conditional viral construct in VGAT-Cre mice (Figure 2.3A, S2.2A). This approach restricted ChR2 expression to GABAergic ASt neurons in order to prevent any confounding behavioral effects caused by ChR2 in excitatory neurons in the adjacent lateral amygdala (Johansen et al., 2010; Tye et al., 2011).

Figure 2.3. ASt neuron activation drives robust freezing and avoidance behavioral states rather than subsecond motor actions.

(A) Targeting strategy and representative image of ChR2 expression in ASt neurons.

(B) Optogenetic activation of ASt neurons during light 'ON' epochs of an open field task resulted in a significant increase in freezing in ChR2 group mice (Two-way ANOVA, group x laser interaction $F(1,32) = 10.98$, $p = 0.0023$. Bonferroni post hoc analysis ***$p < 0.001$).

(C) ChR2 group mice show increased avoidance of an area paired with optogenetic stimulation in a real-time place preference task (Two-way RM ANOVA, group x laser interaction $F(2,42) = 4.386$, $p = 0.0186$. Bonferroni post hoc analysis ** $p < 0.01$, ***$p < 0.001$). N=8 mice ChR2, 10 mice eYFP.

(D) Workflow for classification of defensive behaviors using SLEAP.

(**E**) Representative trials from discrimination task experiments showing simultaneous subsecond behavior, neural spikes, and average neuron firing rate during presentation of CS-shock.

(F) Average ASt Z-score responses to onset of freezing and escape behavior motor actions in paired and unpaired group mice.

(G) Logistic regression decoder change in performance over time relative to chance level for decoding tone identity, freezing or escape in paired and unpaired group mice.

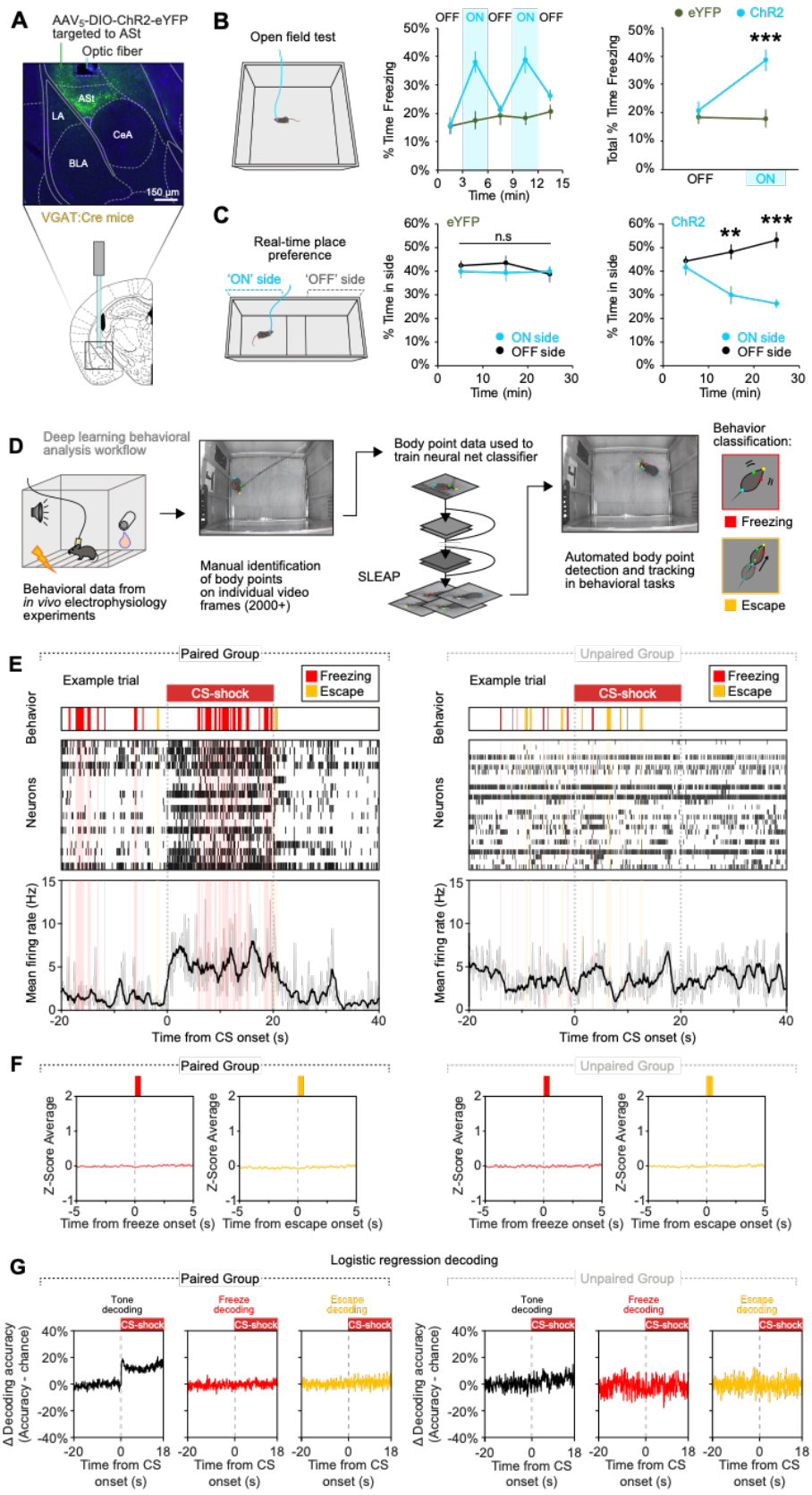
A
AAV5-DIO-ChR2-eYFP targeted to ASt
Optic fiber
ASt
LA
CeA
BLA
150 µm
VGAT:Cre mice
B
Open field test
OFF ON OFF ON OFF
% Time Freezing
Time (min)
eYFP ChR2
***
Total % Time Freezing
OFF ON
C
Real-time place preference
'ON' side
'OFF' side
eYFP
n.s
% Time in side
ON side
OFF side
ChR2
**
***
D
Deep learning behavioral analysis workflow
Behavioral data from in vivo electrophysiology experiments
Manual identification of body points on individual video frames (2000+)
Body point data used to train neural net classifier
SLEAP
Automated body point detection and tracking in behavioral tasks
Behavior classification:
Freezing
Escape
E
Paired Group
Unpaired Group
Example trial
CS-shock
Freezing
Escape
Behavior
Neurons
Mean firing rate (Hz)
Time from CS onset (s)
F
Paired Group
Unpaired Group
Z-Score Average
Time from freeze onset (s)
Time from escape onset (s)
G
Logistic regression decoding
Paired Group
Unpaired Group
Tone decoding
Freeze decoding
Escape decoding
CS-shock
Δ Decoding accuracy (Accuracy - chance)
Time from CS onset (s)

We then examined the effects of optogenetic activation of ASt neurons by stimulation via an implanted optic fiber. We first found that photostimulation of ASt neurons (473nm, 5 mw, 20 Hz) in ChR2-expressing mice led to a striking increase in freezing during 'laser ON' epochs of an open field test of exploratory behavior and locomotion (Figure 2.3B). This effect was reversible, with freezing levels restored during 'laser OFF' epochs, and photostimulation had no effect in eYFP-expressing controls.

We then examined whether activation of ASt neurons was innately rewarding or aversive using a closed-loop real-time place preference task, wherein mice were allowed to freely explore a test apparatus in which one side was paired with optogenetic stimulation. We found that over the course of the task, mice spent less time in the 'laser ON' side, indicating that activation of ASt neurons was aversive and led to avoidance of the side paired with stimulation (Figure 2.3C). We also found that activation of ASt neurons did not lead to any change in overall anxiety-related behaviors such as preference for the center of the open field arena (Figure S2.2B) and preference for open arms of an elevated plus maze task (Figure S2.2C). Together, these data indicated that activation of ASt neurons was innately aversive and sufficient to drive defensive freezing and avoidance behaviors, consistent with a role for the ASt in encoding fearful or aversive stimuli to direct behavioral responses.

2.3.3. ASt neuron activity does not encode specific subsecond motor actions

Having seen the robust freezing elicited by ASt neuron activity, we then wondered whether the ASt represented emotional valence (internal state) or behavioral expression (motor output). The increased activity of ASt neurons during CS-shock observed in our electrophysiology experiments could be due to ASt encoding the valence of the tone, or it could

be due to ASt neuron activity correlating with specific defensive behaviors – such as freezing and escape behavior – which take place in response to the CS. To distinguish between these possibilities, we re-examined our electrophysiology experiment data using SLEAP, a deep-learning based suite for pose estimation (Pereira et al., 2022), and classified behavior of individual mice during our discrimination task experiments to detect freezing and escape (rapid darting) behaviors (Figure 2.3D). Examination of individual trials (Figure 2.3E, see also Figure S2.2D) showed that ASt neuron activity increased in a manner which tracked the CS-shock in paired group mice, and while defensive behaviors also increased during that time period, specific behaviors were not closely correlated with sub-second changes in ASt neuron activity. We identified all bouts of freezing and escape behavior during all trials of the task and found no net relative changes in ASt neuronal activity in response to onsets of either type of motor response (Figure 2.3F). Furthermore, we analyzed ASt neuron activity using logistic regression (Glaser et al., 2020) and found that during presentation of cues decoding of CS-shock was above chance level in paired group mice, but not unpaired controls, and decoding of freezing and dash behavior was not above chance level in either group (Figure 2.3G). Together, these data support the notion that the ASt represents ongoing emotional valence, as the signal is sustained throughout the cue and throughout the period of increased defensive behaviors. However, because the ASt did not show increased activity when shifting behavioral motifs and did not show phasic changes upon the initiation of freezing nor escape, we concluded that the ASt does not mediate differences in defensive strategy or motor output.

2.3.4. ASt displays unique cell type composition and transcriptomic features allowing distinction from other striatal regions

Given that the ASt has unique functional properties and connectivity, we next investigated the degree to which the ASt was in fact a genetically distinct brain region from adjacent structures in the striatum and amygdala. We performed single-nucleus RNA sequencing (snRNA-seq) (Zheng et al., 2017) to determine the cell type composition and transcriptomic identity of the ASt. Due to the ASt's proximity to both the striatum and amygdala complex, we extracted tissue target samples by microdissection and verified accurate histology before pooling qualifying samples for each run of RNA sequencing (see methods; Figure 2.4A, S2.3A-F). We also captured nuclei from the central amygdala (CeA), dorsal striatum (DS), and tail of striatum (TS) to identify differences in gene expression between these regions and the ASt (Figure S2.3G-I).

Visualization of these nuclei via uniform manifold approximation projection (UMAP) showed cluster of nuclei based on cell type, but significant divergence by region of tissue origin, with ASt cells being visibly distinct from other regions in some clusters (Figure 2.4B,C). Intriguingly, this variation occurred in a manner similar to the anatomical structure of brain, with regions spatially ordered in high-dimensional expression space based on their relative proximity to one another (DS > TS > ASt > CeA). We also confirmed there were no region-specific differences in expression of genetic markers for broad nuclear quality (Hicks et al., 2018) (Figure S2.3J,K), and both principal component analysis and hierarchical clustering of pseudobulk batches showed high variation between regions but not between batches within each region (Figure S2.3L-N), indicating that the variation observed reflected real biological differences between these regions and not other confounding methodological factors.

Figure 2.4. ASt cell-type composition is distinct from adjacent brain regions.

(A) Target regions for single-nucleus RNA sequencing (snRNA-seq).

(B) Two-dimensional non-integrated uniform manifold approximation projection (UMAP) of all sequenced nuclei passing quality filters (N = 97,434 nuclei, see also Figure S3), colored by region of origin.

(C) Two-dimensional UMAP, colored by broad cellular identity assigned by graph-based clustering of neuronal and non-neuronal cells.

(D) Cell-type-specific expression of canonical marker genes indicating broad cellular identity in the brain. Dot size is proportional to percentage of nuclei expressing the marker, with color scale representing normalized expression level.

(E) Dendrogram of cell type classification and proportion of cells of each class in the ASt and other target regions.

(F) Difference in overall proportion of each cell type between the ASt compared to the CeA, TS, and DS.

(G) Total proportion of cells of each identified type in each target region.

(H) All nuclei, colored by expression levels of Drd1a (top) or Drd2 (bottom), with cells identified as part of the major Drd1a+ or Drd2+ clusters highlighted.

(I) Drd1a+ cluster (top) or Drd2+ cluster (bottom) neurons, with individual nuclei colored by region of origin.

(J) Relative proportion of nuclei classified in Drd1a+ or Drd2+ clusters in each striatal target region. Nuclei in the Drd1a+ cluster that also expressed Drd2, or in the Drd2+ cluster that expressed Drd1a, were classified as 'dual expressing'. *** $p < 0.001$.

(K) Representative images of in situ RNAscope labeling of Drd1 RNA (green) and Drd2 RNA (red) in striatal target regions.

(L) Relative proportion of cells in each target region positively labeled for Drd1 RNA, Drd2 RNA, or both ('dual expressing'). * $p < 0.05$, ** $p < 0.01$

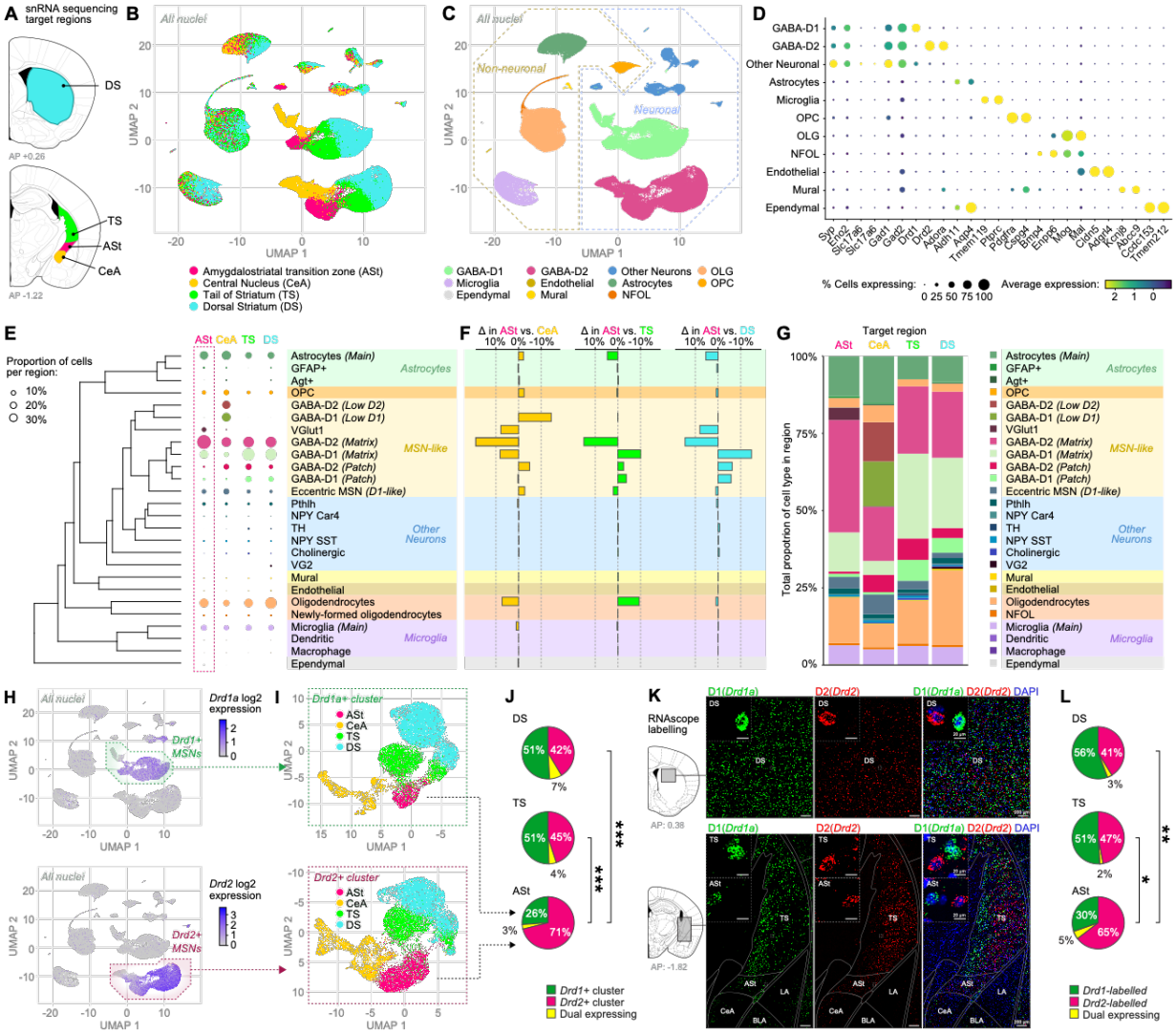
A
snRNA sequencing target regions
DS
AP +0.26
TS
ASt
CeA
AP -1.22
B
All nuclei
UMAP 2
UMAP 1
Amygdalostriatal transition zone (ASt)
Central Nucleus (CeA)
Tail of Striatum (TS)
Dorsal Striatum (DS)
C
All nuclei
Non-neuronal
Neuronal
GABA-D1
GABA-D2
Other Neurons
OLG
Microglia
Endothelial
Astrocytes
OPC
Mural
Ependymal
NFOL
D
GABA-D1
GABA-D2
Other Neuronal
Astrocytes
Microglia
OPC
OLG
NFOL
Endothelial
Mural
Ependymal
Syp
Eno2
Slc17a6
Slc17a6
Gad1
Gad2
Drd1
Drd2
Aqp4
Aldh1l1
Aldh4
Tmem119
Prrc
Pdgfra
Cspg4
Enpp6
Mog
Plp1
Cldn5
Adgrl4
Kcnj8
Abcc9
Cacna1s
Tmem212
% Cells expressing:
0 25 50 75 100
Average expression:
2 1 0
E
ASt CeA TS DS
Proportion of cells per region:
10%
20%
30%
Astrocytes (Main)
GFAP+
Agt+
OPC
GABA-D2 (Low D2)
GABA-D1 (Low D1)
VGlut1
GABA-D2 (Matrix)
GABA-D1 (Matrix)
GABA-D2 (Patch)
GABA-D1 (Patch)
Eccentric MSN (D1-like)
Pthlh
NPY Car4
TH
NPY SST
Cholinergic
VG2
Mural
Endothelial
Oligodendrocytes
Newly-formed oligodendrocytes
Microglia (Main)
Dendritic
Macrophage
Ependymal
Astrocytes
MSN-like
Other Neurons
Microglia
F
Δ in ASt vs. CeA
Δ in ASt vs. TS
Δ in ASt vs. DS
10% 0% -10%
G
Target region
ASt CeA TS DS
Total proportion of cell type in region
100%
75%
50%
25%
0%
H
All nuclei
Drd1a log2 expression
Drd1+ MSNs
Drd2 log2 expression
Drd2+ MSNs
UMAP 2
UMAP 1
I
Drd1a+ cluster
Drd2+ cluster
ASt
CeA
TS
DS
J
DS
51%
42%
7%
TS
51%
45%
4%
ASt
26%
71%
3%
***
***
Drd1+ cluster
Drd2+ cluster
Dual expressing
K
RNAscope labelling
D1(Drd1a)
D2(Drd2)
D1(Drd1a) D2(Drd2) DAPI
AP: 0.38
AP: -1.82
ASt
CeA
TS
LA
BLA
L
DS
56%
41%
3%
TS
51%
47%
2%
ASt
30%
65%
5%
**
*
Drd1-labelled
Drd2-labelled
Dual expressing

Clustering of sequenced nuclei by gene expression allowed us to identify all major canonical cell types in the ASt, TS, DS and CeA based on known gene markers identified in prior scRNA-seq studies of the striatum (Märtin et al., 2019; Saunders et al., 2018; Stanley et al., 2020). Across these four regions the majority of neurons fell broadly into two clusters of medium spiny neuron (MSN) defined by expression of the genes for dopamine receptor 1 (*Drd1a*) and dopamine receptor 2 (*Drd2*) (Figures 2.4C-D). We then further analyzed the various clusters of cells detected in all regions and used these to construct population analyses of relative proportions of cell types in each region and how the cell type composition of the ASt was distinct from the CeA, TS and DS (Figure 2.4E-G). Interestingly, in the ASt we saw a larger proportion of GABAergic *Drd2*+ neurons relative to other regions. To quantify this difference, we examined neurons within the Drd1a+ and Drd2+ clusters, where ASt neurons were clearly visible as a distinct subcluster from other regions (Figure 2.4H-I). In previous studies of the striatum, Drd1a+ and Drd2+ MSNs have been found to comprise the largest subpopulations of neurons, with a roughly equivalent proportion of the two types (Gagnon et al., 2017; Ren et al., 2017). We therefore quantified the overall number of neurons in the ASt in each cluster and compared this with the proportions from the DS and TS (Figure 2.4J). Our data confirmed that while both DS and TS had similar proportions of the two MSN types, the ASt was enriched for Drd2+ MSNs. To confirm these findings and validate our RNAseq data, we used RNAscope labelling to examine the expression of D1 and D2 receptors in situ in the ASt and surrounding regions (Figure 2.4K). We found that the ASt had a much greater proportion of RNAscope-labelled *Drd2*+ neurons than *Drd1a*+ neurons compared to either the TS or DS (Figure 2.4L), and that the proportions of *Drd1a*+ and *Drd2*+ neurons in the ASt, TS and DS was highly consistent with the proportions of these cell types seen in our sequencing data (Figure 2.4J).

Consistent with previous studies, we saw that in the TS, MSNs types were spatially segregated into a D1-rich medial band and a D2-rich lateral band (Figure 2.4K), but that this stratified pattern was not present in the DS or ASt (Gangarossa et al., 2013; Miyamoto et al., 2019, 2018). Furthermore, our RNAscope labelling indicated that *Drd1a/Drd2* dual-expressing neurons were a small proportion of the total populations in the ASt and other striatal subregions. Together, our data identify a previously unknown disparity in MSN ratio for the ASt compared to the rest of the striatum, showing that the ASt is greatly enriched for *Drd2*+ MSNs compared with other regions of the striatum.

We further examined differences in gene expression between the ASt and other structures within cell types, and found that in pairwise comparisons, ASt neurons had large numbers of differentially expressed genes compared to every other region within the Drd1a+ and Drd2+ clusters (Figure S2.4) Additionally, other striatal subregions displayed similarly diverse transcriptomic differences related to neurological function (Figure S2.5B). Taken together, these numerous differences indicate major molecular diversity among MSNs from different striatal and regions, and further indicate that ASt neurons are molecularly distinct from the rest of the striatum.

2.3.5. D2+ ASt neurons specifically encode conditioned stimuli of negative valence

Within the dorsal and ventral striatum, *Drd1a*+ and *Drd2*+ neurons are the two major types of GABAergic MSNs (Gagnon et al., 2017; Gangarossa et al., 2013; Gerfen et al., 1990; Gerfen and Surmeier, 2011; Ren et al., 2017). In the dorsal striatum, *Drd1*+ MSNs promote movement and reinforcement while D2-expressing cells decrease motor output and promote aversion (Kravitz et al., 2012, 2010). These motoric components are not expressed in the nucleus accumbens (NAc), wherein *Drd1*+ MSNs promote reinforcement while *Drd2*+ MSNs promote

aversion (Lobo et al., 2010). These two cell types also define the direct and indirect pathways from the dorsal striatum, which have been shown to play a wide array of critical complementary and opposing roles in motor output, action selection, and control of goal-directed and habitual behaviors (Balleine and O'Doherty, 2010; Kravitz et al., 2012, 2010; Nelson and Kreitzer, 2014; Redgrave et al., 2010; Tai et al., 2012). Given the established importance of these two cell types in motor output and motivated behaviors, the heterogeneity of responses observed in ASt neuron responses in our electrophysiology experiments, and the unique increase in *Drd2*+ MSNs revealed by our RNA sequencing data, we next sought to determine the specific contributions of *Drd1a*+ and *Drd2*+ neurons in encoding conditioned stimuli in the ASt. We targeted a viral vector to the ASt of *Drd1a-Cre* and *Drd2-Cre* mice (Gong et al., 2007) to conditionally express GCaMP7f in *Drd1a*+ and *Drd2*+ ASt neurons and implanted a gradient-index relay lens immediately above the ASt to allow in vivo imaging of calcium transients in ASt neurons via a head-mounted miniature microscope (Figure 2.5A,B, S2.6A-B). We then examined calcium responses in these mice during a two-tone discrimination task (Figure 2.5C) in which distinct conditioned stimuli predicted shock ('CS-shock') and reward ('CS-reward'). Paired group mice showed evidence of discrimination, as reflected by significantly different port entry and defensive behaviors (freezing and escape) to the two cues, while no significant behavioral discrimination was seen in unpaired controls (Figure S2.6C-H).

We found that *Drd1a*+ ASt neurons overall did not show robust responses to either cue (Figure 2.5D, E), though individual neurons did show increases or decreases in activity in response to CS-reward. However, *Drd2*+ ASt neurons showed highly robust responses to CS-shock (Figure 2.5F). These responses were only seen in paired group mice, and not unpaired controls for whom the tones had no predictive value, consistent with encoding the significance of

Figure 2.5. D2+ ASt neurons encode conditioned stimuli of negative valence.

(A) GCaMP7f expression and lens targeting to ASt.

(B) Calcium imaging field of view and representative traces of fluorescence changes in individual neurons (dashed lines indicate concatenated trials).

(C) Two-tone discrimination task design parameters for in vivo calcium imaging of ASt neurons.

(D, E) Drd1a+ ASt neurons group average responses to CS-shock (D) and CS-reward (E) were not significantly different in paired group mice than unpaired controls.

(F) Drd2+ ASt neurons show greater conditioned responses to a shock-predicting cue ('CS-shock') in paired group mice than in unpaired controls (Two-tailed t-test, $t = 3.135$, $df = 60$, ** $p < 0.01$).

(G) Drd2+ ASt neuron group average responses to reward-predicting cue ('CS-reward') were not significantly different from unpaired controls.

(H) Agglomerative hierarchical clustering of calcium imaging responses of neurons from Drd1a-Cre and Drd2-Cre paired and unpaired groups.

(I) Mean z-score traces of responses to CS-shock and CS-reward (left) and proportion of neurons in each cluster from Drd1a-Cre and Drd2-Cre paired and unpaired groups (right) in each cluster. Clusters 1, 2 and 3, which feature robust responses to CS-shock, are dominated by neurons from the Drd2-Cre paired group. Drd1a-Cre paired group neurons are the largest proportion of clusters 4 and 5, which feature significant excitatory or inhibitory responses, respectively, to CS-reward.

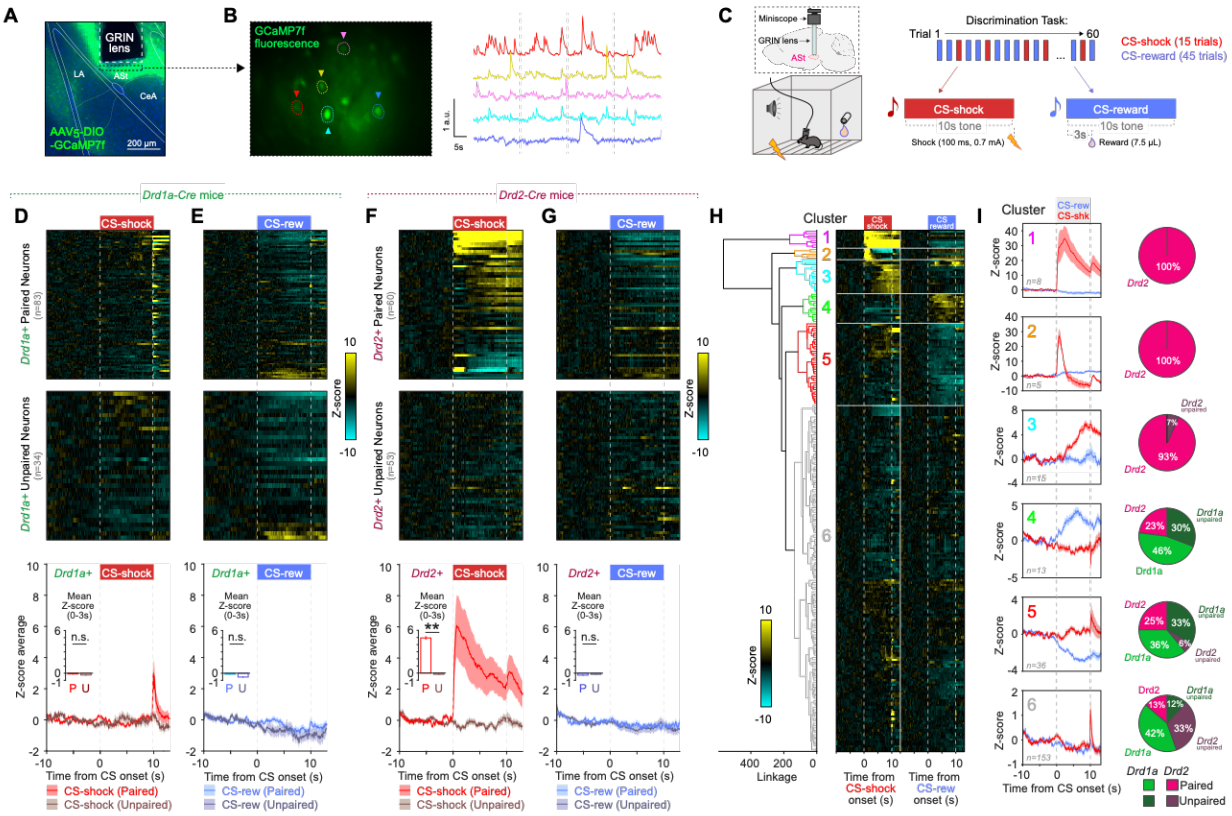
A
GRIN lens
LA
ASt
CeA
AAV5-DIO -GCaMP7f
200 μm
B
GCaMP7f fluorescence
1 a.u.
5s
C
Miniscope
GRIN lens
ASt
Discrimination Task:
Trial 1
60
CS-shock (15 trials)
CS-reward (45 trials)
CS-shock
10s tone
Shock (100 ms, 0.7 mA)
CS-reward
3s
10s tone
Reward (7.5 μL)
Drd1a-Cre mice
Drd2-Cre mice
D
E
F
G
H
I
CS-shock
CS-rew
Drd1a+ Paired Neurons (n=63)
Drd1a+ Unpaired Neurons (n=54)
Drd2+ Paired Neurons (n=60)
Drd2+ Unpaired Neurons (n=53)
Z-score
10
-10
Drd1a+
Drd2+
Mean Z-score (0-3s)
n.s.
**
P U
Z-score average
Time from CS onset (s)
CS-shock (Paired)
CS-shock (Unpaired)
CS-rew (Paired)
CS-rew (Unpaired)
Cluster
Linkage
Time from CS-shock onset (s)
Time from CS-rew onset (s)
CS-rew
CS-shk
n=8
n=5
n=16
n=13
n=36
n=153
100%
93%
7%
23%
30%
46%
25%
33%
36%
6%
13%
12%
42%
Drd1a
Drd2
unpaired
Paired
Unpaired

the cue of negative valence. *Drd2*+ ASt neurons showed minimal responses to CS-reward, and group average responses to this CS in paired group mice were not significantly different than unpaired controls (Figure 2.5G). We also found that upon presentation of either shock and reward unconditioned stimulus (US) alone, subsets of *Drd1a*+ and *Drd2*+ neurons responded to each US type, with more robust responses to shocks (Figure S2.7).

To further characterize the responses of *Drd1a*+ and *Drd2*+ ASt neurons to cues of positive and negative valence, we performed additional agglomerative hierarchical clustering to identify groups of neurons based on their response patterns to each CS (Figure 2.5H). We then examined the average responses to CS-shock and CS-reward of neurons in each cluster, as well as the proportion of cells in each cluster that came from *Drd1a*+ and *Drd2*+ paired and unpaired groups (Figure 1.5I). We first saw three major clusters of cells that showed minimal responses to CS-reward and distinct but robust types of responses to CS-shock; high-amplitude (20+ Z-score) and sustained responses lasting the duration of the 10s cue (Cluster 1), transient responses to the tone onset (Cluster 2), and a gradual ramp up of activity during the CS (Cluster 3). These clusters were almost entirely composed of neurons from the *Drd2*+ paired group, and, overall, 54% of *Drd2*+ ASt neurons were clustered in one of these three groups that responded strongly to CS-shock. We also identified two clusters which responded primarily to CS-reward, one which showed excited responses to CS-reward (Cluster 4) and another which was inhibited by CS-reward (Cluster 5). *Drd1a*+ paired group neurons were the largest portion of these two clusters, though neurons from several other groups were present as well. Finally, many neurons from the unpaired group mice, as well as some *Drd1a*+ and *Drd2*+ neurons from paired group mice, were not strongly responsive to either CS (Cluster 6). Altogether, these data showed that *Drd2*+ neurons were primarily responsible for mediating responses to conditioned cues of negative

valence in the ASt. The *Drd2*+ neurons also exhibited rapid onset and sustained responses, consistent with the requirements for directing defensive responses across behavioral timescales.

2.3.6. *Drd2*+ ASt neurons are necessary for the expression of conditioned fear

Our calcium imaging data showed that *Drd2*+ ASt neurons robustly encoded conditioned stimuli of negative valence during tone discrimination, which raised the possibility that the activity of these neurons was in fact necessary to direct the expression of conditioned behavioral responses to these stimuli. To investigate this, we examined the effects of reversible optogenetic inhibition of *Drd2*+ ASt neurons in a variation of the two-tone discrimination task used in recording experiments (Figure 2.6A). *Drd2*+ ASt neurons were bilaterally targeted with a viral construct to conditionally express the inhibitory opsin halorhodopsin (NpHR) in *Drd2-Cre* mice (Figure 2.6B, S2.8A). These mice were first trained to distinguish tones predicting shock and reward delivery, and then, on a subset of trials, 593 nm light was delivered via optic fibers to the ASt, allowing us to assess the within-animal effects of silencing *Drd2*+ ASt neurons on expression of conditioned behaviors. We found that optogenetic inhibition of *Drd2*+ ASt neurons caused a striking reduction in conditioned defensive behaviors (freezing and escape) in response to CS-shock during 'Laser ON' trials compared with 'Laser OFF' trials (Figure 2.6C). This inhibition of *Drd2*+ ASt neurons had no effect on responses to CS-reward tones presented during the same experimental session, as measured by reward port entry (Figure 2.6D). These behavioral changes were only seen in NpHR group mice, which showed a significant decreased in overall freezing relative to eYFP controls (Figure 2.6E), with no effect on port entry responses to CS-reward observed in either group (Figure 2.6F). Inhibition of *Drd2*+ ASt neurons had no effect on unconditioned freezing behavior in an open field task (Figure 2.6G), indicating that the

Figure 2.6. D2+ ASt neurons are necessary for the expression of fear responses to auditory cues, but conditioned reward responses or contextual fear conditioning.

(A) Behavioral paradigm for selective inhibition of D2+ ASt neurons during discrimination task.

(B) Representative images of AAV-DIO-NpHR-eYFP expression in D2+ ASt neurons (Scale bars = 250 μm).

(C) Defensive behavior heatmaps during 'laser ON' (top) and 'laser OFF' trials (middle) and group averages (bottom) during CS-shock trials with and without photoinhibition.

(D) Port entry behavior heatmaps (top, middle) and group averages (bottom) during CS-reward trials with and without photoinhibition.

(E) Inhibition of D2+ ASt neurons resulted in a significantly greater reduction in conditioned defensive behaviors to CS-shock in NpHR mice compared with eYFP controls, and (F) had no effect on port entry during CS-reward (*$p < 0.05$, Student's t-test, N=8 mice NpHR, 9 mice eYFP).

(G) Optogenetic inhibition of D2+ ASt neurons had no effect on overall locomotion in an open field maze task (N=5 mice NpHR, 10 mice eYFP).

(H) Inhibition of D2+ ASt neurons did not cause preference or aversion for an area paired with inhibition in a real-time place preference task (N=5 mice NpHR, 10 mice eYFP).

(I) Inhibition of D2+ ASt neurons caused no overall changes in exploration of open arms in an elevated plus maze (N=5 mice NpHR, 10 mice eYFP).

(J) Inhibition of D2+ ASt neurons on day 2 of a contextual fear conditioning task had no effect on contextual freezing (N=5 mice NpHR, 9 mice eYFP).

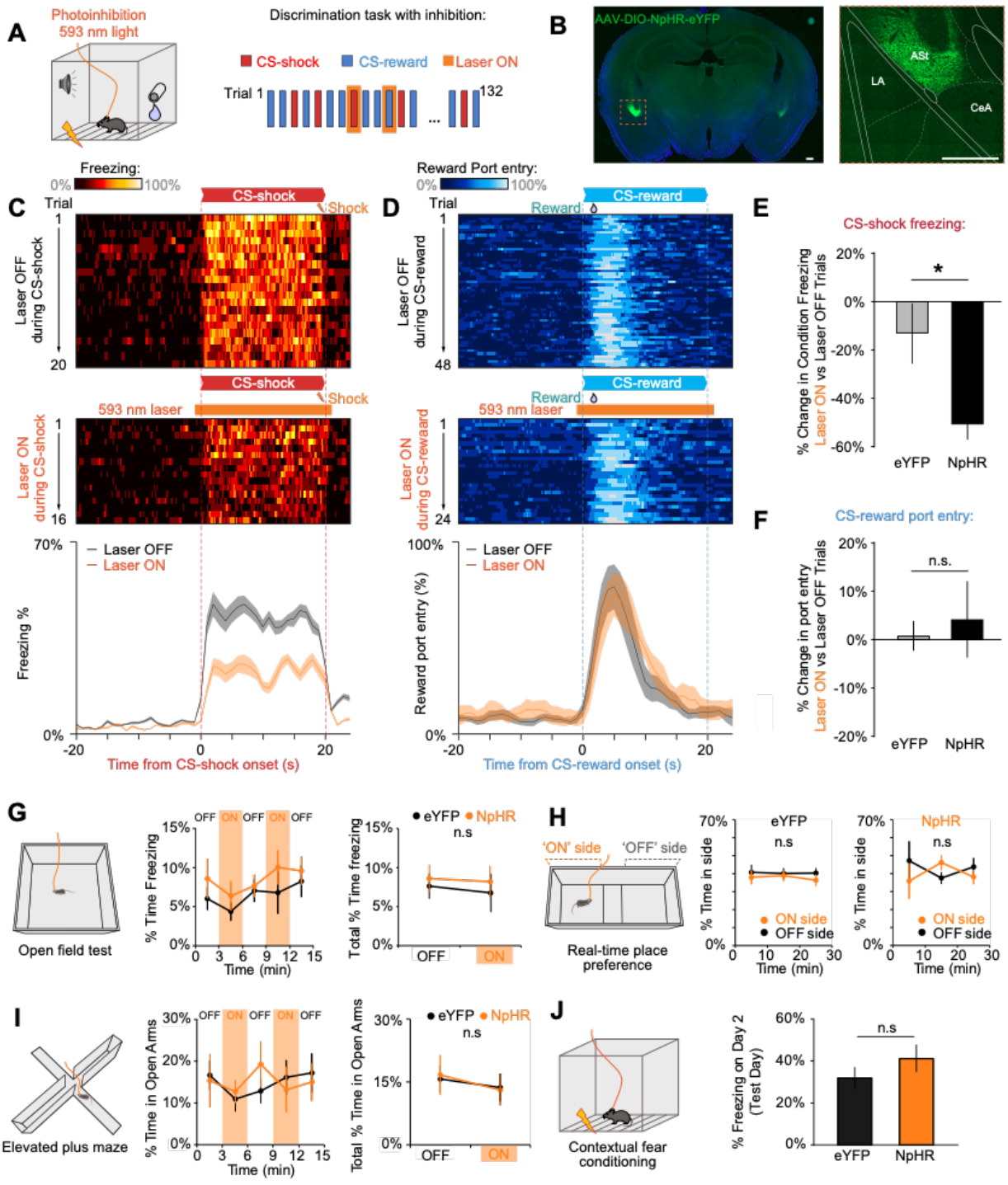
A
Photoinhibition
593 nm light
Discrimination task with inhibition:
CS-shock
CS-reward
Laser ON
Trial 1
132
B
AAV-DIO-NpHR-eYFP
ASt
LA
CeA
C
Freezing:
0%
100%
Trial
CS-shock
Shock
Laser OFF during CS-shock
20
593 nm laser
Laser ON during CS-shock
16
Laser OFF
Laser ON
Freezing %
70%
0%
-20
0
20
Time from CS-shock onset (s)
D
Reward Port entry:
CS-reward
Reward
Laser OFF during CS-reward
48
Laser ON during CS-reward
24
Reward port entry (%)
100%
Time from CS-reward onset (s)
E
CS-shock freezing:
% Change in Condition Freezing
Laser ON vs Laser OFF Trials
20%
0%
-20%
-40%
-60%
*
eYFP
NpHR
F
CS-reward port entry:
% Change in port entry
n.s.
10%
-10%
G
Open field test
% Time Freezing
OFF
ON
Time (min)
Total % Time freezing
eYFP
NpHR
n.s
H
'ON' side
'OFF' side
Real-time place preference
% Time in side
ON side
OFF side
I
Elevated plus maze
% Time in Open Arms
Total % Time in Open Arms
J
Contextual fear conditioning
% Freezing on Day 2 (Test Day)
60%
40%

changes in conditioned behaviors observed in NpHR group mice during the discrimination task were not simply due to overall changes in motor output. We also saw that inhibition of *Drd2*+ ASt neurons was not innately rewarding or aversive, as measured by preference for a 'laser ON' area in real-time place preference task (Figure 2.6H), and did not cause any overall change in preference for open arms in an elevated plus maze task, considered a measure of anxiety-related behaviors (Figure 2.6I). We then examined whether the ASt was necessary for conditioned fear responses to an environmental context, rather than to acute sensory cues. To test this, we placed mice in a novel operant chamber and then instantiated contextual fear conditioning by delivery of unpredicted foot shocks. We returned the mice to this context 24 hours later while also delivering 593 nm light to the ASt. We found that NpHR group mice still showed robust freezing comparable to eYFP controls in the conditioned context despite the inhibition of *Drd2*+ ASt neurons (Figure 2.6J). This indicated that *Drd2*+ ASt neurons were not required for defensive fear responses to a conditioned context, but indeed were specifically required for responses to acute sensory stimuli. This result also further showed that inhibition of *Drd2*+ ASt neurons was not simply driving a motor effect which prevented mice from freezing altogether, but rather was specific to conditioned responses to sensory stimuli. Together, these results demonstrated that the *Drd2*+ ASt neuron population, which our RNA sequencing data showed was a unique feature of the ASt, was in fact critical for defensive behavioral responses to conditioned stimuli of negative valence.

2.4. Discussion

2.4.1. The ASt encodes conditioned stimuli

Here we demonstrate the amygdalostriatal transition zone (ASt) is a genetically distinct brain region from neighboring amygdalar or striatal structures that plays a critical role in encoding stimuli to direct behavioral responses, a previous uncharacterized role for this structure. We find that individual ASt neurons show conditioned responses to cues consistent with encoding valence and behavioral state, including rapid and sustained responses to stimuli of negative valence, which are specifically mediated by the *Drd2*+ population within the ASt. Finally, we find that ASt neurons are essential for the expression of conditioned defensive behaviors.

Our findings identify the ASt as a component of the brain circuitry encoding conditioned stimuli. In conceptual models of emotional responses, it has been proposed that sensory information is assigned salience as well as valence, either sequentially or together (Lang, 1995; Schachter and Singer, 1962), which then serves to direct selection of a behavioral response. Within this framework, ASt neurons appear to encode the learned significance of cues of both positive and negative valence, and not simply sensory information or salience of stimuli. This role is supported by our electrophysiological recordings of ASt neurons, which showed robust responses to auditory cues that predicted shocks or rewards but only in paired group mice, and not in unpaired controls which received the same number of cue, shock and reward presentations but in randomized order and explicitly unpaired. Consequently, the responses seen in paired group mice cannot simply be sensory responses to the auditory cue, or even elevated responses due to sensitization or heightened arousal from receiving rewards and punishments, as these would have been present in unpaired controls as well but were not seen (Rescorla, 1967).

Furthermore, while the information encoded in the ASt may be necessary to direct behavioral responses, in both paired and unpaired group mice, ASt neuron activity was not directly encoding specific motor outputs on subsecond timescales. Thus, we can attribute the changes in ASt neurons' cue responses to encoding the predictive value of the cues, which is the sole distinction between the groups. We also saw markedly distinct directions of response for neural trajectories of ASt neurons in response to cues predicting shock and reward, which is consistent with these neurons encoding valence rather than salience.

2.4.2. Sustained responses and defensive behaviors are mediated by the ASt

A remarkable feature of ASt neurons that we observed was the sustained nature of responses to stimuli during discrimination tasks. Our recordings showed that the ASt neurons had significantly greater sustained responses to stimuli of negative valence than adjacent regions, including the TS and CeA. In the brain, sustained responses in neurons can be found at both 'lower' and 'higher' level representations of stimuli. Regions which represent raw sensory information, such as the sensory thalamus, have been shown to track features of stimuli throughout their duration with sustained responses (Bartlett, 2013; Leppla et al., 2022). However, sustained responses are also seen in the prefrontal cortex (PFC), where in both primates and humans they appears to serve as a high-level neural correlate for representation of task features in working memory (Curtis and Sprague, 2021). Indeed, rodents trained in similar behavioral paradigms to those in the present study have shown sustained responses to conditioned stimuli in PFC neurons but comparatively transient responses in the amygdala (Burgos-Robles et al., 2017, 2009). The ASt appears unique in that it is integrated with amygdalar circuits known to mediate valence processing within the limbic system and responds

rapidly to stimuli, but shows longer time-scale responses with sustained activity tracking the full duration of stimuli and not simply the stimulus onset as seen in the amygdala (Goosens and Maren, 2004; Li et al., 2022; Quirk et al., 1995; Whittle et al., 2021). What is the purpose of this combination of features in the ASt? We propose that encoding of sustained valence would be of value to orchestrate rapid and continuous behavioral responses to stimuli when it is necessary. Transient responses to stimuli are suitable for cases such as reward or pursuit behaviors initiated by an animal, or to trigger aspects of emotional responses such as endocrine and stress hormone responses (Ulrich-Lai and Herman, 2009). In the case of defensive responses to threats, however, a neural correlate tracking the full duration of an aversive stimuli would be ideally suited to continuously maintain a behavioral state critical for survival. Consistent with this proposed role, we found that activity of ASt neurons is indeed crucial for defensive behaviors across behaviorally-relevant timescales. Inhibition of *Drd2*+ ASt neurons, the largest population in the region, caused a striking reduction in freezing behaviors in response to a shock-predicting cue while leaving reward responses unaffected. Importantly, we believe our findings complement rather than contradict the large body of work examining amygdalar circuits mediating learned associations. Many studies have shown that the amygdala complex, especially outputs from the CeA to the periaqueductal grey (PAG), are essential for expression of conditioned fear (Fadok et al., 2017; Keifer et al., 2015; LeDoux et al., 1988; Tovote et al., 2016). Indeed, while inhibition of the ASt did markedly reduce defensive behaviors, there was still considerable residual defensive behaviors in response to the cue (~50% of normal levels), consistent with the fact that the entire 'canonical' amygdala pathway was fully intact as our manipulations targeted only the ASt.

Thus, it seems likely that the output of *Drd2*+ ASt neurons acts in concert with these canonical amygdala circuits and drives defensive behaviors directed via the basal ganglia in a complementary manner to targets of CeA output. It is likely that the ASt and CeA have functional redundancy in some cases but may also have specialized roles for different aspects of fear response and defensive behaviors. For instance, one noteworthy finding in our study was that inhibiting *Drd2*+ ASt neurons had no effect on contextual freezing responses, despite the same manipulation dramatically reducing freezing to auditory cues. The BLA and CeA have been shown to be critical for contextual fear conditioning (Goosens and Maren, 2001) and the hippocampus, a critical structure for spatial and contextual learning (Danielson et al., 2016), sends robust projections to the BLA but not the ASt (Kim and Cho, 2020, 2017). Thus, the ASt may not receive necessary spatial information and play little or no role in contextual freezing, which is instead almost entirely mediated by pathways involving the BLA and CeA. The ASt therefore appears to be critical for sustained behavioral responses to acute sensory stimuli, but not required for responses to environmental context. Further study will be needed to delineate in greater detail the specific conditions and motivated behaviors where the ASt plays an important role. However, our identification of a novel role for the ASt in expression of conditioned behaviors raises some important technical considerations for future studies of amygdala function. Off-target effects on the ASt have never been considered as a potential confound for studies of other amygdalar nuclei, and the ASt is located directly in the vertical path of stereotaxic manipulations targeting the BLA or CeA. Thus, viral injections or pharmacological compounds targeting these nuclei could also inadvertently affect the ASt, which could drive behavioral and cognitive effects that confound interpretation of experimental results. We believe that careful

control of manipulations targeting the ASt and amygdalar nuclei will be necessary to clearly distinguish the shared and distinct functions of these two regions.

2.4.3. The ASt in models of valence encoding

How does the ASt fit in the hierarchy of established circuit models for encoding valence to direct behavior? With respect to the amygdala complex, two major models are possible. First, the ASt may be downstream of the amygdala complex, relying on input from the lateral amygdala for ASt neuron responses to conditioned stimuli, and functioning as an output nucleus of the amygdala complex like the CeA. Second, the ASt may act as a parallel pathway to amygdala, capable of encoding conditioned stimuli and directing behavioral responses independently of the amygdala complex. The first model is supported by the robust and rapid projection from the LA to the ASt, which is a key anatomical feature that distinguishes it from the rest of the striatum (Jolkkonen et al., 2001; Wang et al., 2002). The LA is known to be a site where synapses are potentiated to encode fear memory (Blair et al., 2001), and so it is possible that responses to conditioned stimuli in the ASt to direct behavior are dependent on input from the LA. In contrast, it is also possible the ASt acts independently; synapses from thalamic or cortical projections to the ASt could be directly potentiated to encode learned associations, allowing the ASt to respond to stimuli independently from input from the amygdala. In addition to these two major models, it is also possible that amygdalar inputs to the ASt play an important role in learning, but not expression, of conditioned responses. Determining the functional role of the LA projection to the ASt and investigating plasticity at ASt synapses will be critical areas for future investigation to understand the relationship of the ASt to the amygdala complex. Interestingly, the ASt, along with the tail of striatum, receives a

unique dopaminergic projection which carries information pertaining to novelty and external threat, rather than recording reward prediction error like the dopaminergic signal from medial DA neurons (Menegas et al., 2018). Determining the role of this dopaminergic signal in modulating the activity of ASt neurons will likely be critical for understanding the acquisition of conditioned responses and the overall function of the ASt.

The ASt is uniquely situated to complement known basal ganglia circuits mediating defensive action selection and execution, serving as a distinct subregion of the striatum with a unique functional specialization. The transition from action to habits (Robbins and Everitt, 2002) has been proposed to be mediated through cortico-striatal loops in the basal ganglia (Haber, 2016; Heilbronner et al., 2018), and we speculate that the ASt could serve as a shortcut to directly connect the circuits important for evaluation of stimuli directly to those for motor execution. Previous studies of striatal pathways have shown that *Drd1a*+ 'direct pathway' MSNs and Drd2+ 'indirect pathway' have divergent roles in controlling reinforcement and aversive learning (Cox and Witten, 2019; Kravitz et al., 2012; Nakanishi et al., 2014, 2014). *Drd2*+ neurons are broadly thought to be important for responses to aversive stimuli (Nakanishi et al., 2014), though studies of striatal circuits have overwhelmingly focused on reward learning paradigms rather than fear learning as in the amygdala. Our data suggests a specialized role for the ASt in responding to stimuli of negative valence; while subsets of ASt neurons did respond to positive and negative stimuli, the ASt was highly enriched for *Drd2*+ neurons that responded specifically to stimuli of negative valence, and inhibition of these neurons only affected conditioned responses to aversive stimuli and not reward responses. This is compatible with proposed models of the striatal indirect pathway as a key circuit for motor output elicited by aversive stimuli, suggesting that the sustained activity in the ASt may act to suppress competing

actions to facilitate the selection and execution of defensive behaviors. Regardless of whether the ASt is viewed in the context of amygdala or striatal circuits, it does appear to serve as a specialized structure for mediating defensive responses to aversive stimuli. This role for the ASt would also be consistent with a 'divergent paths' model of valence processing (Tye, 2018), where different sensory inputs mediating CS information can be potentiated on distinct efferent circuits in order to mediate appropriate responses to stimuli of positive and negative valence.

2.4.4. ASt neurons have distinct genetic identities

In addition to our functional dissection of ASt neuron activity in motivated behaviors, we also examined the cell type composition and transcriptomic profile of the ASt. The most notable features of the ASt were the greater proportion of *Drd2*+ MSNs compared to *Drd1a*+ MSNs, a unique feature relative to other regions of the striatum, and that ASt neurons were identifiable as genetically distinct subclusters within those MSN types relative to adjacent GABAergic structures the tail of striatum, dorsal striatum, and central nucleus of the amygdala. We found these differences in clustering were due to the unique expression of genes in the ASt relative to these other target regions, with hundreds of differentially expressed genes (DEGs) in *Drd1a*+ and *Drd2*+ ASt neurons. Intriguingly, these DEGs included several synaptic adhesion molecules such as cadherin 6 and integrin 6, which, in addition to serving as marker genes enriched in the ASt, are likely candidates responsible for establishing the unique connectivity of the ASt. The ASt receives robust projections from thalamic and cortical structures (Barsy et al., 2020; Doron and Ledoux, 1999; Hunnicutt et al., 2016; LeDoux et al., 1990; McDonald, 1998; Shi and Cassell, 1999, 1998, 1997), as well as from the lateral amygdala (Jolkkonen et al., 2001; Wang et al., 2002), and the formation of this circuit connectivity is likely directed by the expression of

genes such as such as adhesion molecules and axon guidance factors. The variation in gene expression between regions was much higher in some cell types than others; while *Drd1a* and *Drd2*-expressing MSNs showed considerable variability in gene expression, non-neuronal cells such as astrocytes, microglia and oligodendrocytes showed far fewer DEGs between regions. In the striatum there is considerable range of inputs and outputs that vary with topography, including the cortical regions which project to each subregion of striatum (Graybiel, 1983; Haber, 2016; Hunnicutt et al., 2016). The changes in expression of genes in MSNs that we observed throughout different subregions could be an underlying molecular basis for establishing these broad patterns of connectivity.

2.4.5. Conclusion

Our findings provide the first evidence that the ASt is an important region for encoding responses to emotionally significant stimuli, a previously unknown role for this structure. Consequently, the present study also identifies the ASt as a novel site of interest in neurological disorders where normal responses to stimuli are disrupted. Valence assignment and responses to stimuli are disrupted in depression, anxiety, and post-traumatic stress disorder (Disner et al., 2011; Kaviani et al., 2004; Morey et al., 2015; Ray et al., 2009). The amygdala complex has been widely studied as a key site for these disorders (Davis, 1992), but the possible contribution of the ASt has never been investigated. Since ASt neurons have distinct genetic identities and downstream targets than the rest of the amygdala complex, these circuits could represent vital new targets for the design of therapeutic approaches for these disorders.

2.5. Methods

2.5.1. Experimental model and subject details

Adult, 8-12 week old, wild-type C57BL6J mice (RRID:IMSR_JAX:000664), DRD1-Cre mice (RRID:MMRRC_036089-UCD), DRD2-Cre mice (RRID:MMRRC_036089-UCD), and VGAT-Cre mice (RRID:IMSR_JAX:028862) were used in all experiments as stated in the text. Mice were housed in the Salk Institute of Biological studies on a 12-h reverse light/dark cycle with ad libitum access to food and water except when otherwise stated in experimental procedures. All experiments were conducted during the dark cycle phase. All experimental procedures were carried out in accordance with NIH guidelines and approval of the Salk Institutional Animal Care and Use Committee.

2.5.2. Stereotactic surgery procedures

d All surgeries were conducted under aseptic conditions. Mice were anesthetized with an isoflurane/oxygen mixture (4-5% for induction, 1-2% for maintenance) and placed in a stereotaxic head frame (David Kopf Instruments, Tujunga, CA, USA). A heating pad was placed beneath the mice to maintain body temperature, and Sterile Lubricant Eye Ointment (Stye, INSIGHT Pharmaceuticals Corp. Langhorne, PA) was applied to the eyes to prevent drying. An incision was made along the midline to expose the skull and a dental drill was used to perform a craniotomy. During all surgeries, animals were injected subcutaneously with 1 mL of Ringer's solution, Buprenorphine (1 mg/kg), and Meloxicam (5 mg/kg). For recovery animals were placed in a clean cage on a heating pad. Animals were given >7 days of recovery period before being subjected to behavioral paradigms.

Stereotaxic coordinates were measured relative to bregma. Coordinates for injections targeting Amygdalostriatal transition zone (ASt) were +/- 3.17 ML (mediolateral), -1.52 mm AP (anteroposterior), and -4.28 mm DV (dorsoventral) relative to bregma. All injections of viral vectors were performed using glass pipettes (Drummond Scientific) pulled to a 130-140 μm tip diameter with a pipette puller (Narishige PC-10, Amityville, NY, USA). Pipettes were either attached to 10 μL microsyringes (Hamilton Microlitre 701, Hamilton Co., Reno, NV, USA) with a microsyringe pump (UNP3; WPI, Worcester, MA, USA) and digital controller (Micro4; WPI, Worcester, MA, USA), or to the Nanoject III Programmable Nanoliter Injector (Drummond Scientific, Broomall, PA, USA) with digital controller (Drummond Scientific, Broomall, PA, USA). For each injection, micropipettes were slowly lowered to the target site and viral vectors were delivered at a rate of 0.1-5.0 nL per second. The pipette was then slowly raised 0.02 mm and left in place for 15-20 min to allow diffusion of the virus, then slowly withdrawn.

2.5.3. Surgery for *in vivo* electrophysiology

An electrode consisting of a bundle of 16 single nichrome wires of 9 μm diameter (Stablohm 675, CFW Material #: 100-188, California Fine Wire Company, Grover Beach, CA, USA) was implanted unilaterally in the ASt. Electrodes were lowered into the brain at a rate of 0.01 mm/s. Electrodes were secured with C&B-Metabond Quick adhesive Luting Cement (Parkell, Long Island, NY, USA) and dental cement (Ortho-Jet powder, Lang Dental, Wheeling, IL, USA). Two to three skull screws (00-96 x 1/16 (stainless steel) 1.6mm cut length, Plastics One) were secured in the skulls around the implanted electrode, with a layer of C&B-Metabond Quick adhesive Luting Cement and dental cement for stabilization. For additional in vivo electrophysiology experiments, animals were implanted with Neuropixels probes. Neuropixels

probes (Version 1.0) wereassembled into a custom made 3D printed probe holder prior to implantation. Before surgery, the probe shank was soaked in 70% ethanol for 20 minutes. The petroleum jelly was gently applied around the base of the probe shank to form a hermetic seal. The remaining length of the probe shank was dipped into a fluorescent Dil (Vybrant Dil Cell-Labeling Solution, Waltham, MA, USA). For implantation, the probe holder with the probe was attached to a stereotaxic arm and centered at ML ± 3.17 mm, AP -1.52 mm relative to bregma. The probe was then lowered to DV -5.00 mm relative to bregma at a rate of 0.01 mm/s.

2.5.4. Surgery for *in vivo* calcium imaging

For calcium imaging experiments, 50 nL of AAV1-Syn-FLEX-GCaMP7f was injected in the ASt at a rate of 1 nL per second. Following injection, a 0.5 mm x 6.1 mm 0.5 pitch gradient refractive index (GRIN) lens (Inscopix Inc, Mountain View, CA, USA) was centered over the injection site and lowered to a depth 0.05 mm above the injection site at a rate of 0.01 mm/s. On the contralateral side, a screw (00-96 x 1/16 (stainless steel) 1.6mm cut length, Plastics One) was secured into the skull. Both the lens and the skull screw were secured with super glue (Krazy Glue All Purpose, The Original Super Glue Corporation, Ontario, CA, USA) and dental cement (Ortho-Jet powder, Lang Dental). A small platform flush with the GRIN lens was created with dental cement, and a plastic cover fixed over the GRIN lens with dental cement to prevent damage to the lens prior to securing the baseplate. Approximately 4 weeks following implantation, a 1.8 mm objective 0.25 pitch GRIN lens (Edmund Optics, Barrington, NJ, CA) was placed over the GRIN lens with dental cement at a height resulting in the optimal focal plane. A small baseplate (miniscopeparts.com) was then secured to the previously formed dental cement.

2.5.5. Electrode construction

For recording single-unit activity, multi-electrode arrays were constructed. Arrays consisted of one multi-channel single wire probe, using Super Glue Corporation (Omnetics Connector Corp., Minneapolis, MN) as the structural component. This array was connected directly to the plug using a plastic spacer. The array was comprised of 16 single wires (Stablohm 675, CFW Material #: 100-188, California Fine Wire Company, Grover Beach, CA). Wires were aligned using the length of syringe needle (2-3 mm). The wire insulation was then stripped using forceps and wires were connected to the Omnetics connector using a conductive adhesive (Super Shield Silver Conductive Paint; MG Chemicals, Burlington ON). Super glue and epoxy were used to ensure connections were secure. Serrated tungsten scissors (Fine Science Tools, Foster City, CA) were used to cut the arrays to length. A 50/50 gold plating solution consisting of gold solution (Neuralynx, Bozeman, MT) and 1 μM polyethylene glycol was then applied to decrease the impedance of the wires to 150-250MΩ. Finally, a low impedance bare silver wire (California Fine Wire, Grover Beach, CA) was soldered to the last pin on the connector, and then the connection was covered with dental cement.

2.5.6. Behavioral tasks

All behavioral tasks involving optogenetic manipulation or calcium imaging were performed 6-8 weeks after injection of viral vectors to allow sufficient expression of opsins or genetically-encoded calcium indicators. For at least four days prior to behavioral experiments mice were habituated to experimenter handling and attachment of optic fiber patch cables to surgically implanted optic fibers or tethers for calcium imaging and electrophysiology recordings. All behavioral experiments except the discrimination task were analyzed using

Ethovision XT software (Noldus, Wagenigen, Netherlands) and recorded with a digital video camera above the test arena.

2.5.6.1. Open field test

Mice were placed in a 53 x 50 cm arena with four transparent plexiglass walls, and allowed to move freely throughout the arena for 15 min. Light stimulation was delivered during the 3-6 min and 9-12 min epochs (ChR2 mice and eYFP controls: 10 mW 473 nm light at 20Hz, 5 ms pulse width. NpHR mice and eYFP controls: 3 mW 593 nm light, constant delivery). Overall locomotion and time spent in edges (50% of arena area closest to walls) and center region of arena during each epoch was analyzed for each mouse.

2.5.6.2. Elevated plus maze

Mice were placed in the center of the elevated plus maze (EPM) apparatus, consisting of two open arms (30 x 5 cm) and two enclosed arms (30 x 5 x 30 cm) extending from the center platform (5 x 5 cm). The entire apparatus was elevated 75 cm from the floor. Mice were given 1-5 min to recover from handling before the 25 min testing phase began. Light stimulation was delivered during the 5-10 min and 15-20 min epochs (ChR2 mice and eYFP controls: 10 mW 473 nm light at 20Hz, 5 ms pulse width. NpHR mice and eYFP controls: 3 mW 593 nm light, constant delivery), and time spent in open and closed arms of the apparatus throughout each epoch was quantified.

2.5.6.3. Real-time place preference

Mice were placed in the center of a transparent Plexiglass chamber (57.15 x 22.5 x 30.5 cm). The chamber was divided into 'ON side' and 'OFF side' compartments (counterbalanced between and within groups). The chamber was then illuminated with 30 lux ambient light. Mice were allowed to freely explore the chambers for 30 min during which entry into the 'ON side' triggered photostimulation (ChR2 mice and eYFP controls: 10 mW 473 nm light at 20Hz, 5 ms pulse width. NpHR mice and eYFP controls: 3 mW 593 nm light, constant delivery) until the side was exited, and total time spent in each side throughout the task was quantified.

2.5.6.4. Two-tone discrimination tasks

Animals were trained and tested in standard operant chambers (23 x 30 x 40 cm; Med Associates inc.) within a sound attenuating cubicle. Each chamber was equipped with speakers for tone delivery, a syringe pump for reward delivery, a reward port with an infrared beam to detect port entries, a grid floor for shock delivery, infrared house lights and a camera for behavioral recording.

Prior to discrimination training, mice were sequentially trained to recognize reward-predicting and shock-predicting cues. On all tasks with rewards, mice were food-restricted (3.0 g food per mouse per day) prior to testing. In the first phase of training animals were trained to associate a conditioned stimulus ('CS-reward') with delivery of a high-calorie reward (Ensure™, Abbott Laboratories). During reward conditioning animals were presented with 60 trials in which a pure auditory tone cue of (20 kHz or 3.5 kHz, counterbalanced) predicted the delivery of a Ensure reward (7.5 μL per trial) to the reward port. Collection of the reward prior to the end of the tone resulted in termination of the tone. The inter-trial interval was variable with an average

of 90 sec (+/- 20 sec). Unpaired mice were presented with the same number of CS-rewards and Ensure deliveries, explicitly unpaired from one another and presented in a randomized order. Animals underwent four sessions of reward training (1 session per day). In the second phase of training animals were trained to associate a conditioned stimulus (CS-shock) with a shock delivery. During fear conditioning animals were presented with 30 trials in which a tone cue (3.5 kHz or 20 kHz, counterbalanced, and reversed from the tone pairing used for CS-reward for each mouse) predicted the delivery of a 0.25 sec shock (0.7 mA). The delivery of the shock co-terminated with the predicting tone. ITI was variable with an average of 90 sec (+/- 20 sec). Unpaired mice were presented with the same number of CS-shocks and shock deliveries, explicitly unpaired from one another and presented in a randomized order. Animals underwent two sessions of fear training ('training' and 'test' sessions, 1 session per day). In the second session ('test'), animals were presented with tones only and no shocks.

Following training to recognize each CS, animals were then tested in a two-tone discrimination task. During the discrimination task, animals were presented with 45 CS-reward trials (3.5 kHz or 20 kHz, counterbalanced) and 15 CS-shock trials (20 kHz or 3.5 kHz, counterbalanced), for a total of 60 trials per session. Trials were presented in a pseudorandom manner, and the ITI was variable with an average of 90 sec (+/- 20 sec). Unpaired mice received the same number of CS and US deliveries, explicitly unpaired from one another and presented in a randomized order. Animals underwent discrimination testing for 4-6 sessions (1 session per day) until they achieved 85% reward collection.

For electrophysiology experiments conditioned tones associated with Ensure and shock delivery were 20 seconds in length. Recordings from electrodes were collected continuously throughout the session. For calcium imaging experiments conditioned tones associated with

Ensure and shock delivery were 10 seconds inlength. For the discrimination task, recordings from miniscopes were collected on select trials (every shock trial, every other reward trial), using a 5V TTL signal to trigger miniscope recordings. Blue LED houselights were also included in the operant chamber to reduce changes in illumination caused by activation of the blue excitation LED from the miniscope. For optogenetic inhibition experiments, conditioned tones associated with Ensure and shock delivery were 20 seconds in length. On a subset of interleaved CS-shock and CS-reward trials both NpHR and eYFP control mice received laser delivery (593 nm light, 3 mW, constant delivery) beginning 1s prior and ending 1s after the tone on period.

2.5.6.5. US Experiment

For calcium imaging cohort mice, animals underwent an additional session of US testing to determine responses to both shock and reward when unpredicted by the CS. Over a 45-minute training session, animals experienced foot shock (0.25 sec, 0.7 mA) and Ensure reward (7.5 μL) deliveries of the same magnitude as the discrimination task, presented in a pseudo-random order.

2.5.6.6. Contextual fear conditioning

For NpHR cohort mice, animals two sessions of contextual fear conditioning over two days. On the first day (‘training’) mice were placed in a novel environment, allowed to habituate for five minutes, and ten foot shocks (1s, 0.7 mA) were delivered in a randomized order over ten minutes. On the second day (‘test day’) mice were returned to the environment, and both NpHR and eYFP control mice received laser delivery (593 nm light, 3 mW, constant delivery) during a 10 minute test session, and behavioral responses to conditioned context recorded.

2.5.7. Electrophysiology recordings

2.5.7.1. *In vivo* electrophysiology data acquisition

Electrophysiology data from single-wire probes was recorded using an Open Ephys acquisition board (Siegle et al., 2017) in conjunction with 16 channel Intan headstages (Intan Technologies, Los Angeles, CA). Data was collected at a sampling rate of 30 kHz with a band pass filer to only collect signals between 1 and 7000 Hz.

2.5.7.2. Neuropixels data acquisition

During behavior, Neuropixels data was acquired using SpikeGLX software (http://billkarsh.github.io/SpikeGLX/) via a National Instruments DAQ (PXIe-1071, PCIe-8381, and PXI-6133) at 30k Hz. Event timestamps were acquired in TTL signals to the National Instruments DAQ at 10k Hz.

2.5.8. Calcium imaging

2.5.8.1. Calcium imaging data acquisition

UCLA miniscopes V3.2 (http://miniscope.org) were used to collect calcium imaging data (Cai et al., 2016). During behavior, a 5V TTL signal was used to trigger the miniscope recording on select trials. When the scope was triggered, imaging data from the CMOS imaging sensor (Aptina, MT9V032) was transferred to data acquisition (DAQ) electronics and USB Host Controller (Cypress, CYUSB3013) via a co-axial cable. Images were acquired at 15 frames per second at a resolution of 752 X 480 and saved as uncompressed .avi files.

2.5.8.2. Histology

Following experiments, mice were deeply anaesthetized deeply with sodium pentobarbital (200 mg/kg, intraperitoneal injection). Animals were transcardially perfused with 10 mL of Ringer's solution followed by 10 mL of cold 4% PFA in 1X PBS. Following decapitation and extraction, brains were fixed in 4% PFA in 1X PBS for 24 hrs at 4C. Brains were then transferred to 30% sucrose in 1X PBS at 4C until they sunk to the bottom of the sucrose solution. Brains were sectioned coronally at 50 µm using a microtome (Thermo Scientific) and were stored at 4C in 1X PBS until staining. Sections were mounted directly onto glass microscope slides and cover slipped with EMS-Shield Mounting Medium w/ DAPI. Slides were then imaged at 10x using the Keyence BZ-X710 Fluorescence microscope. For Neuropixels implants, the trajectory of each Neuropixels probe was reconstructed from brain slices based on The Allen Mouse Brain Common Coordinate Framework (https://www.sciencedirect.com/science/article/pii/S0092867420304025) using Allen CCF tools (https://github.com/cortex-lab/allenCCF).

2.5.9. RNAscope *in situ* hybridization

2.5.9.1. Preparation of fresh frozen sections for fluorescence *in situ* hybridization

8-10 week old C57BL/6J mice from Jackson Laboratories were anesthetized with 5% isoflurane, and brains were immediately extracted and covered with powdered dry ice for 2 minutes, and then stored at -80°C. Brains were then sectioned at 20 µm thick using a cryostat (CM3050 S; Leica, Buffalo Grove, IL) at -16°C. Sections were placed on a glass slide, gently heated from the bottom with the tip of a finger to encourage adhesion of the slice to the slide, and stored at -80°C until further processing.

2.5.9.2. Fluorescence *in situ* hybridization using RNAscope

Fluorescence in-situ hybridization was performed using the Advanced Cell Diagnostics bio V2 RNAScope kit and protocol (Advanced Cell Diagnostics, Newark, CA) using the RNAscope Multiplex Fluorescent Reagent Kit V2 (Catalog #323110), Fluorescent Multiplex Detection Reagents (#323110), probes for Drd1a (#406491-C1 and #406491-C3) and Drd2 (#406501-C3 and #406501-C1), and the Perkin Elmer TSA Plus Fluorescence Palette Kit (NEL760001KT). Fresh frozen slices were fixed in 4% paraformaldehyde for 1 hour at 4°C. Slices were dehydrated in ethanol, and incubated in hydrogen peroxide for 8 minutes, with protease steps omitted to prevent tissue degradation. Slides were incubated in desired probe combinations (Drd1a and Drd2, which were then counterbalanced for each fluorophore channel) for 2 hours at 40°C. For each channel, slides were incubated in channel-specific HRP for 10 minutes, followed by incubation in TSA fluorophore for 20 minutes, and then incubation in HRP-blocker for 10 minutes. Between all steps, slides were washed 2 times in 1x RNAscope wash buffer for 1-2 minutes. Slides were then incubated in ACDbio DAPI for 10 minutes, washed, dried for 20 minutes, coverslipped with PVA Dabco, and left to dry overnight before imaging.

2.5.9.3. Confocal microscopy

Confocal fluorescence images were acquired on an Olympus FV1000 confocal laser scanning microscope using a 40x/1.30NA oil immersion objective. Serial Z-stack images were acquired using the FluoView software (Olympus, Center Valley, PA) at a thickness of 1.5 µm per Z stack, with 3-7 planes taken per image. Images were acquired with identical settings for laser power, detector gain, and amplifier offset.

2.5.9.4. Image processing

Images were opened in ImageJ and individual Z-planes encompassing the entire ROI were selected from each image for further image processing. Background was subtracted from all channels in all images using the subtract background feature in ImageJ. Each channel was then further thresholded using the brightness and contrast feature in ImageJ. Thresholds were determined by manually thresholding 10 images to a level with no background, and then computing the average minimum threshold necessary to remove background. The average threshold across 10 images was then used as the threshold for all images. Masks of each region were drawn based on the mouse brain atlas (Paxinos and Franklin, 2004) Images were then saved as 8bit TIFFs for further cell and puncta identification in CellProfiler.

2.5.10. Single-nucleus RNA sequencing

2.5.10.1. Tissue extraction and cryopreservation

All procedures were performed in accordance with Institutional Animal Care and Use Committee protocol S16054 at the University of California, San Diego. All mice in the study were wild-type C57BL/6J background and received directly from Jackson Laboratories at 6 weeks of age and acclimated to the colony prior to experiments. Animals were single-housed and maintained free from noise or disturbance for 24 hours prior to sacrifice to reduce artifactual immediate early gene expression. Sacrifice was performed at P60 ± 3 days (n = 10-15 mice per pool for ASt, 10 for CeA, 9-10 for tail of striatum, 5 for body of striatum). Sample size was determined based on amount of expected nuclei per region per mouse: estimates of expected nuclei were determined empirically, though nuclear recovery was approximately 20% of total based on cellular density estimates from the Blue Brain Cell Atlas. 12,000 nuclei were targeted

per combination of assay, condition, and region, which was determined using Single-Cell One-sided Probability Interactive Tool (SCOPIT) v1.1.4, allowing potential detection of at least 5 nuclei from 10 rare subpopulations at 0.1% frequency with 95% probability (Davis et al., 2019). All sacrifices were performed during the dark period of the light cycle. Animals were anesthetized via combined intraperitoneal injection of 150 mg/kg ketamine and 15 mg/kg xylazine. Once unconscious, mice animals were transcardially perfused with ice-cold, carbogen-bubbled (95% O2, 5% CO2), nuclease-free, 0.22 μm sterile-filtered artificial cerebrospinal fluid (ACSF) with a composition of 93 mM N-methyl-D-glucamine, 2.5 mM KCl, 1.2 mM NaH2PO4, 30 mM NaHCO3, 20 mM HEPES, 25 mM glucose, 5 mM sodium ascorbate, 2 mM thiourea, 3 mM sodium pyruvate, 13.2 mM trehalose, 12 mM N-acetyl-cysteine, 0.5 mM CaCl2, 10 mM MgSO4, and 93 mM HCl, at pH 7.3-7.4.(Tasic et al., 2018; Ting et al., 2014) Following transcardial perfusion, brains were immediately extracted and submerged into ice-cold carbogen-bubbled ACSF, with less than 5 minutes between the beginning of perfusion and final submersion after extraction. Brains were serially sectioned in ice-cold, carbogen-bubbled ACSF on a VT1000S vibratome (Leica) with polytetrafluoroethane-coated razor blades (Ted Pella) at 0.15 mm/sec and 100 Hz, dividing the whole cerebrum into 400 μm coronal slices. Target regions were microdissected from these slices under a stereomicroscope using a sterile blunt-end needle (22 gauge for CeA, ASt, and tail of striatum, 16 gauge for dorsal striatum). All regions were targeted using Paxinos and Franklin's the Mouse Brain in Stereotaxic Coordinates as reference (Paxinos and Franklin, 2019). Extracted tissue samples were recovered in ice-cold, nuclease-free, 0.22 μm sterile-filtered cryoprotective nuclear storage buffer, composed of 0.32 M sucrose, 5 mM CaCl2, 3 mM magnesium acetate, 10 mM Trizma hydrochloride buffer (pH 8.0), 1 mM dithiothreitol, 0.02 U/μl SUPERase•In RNAse Inhibitor (Invitrogen), and 1X cOmplete

Protease Inhibitor Cocktail with EDTA (Roche). Tissue was then snap frozen using a metal CoolRack M90 (Biocision) pre-chilled to -80˚C and stored at -80˚C until nuclear isolation. Following extraction of tissue regions of interest, remaining portions of sections were fixed in 4% paraformaldehyde and 4′,6-diamidino-2-phenylindole (DAPI) was applied to sections at 1 µg/ml. After fixation and staining, sections were mounted and imaged on an VS120 slide scanner (Olympus). From these images, dissection accuracy was assessed for each region, and individual samples were only selected for downstream nuclear isolation if the extracted tissue fell entirely within the defined target regions.

2.5.10.2. Nuclear isolation and sorting

Nuclear isolation procedures were adapted from multiple methods described previously.(Krishnaswami et al., 2016; Preissl et al., 2018) All procedures were performed on ice, and all solutions were ice-cold, nuclease-free, and 0.22 µm sterile-filtered. Cryopreserved tissue pieces were slow-thawed by incubation at 4˚C for 1 hour prior to isolation. Tissue pieces were then pooled and resuspended in nuclear isolation medium composed of 0.25 M sucrose, 25 mM KCl, 5 mM MgCl2, 10 mM Trizma hydrochloride buffer (pH 7.4), 1 mM dithiothreitol, 0.04 U/µl RNasin Plus RNAse Inhibitor (Promega), 1X cOmplete Protease Inhibitor Cocktail with EDTA (Roche), and 0.1% Triton-X. The pooled tissue pieces in nuclear isolation medium were transferred to a 2 mL Dounce tissue grinder. Tissue was homogenized by 5 strokes from the loose pestle and 15 followed by the tight pestle, and the resulting homogenate was filtered through a 40 µm Flowmi cell strainer (Bel-Art) into a 1.5 ml Lo-Bind tube (Eppendorf). The homogenate was then centrifuged with a swinging bucket rotor at 4˚C and 1000 x g for 8 minutes. Nuclei were then washed with nuclear flow buffer composed of DPBS with 1% bovine

serum albumin, 1 mM dithiothreitol, and 0.04 U/µl RNAsin Plus RNAse Inhibitor (Promega) and centrifuged at 4˚C and 500 x g for 5 minutes, which was subsequently repeated. Nuclei were finally resuspended in nuclear flow buffer containing 3 µm DRAQ7 (Cell Signaling Technology) and again filtered through a 40 µm Flowmi cell strainer into a 5 ml round-bottom polystyrene tube. Each isolation took under 45 minutes to perform, from homogenization to final suspension.

Fluorescence-activated nuclei sorting (FANS) was carried out on a FACSAria II SORP (BD Biosciences) using a 70 µm nozzle at 52 PSI sheath pressure. For FANS, debris was first excluded by gating on forward and side scatter pulse area parameters (FSC-A and SSC-A), followed by exclusion of aggregates (FSC-W and SSC-W), and finally gating for nuclei based on DRAQ7 fluorescence (FSC-A and APC-Cy7-A). Only the set of DRAQ7+ nuclei at the first level of fluorescence were sorted to enrich for singlets, given stoichiometric DNA binding. Nuclei were successively sorted into 1.5 ml LoBind tubes (Eppendorf) under the purity sort mode. The tube contained 10X RT master mix without RT Buffer C. 16,000 total nuclei were targeted for downstream processing, and to account for cytometer errors and subsequent loss of nuclei, up to 21,000 detected nuclei were sorted into the tube to yield 16,000 viable nuclei for downstream sequencing (if fewer than 21,000 nuclei were detected, all were sorted into the tube). Nuclei were then immediately processed for snRNA-seq.

2.5.10.3. Library preparation and sequencing

Nuclear suspensions were converted into barcoded snRNA-seq libraries using the Chromium Next GEM Single Cell 3’ v3.1 Reagent Kits v3.1 Single Index (10X Genomics). Library preparation for both assays was performed in accordance with the manufacturer’s instructions. 10,000 nuclei were targeted during each snRNA-seq library preparation run, and

each region was performed in duplicate at minimum (n = 2 libraries for ASt, 3 for CeA and tail of striatum, 4 for body of striatum).

10X libraries were first sequenced at low depth on a NextSeq 550 Sequencing System (Illumina) to estimate quality and number of nuclei for each library, followed by deep sequencing on a NovaSeq 6000 Sequencing System. All runs were performed using 2 x 100-bp paired-end reads, outputting data in 28/8/91-bp read format. All sequences were demultiplexed using bcl2fastq.

2.5.11. Statistical analysis

Statistical analyses were performed using either GraphPad Prism (GraphPad Software, Inc, La Jolla, CA, USA) or MATLAB (Mathworks, Natick, MA, USA). Group comparisons were made using either one-way or two-way analysis of variance (ANOVA) followed by Bonferroni post hoc tests. Non-parametric Wilcoxon signed-rank tests were used to compare in vivo neural firing rates across conditions, using an a = 0.01. An a = 0.01 was also used to determine whether z-score transformed peri-stimulus time histograms of neural data exhibited significant neural responses. Multiple comparisons were corrected when appropriate by adjusting P values using the Bonferroni method. The number of animals (N) and the number of neurons (n) recorded is specified in the figures, the figure legends, and the text.

2.5.12. Statistical analysis of behavior

2.5.12.1. Behavioral Analysis of Open Field Test, Elevated Plus Maze, and Real-Time Place Preference

Behavioral performance was recorded by digital cameras positioned above the test arena. Ethovision XT software (Noldus, Wagenigen, Netherlands) was used to track mouse location.

2.5.12.2. Behavioral Analysis of Two-tone Discrimination Task

To automatically detect animal defensive behaviors, SLEAP (Pereira et al., 2022) was used to estimate animal poses in behavioral videos. A training data set of over 6000 frames was labeled using a 14-point skeleton to represent the mouse (nose, left ear tip, left ear base, right ear base, right ear tip, skull base, shoulders, haunch, tail base, tail segment, left arm, right arm, right leg, and left leg). This data set was used to train a top-down model; in this model, first the animal is detected using a centroid model, then the location of each labeled body part is identified using a centered instance model. To identify times when an animal was freezing, the total sum of distance travelled of each body point between the current and previous frames had to surpass a freezing-threshold. To detect escape behavior, the distance traveled of the haunch point in the current and previous frame compared to a dashing-threshold was examined. Thresholds were set for each experiment by visual inspection to ensure the automatically detected freeze and escape frames aligned with the animal's true behavior, and 'total defensive behaviors' was calculated as the sum of freezing or escape behaviors. To detect reward seeking behavior, port entries and exits were determined from reward port infrared beam breaks (Med-PC IV, Med Associates).

2.5.13. Statistical analysis of electrophysiology recordings

2.5.13.1. Neuropixel recordings

Acquired data were prepossessed using CatGT (https://billkarsh.github.io/SpikeGLX/#catgt). Preprocessed data were then sorted into spike clusters using Kilosort 2.5 (https://github.com/MouseLand/Kilosort), which provides a drift-tracking feature that detects the footprints of the same neuron during a recording session while

correcting for drift. To determine the quality metrics of sorted spike clusters, we used modules for processing extracellular electrophysiology data provided by the Allen Institute. All tools described above were combined in Python using custom-written scripts (https://github.com/jenniferColonell/ecephys_spike_sorting). Finally, manual curation was performed to identify individual neurons and to remove multiunit and noise clusters using phy (https://phy.readthedocs.io/en/latest/).

2.5.13.2. *In vivo* electrophysiology recordings

Preparation of files for cluster sorting was carried out using a custom MATLAB algorithm. Spikes were thresholded to a 6 sigma criteria and traces were aligned to their depolarization peak. Spikes were exported in a .plx file format to be imported into Offline Sorter (Plexon Inc., Dallas TX). Once spikes were imported, principal component analysis was used to cluster spikes into individual units.

2.5.13.3. Analysis of neural responses to cue delivery

For all electrophysiology experiments, to calculate the neuronal response to each conditioned stimulus, the mean activity for each neuron across all trials of a given trial type was calculated and Z-score of changes in firing rate was calculated based on mean and standard deviation for that neuron during a 20 second baseline period immediately preceding the onset of the cue. For hierarchical clustering, each neuron's Z-score response for reward trials and fear trials were horizontally concatenated then clustered using agglomerative hierarchical clustering based on Euclidean distance with a custom MATLAB script. For 'phasic' and 'sustained'

responses, the mean Z-score was calculated during a period of 1ms-100 ms following the cue and 100ms to 18s following the cue, respectively.

2.5.13.4. Neural trajectory analysis

To visualize the population-level firing rate dynamics, a single global Principal Component Analysis (PCA) was applied to a matrix containing the standardized, trial-averaged neural activity (concatenated activity during shock and reward trials) of all animals (paired and unpaired). This enabled the comparison of the neural trajectories across the experimental groups. The mean firing rate for each group of animals and each trial type was then projected into this principal component space and their trajectories within the first three dimensions are shown. The distance between the shock and reward trajectories for each experimental group was calculated as the Euclidean distance within each time-bin using the complete principal component space. For the visualization, we smoothed each trajectory by convolving the signal with a one-directional Gaussian.

2.5.13.5. Logistic regression classifier

To test whether ASt neural activity within a trial is correlated with various behavioral variables logistic regression models were used (Glaser et al., 2020). For each mouse separately, the neural activity of all trials was divided into five non overlapping folds to use for cross-validation. To classify whether CS-shock or CS-reward was presented during a trial, a logistic regression classifier was trained on the training folds and evaluated time-bin by time-bin on the held-out trials. Similarly, separate classifiers were trained to decode whether the mouse was

engaging in freezing or escape behavior. The training data was balanced to ensure there were an equal number of time points for each class.

2.5.14. Statistical analysis of calcium recordings

Imaging data was then concatenated and temporally downsampled by a factor of two using a custom MATLAB script before motion correction (rigid registration) via the NoRMCorre algorithm (Pnevmatikakis and Giovannucci, 2017). Neuron detection and signal extraction was done using the CNMF-E algorithm (Zhou et al., 2018). Using a MATLAB Neuron Deletion GUI, neurons exhibiting abnormalities in morphology and calcium trace were manually excluded. Neuron curation was performed by experimenters blinded to the experimental condition.

2.5.14.1. Analysis of neural responses to cue delivery

To calculate the neuronal response to each conditioned stimulus, the mean GCaMP7f fluorescence for each neuron across trials for each trial type was calculated, and Z-score of fluorescence values calculated based on mean and standard deviation for that neuron during a 10 second baseline period immediately preceding the onset of the cue. For clustering, each neuron's individual Z-score response for CS-shock trials and CS-reward trials were horizontally concatenated using a custom MATLAB script and clustered using agglomerative hierarchical clustering based on Euclidean distance, with soft normalization of neurons to a maximum Z-score of 10. For the US-only experiment, Z-scores were calculated for each neuron based on a 5 second baseline period immediately preceding shock delivery or consumption of reward.

2.5.15. Statistical analysis of RNAScope *in situ* hybridization

Image TIFFs were run through CellProfiler using an optimized version of the CellProfiler Colocalization pipeline (https://cellprofiler.org/examples/). The pipeline was optimized to identify DAPI labelled cells (18-45 pixels in diameter) and then subsequently identify mRNA puncta (4-10 pixels in diameter). DAPI cell detection was further restricted by shrinking DAPI ROIs by 1 pixel. Puncta overlapping with DAPI-identified cells (using the relate objects module) were considered for analysis to assess the level of mRNA expression per cell. To determine if cells were expressing mRNA, a threshold of 5 or more puncta within twice the diameter of nucleus centered over the nucleus was used (McCullough et al., 2018). Total number and density of *Drd1a*+ and *Drd2*+ cells in each region of interest were calculated from CellProfiler .csv outputs using custom MATLAB code.

2.5.16. Statistical analysis of single-nucleus RNA sequencing

2.5.16.1. Sequence alignment

All samples were processed using CellRanger (v5.0.0) (Zheng et al., 2017). All processing was done by using CellRanger's implementation of STAR to align sample sequence reads to their pre-built mm10 vm23/Ens98 reference transcriptome index 2020-A, with predicted and non-validated transcripts removed. All sequencing reads were aligned to both the exons and the introns present in the index. Samples were demultiplexed to produce a pair of FASTQ files for each sample. FASTQ files containing raw read sequence information were aligned to the CellRanger index using the cellranger count command with --chemistry SC3Pv3 and --include-introns flags enabled. CellRanger corrected sequencing errors in cell barcodes to pre-defined sequences in the 10X v3 single-index whitelist within Hamming distance 1. PCR duplicates were

removed by selecting unique combinations of corrected cell barcodes, unique molecular identifiers, gene names, and location within the transcript. Raw unfiltered count data was read into R (v4.0.3) using the Seurat package (v4.0) (Butler et al., 2018; Hao et al., 2021; Satija et al., 2015; Stuart et al., 2019). The final result of the pipeline was a barcode x gene expression matrix for further analysis downstream.

2.5.16.2. Quality control

We used the raw, unfiltered matrix output from CellRanger as the input to the beginning of the pipeline. However, to apply a more stringent filter, the emptyDrops dirichlet-multinomial model from the DropletUtils package (v1.10.2) was applied to each library individually (Griffiths et al., 2018; Lun et al., 2019). Droplets with less than 100 total counts were used to construct the ambient RNA profile and an FDR threshold below 0.001 was used to select putatively occupied droplets. All barcodes with greater than 1000 UMIs were further assumed non-empty. Most quality filtration choices were heavily influenced by the recommendations presented in pipeComp (Germain et al., 2020). All quality control was performed on each library individually prior to merging. Minimal quality filtering for each barcode was performed by setting a floor of 1000 features per barcode for downstream inclusion to ensure the dataset is entirely composed of high-quality nuclei. Next, to remove highly likely multiplet barcodes, barcodes were filtered out if their count depth was more than 5 median absolute deviations above the median count depth. Barcodes were then removed if their proportion of ribosomal or mitochondrial reads was more than 5 interquartile ranges above the 75th percentile. Heterotypic doublets were identified by creating simulated artificial doublets in scDblFinder (v1.4.1), which uses a DoubletFinder-like model to remove barcodes similar to simulated doublets, with an assumed doublet rate of 1% per

1000 nuclei in the library (Germain and Lun, 2021; McGinnis et al., 2019). Scater (v1.18.3) was used to produce initial diagnostic tSNE and UMAP plots for visually checking the influence of each above metric on the structure of the data (McCarthy et al., 2017). Downstream, one cluster of diffusely-distributed neurons with few marker genes and disproportionately low read depth and disproportionately high mitochondrial and ribosomal gene proportions was removed as low-quality cells.

2.5.16.3. Data processing/transformation

All datasets (initially for all nuclei and again for selected subclusters) were formatted into Seurat objects (v4.0.0), merged, and then normalized and transformed individually using the SCTransform (v2) variance stabilizing transform, which performs best according to prior comparisons in pipeComp (Choudhary and Satija, 2022; Germain et al., 2020; Hafemeister and Satija, 2019). Following the merge, all genes expressed in 3 or fewer cells were removed from analysis. SCTransform was run returning Pearson residuals regressing out mitochondrial gene expression, first with 5000 highly variable features, and then with 3000 for subsequent iterations on subsets of the data. Dimensionality of the dataset was first reduced using principal component analysis, as implemented in Seurat's RunPCA function (Jolliffe and Cadima, 2016). The top 50 principal components were retained for downstream analysis. These principal components (top 25 for all nuclei, top 15 for subclusters) were used as input to the non-linear tSNE and UMAP dimensionality reduction methods as implemented by Seurat's RunTSNE and/or RunUMAP functions (n.epochs = 1000, min.dist = 0.5) at default settings unless otherwise specified (Becht et al., 2019; Maaten and Hinton, 2008; McInnes et al., 2018).

2.5.16.4. Differential expression

Marker genes were identified using Wilcoxon rank-sum test as implemented by the FindConservedMarkers function in Seurat, using the region as a grouping variable. Genes were accepted as differentially expressed with a minimum proportion cutoff at 0.1 and minimum fold change at 1.5-fold (log2-fold change of 0.585), with a p-value cutoff of 0.01 after Bonferroni correction. To identify genes differentially expressed by region, single- cell values were converted to pseudo-bulk by batch using the run_de function as implemented in the Libra package (v1.0.0) using default settings, and tested for differential expression using edgeR's likelihood ratio test (Robinson et al., 2010; Squair et al., 2021). Region-specific genes were identified by comparing batches from one region to all others, while pairwise differentially-expressed genes were identified between batches from just the two regions of interest, and genes were retained with a minimum fold change at 1.5-fold (log2-fold change of 0.585), at a p-value cutoff of 0.01 after Benjamini-Hochberg correction. Neurologically-related genes of interest were determined by filtering region-specific differentially expressed genes through a subset of pre-selected gene families from HGNC with known functions related to neural structure and function (Tweedie et al., 2021).

2.6. Acknowledgments

We thank Chris Leppla, Praneeth Namburi, and Kanha Batra for their contributions to the project. We also thank Alcino Silva, Peyman Golshani, Daniel Aharoni, Tristan Shuman, and Denise Cai for their assistance and contributions to UCLA Miniscope resources used in the project. K.M.T. is an HHMI Investigator and the Wylie Vale chair at the Salk Institute for

Biological Studies and this work was supported by funding from the JPB Foundation, the PIIF, PNDRF, JFDP, New York Stem Cell Foundation, Klingenstein Foundation, McKnight Foundation, The Salk Institute, Howard Hughes Medical Institute, Clayton Foundation, Kavli Foundation, Dolby Family Fund, R01-MH115920 (NIMH), R37-MH102441 (NIMH), the NIH Director's New Innovator Award DP2- DK102256 (NIDDK) and Pioneer Award DP1 AT009925 (NCCIH). F.M. was supported by a CIHR Postdoctoral Fellowship and a K99/R00 NIH Pathways to Independence Award (K99 MH121563). H.L. was supported by a K99/R00 NIH Pathways to Independence Award (K99 DA055111-01). S.S. was supported by China Scholarship Council grant 201806010370.

Chapter 2, in full, is a reprint of the material as it was submitted for publication to Cell. Mills, F., Lee, C.R., Howe, J.R., Li, H., Shao, S., Keisler, M.N., Lemieux, M.E., Taschbach, F.H., Keyes, L.R., Borio, M.R., Chen, H.S., Patel, R.R., Gross, A.L., Delahanty, J., Cazares, C., Maree, L., Wichmann, R., Pereira, T.D., Benna, M.K., Root, C.M., Tye, K.M. Amygdalostriatal transition zone neurons encode sustained valence to direct conditioned behaviors. Cell, in revision. The dissertation author was one of the primary investigators and a co-first author on the paper, responsible for all matters pertaining to single-nucleus RNA sequencing.

2.7. Appendix

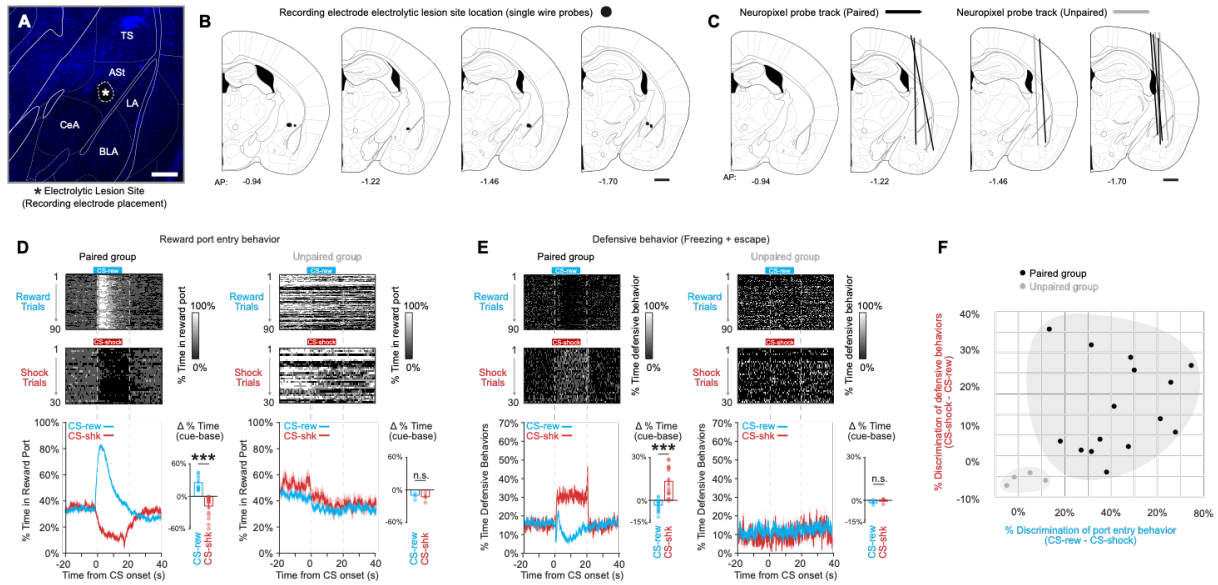

Figure S2.1. Histological targeting and behavioral validation for in vivo electrophysiology recordings.

(A) Representative image of electrolytic lesion site to confirm recording electrode targeting to the ASt (Blue = DAPI, Scale bar = 100 µm).

(B) Histologically verified lesion sites of single-wire electrode placements in recording experiments targeting ASt.

(C) Histologically verified probe tracks of Neuropixels probes in recording experiments.

(D-F) Validation of conditioned behavioral responses during two-tone discrimination task in mice in electrophysiological recording experiments (N=15 mice paired, 4 mice unpaired). Paired group mice showed distinct responses to the CS-shock and CS-reward tones in reward port entry behavior (Two-tailed t-test, t = -9.204, df = 14, *** p = 2.584e-07) (D) and defensive responses (Two-tailed t-test, t = 5.927, df = 14, *** p =.000018) (E), consistent with successful discrimination between the two tones compared with unpaired mice (F).

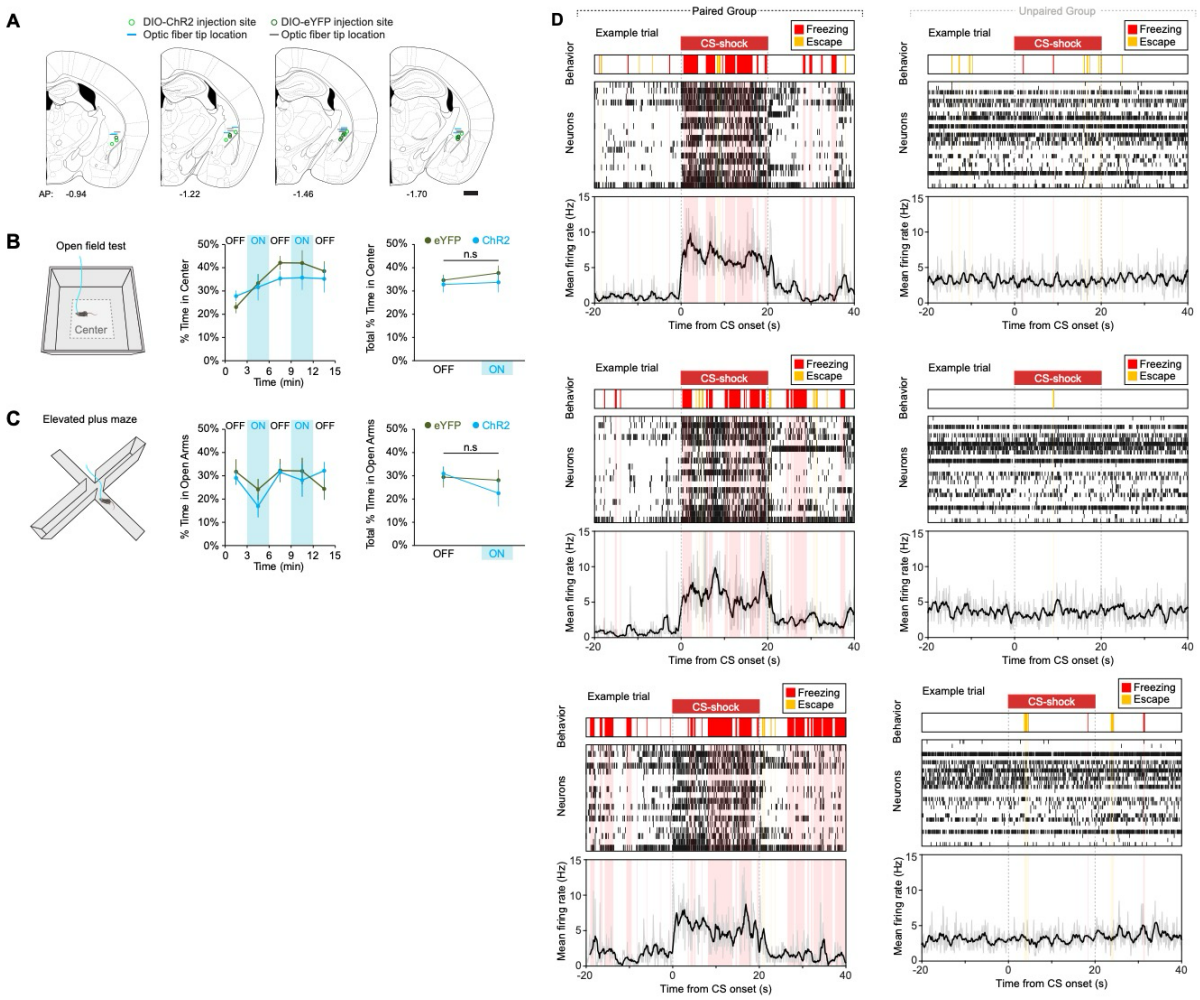

Figure S2.2. Optogenetic activation of ASt neurons does not affect anxiety-related behaviors.

(A) Histologically verified optic fiber implant locations and viral injection sites for AAV-DIO-ChR2-eYFP and AAV-DIO-eYFP controls in optogenetic excitation experiments targeting ASt neurons in VGAT:Cre mice.

(B) Optogenetic activation of ASt neurons does not affect time in center of an open field arena.

(C) Optogenetic activation of ASt neurons does not affect time spent in open arms of an elevated plus maze. N=8 mice ChR2, 10 mice eYFP.

(D) Additional representative trials from discrimination task experiments showing simultaneous subsecond behavior, neural spikes, and average neuron firing rate during presentation of CS-shock.

Figure S2.3. Quality control metrics for single-nucleus RNA sequencing.

(A) Representative images of tissue microdissection sites from RNA sequencing target regions, the dorsal striatum (DS), tail of striatum (TS), amygdalostriatal transition zone (ASt), and central nucleus of the amygdala (CeA) (Blue = DAPI, scale bars = 500 μm).

(B) Location of all tissue sample sites used for single-nucleus RNA sequencing, color coded by region. AP = anteroposterior distance from bregma (mm), scale bar = 500 μm.

(C-F) Density plots outlining the gating strategy for FANS isolation of single nuclei. Nuclei isolated from regions of interest were FANS sorted using 70 μm nozzle at 52 psi. Nuclei were sorted based on size (C), duplicates and/or morphology (D, E), and by high DRAQ7 signal, which stains DNA in nuclei (F). Single $DRAQ7^{+}$ events at the lowest stoichiometric fluorescence multiple were considered nuclei.

(G) Absolute number and proportion of nuclei passing quality control filters from each batch in each region.

(H) UMIs detected per nucleus, filtered at the median per library + five times the median absolute deviation.

(I) Genes detected per nucleus, filtered at minimum 1000 genes.

(J) Percent mitochondrial reads per nucleus, filtered at median per library + five times the median absolute deviation.

(K) Percent ribosomal reads per nucleus, no quality filter applied.

(L) PCA of pseudobulk samples created from each batch, colored by both target region and batch identity.

(M) UMAP of all sequenced nuclei colored by both target region and batch identity.

(N) Evaluation of transcriptional homology on a per-batch basis, where the distance matrix is based on Spearman correlation between median expression of genes on a per-region basis, and the dendrogram was created via hierarchical clustering on this correlation matrix.

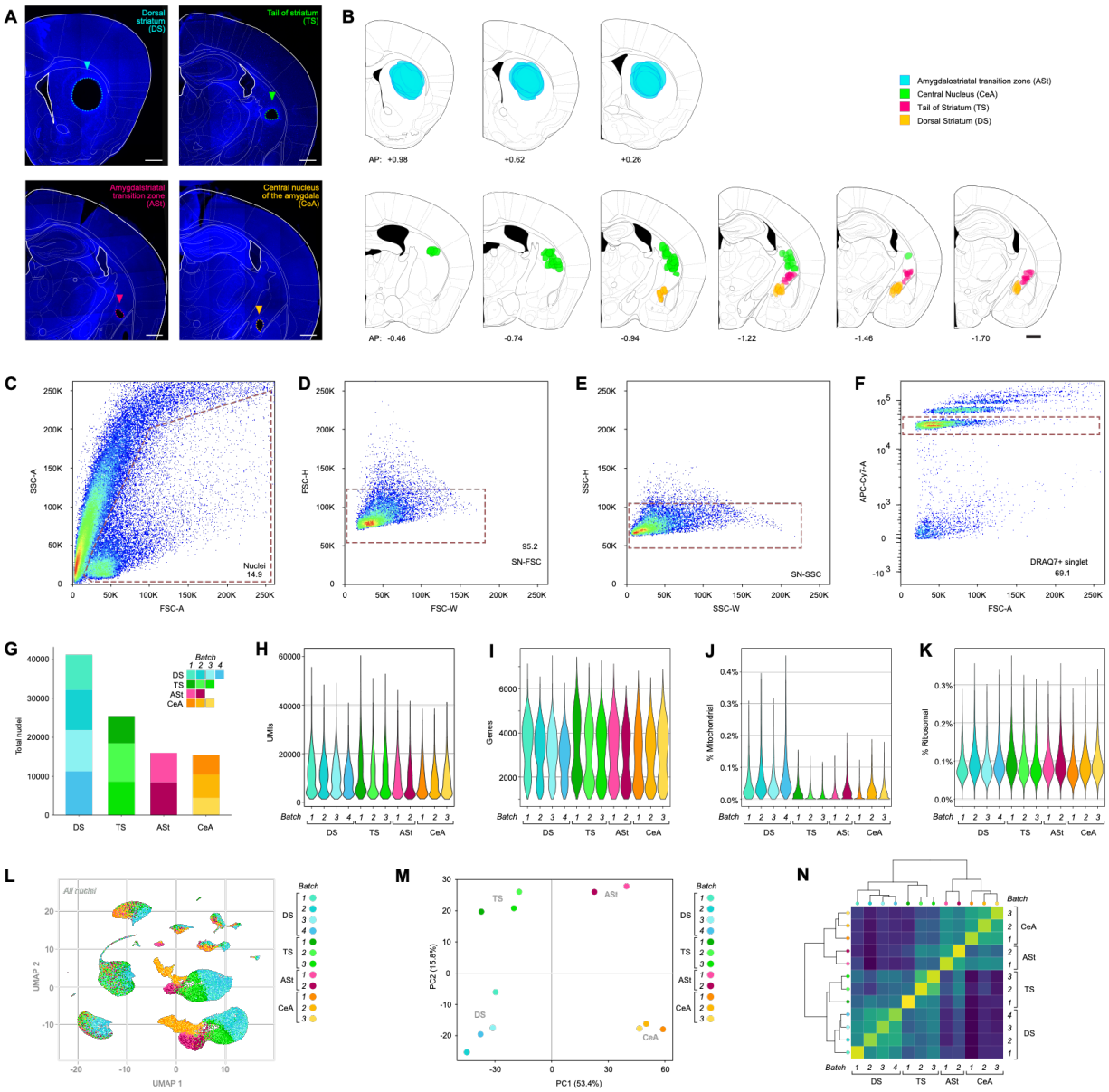
A
Dorsal striatum (DS)
Tail of striatum (TS)
Amygdalostriatal transition zone (ASt)
Central nucleus of the amygdala (CeA)
B
Amygdalostriatal transition zone (ASt)
Central Nucleus (CeA)
Tail of Striatum (TS)
Dorsal Striatum (DS)
AP: +0.98
+0.62
+0.26
AP: -0.46
-0.74
-0.94
-1.22
-1.46
-1.70
C
SSC-A
FSC-A
Nuclei
14.9
D
FSC-H
FSC-W
95.2
SN-FSC
E
SSC-H
SSC-W
SN-SSC
F
APC-Cy7-A
FSC-A
DRAQ7+ singlet
69.1
G
Total nuclei
Batch
DS
TS
ASt
CeA
H
UMIs
I
Genes
J
% Mitochondrial
K
% Ribosomal
L
All nuclei
UMAP 1
UMAP 2
M
PC1 (53.4%)
PC2 (15.8%)
N

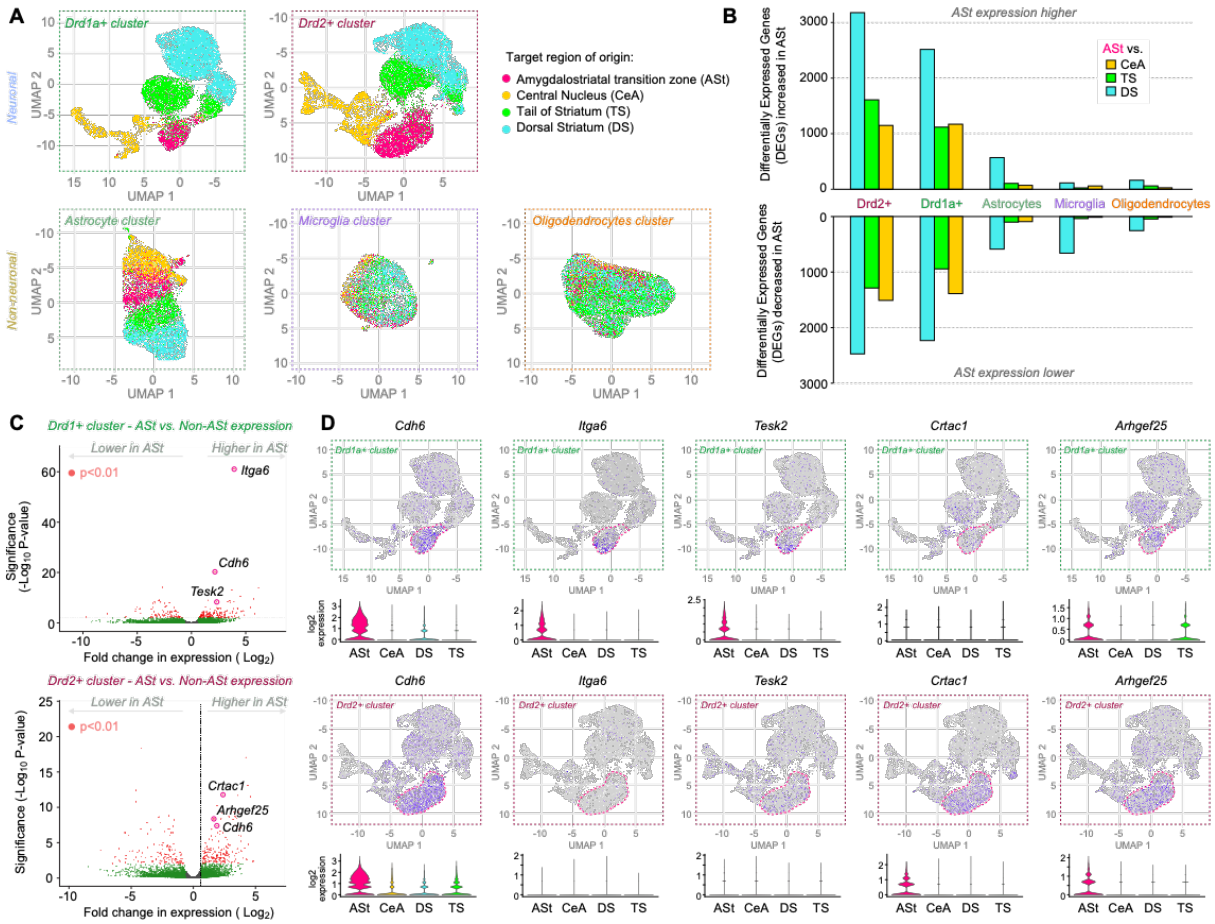

Figure S2.4. Single-nucleus RNA sequencing identifies unique transcriptomic signatures for ASt cells.

(A) UMAP projections of nuclei from the largest cell type clusters (Drd1a+, Drd2+, Astrocytes, Microglia and Oligodendrocytes) colored by tissue region of origin.

(B) Number of differentially expressed genes ($p < 0.01$, 1.5 log-fold change) with increased expression (top) or decreased expression (top) in ASt nuclei relative to nuclei from the central nucleus of the amygdala (CeA), tail of striatum (TS) and dorsal striatum (DS) within each cell type cluster.

(C) Volcano plot showing differentially expressed genes between ASt and non-ASt nuclei in Drd1+ cluster (top) and Drd2+ cluster (bottom). Dashed lines indicate $p < 0.01$ and a fold-change of 1.5. Dots colored grey fail to meet ether standard, dots colored green have sufficient fold change but not significance, while red dots meet both standards. Marker genes of interest for further analysis are circled.

(D) Expression of specific marker genes of interest in Drd1+ cluster (top) and Drd2+ cluster (bottom) neurons. Expression is visualized via UMAP and violin plot. UMAP expression is colored based on increasing normalized expression intensity. Violin plots show smoothed expression density, colored and split based on regional identity within each cluster.

Figure S2.5. Differentially expressed genes of interest with neurologically-relevant function in striatal subregions of interest.

(A) Differentially expressed genes with increased expression in ASt falling into predefined HGNC gene families related to neurological function, increased in Drd1a+ and/or Drd2+ MSNs.

(B) Differentially expressed genes with increased expression in batched non-ASt regions (DS, TS, and/or CeA) falling into predefined HGNC gene families related to neurological function, increased in Drd1a+ and/or Drd2+ MSNs.

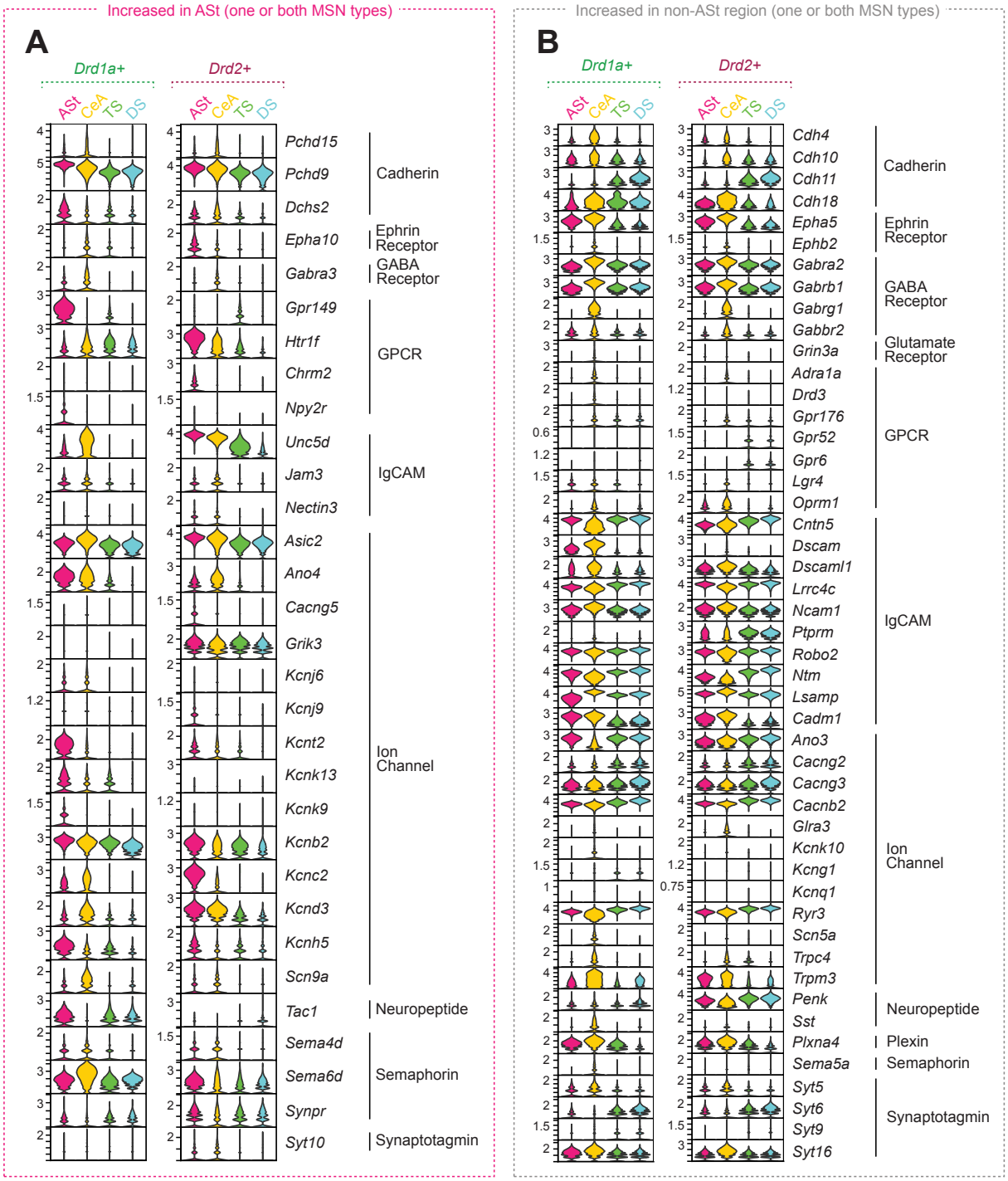
Increased in ASt (one or both MSN types)
A
Drd1a+
Drd2+
ASt
CeA
TS
DS
Pchd15
Pchd9
Dchs2
Epha10
Gabra3
Gpr149
Htr1f
Chrm2
Npy2r
Unc5d
Jam3
Nectin3
Asic2
Ano4
Cacng5
Grik3
Kcnj6
Kcnj9
Kcnt2
Kcnk13
Kcnk9
Kcnb2
Kcnc2
Kcnd3
Kcnh5
Scn9a
Tac1
Sema4d
Sema6d
Synpr
Syt10
Cadherin
Ephrin Receptor
GABA Receptor
GPCR
IgCAM
Ion Channel
Neuropeptide
Semaphorin
Synaptotagmin
Increased in non-ASt region (one or both MSN types)
B
Cdh4
Cdh10
Cdh11
Cdh18
Epha5
Ephb2
Gabra2
Gabrb1
Gabrg1
Gabbr2
Grin3a
Adra1a
Drd3
Gpr176
Gpr52
Gpr6
Lgr4
Oprm1
Cntn5
Dscam
Dscaml1
Lrrc4c
Ncam1
Ptprm
Robo2
Ntm
Lsamp
Cadm1
Ano3
Cacng2
Cacng3
Cacnb2
Glra3
Kcnk10
Kcng1
Kcnq1
Ryr3
Scn5a
Trpc4
Trpm3
Penk
Sst
Plxna4
Sema5a
Syt5
Syt6
Syt9
Syt16
Glutamate Receptor
Plexin

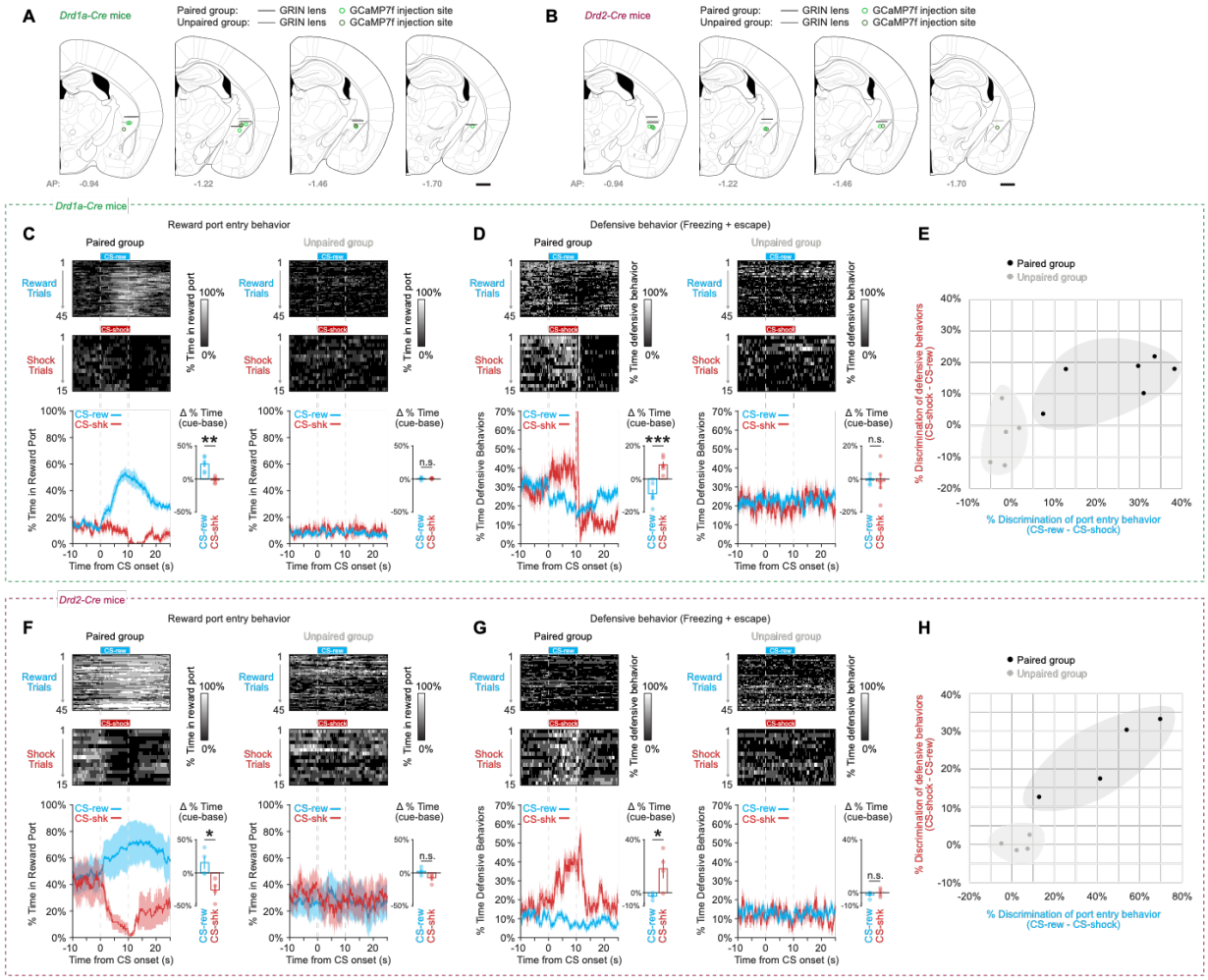

Figure S2.6. Targeting of ASt neurons and behavioral validation for in vivo calcium imaging.

(A-B) Histologically verified GRIN lens implant locations and AAV1-Syn-FLEX-GCaMP7f viral injection sites in recording experiments targeting Drd1a+ neurons (A) and Drd2+ neurons (B) in the ASt.

(C-E) Validation of conditioned behavioral responses during two-tone discrimination task in Drd1a-Cre mice (N=6 mice paired, 5 mice unpaired). Paired group mice showed distinct responses to the CS-shock and CS-reward tones in reward port entry behavior (Two-tailed t-test, $t = 5.0019$, $df = 5$, *** $p < 0.0038$) (C) and defensive responses (Two-tailed t-test, $t = 5.2045$, $df = 5$, *** $p = 0.0035$) (D), consistent with successful discrimination between the two tones compared with unpaired mice (E).

(F-H) Validation of conditioned behavioral responses during two-tone discrimination task in Drd2-Cre mice (N=4 mice paired, 4 mice unpaired). Paired group mice showed distinct responses to the CS-shock and CS-reward tones in reward port entry behavior (Two-tailed t-test, $t = 3.5442$, $df = 3$, * $p = 0.0382$) (F) and defensive responses (Two-tailed t-test, $t = 4.7145$, $df = 3$, * $p = 0.0181$) (G), consistent with successful discrimination between the two tones compared with unpaired mice (H).

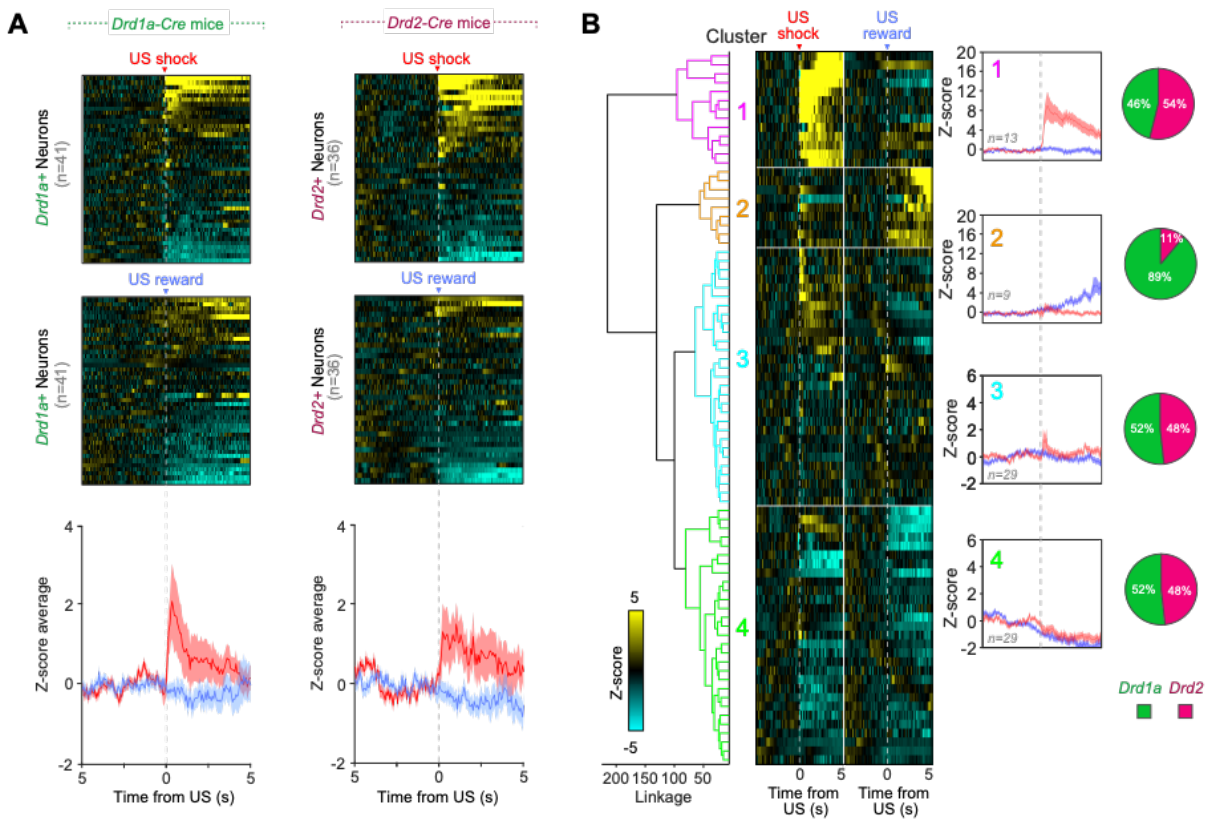

Figure S2.7. ASt neuron responses to aversive and rewarding unconditioned stimuli.

(A) Individual neuron (top) and group average traces (bottom) of Z-score changes in GCaMP7f fluorescence in response to presentation of an aversive US (0.7 mA foot shock) or consumption of a rewarding US (7.5 uL chocolate Ensure™).

(B) Agglomerative hierarchical clustering of calcium imaging responses to each US of neurons from Drd1a-Cre and Drd2-Cre mice. Drd1a+ and Drd2+ neurons both responded to CS shock, but a subcluster of reward-responsive neurons was predominantly composed of Drd1a+ neurons.

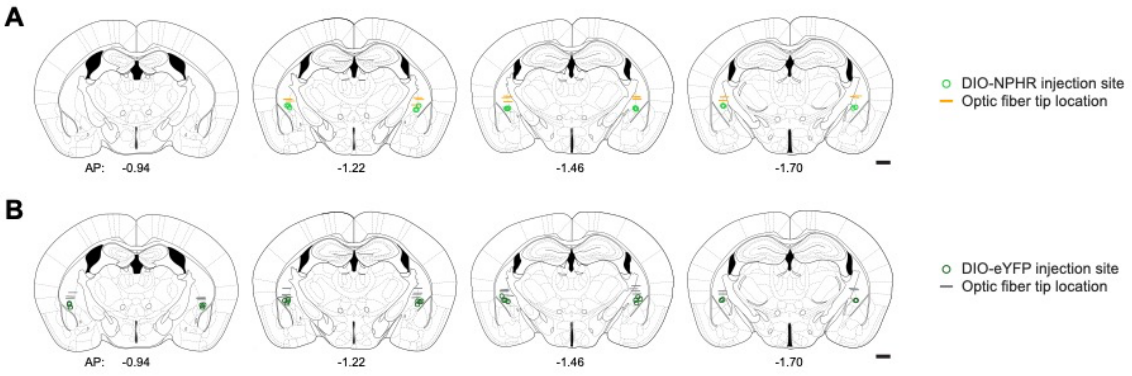

Figure S2.8. Targeting of Drd2+ ASt neurons and for optogenetic inhibition.

(A-B) Histologically verified optic fiber implant locations and injection sites of (A) AAV-DIO-NpHR-eYFP group mice and (B) AAV-DIO-eYFP control group mice in optogenetic inhibition experiments targeting Drd2+ ASt neurons. Scale bars = 500 μm.

2.8. References

Allsop, S.A., Wichmann, R., Mills, F., Burgos-Robles, A., Chang, C.-J., Felix-Ortiz, A.C., Vienne, A., Beyeler, A.,Izadmehr, E.M., Glober, G., Cum, M.I., Stergiadou, J., Anandalingam, K.K., Farris, K., Namburi, P., Leppla, C.A., Weddington, J.C., Nieh, E.H., Smith, A.C., Ba, D., Brown, E.N., Tye, K.M. (2018). Corticoamygdala transfer of socially derived information gates observational learning. Cell *173*, 1329-1342.e18.

Balleine, B.W., O'Doherty, J.P. (2010). Human and Rodent Homologies in Action Control: Corticostriatal Determinants of Goal-Directed and Habitual Action. Neuropsychopharmacol. *35*, 48-69.

Barsy, B., Kocsis, K., Magyar, A., Babiczky, Á., Szabó, M., Veres, J.M., Hillier, D., Ulbert, I., Yizhar, O., Mátyás, F. (2020). Associative and plastic thalamic signaling to the lateral amygdala controls fear behavior. Nat. Neurosci. *23*, 625-637.

Bartlett, E.L. (2013). The organization and physiology of the auditory thalamus and its role in processing acoustic features important for speech perception. Brain Lang. *126*, 29-48.

Becht, E., McInnes, L., Healy, J., Dutertre, C.-A., Kwok, I.W.H., Ng, L.G., Ginhoux, F., Newell, E.W. (2019). Dimensionality reduction for visualizing single-cell data using UMAP. Nat. Biotechnol. *37*, 38-44.

Blair, H.T., Schafe, G.E., Bauer, E.P., Rodrigues, S.M., LeDoux, J.E. (2001). Synaptic Plasticity in the Lateral Amygdala: A Cellular Hypothesis of Fear Conditioning. Learn. Mem. *8*, 229-242.

Bordi, F., LeDoux, J., Clugnet, M.C., Pavlides, C. (1993). Single-unit activity in the lateral nucleus of the amygdala and overlying areas of the striatum in freely behaving rats: rates, discharge patterns, and responses to acoustic stimuli. Behav. Neurosci. *107*, 757-769.

Burgos-Robles, A., Kimchi, E.Y., Izadmehr, E.M., Porzenheim, M.J., Ramos-Guasp, W.A., Nieh, E.H., Felix-Ortiz, A.C., Namburi, P., Leppla, C.A., Presbrey, K.N., Anandalingam, K.K., Pagan-Rivera, P.A., Anahtar, M., Beyeler, A., Tye, K.M. (2017). Amygdala inputs to prefrontal cortex guide behavior amid conflicting cues of reward and punishment. Nat. Neurosci. *20*, 824-835.

Burgos-Robles, A., Vidal-Gonzalez, I., Quirk, G.J. (2009). Sustained conditioned responses in prelimbic prefrontal neurons are correlated with fear expression and extinction failure. J. Neurosci. *29*, 8474–8482.

Butler, A., Hoffman, P., Smibert, P., Papalexi, E., Satija, R., (2018). Integrating single-cell transcriptomic data across different conditions, technologies, and species. Nat. Biotechnol. *36*, 411-420.

Cai, D.J., Aharoni, D., Shuman, T., Shobe, J., Biane, J., Song, W., Wei, B., Veshkini, M., La-Vu, M., Lou, J., Flores, S.E., Kim, I., Sano, Y., Zhou, M., Baumgaertel, K., Lavi, A., Kamata, M.,

Tuszynski, M., Mayford, M., Golshani, P., Silva, A.J. (2016). A shared neural ensemble links distinct contextual memories encoded close in time. Nature *534*, 115-118.

Choudhary, S., Satija, R. (2022). Comparison and evaluation of statistical error models for scRNA-seq. Genome Biol. *23*, 27.

Ciocchi, S., Herry, C., Grenier, F., Wolff, S.B.E., Letzkus, J.J., Vlachos, I., Ehrlich, I., Sprengel, R., Deisseroth, K., Stadler, M.B., Muller, C., Luthi, A. (2010). Encoding of conditioned fear in central amygdala inhibitory circuits. Nature *468*, 277-282.

Cox, J., Witten, I.B. (2019). Striatal circuits for reward learning and decision-making. Nat. Rev. Neurosci. *20*, 482–494.

Cui, G., Jun, S.B., Jin, X., Pham, M.D., Vogel, S.S., Lovinger, D.M., Costa, R.M. (2013). Concurrent activation of striatal direct and indirect pathways during action initiation. Nature *494*, 238-242.

Cunningham, J.P., Yu, B.M. (2014). Dimensionality reduction for large-scale neural recordings. Nat. Neurosci. *17*, 1500-1509.

Curtis, C.E., Sprague, T.C. (2021). Persistent activity during working memory from front to back. Front. Neural Circuits *15*.

Danielson, N.B., Kaifosh, P., Zaremba, J.D., Lovett-Barron, M., Tsai, J., Denny, C.A., Balough, E.M., Goldberg, A.R., Drew, L.J., Hen, R., Losonczy, A., Kheirbek, M.A. (2016). Distinct contribution of adult-born hippocampal granule cells to context encoding. Neuron *90*, 101-112.

Davis, A., Gao, R., Navin, N.E. (2019). SCOPIT: Sample size calculations for single-cell sequencing experiments. BMC Bioinform. *20*, 566.

Davis, M. (1992). The role of the amygdala in fear and anxiety. Annu. Rev. Neurosci. *15*, 353-375.

Disner, S.G., Beevers, C.G., Haigh, E.A.P., Beck, A.T. (2011). Neural mechanisms of the cognitive model of depression. Nat. Rev. Neurosci. *12*, 467-477.

Doron, N.N., Ledoux, J.E. (1999). Organization of projections to the lateral amygdala from auditory and visual areas of the thalamus in the rat. J. Comp. Neurol. *412*, 383-409.

Fadok, J.P., Krabbe, S., Markovic, M., Courtin, J., Xu, C., Massi, L., Botta, P., Bylund, K., Müller, C., Kovacevic, A., Tovote, P., Lüthi, A. (2017). A competitive inhibitory circuit for selection of active and passive fear responses. Nature *542*, 96–100.

Fanselow, M.S., LeDoux, J.E. (1999). Why we think plasticity underlying Pavlovian fear conditioning occurs in the basolateral amygdala. Neuron *23*, 229-232.

Gagnon, D., Petryszyn, S., Sanchez, M.G., Bories, C., Beaulieu, J.M., De Koninck, Y., Parent, A., Parent, M. (2017). Striatal neurons expressing D1 and D2 receptors are morphologically distinct and differently affected by dopamine denervation in mice. Sci. Rep. *7*, 41432.

Gallagher, M., Holland, P.C. (1994). The amygdala complex: multiple roles in associative learning and attention. Proc. Natl. Acad. Sci. U.S.A. *91*, 11771-11776.

Gangarossa, G., Espallergues, J., Mailly, P., De Bundel, D., De Kerchove D'Exaerde, A., Hervé, D., Girault, J.-A., Valjent, E., Krieger, P. (2013). Spatial distribution of D1R- and D2R-expressing medium-sized spiny neurons differs along the rostro-caudal axis of the mouse dorsal striatum. Front. Neural Circuits *7*.

Gerfen, C.R., Engber, T.M., Mahan, L.C., Susel, Z., Chase, T.N., Monsma, F.J., Sibley, D.R., (1990). D1 and D2 dopamine receptor-regulated gene expression of striatonigral and striatopallidal neurons. Science *250*, 1429–1432.

Gerfen, C.R., Surmeier, D.J. (2011). Modulation of striatal projection systems by dopamine. Annu Rev Neurosci. *34*, 441-466.

Germain, P.-L., Lun, A. (2021). scDblFinder. Bioconductor version: Release (3.12).

Germain, P.-L., Sonrel, A., Robinson, M.D. (2020). pipeComp, a general framework for the evaluation of computational pipelines, reveals performant single cell RNA-seq preprocessing tools. Genome Biol. *21*, 227.

Glaser, J.I., Benjamin, A.S., Chowdhury, R.H., Perich, M.G., Miller, L.E., Kording, K.P. (2020). Machine learning for neural decoding. eNeuro *7*.

Gong, S., Doughty, M., Harbaugh, C.R., Cummins, A., Hatten, M.E., Heintz, N., Gerfen, C.R., (2007). Targeting Cre recombinase to specific neuron populations with bacterial artificial chromosome constructs. J. Neurosci. *27*, 9817-9823.

Goosens, K.A., Maren, S. (2004). NMDA receptors are essential for the acquisition, but not expression, of conditional fear and associative spike firing in the lateral amygdala. Eur. J. Neurosci. *20*, 537-548.

Goosens, K.A., Maren, S. (2001). Contextual and auditory fear conditioning are mediated by the lateral, basal, and central amygdaloid nuclei in rats. Learn. Mem. *8*, 148–155.

Graybiel, A.M. (1983). Compartmental Organization of the Mammalian Striatum, in: Changeux, J.-P., Glowinski, J., Imbert, M., Bloom, F.E. (Eds.), Progress in Brain Research. Elsevier, pp. 247–256.

Griffiths, J.A., Richard, A.C., Bach, K., Lun, A.T.L., Marioni, J.C. (2018). Detection and removal of barcode swapping in single-cell RNA-seq data. Nat. Commun. *9*.

Haber, S.N. (2016). Corticostriatal circuitry. Dialogues Clin. Neurosci. *18*, 7–21.

Hafemeister, C., Satija, R. (2019). Normalization and variance stabilization of single-cell RNA-seq data using regularized negative binomial regression. Genome Biol. *20*, 296.

Hao, Y., Hao, S., Andersen-Nissen, E., Mauck, W.M., Zheng, S., Butler, A., Lee, M.J., Wilk, A.J., Darby, C., Zager, M., Hoffman, P., Stoeckius, M., Papalexi, E., Mimitou, E.P., Jain, J., Srivastava, A., Stuart, T., Fleming, L.M., Yeung, B., Rogers, A.J., McElrath, J.M., Blish, C.A., Gottardo, R., Smibert, P., Satija, R. (2021). Integrated analysis of multimodal single-cell data. Cell *184*, 3573-3587.e29.

Haubensak, W., Kunwar, P.S., Cai, H., Ciocchi, S., Wall, N.R., Ponnusamy, R., Biag, J., Dong, H.-W., Deisseroth, K., Callaway, E.M., Fanselow, M.S., Luthi, A., Anderson, D.J. (2010). Genetic dissection of an amygdala microcircuit that gates conditioned fear. Nature *468*, 270-276.

Heilbronner, S.R., Meyer, M.A.A., Choi, E.Y., Haber, S.N. (2018). How do cortico-striatal projections impact on downstream pallidal circuitry? Brain Struct. Funct. *223*, 2809-2821.

Hicks, S.C., Townes, F.W., Teng, M., Irizarry, R.A. (2018). Missing data and technical variability in single-cell RNA-sequencing experiments. Biostatistics 19, 562-578.

Hunnicutt, B.J., Jongbloets, B.C., Birdsong, W.T., Gertz, K.J., Zhong, H., Mao, T. (2016). A comprehensive excitatory input map of the striatum reveals novel functional organization. eLife *5*, e19103.

Jennings, J.H., Sparta, D.R., Stamatakis, A.M., Ung, R.L., Pleil, K.E., Kash, T.L., Stuber, G.D. (2013). Distinct extended amygdala circuits for divergent motivational states. Nature *496*, 224-8.

Johansen, J.P., Hamanaka, H., Monfils, M.H., Behnia, R., Deisseroth, K., Blair, H.T., LeDoux, J.E. (2010). Optical activation of lateral amygdala pyramidal cells instructs associative fear learning. Proc. Natl. Acad. Sci. U.S.A. *107*, 12692–12697.

Jolkkonen, E., Pikkarainen, M., Kemppainen, S., Pitkänen, A. (2001). Interconnectivity between the amygdaloid complex and the amygdalostriatal transition area: a PHA-L study in rat. J. Comp. Neurol. *431*, 39–58.

Jolliffe, I.T., Cadima, J. (2016). Principal component analysis: a review and recent developments. Phil. Trans. of the Royal Soc. A *374*, 20150202.

Josselyn, S.A., Köhler, S., Frankland, P.W. (2015). Finding the engram. Nat. Rev. Neurosci. *16*, 521-534.

Kaviani, H., Gray, J.A., Checkley, S.A., Raven, P.W., Wilson, G.D., Kumari, V. (2004). Affective modulation of the startle response in depression: influence of the severity of depression, anhedonia, and anxiety. J. Affective Disord. 83, 21-31.

Keifer, O.P., Hurt, R.C., Ressler, K.J., Marvar, P.J., 2015. The physiology of fear: reconceptualizing the role of the central amygdala in fear learning. Physiology *30*, 389-401.

Kim, J., Pignatelli, M., Xu, S., Itohara, S., Tonegawa, S. (2016). Antagonistic negative and positive neurons of the basolateral amygdala. Nat. Neurosci. *19*, 1636-1646.

Kim, W.B., Cho, J.-H. (2020). Encoding of contextual fear memory in hippocampal–amygdala circuit. Nat. Commun. *11*, 1382.

Kim, W.B., Cho, J.-H. (2017). Synaptic targeting of double-projecting ventral CA1 hippocampal neurons to the medial prefrontal cortex and basal amygdala. J. Neurosci. 37, 4868-4882.

Kong, M.-S., Zweifel, L.S. (2021). Central amygdala circuits in valence and salience processing. Behav. Brain Res. *410*, 113355.

Kravitz, A.V., Freeze, B.S., Parker, P.R.L., Kay, K., Thwin, M.T., Deisseroth, K., Kreitzer, A.C. (2010). Regulation of parkinsonian motor behaviors by optogenetic control of basal ganglia circuitry. Nature *466*, 622-626.

Kravitz, A.V., Tye, L.D., Kreitzer, A.C. (2012). Distinct roles for direct and indirect pathway striatal neurons in reinforcement. Nat. Neurosci. 15, 816-818.

Krishnaswami, S.R., Grindberg, R.V., Novotny, M., Venepally, P., Lacar, B., Bhutani, K., Linker, S.B., Pham, S., Erwin, J.A., Miller, J.A., Hodge, R., McCarthy, J.K., Kelder, M., McCorrison, J., Aevermann, B.D., Fuertes, F.D., Scheuermann, R.H., Lee, J., Lein, E.S., Schork, N., McConnell, M.J., Gage, F.H., Lasken, R.S. (2016). Using single nuclei for RNA-seq to capture the transcriptome of postmortem neurons. Nat. Protoc. *11*, 499-524.

Lang, P.J. (1995). The emotion probe. Studies of motivation and attention. Am. Psychol. *50*, 372–385.

LeDoux, J.E. (1992). Brain mechanisms of emotion and emotional learning. Curr. Opin. Neurobiol. *2*, 191-197.

LeDoux, J.E., Farb, C., Ruggiero, D.A. (1990). Topographic organization of neurons in the acoustic thalamus that project to the amygdala. J. Neurosci. *10*, 1043-1054.

LeDoux, J.E., Iwata, J., Cicchetti, P., Reis, D.J. (1988). Different projections of the central amygdaloid nucleus mediate autonomic and behavioral correlates of conditioned fear. J. Neurosci. *8*, 2517–2529.

Leppla, C.A., Keyes, L.R., Glober, G., Matthews, G.A., Batra, K., Jay, M., Feng, Y., Chen, H.S., Mills, F., Delahanty, J., Olsen, J., Nieh, E.H., Namburi, P., Wildes, C., Wichmann, R., Beyeler, A., Kimchi, E.Y., Tye, K.M., (2022). Thalamus sends information about arousal but not valence to the amygdala. Psychopharmacology (Berl). *240*, 477-499.

Li, H., Namburi, P., Olson, J.M., Borio, M., Lemieux, M.E., Beyeler, A., Calhoon, G.G., Hitora-Imamura, N., Coley, A.A., Libster, A., Bal, A., Jin, X., Wang, H., Jia, C., Choudhury, S.R., Shi, X., Felix-Ortiz, A.C., de la Fuente, V., Barth, V.P., King, H.O., Izadmehr, E.M., Revanna, J.S., Batra, K., Fischer, K.B., Keyes, L.R., Padilla-Coreano, N., Siciliano, C.A., McCullough, K.M., Wichmann, R., Ressler, K.J., Fiete, I.R., Zhang, F., Li, Y., Tye, K.M. (2022). Neurotensin orchestrates valence assignment in the amygdala. Nature. *608*, 586-592.

Lobo, M.K., Covington, H.E., Chaudhury, D., Friedman, A.K., Sun, H., Damez-Werno, D., Dietz, D.M., Zaman, S., Koo, J.W., Kennedy, P.J., Mouzon, E., Mogri, M., Neve, R.L., Deisseroth, K., Han, M.-H., Nestler, E.J. (2010). Cell type-specific loss of BDNF signaling mimics optogenetic control of cocaine reward. Science *330*, 385-390.

Lun, A.T.L., Riesenfeld, S., Andrews, T., Dao, T.P., Gomes, T., Marioni, J.C., participants in the 1st Human Cell Atlas Jamboree. (2019). EmptyDrops: distinguishing cells from empty droplets in droplet-based single-cell RNA sequencing data. Genome Biol. *20*, 63.

Maaten, L. van der, Hinton, G. (2008). Visualizing Data using t-SNE. Journal of Machine Learning Research *9*, 2579-2605.

Marcinkiewcz, C.A., Mazzone, C.M., D'Agostino, G., Halladay, L.R., Hardaway, J.A., DiBerto, J.F., Navarro, M., Burnham, N., Cristiano, C., Dorrier, C.E., Tipton, G.J., Ramakrishnan, C., Kozicz, T., Deisseroth, K., Thiele, T.E., McElligott, Z.A., Holmes, A., Heisler, L.K., Kash, T.L., (2016). Serotonin engages an anxiety and fear-promoting circuit in the extended amygdala. Nature *537*, 97-101.

Maren, S. (2005). Synaptic mechanisms of associative memory in the amygdala. Neuron *47*, 783-786.

Maren, S., Quirk, G.J. (2004). Neuronal signalling of fear memory. Nat. Rev. Neurosci. *5*, 844–852.

Markowitz, J.E., Gillis, W.F., Beron, C.C., Neufeld, S.Q., Robertson, K., Bhagat, N.D., Peterson, R.E., Peterson, E., Hyun, M., Linderman, S.W., Sabatini, B.L., Datta, S.R. (2018). The striatum organizes 3D behavior via moment-to-moment action selection. Cell *174*, 44-58.e17.

Märtin, A., Calvigioni, D., Tzortzi, O., Fuzik, J., Wärnberg, E., Meletis, K. (2019). A spatiomolecular map of the striatum. Cell Rep. *29*, 4320-4333.e5.

McCarthy, D.J., Campbell, K.R., Lun, A.T.L., Wills, Q.F., Hofacker, I. (2017). Scater: pre-processing, quality control, normalization and visualization of single-cell RNA-seq data in R. Bioinformatics *33*, btw777.

McCullough, K.M., Daskalakis, N.P., Gafford, G., Morrison, F.G., Ressler, K.J. (2018). Cell-type-specific interrogation of CeA Drd2 neurons to identify targets for pharmacological modulation of fear extinction. Transl. Psychiatry *8*, 1-16.

McDonald, A.J. (1998). Cortical pathways to the mammalian amygdala. Prog. Neurobiol. *55*, 257-332.

McGinnis, C.S., Murrow, L.M., Gartner, Z.J. (2019). DoubletFinder: Doublet detection in single-cell RNA sequencing data using artificial nearest neighbors. Cell Syst. *8*, 329-337.e4.

McInnes, L., Healy, J., Melville, J., (2018). UMAP: Uniform Manifold Approximation and Projection for dimension reduction. arXiv:1802.03426 [cs, stat].

Menegas, W., Akiti, K., Amo, R., Uchida, N., Watabe-Uchida, M. (2018). Dopamine neurons projecting to the posterior striatum reinforce avoidance of threatening stimuli. Nat. Neurosci. *21*, 1421-1430.

Miyamoto, Y., Katayama, S., Shigematsu, N., Nishi, A., Fukuda, T. (2018). Striosome-based map of the mouse striatum that is conformable to both cortical afferent topography and uneven distributions of dopamine D1 and D2 receptor-expressing cells. Brain Struct. Funct. *223*, 4275-4291.

Miyamoto, Y., Nagayoshi, I., Nishi, A., Fukuda, T. (2019). Three divisions of the mouse caudal striatum differ in the proportions of dopamine D1 and D2 receptor-expressing cells, distribution of dopaminergic axons, and composition of cholinergic and GABAergic interneurons. Brain Struct. Funct. *224*, 2703-2716.

Morey, R.A., Dunsmoor, J.E., Haswell, C.C., Brown, V.M., Vora, A., Weiner, J., Stjepanovic, D., Wagner, H.R., LaBar, K.S. (2015). Fear learning circuitry is biased toward generalization of fear associations in posttraumatic stress disorder. Transl. Psychiatry *5*, e700.

Nakanishi, S., Hikida, T., Yawata, S. (2014). Distinct dopaminergic control of the direct and indirect pathways in reward-based and avoidance learning behaviors. Neuroscience *282*, 49-59.

Nelson, A.B., Kreitzer, A.C. (2014). Reassessing models of basal ganglia function and dysfunction. Annu. Rev. Neurosci. *37*, 117-135.

Padilla-Coreano, N., Batra, K., Patarino, M., Chen, Z., Rock, R.R., Zhang, R., Hausmann, S.B., Weddington, J.C., Patel, R., Zhang, Y.E., Fang, H.-S., Mishra, S., LeDuke, D.O., Revanna, J., Li, H., Borio, M., Pamintuan, R., Bal, A., Keyes, L.R., Libster, A., Wichmann, R., Mills, F., Taschbach, F.H., Matthews, G.A., Curley, J.P., Fiete, I.R., Lu, C., Tye, K.M. (2022). Cortical ensembles orchestrate social competition through hypothalamic outputs. Nature *603*, 667-671.

Paxinos, G., Franklin, K.B.J. (2019). Paxinos and Franklin's the Mouse Brain in Stereotaxic Coordinates. Academic Press.

Pereira, T.D., Tabris, N., Matsliah, A., Turner, D.M., Li, J., Ravindranath, S., Papadoyannis, E.S., Normand, E., Deutsch, D.S., Wang, Z.Y., McKenzie-Smith, G.C., Mitelut, C.C., Castro, M.D., D'Uva, J., Kislin, M., Sanes, D.H., Kocher, S.D., Wang, S.S.-H., Falkner, A.L., Shaevitz, J.W., Murthy, M. (2022). SLEAP: A deep learning system for multi-animal pose tracking. Nat. Methods *19*, 486-495.

Piantadosi, S.C., Zhou, Z.C., Pizzano, C., Pedersen, C.E., Nguyen, T.K., Thai, S., Stuber, G.D., Bruchas, M.R. (2023). Holographic stimulation of opposing amygdala ensembles bidirectionally modulates valence-specific behavior. Neuron *112*, 1-18.

Pnevmatikakis, E.A., Giovannucci, A. (2017). NoRMCorre: An online algorithm for piecewise rigid motion correction of calcium imaging data. J. Neurosci. Methods *291*, 83-94.

Preissl, S., Fang, R., Huang, H., Zhao, Y., Raviram, R., Gorkin, D.U., Zhang, Y., Sos, B.C., Afzal, V., Dickel, D.E., Kuan, S., Visel, A., Pennacchio, L.A., Zhang, K., Ren, B. (2018). Single-nucleus analysis of accessible chromatin in developing mouse forebrain reveals cell-type-specific transcriptional regulation. Nat. Neurosci. *21*, 432-439.

Quirk, G.J., Repa, J.C., LeDoux, J.E. (1995). Fear conditioning enhances short-latency auditory responses of lateral amygdala neurons: Parallel recordings in the freely behaving rat. Neuron *15*, 1029-1039.

Ray, W.J., Molnar, C., Aikins, D., Yamasaki, A., Newman, M.G., Castonguay, L., Borkovec, T.D. (2009). Startle response in generalized anxiety disorder. Depression and Anxiety *26*, 147-154.

Redgrave, P., Rodriguez, M., Smith, Y., Rodriguez-Oroz, M.C., Lehericy, S., Bergman, H., Agid, Y., DeLong, M.R., Obeso, J.A. (2010). Goal-directed and habitual control in the basal ganglia: implications for Parkinson's disease. Nat. Rev. Neurosci. *11*, 760-772.

Ren, K., Guo, B., Dai, C., Yao, H., Sun, T., Liu, X., Bai, Z., Wang, W., Wu, S. (2017). Striatal distribution and cytoarchitecture of dopamine receptor subtype 1 and 2: Evidence from double-labeling transgenic mice. Front. Neural Circuits *11*.

Rescorla, R.A. (1967). Pavlovian conditioning and its proper control procedures. Psychol. Rev. *74*, 71–80.

Robbins, T.W., Everitt, B.J. (2002). Limbic-striatal memory systems and drug addiction. Neurobiol. Learn. Mem. *78*, 625–636.

Robinson, M.D., McCarthy, D.J., Smyth, G.K. (2010). edgeR: a Bioconductor package for differential expression analysis of digital gene expression data. Bioinformatics *26*, 139.

Romanski, L.M., Clugnet, M.-C., Bordi, F., LeDoux, J.E., 1993. Somatosensory and auditory convergence in the lateral nucleus of the amygdala. Behavioral Neuroscience 107, 444–450.

Satija, R., Farrell, J.A., Gennert, D., Schier, A.F., Regev, A. (2015). Spatial reconstruction of single-cell gene expression data. Nat, Biotechnol. *33*, 495-502.

Sah, P., Westbrook, R.F., Lüthi, A. (2008). Fear conditioning and long-term potentiation in the amygdala. Ann. New York Acad. Sci. *1129*, 88-95.

Saunders, A., Macosko, E.Z., Wysoker, A., Goldman, M., Krienen, F.M., de Rivera, H., Bien, E., Baum, M., Bortolin, L., Wang, S., Goeva, A., Nemesh, J., Kamitaki, N., Brumbaugh, S., Kulp, D., McCarroll, S.A. (2018). Molecular diversity and specializations among the cells of the adult mouse brain. Cell *174*, 1015-1030.e16.

Schachter, S., Singer, J.E. (1962). Cognitive, social, and physiological determinants of emotional state. Psychol. Rev. *69*, 379–399.

Shammah-Lagnado, S.J., Alheid, G.F., Heimer, L. (1999). Afferent connections of the interstitial nucleus of the posterior limb of the anterior commissure and adjacent amygdalostriatal transition area in the rat. Neuroscience *94*, 1097-1123.

Shi, C.-J., Cassell, M.D. (1999). Perirhinal cortex projections to the amygdaloid complex and hippocampal formation in the rat. J. Comp. Neurol. *406*, 299-328.

Shi, C.-J., Cassell, M.D. (1998). Cascade projections from somatosensory cortex to the rat basolateral amygdala via the parietal insular cortex. J. Comp. Neurol. *399*, 469-491.

Shi, C.-J., Cassell, M.D. (1997). Cortical, thalamic, and amygdaloid projections of rat temporal cortex. J. Comp. Neurol. *382*, 153-175.

Siegle, J.H., López, A.C., Patel, Y.A., Abramov, K., Ohayon, S., Voigts, J. (2017). Open Ephys: an open-source, plugin-based platform for multichannel electrophysiology. J. Neural Eng. *14*, 045003.

Squair, J.W., Gautier, M., Kathe, C., Anderson, M.A., James, N.D., Hutson, T.H., Hudelle, R., Qaiser, T., Matson, K.J.E., Barraud, Q., Levine, A.J., La Manno, G., Skinnider, M.A., Courtine, G. (2021). Confronting false discoveries in single-cell differential expression. Nat. Commun. *12*, 5692.

Stuart, T., Butler, A., Hoffman, P., Hafemeister, C., Papalexi, E., Mauck, W.M., Hao, Y., Stoeckius, M., Smibert, P., Satija, R. (2019). Comprehensive integration of single-cell data. Cell *177*, 1888-1902.e21.

Stanley, G., Gokce, O., Malenka, R.C., Südhof, T.C., Quake, S.R. (2020). Continuous and discrete neuron types of the adult murine striatum. Neuron *105*, 688-699.e8.

Tai, L.H., Lee, A.M., Benavidez, N., Bonci, A., Wilbrecht, L. (2012). Transient stimulation of distinct subpopulations of striatal neurons mimics changes in action value. Nat. Neurosci. *15*, 1281-1289.

Tasic, B., Yao, Z., Graybuck, L.T., Smith, K.A., Nguyen, T.N., Bertagnolli, D., Goldy, J., Garren, E., Economo, M.N., Viswanathan, S., Penn, O., Bakken, T., Menon, V., Miller, J., Fong, O., Hirokawa, K.E., Lathia, K., Rimorin, C., Tieu, M., Larsen, R., Casper, T., Barkan, E., Kroll, M., Parry, S., Shapovalova, N.V., Hirschstein, D., Pendergraft, J., Sullivan, H.A., Kim, T.K., Szafer, A., Dee, N., Groblewski, P., Wickersham, I., Cetin, A., Harris, J.A., Levi, B.P., Sunkin, S.M., Madisen, L., Daigle, T.L., Looger, L., Bernard, A., Phillips, J., Lein, E., Hawrylycz, M., Svoboda, K., Jones, A.R., Koch, C., Zeng, H. (2018). Shared and distinct transcriptomic cell types across neocortical areas. Nature *563*, 72-78.

Ting, J.T., Daigle, T.L., Chen, Q., Feng, G. (2014). Acute brain slice methods for adult and aging animals: application of targeted patch clamp analysis and optogenetics. Methods Mol. Biol. *1183*, 221-242.

Tovote, P., Esposito, M.S., Botta, P., Chaudun, F., Fadok, J.P., Markovic, M., Wolff, S.B.E., Ramakrishnan, C., Fenno, L., Deisseroth, K., Herry, C., Arber, S., Lüthi, A. (2016). Midbrain circuits for defensive behaviour. Nature *534*, 206-212.

Tweedie, S., Braschi, B., Gray, K., Jones, T.E.M., Seal, R.L., Yates, B., Bruford, E.A. (2021). Genenames.org: the HGNC and VGNC resources in 2021. Nucleic Acids Res. *49*, D939–D946.

Tye, K.M. (2018). Neural circuit motifs in valence processing. Neuron *100*, 436–452.

Tye, K.M., Prakash, R., Kim, S.Y., Fenno, L.E., Grosenick, L., Zarabi, H., Thompson, K.R., Gradinaru, V., Ramakrishnan, C., Deisseroth, K. (2011). Amygdala circuitry mediating reversible and bidirectional control of anxiety. Nature *471*, 358–362.

Tye, K.M., Stuber, G.D., De Ridder, B., Bonci, A., Janak, P.H. (2008). Rapid strengthening of thalamo-amygdala synapses mediates cue–reward learning. Nature *453*, 1253-1257.

Ulrich-Lai, Y.M., Herman, J.P. (2009). Neural regulation of endocrine and autonomic stress responses. Nat. Rev. Neurosci. 10, 397-409.

Uwano, T., Nishijo, H., Ono, T., Tamura, R. (1995). Neuronal responsiveness to various sensory stimuli, and associative learning in the rat amygdala. Neuroscience *68*, 339–361.

Wang, C., Kang-Park, M.-H., Wilson, W.A., Moore, S.D. (2002). Properties of the pathways from the lateral amygdala nucleus to basolateral nucleus and amygdalostriatal transition area. J. Neurophysiol. *87*, 2593-2601.

Weiskrantz, L. (1956). Behavioral changes associated with ablation of the amygdaloid complex in monkeys. J. Comp. Physiol. Psych. *49*, 381-391.

Whittle, N., Fadok, J., MacPherson, K.P., Nguyen, R., Botta, P., Wolff, S.B.E., Müller, C., Herry, C., Tovote, P., Holmes, A., Singewald, N., Lüthi, A., Ciocchi, S. (2021). Central amygdala micro-circuits mediate fear extinction. Nat. Commun. *12*, 4156.

Zheng, G.X.Y., Terry, J.M., Belgrader, P., Ryvkin, P., Bent, Z.W., Wilson, R., Ziraldo, S.B., Wheeler, T.D., McDermott, G.P., Zhu, J., Gregory, M.T., Shuga, J., Montesclaros, L., Underwood, J.G., Masquelier, D.A., Nishimura, S.Y., Schnall-Levin, M., Wyatt, P.W., Hindson, C.M., Bharadwaj, R., Wong, A., Ness, K.D., Beppu, L.W., Deeg, H.J., McFarland, C., Loeb, K.R., Valente, W.J., Ericson, N.G., Stevens, E.A., Radich, J.P., Mikkelsen, T.S., Hindson, B.J., Bielas, J.H. (2017). Massively parallel digital transcriptional profiling of single cells. Nat. Commun. *8*, 14049.

Zhou, P., Resendez, S.L., Rodriguez-Romaguera, J., Jimenez, J.C., Neufeld, S.Q., Giovannucci, A., Friedrich, J., Pnevmatikakis, E.A., Stuber, G.D., Hen, R., Kheirbek, M.A., Sabatini, B.L., Kass, R.E., Paninski, L. (2018). Efficient and accurate extraction of in vivo calcium signals from microendoscopic video data. eLife *7*, e28728.

Chapter 3: Control of Innate Olfactory Valence by Segregated Cortical Amygdala Circuits

3.1 Abstract

All animals perform innate behaviors, displaying stereotyped responses to numerous specific evolutionarily relevant stimuli in the absence of prior learning or experience. Specific odorants have innate valence, consistently evoking opposing appetitive or aversive responses. Though innate valence has long been identified as a central feature of olfaction, the underlying neural circuits have not been identified, and disparate theories have attempted to bridge this gap. Here, we examine and characterize the neural substrate underlying these stereotyped olfactory valence responses, identifying a divergent, segregated organization that specifically and selectively controls innate olfactory valence responses. Optogenetic stimulation of the anterior domain of plCoA induces avoidance responses, while photostimulation of the posterior induces approach responses. We then comprehensively identified all cell types in plCoA using single-cell and spatial sequencing, finding a hardwired anteroposterior cell type gradient, where anterior glutamatergic neurons preferentially express *Slc17a6* and posterior neurons express *Slc17a7*. While activation of these respective cell types recapitulates appetitive and aversive valence behaviors, inhibition reveals only partial necessity for valence responses to innately appetitive or aversive olfactory stimuli. We next identified topographically organized circuits and their relationship to cortical amygdala cell types, where anterior neurons preferentially project to medial amygdala, and posterior neurons preferentially project to nucleus accumbens, which are respectively sufficient and necessary for negative and positive olfactory valence. Together, these data advance our understanding of how the olfactory system generates stereotypic, predetermined attractive and aversive olfactory behaviors, and supports a model where distinct, hardwired, topographically distributed plCoA populations direct innate olfactory valence

responses by signaling to divergent valence-specific targets, linking upstream olfactory identity to downstream valence behaviors, even in the absence of explicit valence encoding.

3.2 Introduction

Innate behaviors are ubiquitous across the animal kingdom, allowing specific sensory stimuli to yield stereotypic behavioral responses even in the absence of learning or past individual experience. These behaviors include feeding, fighting, fleeing, and mating, among others, and many can be simplified onto an axis of positive or negative valence representing approach and avoidance. Innate behaviors are the result of evolutionary selection, guiding initial behaviors that can be updated by future experiences. Moreover, theoretical models suggest innate circuitry facilitates learning by improving initial performance, increasing information efficiency, and raising the plateau once fully trained (Koulakov et al., 2022; Barabási et al., 2023). These innate behaviors arise via a genetic bottleneck, where the genome encodes general rules for circuit organization and development that nevertheless yield specific responses to specific stimuli (Zador, 2019). However, defects in these innate behaviors, especially innate valence, can underlie multiple neuropsychiatric disorders, including specific phobias and post-traumatic stress disorder (Garcia, 2017; Daviu et al., 2019). Understanding these circuits' organization is therefore important to understanding the basis for these disorders (Zador, 2019; Koulakov et al., 2022; Barabási et al., 2023).

Innate valence and behavioral responses are important in olfaction, where numerous diverse chemical signals, critical to survival and reproduction, must be detected and processed robustly. For instance, predator odors represent a potentially imminent threat and necessitate a quick, decisive, aversive response (Stowers et al, 2013). Conversely, innately appetitive odors

represent potentially rewarding stimuli like food or heterospecifics, inducing attraction (Root et al., 2014; Stowers and Kuo, 2015; Li and Liberles, 2015). These odors comprise a small subset of perceptible chemical space, and the detection of specific odorants is both species-specific and under genetic control (Hayden et al., 2010; Ibarra-Soria et al., 2017; Saraiva et al., 2019). There is evidence that even humans display innate olfactory responses: the valence of specific odors is constant across cultures, and the perceptual features of novel odors are predictable *in silico* from structural features alone, revealing that olfactory responses are highly stereotyped and independent of individual experience (Keller et al., 2017; Arshamian et al., 2022; Lee et al., 2023). Odor intensity and valence for a wide range of odors are strongly modulated by individual genotype and human olfactory receptor expression is biased to recognize key food odorants, which points to an underlying genetic origin for these olfactory perceptual features (Menashe et al., 2007; Keller et al., 2007; McRae et al., 2012; Jaeger et al., 2013; Mainland et al., 2014; Saraiva et al., 2019; Trimmer et al., 2019; Li et al., 2022).

Olfactory sensation begins with olfactory sensory neurons (OSNs) that each express a single receptor, projecting to spatially stereotyped glomeruli in the olfactory bulb (OB). Postsynaptic mitral/tufted cells within OB project in parallel to third-order olfactory areas, including the posterolateral cortical amygdala (plCoA). Unlike in other third-order olfactory areas, such as pirifom cortex, projections from individual glomeruli in OB to plCoA are spatially specific and stereotyped, consistent with genetically hardwired circuits (Miyamichi et al., 2011; Sosulski et al., 2011; Chen et al., 2022; Wang et al., 2022). Past work has demonstrated that plCoA is necessary and sufficient for innate olfactory responses, with spatially stereotyped labeling of responsive neurons via Arc-labeling (Root et al., 2014). However, little is known about the organization of plCoA in general, how it imparts valence on odor, and what

downstream circuits are involved in innate olfactory valence, which is more poorly described than all other analogous innate sensory circuits. Thus, a more complete understanding of plCoA organization is crucial to understanding how this structure controls innate olfactory responses.

In contrast to these organizational principles, encoding properties of plCoA neurons could also be crucial how the region processes innate olfactory valence. Neuronal ensembles within all major olfactory regions observed thus far, such as anterior olfactory nucleus, OB, olfactory epithelium, olfactory tubercle, piriform cortex, and tenia tecta all generally perform sparse population encoding of odor identity alone, despite the major differences in neuronal composition, organization, and function between the four regions. (Malnic et al., 1999; Stettler and Axel, 2009; Nara et al., 2011; Ma et al., 2012; Payton 2012; Iurilli and Datta, 2017; Roland et al., 2017; Chae et al., 2019; Tsuji et al., 2019; Cousins, 2020; Lee et al., 2023). On the other hand, ensembles within amygdala subnuclei, most notably the BLA, instead tend to represent the valence of stimuli instead, with considerable heterogeneity based on a given population's projection target, molecular identity, and topography (Beyeler et al., 2016, 2018; Kim et al., 2016). A joint investigation of the encoding properties and organization of plCoA would be far more likely to achieve a fuller understanding of how innate olfactory valence manifests in plCoA, and how olfactory processing relates to its hardwired circuitry.

To identify the plCoA circuitry that supports innate valence, we investigated multiple intersecting levels of organization, from single cell epigenomes, transcriptomes, and calcium transients to spatial gene expression, histology, and projection mapping, to circuit collateralization and optogenetic and chemogenetic manipulations, to innate valence behaviors. We first use 2-photon calcium imaging to show that plCoA ensembles encode odor identity, but not valence. We then instead identify a gradient in plCoA where activation of anterior neurons

drives aversion, while activation of posterior neurons drives attraction. Next we characterized the cell types within plCoA, identifying novel, molecularly-defined populations specific to each domain of plCoA, which are respectively sufficient and partially necessary for innate olfactory valence. To resolve this incongruity, we perform comprehensive projection mapping to identify novel downstream projection targets of plCoA, identifying projections to medial amygdala (MeA) and nucleus accumbens (NAc) that are enriched based on molecular and topographic identity, and are dissociably sufficient and necessary to control innate olfactory valence responses. Together, these findings identify a novel topographically distributed circuit from plCoA to MeA and NAc that controls innate olfactory aversion and attraction, respectively, and suggests simple, generalized, hardwired organizational motifs to support and segregate innate olfactory valence, even in the absence of explicit plCoA olfactory valence encoding.

3.3. Results

3.3.1. A topographical distribution of valence in plCoA

Given the relationship between plCoA inputs, histology, and activity patterns associated with innately-valenced odorants, we first sought to define a potential spatial relationship between valence and plCoA topography. Based on previously-described histology and activity patterns, , we initially parcellated plCoA into three domains: the anterior plCoA (aplCoA), a two-layered region on the ventral surface lateral to the anterior cortical amygdala, the posterior plCoA (pplCoA), a three-layered region on the ventrolateral surface lateral to the posteromedial cortical amygdala, and a middle transition zone (mplCoA) between them (Figure 3.1A) (Paxinos and Franklin, 2008; Root et al., 2014). To determine the potential relationship between position on the anterior-posterior axis of plCoA and evoked valence, we performed optogenetic stimulation

at points along this entire axis, expressing channelrhodopsin (ChR2) and implanting fibers into each zone (Figures 3.1B-C, S3.1A). We measured valence using the four-quadrant open field assay, where mice were initially allowed to freely explore a chamber, and then one quadrant was paired with optogenetic (470nm, increasing up to a maximum of 5 Hz as the mouse proceeds closer to the corner port) stimulation (Figure 3.1D).

Throughout the trial period, we observed a negative linear relationship between the anterior-posterior position of the photostimulation site and the evoked change in performance index and distance to the corner port in ChR2, but not eYFP-infected mice, where evoked valence shifted from positive to negative as stimulation became more anterior. (Figure 3.1E-F). We then grouped these responses to determine whether these bidirectional responses were specific to the identified plCoA zones. We found that photostimulation in aplCoA significantly reduced time spent in the 'on' quadrant and increased the average distance to the corner port during the treatment period, indicating activation of aplCoA neurons is aversive and leads to avoidance of the quadrant paired with stimulation (Figure 3.1G-H). We also found the opposite was true in pplCoA, where stimulation in that zone instead increased the time in the 'on' quadrant and decreased average distance to the corner port, indicating pplCoA neuron activation instead is appetitive and leads to attraction to the stimulation quadrant (Figure 3.1I-J).

We further examined the effects of anterior-posterior plCoA stimulation on other behaviors to determine whether these effects were specific to valence, or if they extended to other affective or motor phenomena. Using the elevated plus maze, we found no change in anxiety based on open arm time or entries, across both the length of plCoA or within either aplCoA or pplCoA (Figure S3.2A-C, S3.2E-F, S3.2H-I).

Figure 3.1. Valence behaviors in plCoA are topographically distributed along an anterior-posterior axis.

(A) Schematic of plCoA zonation to parcellate plCoA into anterior (aplCoA), middle (mplCoA), and posterior (pplCoA) fields based on histology, positioning, and gradients observed in past literature (Miyamichi et al., 2011; Root et al., 2014)

(B) Strategy to activate anterior-posterior topographical ensembles via optogenetics.

(C) Representative histology and fiber/virus placement for aplCoA and pplCoA ChR2 animals.

(D) Behavioral paradigm and schematic of four-quadrant open field behavioral assay with photostimulation.

(F-G) Linear-fit relationships between change in performance index (F) or mean port distance (G) and anterior-posterior position along plCoA for channelrhodopsin and control virus-infected mice. Both metrics are significantly correlated with topographical position along the plCoA anterior-posterior axis.

(H) Paths traveled during the treatment period for a representative mouse (left) and baseline-normalized collective heatmaps (right) from both the ChR2- and eYFP-infected groups with aplCoA-localized fiber implants. Lower right stimulus quadrant marked in blue.

(I-J) Photostimulation of aplCoA neurons infected with ChR2, but not eYFP, is sufficient to reduce time spent in the stimulation quadrant (I) and increase its average distance from the stimulation port (J) during the stimulation period.

(K) Paths traveled during the treatment period for a representative mouse (left) and baseline-normalized collective heatmaps (right) from both the ChR2- and eYFP-infected groups with pplCoA-localized fiber implants. Lower right stimulus quadrant marked in blue.

(L-M) Photostimulation of pplCoA neurons infected with ChR2, but not eYFP, is sufficient to increase time spent in the stimulation quadrant (L) and reduce its average distance from the stimulation port during the stimulation period (M).

Abbreviations: aplCoA, anterior zone of posterolateral cortical amygdala; mplCoA, middle zone of posterolateral cortical amygdala; pplCoA, posterior zone of posterolateral cortical amygdala.

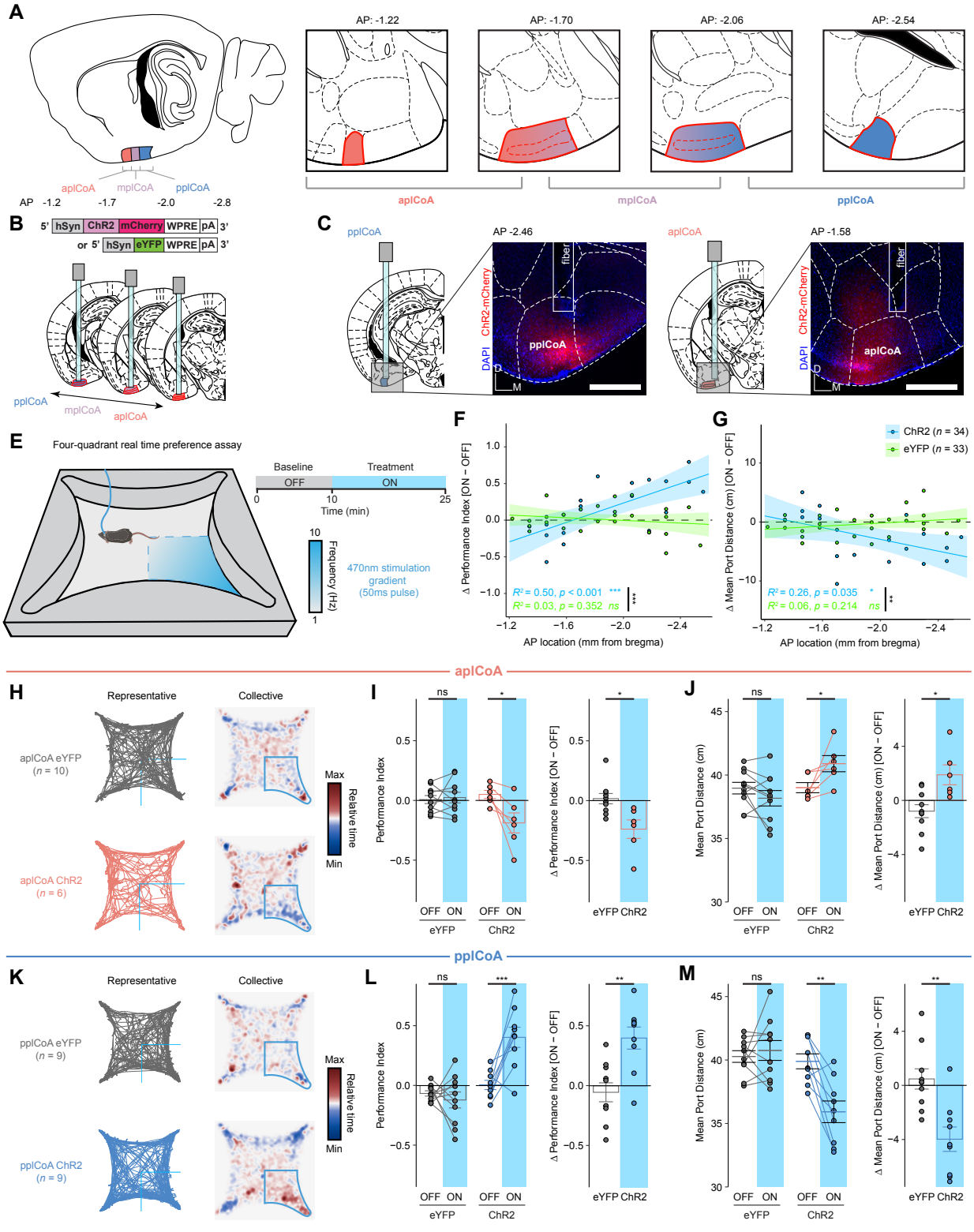
A
AP: -1.22
AP: -1.70
AP: -2.06
AP: -2.54
aplCoA
mplCoA
pplCoA
AP -1.2 -1.7 -2.0 -2.8
B
5' hSyn ChR2 mCherry WPRE pA 3'
or 5' hSyn eYFP WPRE pA 3'
pplCoA
mplCoA
aplCoA
C
pplCoA
AP -2.46
ChR2-mCherry
DAPI
fiber
pplCoA
D
M
aplCoA
AP -1.58
aplCoA
E
Four-quadrant real time preference assay
Baseline
Treatment
OFF
ON
0
10
25
Time (min)
10
Frequency (Hz)
1
470nm stimulation gradient (50ms pulse)
F
Δ Performance Index [ON − OFF]
1.0
0.5
0.0
−0.5
−1.0
R² = 0.50, p < 0.001 ***
R² = 0.03, p = 0.352 ns
***
−1.2 −1.6 −2.0 −2.4
AP location (mm from bregma)
G
ChR2 (n = 34)
eYFP (n = 33)
Δ Mean Port Distance (cm) [ON − OFF]
10
0
−10
R² = 0.26, p = 0.035 *
R² = 0.06, p = 0.214 ns
**
−1.2 −1.6 −2.0 −2.4
AP location (mm from bregma)
aplCoA
H
Representative
Collective
aplCoA eYFP (n = 10)
aplCoA ChR2 (n = 6)
Max
Relative time
Min
I
Performance Index
ns
*
*
0.5
0.0
−0.5
OFF ON
eYFP
OFF ON
ChR2
Δ Performance Index [ON − OFF]
eYFP ChR2
J
Mean Port Distance (cm)
45
40
35
30
ns
*
OFF ON
eYFP
OFF ON
ChR2
Δ Mean Port Distance (cm) [ON − OFF]
4
0
−4
*
eYFP ChR2
pplCoA
K
Representative
Collective
pplCoA eYFP (n = 9)
pplCoA ChR2 (n = 9)
Max
Relative time
Min
L
Performance Index
ns
***
**
0.5
0.0
−0.5
OFF ON
eYFP
OFF ON
ChR2
Δ Performance Index [ON − OFF]
eYFP ChR2
M
Mean Port Distance (cm)
45
40
35
30
ns
**
OFF ON
eYFP
OFF ON
ChR2
Δ Mean Port Distance (cm) [ON − OFF]
4
0
−4
**
eYFP ChR2

In the open field test, we similarly found no changes to thigmotaxis, based on time spent in corners of the open field, or exploration, based on time spent in the center of the open field (Figure S3.2K-M, S3.2EO-P, S3.2R-S). Further, locomotion remained constant during stimulation across both assays and the entirety of plCoA (Figure S3.2D, S3.2G, S3.2J, S3.2N, S3.2Q, S3.2T). Together, these data indicate that the effects of plCoA neuron activation across the entire anterior-posterior axis are specific to valence, with few other behavioral effects. Overall, we find activation of plCoA neurons is sufficient to drive valence behaviors in a topographically organized and bidirectional manner, where aplCoA drives aversion and pplCoA drives attraction. This relationship is consistent with previously described spatial zonation of plCoA based on relationships between odor, plCoA activity, and inputs to plCoA from OB.

3.3.2. Molecular diversity of plCoA cell types along the anteroposterior axis

Given the differences in innate response along the plCoA anteroposterior axis, we sought to determine if different cell types could be present within the anterior and posterior fields of plCoA. To investigate this phenomenon, we performed single-nucleus RNA sequencing (snRNA-seq) to determine the cell type composition and its relationship to the anterior-posterior axis of plCoA (Zheng et al., 2017). To simultaneously profile these cell types and identify zone-specific patterns, we separately extracted tissue target samples from aplCoA and pplCOA by microdissection and verified accurate histology before pooling qualifying samples from within each field for each sequencing run (Figure 3.2A, S3.3A-D). We also confirmed there were few region- or batch-specific differences in sequencing depth or nuclear quality markers (Figure S3.3E-M).

Figure 3.2. Molecular cell types in plCoA are differentially heterogeneous.

(A) Schematic of freeze-and-repool strategy for single-nucleus sequencing.

(B) Two-dimensional UMAP (n = 47,132 nuclei, see also Figure S3.3), colored by broad cellular identity assigned by graph-based clustering of neuronal and non-neuronal nuclei.

(C) Cell-type-specific expression of canonical marker genes indicating broad cellular identity in the brain. Dot size is proportional to percentage of nuclei expressing the marker, with color scale representing normalized expression level.

(D) Total proportion of cells of each identified type in each domain of plCoA.

(E) Two-dimensional UMAP of glutamatergic neurons, colored by molecular cell type.

(F) Clustered heatmap showing Euclidean distance between averages of each subtype positioned based on hierarchical clustering (left), and dot plot of marker genes for all glutamatergic subtypes (right).

(G) Two-dimensional UMAP of GABAergic neurons, colored by molecular cell type, like in (E).

(H) Clustered heatmap showing Euclidean distance between averages of each subtype positioned based on hierarchical clustering (left), and dot plot of marker genes for all GABAergic subtypes (right), like in (F).

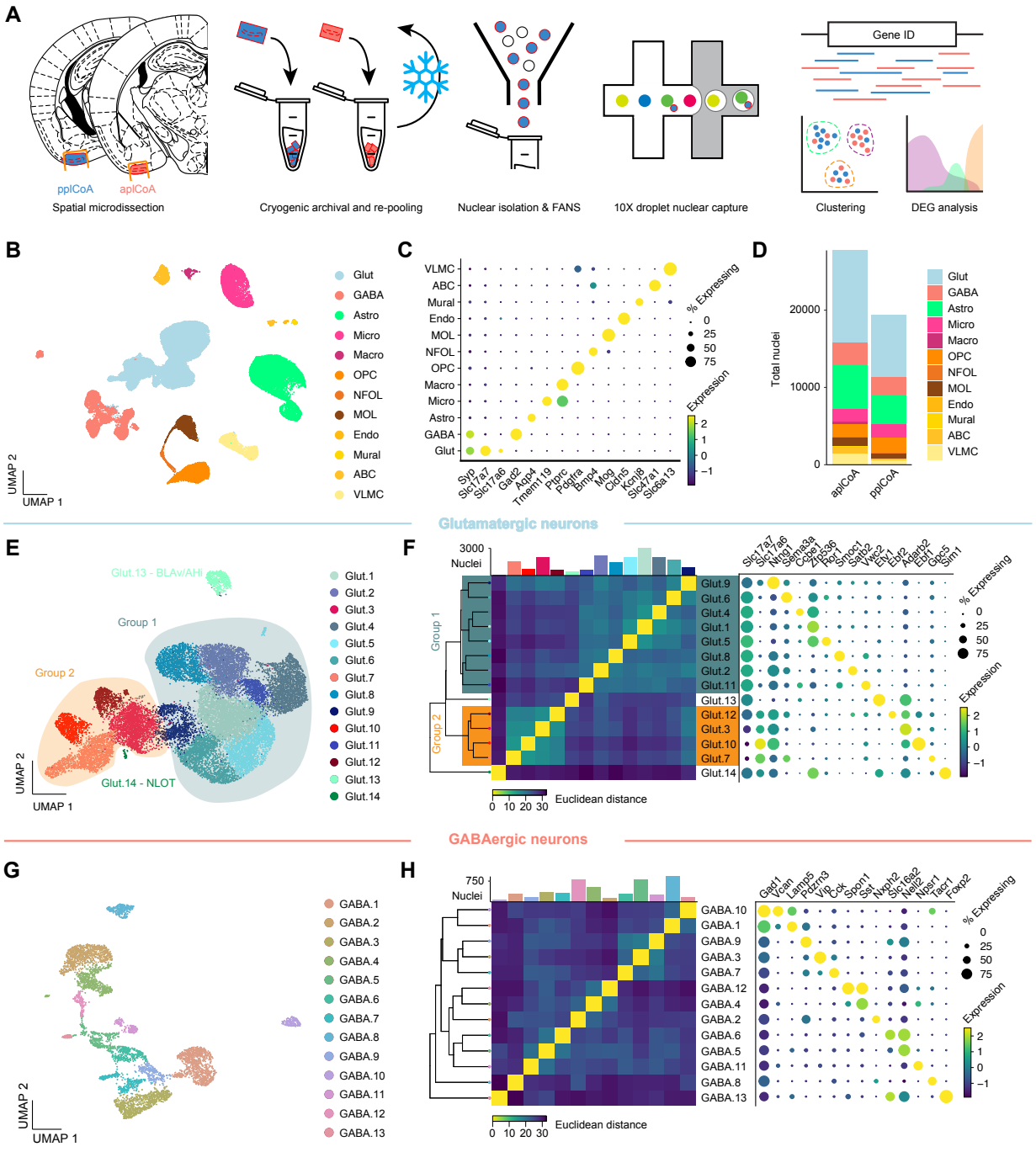
A
ppICoA
apICoA
Spatial microdissection
Cryogenic archival and re-pooling
Nuclear isolation & FANS
10X droplet nuclear capture
Gene ID
Clustering
DEG analysis
B
UMAP 2
UMAP 1
Glut
GABA
Astro
Micro
Macro
OPC
NFOL
MOL
Endo
Mural
ABC
VLMC
C
VLMC
ABC
Mural
Endo
MOL
NFOL
OPC
Macro
Micro
Astro
GABA
Glut
Syp
Slc17a7
Slc17a6
Gad2
Aqp4
Tmem119
Ptprc
Pdgfra
Bmp4
Mog
Cldn5
Kcnj8
Slc47a1
Slc6a13
% Expressing
0
25
50
75
Expression
2
1
0
−1
D
Total nuclei
20000
10000
0
apICoA
ppICoA
Glut
GABA
Astro
Micro
Macro
OPC
NFOL
MOL
Endo
Mural
ABC
VLMC
Glutamatergic neurons
E
Glut.13 - BLAv/AHi
Group 1
Group 2
Glut.14 - NLOT
UMAP 2
UMAP 1
Glut.1
Glut.2
Glut.3
Glut.4
Glut.5
Glut.6
Glut.7
Glut.8
Glut.9
Glut.10
Glut.11
Glut.12
Glut.13
Glut.14
F
3000
Nuclei
Group 1
Group 2
Glut.9
Glut.6
Glut.4
Glut.1
Glut.5
Glut.8
Glut.2
Glut.11
Glut.13
Glut.12
Glut.3
Glut.10
Glut.7
Glut.14
Slc17a7
Slc17a6
Nrgn
Satb2
Vwc2
Ebf1
Adarb2
Ebf3
Gfap
Gfap5
Slm1
% Expressing
0
25
50
75
Expression
2
1
0
−1
0 10 20 30
Euclidean distance
GABAergic neurons
G
UMAP 2
UMAP 1
GABA.1
GABA.2
GABA.3
GABA.4
GABA.5
GABA.6
GABA.7
GABA.8
GABA.9
GABA.10
GABA.11
GABA.12
GABA.13
H
750
Nuclei
GABA.10
GABA.1
GABA.9
GABA.3
GABA.7
GABA.12
GABA.4
GABA.2
GABA.6
GABA.5
GABA.11
GABA.8
GABA.13
Gad1
Vcan
Lamp5
Pdzrn3
Vip
Cck
Spon1
Sst
Nxph2
Slc16a2
Nell2
Npsr1
Tacr1
Foxp2
% Expressing
0
25
50
75
Expression
2
1
0
−1
0 10 20 30
Euclidean distance

Clustering of sequenced nuclei by gene expression allowed us to initially identify all major canonical neuronal and glial cell types in plCoA based on known gene markers identified in past scRNA-seq studies (Figure 3.2B-C) (Tasic et al., 2018). Neurons in plCoA are primarily glutamatergic, with a minority subset of GABAergic neurons (Figure 3.2D), with proportions broadly similar to cortical regions (Tasic et al., 2018). Notably, we also identified large numbers of vascular leptomeningeal cells (VLMCs) and arachnoid barrier cells (ABCs), two fibroblast-like meningeal cell types that respectively interface with vasculature and form a barrier between the brain and CSF, most likely due to meningeal presence on the cortical surface during extraction (Yasuda et al., 2013; Marques et al., 2016).

We then posited that there is far more heterogeneity within neuronal cell type in plCoA, given that cortical and amygdala subregions both display significant heterogeneity with both glutamatergic and GABAergic neurons. To this end, we re-processed and subclustered each major cell type to examine their specific heterogeneity. Within glutamatergic neurons, we were able to identify 14 distinct subtypes by gene expression, with largely continuous variation between glutamatergic subtypes (Figure 3.2E). However, when examining the relationships between these subtypes, we identified two broader groups of glutamatergic neurons via hierarchical clustering, where subtypes within each group displayed a lower Euclidean distance from one another in high-dimensional gene expression space (Figure 3.2F). Each of these two broader groups had a marker for every type within either group, where the larger Group 1 of glutamatergic neurons express *Slc17a7,* and the smaller Group 2 expresses *Slc17a6.* Within each of these glutamatergic groups, most observed marker genes are non-canonical in the amygdala and cortex, suggesting unique glutamatergic ensembles or patterns of gene expression within glutamatergic neurons in plCoA compared to other regions previously described. Two subtypes

(Glut.13 and Glut.14) did fall outside of either broad glutamatergic group, varying in a far more discrete manner than most plCoA glutamatergic neuron subtypes. Interestingly, examination of data from the Allen ISH Atlas for their respective marker genes *Etv1* and *Sim1* showed these two groups fall into adjacent regions outside of plCoA, where Glut.13 neurons localize to the posterior basomedial amygdala and Glut.14 neurons localize to the nucleus of the lateral olfactory tract (Figure S3.4A). GABAergic neuron gene expression patterns displayed an opposing form of heterogeneity, where subtypes are far more discrete, without broad groups linking related subtypes (Figure 2G). GABAergic neuron marker genes are also more canonical than those in glutamatergic neurons, where most GABAergic neurons in plCoA have interneuron-like identities, expressing marker genes like *Vip*, *Sst*, and *Cck* (Figure 3.2H).

We then hypothesized that differences in these populations could potentially be responsible for the difference observed between different plCoA domains and thus examined potential domain-specific enrichment of certain cell types within plCoA. Visualization of these nuclei showed little clear region-specific structure in dimension-reduced space for any major cell types (Figure 3.3A). This lack of structure was broadly confirmed quantitatively, where few major cell types showed significant domain-specific enrichment (Figure 3.3A-B). Of those that did (Micro, Macro, and OPC), the variable major cell types were relatively low-abundance, and we could not observe clear divergence in dimension-reduced space or subtypes that clearly diverged from expected enrichment patterns (Figure 3.2D, Figure S3.4B-D). When looking to other regions, however, heterogeneity is usually more pronounced between subsets of the major cell types, instead of the quantities of the major cell types themselves (Tasic et al., 2018). We then examined abundance of differentially expressed genes (DEGs) between plCoA domains for each major cell type.

Figure 3.3. Glutamatergic neurons subtypes in plCoA are spatially biased along an anteroposterior *Slc17a6/Slc17a7* molecular gradient.

(A) UMAP of all plCoA nuclei, colored by domain of origin, with dotted outlines and labels denoting the broad identity class for each grouped cell type.

(B) (B) Relative proportion of nuclei from each domain within each broad identity class. Dotted line indicates chance level for all plCoA nuclei.

(C) Top, abundance of domain-specific DEGs for each major cell type, either enriched in aplCoA nuclei (top) or pplCoA nuclei (bottom). Bottom, volcano plots for domain-specific DEGs for glutamatergic neurons (left) and VLMCs (right), the cell types with the most- and least-domain specific gene expression, where negative log-fold changes indicate enrichment in pplCoA and positive indicates enrichment in aplCoA.

(D) UMAP of all plCoA glutamatergic neurons, colored by domain of origin, with dotted outlines and labels denoting the subtypes on the graph. Groups of glutamatergic neuron types identified previously via Euclidean distance and hierarchical clustering are overlaid on top of the neuron types of interest.

(E) Relative proportion of molecular subtype nuclei from each domain within glutamatergic neurons, where relevant subtypes are outlined according to their glutamatergic neuron group. Dotted line indicates chance level for plCoA glutamatergic neuron nuclei.

(F) UMAP of all glutamatergic neuron nuclei, colored by expression levels of *Slc17a6* (top) or *Slc17a7* (bottom).

(G) Left, representative images of in situ RNAscope labeling of *Slc17a6* RNA (red) and *Slc17a7* RNA (green) across plCoA domains. Right, proportions of glutamatergic neurons expressing *Slc17a6*, *Slc17a7*, or both. Scale bars, 500 μm (main image), 50 μm (inset).

(H) UMAP of all plCoA-overlapping Visium capture spots, colored by cluster. Broad spatial position of groups of clusters are overlaid on top of the capture spots of interest.

(I) UMAP of all plCoA-overlapping Visium capture spots, colored by expression levels of *Slc17a6* (top) or *Slc17a7* (bottom).

(J) Representative plCoA-overlapping region of one section on a Visium slide capture area, with capture spots colored by cluster.

(K) Representative plCoA-overlapping region of one section on a Visium slide capture area, with capture spots colored by expression levels of *Slc17a6* (top) or *Slc17a7* (bottom).

(L) Prediction scores for representative glutamatergic neuron subtypes within Group 1 (left) and Group 2 (right), shown on a UMAP of all plCoA-overlapping capture spots across all sections (top) and on a representative plCoA-overlapping region of one section (bottom).

(M) Prediction scores for a representative GABAergic neuron subtype, shown on a UMAP of all plCoA-overlapping capture spots across all sections (top) and on a representative plCoA-overlapping region of one section (bottom).

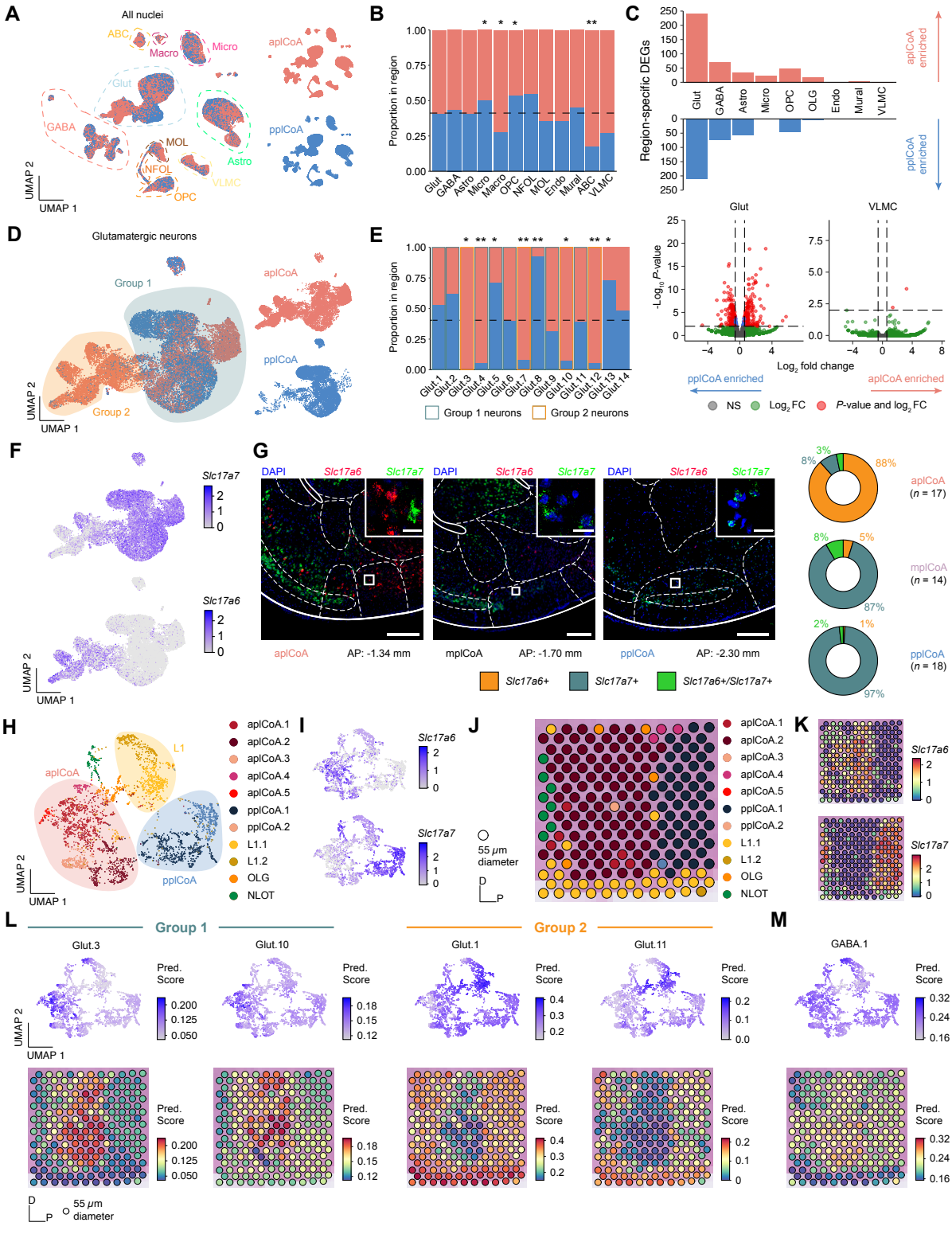
A
All nuclei
ABC
Macro
Micro
Glut
GABA
MOL
NFOL
Astro
VLMC
OPC
UMAP 2
UMAP 1
aplCoA
pplCoA
B
Proportion in region
Glut
GABA
Astro
Micro
Macro
OPC
NFOL
MOL
Endo
Mural
ABC
VLMC
C
Region-specific DEGs
aplCoA enriched
pplCoA enriched
D
Glutamatergic neurons
Group 1
Group 2
E
Group 1 neurons
Group 2 neurons
Glut
VLMC
-Log10 P-value
Log2 fold change
pplCoA enriched
aplCoA enriched
NS
Log2 FC
P-value and log2 FC
F
Slc17a7
Slc17a6
G
DAPI
aplCoA
AP: -1.34 mm
mplCoA
AP: -1.70 mm
pplCoA
AP: -2.30 mm
Slc17a6+
Slc17a7+
Slc17a6+/Slc17a7+
aplCoA (n = 17)
mplCoA (n = 14)
pplCoA (n = 18)
H
L1
aplCoA.1
aplCoA.2
aplCoA.3
aplCoA.4
aplCoA.5
pplCoA.1
pplCoA.2
L1.1
L1.2
OLG
NLOT
I
J
55 μm diameter
K
L
Group 1
Group 2
Glut.3
Glut.10
Glut.1
Glut.11
Pred. Score
M
GABA.1

Here, we found that both major neuronal cell types had more abundant DEGs than all major glial cell types (Figure 3.3C). Glutamatergic neurons DEGs exceeded all other major cell types to a major degree, making it highly likely that differences between the anterior and posterior domains are most likely to be observed via intra-glutamatergic neuron variation. When examining domain-specific variation in plCoA glutamatergic neurons, we initially observed a far greater degree of domain-specific clustering in dimension-reduced space (Figure 3.3D). Glutamatergic neuron subtypes correspondingly displayed a much greater degree of domain-specific enrichment, where more than half of glutamatergic neuron subtypes were significantly enriched in the anterior or posterior domain (Figure 3.3E). Upon closer examination, we found that every glutamatergic subtype in the *Slc17a6*-expressing Group 1 was enriched in aplCoA, while *Slc17a7*-expressing Group 2 subtypes are evenly distributed across fields or biased towards the posterior, with one exception, Glut.4, which likely derives from the adjacent amygdalopiriform transition area, based on Allen ISH data of *Ccbe1* expression (Figure 3.3F, S3.4A). In contrast to glutamatergic neurons, we did not observe significant plCoA domain-specific variation regarding any GABAergic neuron subtypes (Figure S3.4E).

To confirm these findings and validate our snRNA-seq data, we used RNAscope labelling to examine the expression of *Slc17a6* and *Slc17a7 in situ* in the plCoA. We found that aplCoA had a much greater proportion of RNAscope-labelled *Slc17a6*+ neurons than *Slc17a7*+ neurons compared to the rest of plCoA, where *Slc17a7*+ neurons predominate, and these numbers were generally consistent with those identified in our sequencing data (Figure 3.3J). Next, we then extracted plCoA from an existing Visium spatial transcriptomics dataset sagitally bisecting the region along the midline to determine if the domain-specific molecular cell type composition can be recovered directly from spatial information, as well as determine the

robustness of our results to different experimental conditions (Romero et al., in preparation) (Figure S3.4S). All sections used were of similarly high quality and did not display any clearly observable batch effects, with all but one having more than 100 spots covering the plCoA (Figure S3.4T-W). When clustering directly on spatial data, we observed significant heterogeneity separating into three broad groups (Figure 3.3H). Like in scRNA-seq, we found highly specific expression of *Slc17a6* and *Slc17a7* to two of the three braod groups (Figure 3.3I). When examining the spatial configuration of these groups, we found the *Slc17a6*-expressing group of clusters was in aplCoA, while the *Slc17a7*-expressing group was in pplCoA, with the third intermediate group corresponding to layer 1 (Figure 3.3J-K). When computationally projecting transcriptomic cell type identities onto spatial data, we observed that Group 1 glutamatergic neuron types would project onto aplCoA spots and Group 2 glutamatergic neuron types would project onto pplCoA spots, while little to no anteroposterior bias could be observed when projecting GABAergic neuron types onto plCoA spots (Figure 3.3L-M). Overall, this data shows that plCoA contains an extremely diverse population of numerous glutamatergic and GABAergic neuron subtypes, where glutamatergic neuron subtypes vary significantly along the anteroposterior axis, where aplCoA-enriched subtypes express *Slc17a6* and pplCoA-enriched subtypes express *Slc17a7*.

3.3.3. Molecularly defined plCoA glutamatergic neuron populations are sufficient to drive valence behavior

Given this spatial distribution bias of plCoA$^{Slc17a6+}$ neurons into aplCoA and plCoA$^{Slc17a7+}$ neurons into pplCoA, we sought to determine if these glutamatergic neuron groups

could specifically drive the opposing valence behaviors observed during topographic plCoA stimulation of plCoA, where such behaviors could be driven in a topography-independent manner by targeting each subpopulation molecularly. To investigate this, we expressed ChR2 in a non-spatially-biased, cell type-specific manner using a Cre-conditional viral construct in *Slc17a6::Cre* and *Slc17a7::Cre* transgenic mice (Figures 3.4A-B, S3.1B) (Vong et al., 2011; Harris et al., 2014). Using the four-quadrant open field task again, we found that photostimulation of plCoA$^{Slc17a6+}$ neurons significantly reduced time spent in the 'on' quadrant and increased the average distance to the corner port during the treatment period, indicating activation of plCoA$^{Slc17a6+}$ neurons is aversive and leads to avoidance of the quadrant paired with stimulation (Figure 3.4C-D). We also found the opposite was true for plCoA$^{Slc17a7+}$ neurons, where stimulation in that zone instead increased the time in the 'on' quadrant and decreased average distance to the corner port, indicating pplCoA neuron activation instead is appetitive and leads to attraction to the stimulation quadrant (Figure 3.4E-H). These data clarify that the divergent field-specific valence effects of plCoA activity are likely due to the divergent molecularly defined neuronal ensembles predominant in each topographical field of plCoA.

Though we know these neurons can induce valence behavior in a cell-type-specific manner, we cannot yet say if they are required for their physiological role in innate olfactory valence. To determine whether these two glutamatergic populations are respectively required for innate olfactory aversion and/or attraction, we instead used the previously mentioned transgenic mouse lines to drive expression of a viral Cre-conditional hM4D(Gi) construct to selectively inhibit these neurons' activity via chemogenetics, using designer receptors exclusively activated by designer drugs (DREADD; Figure 3.4I) (Krashes et al., 2011).

Figure 3.4. Glutamatergic plCoA$^{Slc17a6+}$ and plCoA$^{Slc17a7+}$ neurons are dissociably sufficient but only partially necessary for innate olfactory valence.

(A) Schematic for selective plCoA$^{Slc17a6+}$ photostimulation. Strategy to activate glutamatergic plCoA$^{Slc17a6+}$ neurons via Cre-dependent optogenetics (left) and representative histology from ChR2 viral injection and fiber implantation site in an *Slc17a6::Cre* animal (right).

(B) Baseline-normalized collective heatmaps from both the ChR2- and eYFP-infected groups in *Slc17a6::Cre* animals with plCoA-localized fiber implants. Lower right stimulus quadrant marked in blue.

(C-D) Cre-dependent photostimulation of plCoASlc17a6+ neurons infected with ChR2, but not eYFP, is sufficient to reduce time spent in the stimulation quadrant (C) and increase its average distance from the stimulation port (D) during the stimulation period.

(E) Schematic for selective plCoASlc17a7+ photostimulation. Strategy to activate glutamatergic plCoASlc17a7+ neurons via Cre-dependent optogenetics (left) and representative histology from ChR2 viral injection and fiber implantation site in an Slc17a6::Cre animal (right).

(F) Baseline-normalized collective heatmaps from both the ChR2- and eYFP-infected groups in Slc17a7::Cre animals with plCoA-localized fiber implants. Lower right stimulus quadrant marked in blue.

(G-H) Cre-dependent photostimulation of plCoASlc17a7+ neurons infected with ChR2, but not eYFP, is sufficient to increase time spent in the stimulation quadrant (G) and decrease its average distance from the stimulation port (H) during the stimulation period.

(I) Behavioral paradigm to assess innate olfactory valence responses. Left, schematic of four-quadrant open field behavioral assay for spatially-specific odor delivery. Upper right, within-trial timeline. Lower right, odors delivered and their associated innate valence (Root et al., 2014).

(J) Schematic for selective chemoinhibition of molecularly defined glutamatergic plCoA neurons.

(K-L) Chemoinhibition of plCoA Slc17a6+ neurons does not significantly reduce the 2PE-evoked increase in time spent in the odor quadrant (K) or decrease in mean port distance (L).

(M-N) Chemoinhibition of plCoA Slc17a6+ neurons does not significantly reduce the TMT-evoked reduction in time spent in the odor quadrant (M) or increase in mean port distance (N).

(O-P) Chemoinhibition of plCoA Slc17a7+ neurons significantly, completely ablates the 2PE-evoked increase in time spent in the odor quadrant (O) or decrease in mean port distance (P), returning them to baseline.

(Q-R) Chemoinhibition of plCoA Slc17a7+ neurons does not significantly reduce the TMT-evoked reduction in time spent in the odor quadrant (Q) or increase in mean port distance (R).

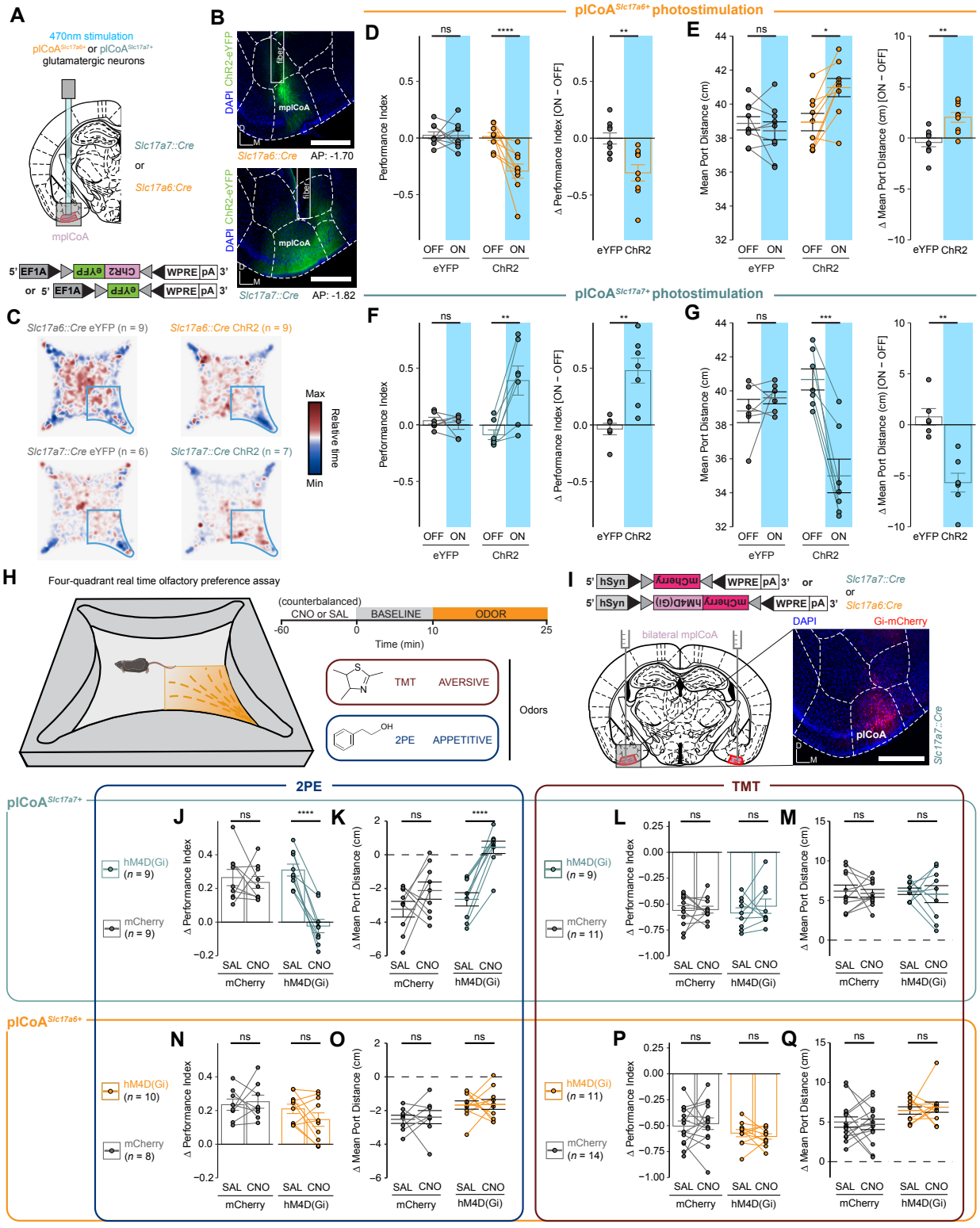
A
470nm stimulation
pICoA Slc17a6+ or pICoA Slc17a7+
glutamatergic neurons
Slc17a7::Cre
or
Slc17a6:Cre
mplCoA
5' EF1A ChR2 eYFP WPRE pA 3'
or 5' EF1A eYFP WPRE pA 3'
B
DAPI ChR2-eYFP
fiber
mplCoA
Slc17a6::Cre AP: -1.70
Slc17a7::Cre AP: -1.82
C
Slc17a6::Cre eYFP (n = 9)
Slc17a6::Cre ChR2 (n = 9)
Slc17a7::Cre eYFP (n = 6)
Slc17a7::Cre ChR2 (n = 7)
Max
Relative time
Min
pICoA Slc17a6+ photostimulation
D
Performance Index
Δ Performance Index [ON – OFF]
OFF ON
eYFP
ChR2
eYFP ChR2
E
Mean Port Distance (cm)
Δ Mean Port Distance (cm) [ON – OFF]
pICoA Slc17a7+ photostimulation
F
G
H
Four-quadrant real time olfactory preference assay
(counterbalanced)
CNO or SAL
BASELINE
ODOR
-60
0
10
25
Time (min)
TMT AVERSIVE
2PE APPETITIVE
Odors
I
5' hSyn mCherry WPRE pA 3'
5' hSyn hM4D(Gi) mCherry WPRE pA 3'
or
Slc17a7::Cre
or
Slc17a6:Cre
bilateral mplCoA
DAPI
Gi-mCherry
pICoA
Slc17a7::Cre
2PE
TMT
pICoA Slc17a7+
pICoA Slc17a6+
J
K
L
M
N
O
P
Q
hM4D(Gi) (n = 9)
mCherry (n = 9)
hM4D(Gi) (n = 11)
mCherry (n = 11)
hM4D(Gi) (n = 10)
mCherry (n = 8)
hM4D(Gi) (n = 11)
mCherry (n = 14)
Δ Performance Index
Δ Mean Port Distance (cm)
SAL CNO
mCherry
hM4D(Gi)

We administered clozapine-N-oxide (CNO) or a vehicle control and used the four-quadrant open field assay to deliver odorants in a quadrant-specific manner to assess their olfactory valence responses to either an innately appetitive odor, 2-phenylethanol (2PE) or an innately aversive odor, 2,5-dihydro-2,4,5-trimethylthiazoline (TMT) to determine the difference in the magnitude of temporally-counterbalanced valence responses when the respective populations are either responding normally or are chemogenetically silenced (Figure 3.4J) (Root et al., 2014). Interestingly, we observed that while both transgenic mouse lines preserved the baseline appetitive responses to exposure for both 2PE and TMT following administration of the vehicle control, silencing plCoA$^{Slc17a6+}$ neurons left the phenotype intact in all cases (Figure 3.4K-N). However, silencing plCoA$^{Slc17a7+}$ neurons would ablate the positive valence response to 2PE, without having any effect on TMT aversion (Figure 3.4O-R). In other words, neither group of plCoA glutamatergic neurons was necessary for TMT aversion, but plCoA$^{Slc17a7+}$ neurons are required for expression of 2PE attraction behaviors. Further, silencing of either population did not lead to any broader non-olfactory behavior effects as measured by the EPM and OFT assays, including anxiety, exploration, and motility, showing the effects of silencing these neurons are likely limited to valence and/or olfaction alone, instead of exploratory or defensive behaviors (Figure S3.5C-N). The necessity of plCoA$^{Slc17a7+}$ neurons for 2PE attraction, combined with their ability to drive positive valence responses show that these of plCoA$^{Slc17a7+}$ neurons control innate olfactory attraction, but plCoA$^{Slc17a6+}$ neurons do not completely control innate olfactory aversion, instead proving sufficient but not necessary.

3.3.4. Downstream projections from plCoA to limbic targets are topographically distributed

We posited that these differences in necessity could be due to divergent function being dependent on divergent downstream circuit motifs, instead of divergent molecular cell types, which may partially, but not completely overlap. To further explore this hypothesis, we next sought to identify distinct circuit motifs in plCoA that could explain the bidirectional valence effects of its topography. To initially characterize the downstream outputs of plCoA, we began by injecting an anterograde tracer into plCoA to label presynaptic terminals with EGFP (Figure 3.5A). We first observed that a high proportion of terminal fluorescence was found within plCoA itself, indicating a high degree of recurrent connections within the region (Figure 3.5B,D). The plCoA also sends out long-range projections in a highly diffuse matter to a diverse set of regions, including surrounding extended amygdala subregions, such as MeA and the amygdalo-hippocampal transition area (AHi), regions controlling valence and emotion, like the NAc and the bed nucleus of the stria terminalis (BNST), and regions involved in olfactory processing, primarily PIR and OT (Figure 3.5C-D).

Among these outputs, we hypothesized that the NAc and the MeA could be responsible for the behavior divergence in these two fields, given their known involvement in reward and olfactory aversion, respectively (Mueller and Fendt, 2006; Ikemoto, 2007). To determine if these projection patterns co-varied with the observed behavioral differences between aplCoA and pplCoA, we injected red retrobeads into the MeA or NAc (Figure 3.5E). For both downstream targets, we observed retrobead labeling of projectors throughout the entire plCoA anteroposterior axis, though both displayed opposing anterior-posterior gradients (Figure 3.5F). MeA-projecting neurons are enriched in aplCoA, and NAc-projecting neurons are enriched in pplCoA,

Figure 5. Projection mapping in plCoA identifies downstream targets of plCoA, including two divergent, non-collateralizing, topographically-distributed, and molecularly-biased projections to MeA and NAc.

(A) Schematic for general anterograde output mapping strategy, where a virus labeling cell bodies in plCoA with mRuby and presynaptic terminals in downstream regions with synaptophysin-bound eYFP.

(B) Histological image of plCoA injection site in a representative animal. Scale bar, 200 µm.

(C) Representative histological images of strongest targets of plCoA projections. All scale bars, 200 µm.

(D) Magnitude of anterograde synaptophysin-eYFP fluorescence in primary downstream targets of plCoA projection neurons ordered by total output strength.

(E) Schematic for topographic retrograde mapping strategy from MeA and NAc into plCoA. Red retrobeads are injected into MeA or NAc and topographical projection bias is examined along the anterior-posterior axis.

(F) Representative images (top) for injection into and number of neurons labeled along the anterior-posterior axis (bottom) for MeA (left) or NAc (right). Gray lines denote individual replicates, where colored lines indicate mean +/- s.e.m.

(G) Proportion of retrobead-labeled neurons projecting to MeA or NAc for each 100 µm segment. Dashed line indicates overall balance of all retrobead-labeled neurons across entire plCoA.

(H) Proportion of retrobead-labeled neurons from either target within each plCoA zone. MeA-labeled neurons are significantly enriched in aplCoA compared to NAc-labeled neurons, while NAc-labeled neurons are significantly enriched in pplCoA compared to those labeled from MeA.

(I) Schematic for topographic output mapping strategy, where two counterbalanced fluorophores were injected into aplCoA and pplCoA, and each color was quantified in major projection targets of plCoA.

(J) Representative histological images for the injection sites in aplCoA and pplCoA from an representative animal. Scale bar, 500 µm.

(K) Representative histological images for selected regions of interest from the animal in (J). Scale bar, 200 µm

(L) Output strength as a proportion of total fluorescence from aplCoA and pplCoA to MeA and NAc.

(M) Schematic for Cre-dependent anterograde output mapping strategy, where a Cre-dependent virus expressing eYFP is injected into either an *Slc17a6::Cre* or *Slc17a7::Cre* animal to determine relative output enrichment for either broad cell type.

(N) Representative histological images for the injection site in plCoA as well as MeA and NAc from a representative animal of either genotype. Scale bar, 200 µm.

(O) Output strength as a proportion of total fluorescence from plCoA$^{Slc17a6+}$ and plCoA$^{Slc17a7+}$ neurons to MeA and NAc.

(P) Comparison of same data as in (O), but by target region within the same genotype.

(Q) Schematic of anterograde viral strategy to explore collateralization of MeA projection neurons to other regions.

(R) Left, Representative histological images for MeA and NAc from a representative mouse in the plCoA-NAc group. Right, Quantification of fluorescence in selected downstream

brain regions from plCoA originating from plCoA-MeA neurons proportional to eYFP fluorescence in NAc. Scale bar, 200 μm.

(S) Left, Representative histological images for MeA and NAc from a representative mouse in the plCoA-MeA group. Right, Quantification of fluorescence in selected downstream brain regions from plCoA originating from plCoA-MeA neurons proportional to eYFP fluorescence in MeA. Scale bar, 200 μm.

(T) Comparison of absolute integrated fluorescence intensities in MeA and NAc when retroAAV was injected into MeA or NAc.

Abbreviations: NAc, nucleus accumbens; BNST, bed nucleus of stria terminalis; MeA, medial amygdala; Pir, piriform cortex; BLA, basolateral amygdala; Ahi, amygdalo-hippocampal transition area; pmCoA, posteromedial cortical amygdala; Str, striatum; OT, olfactory tubercle; EA, extended amygdala; IPAC, inferior peduncle of the anterior commissure; AA, anterior amygdala; LA, lateral amygdala; HDB, horizontal limb of the diagonal band; VP, ventral pallidum; AIC, anterior insular cortex; mfb, medial forebrain bundle; MO, medial orbitofrontal cortex; LOT, lateral olfactory tract; ACo, anterior cortical amygdala; AOA, anterior olfactory area; DG, dentate gyrus; Rt, reticular nucleus; LPO, lateral preoptic area; VMH, ventromedial hypothalamus; DEn, dorsal endopiriform claustrum; LH, lateral hypothalamus; IL, infralimbic cortex; DP, dorsal peduncular cortex; LS, lateral septum; CxA, cortex-amygdala transition area; sox, supraoptic decussation; StHy, striohypothalamic nucleus; GP, globus pallidus; PLH, perirhinal cortex; ZI, zona incerta.

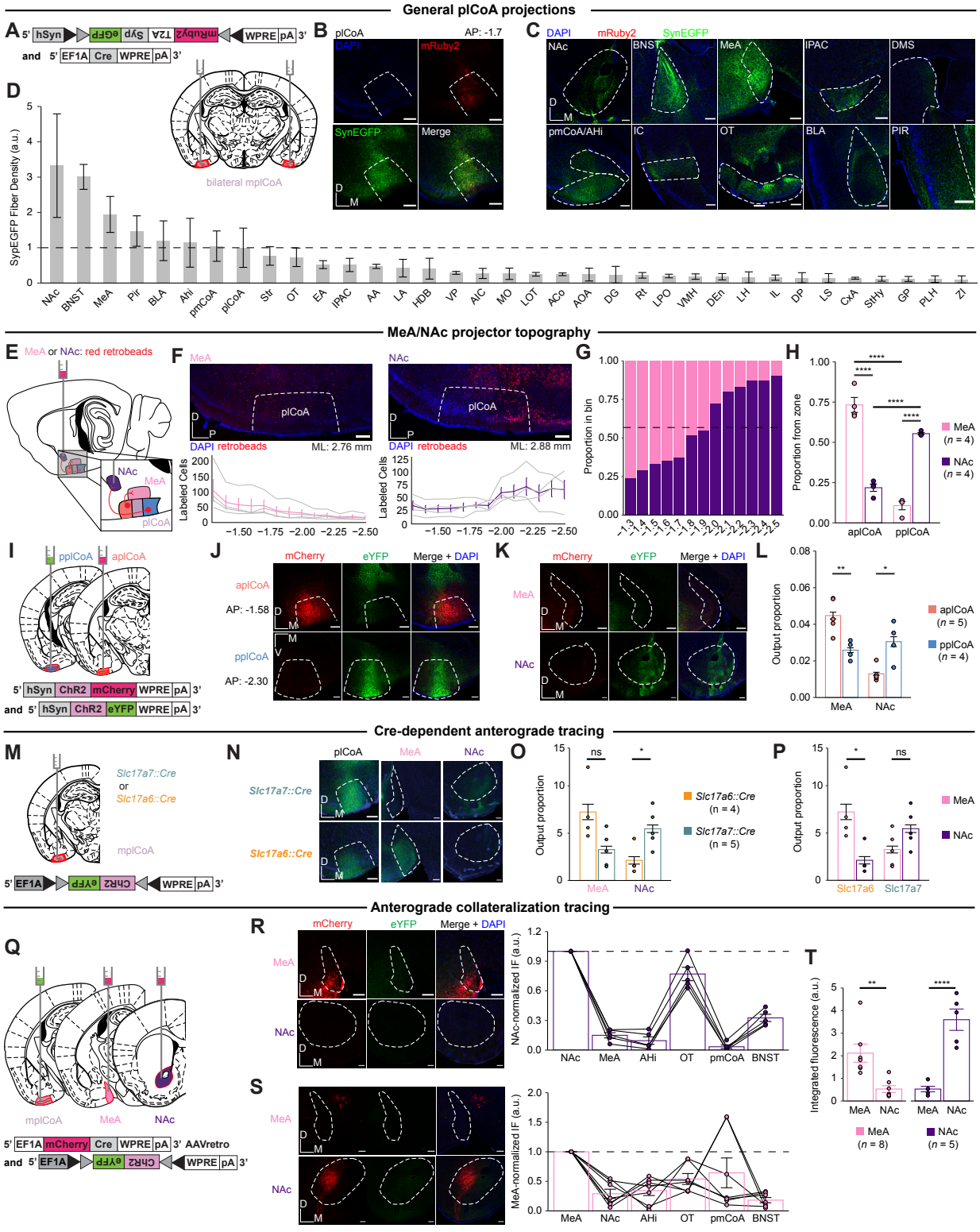
General plCoA projections
MeA/NAc projector topography
Cre-dependent anterograde tracing
Anterograde collateralization tracing
bilateral mplCoA
SypEGFP Fiber Density (a.u.)
NAc BNST MeA Pir BLA Ahi pmCoA plCoA Str OT EA lPAC AA LA HDB VP AIC MO LOT ACo AOA DG Rt LPO VMH DEn LH IL DP LS CxA StHy GP PLH ZI
MeA or NAc: red retrobeads
DAPI retrobeads
ML: 2.76 mm
ML: 2.88 mm
Labeled Cells
Proportion in bin
Proportion from zone
aplCoA
pplCoA
Output proportion
Slc17a6
Slc17a7
mplCoA
NAc-normalized IF (a.u.)
MeA-normalized IF (a.u.)
Integrated fluorescence (a.u.)
(n = 4)
(n = 5)
(n = 8)
129

with each having a frequency of around chance level in mplCoA (Figure 3.5G). Further, the majority of labeled plCoA-MeA projection neurons were in aplCoA, while a majority of labeled plCoA-NAc projection neurons were located in pplCoA (Figure 3.5H). To confirm these findings in the same manner these projections were identified, via anterograde tracing, we injected viruses expressing either mCherry or EGFP into the aplCoA and pplCoA in a counterbalanced manner (Figure 3.5I). Anterograde projection strength from aplCoA and pplCoA generally confirmed retrograde tracing, where projections to MeA were far more dense from aplCoA, and projections to NAc were more dense from pplCoA (Figure 3.5J-K). Proportionally, aplCoA sent a significantly higher proportion of its projections to MeA than pplCoA, while pplCoA sent a significantly higher proportion of its projections to NAc (Figure 3.5L).

Such topographical biases could be explained by a divergence in projection target based on cell type, where the topographical biases in downstream targets are recapitulated by their underlying molecular cell type even when examining projections arising from similar locations along the plCoA anteroposterior axis. To determine the relationship between cell types and projection targets, we injected Cre-dependent eYFP into mplCoA in *Slc17a6::Cre* and *Slc17a7::Cre* transgenic mice (Figure 3.4M). Interestingly, the relationship was not as simple as one cell type, one primary projection target. Instead, though plCoA$^{Slc17a6+}$ neurons primarily project to MeA with a significant bias for that target rather than NAc, plCoA$^{Slc17a7+}$ neurons project to both MeA and NAc, without a significant enrichment for either target compared to the other (Figure 5N-P). These findings largely support a near-exclusive projection from plCoA$^{Slc17a7+}$ neurons to NAc, though with cell type redundancy in the output to MeA.

Given that both populations are found in both plCoA zones and both cell types to some degree, despite enrichment, these neurons could possibly collateralize to both downstream

regions of interest. To test whether plCoA-MeA and plCoA-NAc projection neurons project to multiple or overlapping downstream targets, we injected a retroAAV-Cre virus into either MeA or NAc, and AAV-ChR2-eYFP into plCoA to label outputs of MeA- or NAc-projecting neurons (Figure 3.5Q), with a focus on MeA and NAc, as well as the ancillary primary downstream targets AHi and BNST, which are involved in valence behaviors, and OT and pmCoA, additional third-order olfactory regions (Lebow and Chen, 2016; Sedwick and Autry, 2022; Pardo-Bellver et al., 2022; Lee et al., 2023). We found different collateralization patterns for both populations, where MeA-projecting neurons minimally collateralized to NAc and most strongly collateralized to pmCoA (Figure 3.5R). In contrast, NAc-projecting neurons did not collateralize to MeA, but very strongly collateralized to OT (Figure 3.5R-S). Overall, neither projection of interest significantly collateralized with the other (Figure 5T). These data support plCoA-MeA and plCoA-NAc projection neurons as non-overlapping, spatially biased populations that output to different subnetworks.

3.3.5. Projections from plCoA to MeA and NAc respectively control innate olfactory aversion and attraction in a dissociable manner

Given the spatial distribution of MeA and NAc projection neurons and their lack of collateralization, we thought that innate valence in plCoA could be controlled based on the neurons' downstream projection target instead of their specific molecular phenotype. To investigate the behavioral effects each circuit evokes, we expressed ChR2 in a non-spatially-biased manner in plCoA, placing a fiber just above MeA or NAc for selective optogenetic stimulation of each circuit (Figure 3.6A, S3.1C). We found that photostimulation of the plCoA-MeA pathway in the four-quadrant open field task significantly reduced time spent in the 'on' quadrant and increased the average distance to the corner port during the treatment period,

indicating activation of the plCoA-MeA circuit is aversive and leads to avoidance of the quadrant paired with stimulation (Figure 3.6B, 3.6C-D). The opposite was true for the plCoA-NAc projection, where stimulation in that zone instead increased the time in the 'on' quadrant and decreased average distance to the corner port, indicating activation of the plCoA-NAc circuit instead is instead appetitive and leads to attraction to the stimulation quadrant (Figure 3.6E-F). We then examined the effects of the stimulation of these circuits on other behaviors in the EPM and OFT to determine whether these effects were specific to valence. Using the elevated plus maze, we found no change in anxiety based on open arm time or entries, across both the length of plCoA or within either aplCoA or pplCoA (Figure S3.6A-C, S3.6E-F, S3.6H-I). In the open field test, we similarly found no changes to thigmotaxis, based on time spent in corners of the open field, or exploration, based on time spent in the center of the open field (Figure S3.6K-M, S3.6O-P, S3.6R-S). Further, locomotion remained constant during stimulation across both assays (Figure S3.6D, S3.6G, S3.6J, S3.6N, S3.6Q, S3.6T). These data clarify that the divergent domain- and genotype-specific valence effects of plCoA activity are likely due to the divergent circuit engagement that results from the correlation between both ensembles and their downstream targets.

Finally, we sought to confirm whether the projection neurons from plCoA to MeA or NAc were necessary for the expression of these appetitive or aversive behaviors when exposed to innately-valenced odors, especially given that their relationship to glutamatergic cell type identity would explain the partial necessity observed in those silencing experiments. To target these projection neurons for chemogenetic silencing, we injected a retroAAV bearing an hSyn-

Figure 3.6. Projections from plCoA to MeA control innate olfactory aversion, while projections to NAc control innate olfactory attraction.

(A) Schematic for optogenetic MeA and NAc terminal stimulation in plCoA neurons. Strategy to activate MeA-projecting plCoA neuron terminals via optogenetics (top) and representative histology from ChR2 viral injection and fiber implantation site (bottom).

(B) Baseline-normalized collective heatmaps from both the ChR2- and eYFP-infected plCoA groups with MeA- and NAc-localized fiber implants. Lower right stimulus quadrant marked in blue.

(C-D) Optogenetic MeA terminal stimulation of plCoA neurons infected with ChR2, but not eYFP, is sufficient to reduce time spent in the stimulation quadrant (C) and increase its average distance from the stimulation port (D) during the stimulation period.

(E-F) Optogenetic NAc terminal stimulation of plCoA neurons infected with ChR2, but not eYFP is sufficient to increase time spent in the stimulation quadrant (E) and decrease its average distance from the stimulation port (F) during the stimulation period.

(G) Schematic for selective retrograde chemoinhibition of projection-defined plCoA neurons.

(**H**) Histological schematic for selective retrograde chemoinhibition of projection-defined plCoA neurons.

(I-J) Chemoinhibition of MeA-projecting plCoA neurons does not significantly reduce the 2PE-evoked increase in time spent in the odor quadrant (I) or decrease in mean port distance (J).

(K-L) Chemoinhibition of MeA-projecting plCoA neurons significantly ablates the TMT-evoked reduction in time spent in the odor quadrant (K) or increase in mean port distance (L).

(M-N) Chemoinhibition of NAc-projecting plCoA neurons significantly, completely ablates the 2PE-evoked increase in time spent in the odor quadrant (M) or decrease in mean port distance (N), returning them to baseline.

(O-P) Chemoinhibition of NAc-projecting plCoA neurons does not significantly reduce the TMT-evoked reduction in time spent in the odor quadrant (O) or increase in mean port distance (P).

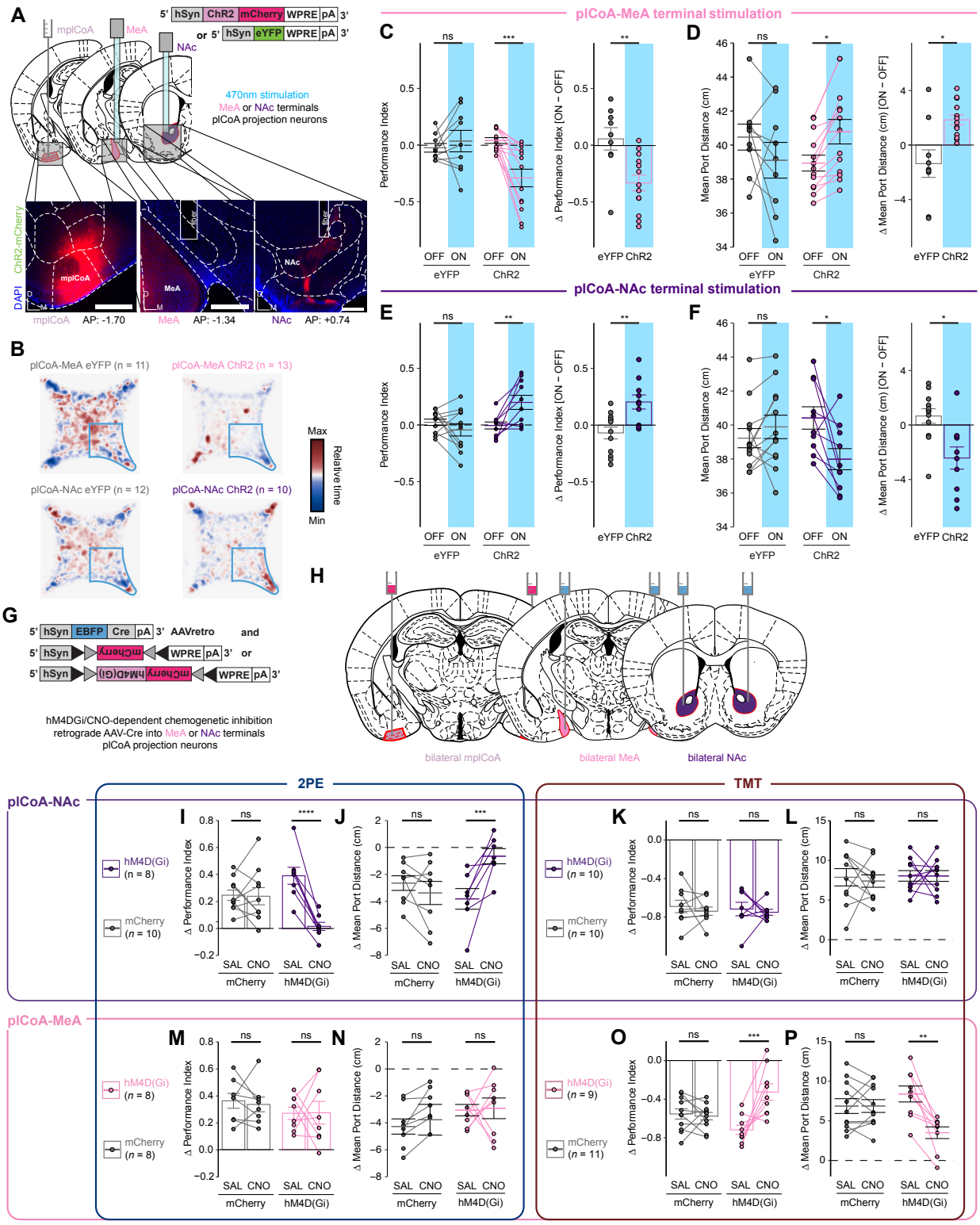
A
5' hSyn ChR2 mCherry WPRE pA 3'
or 5' hSyn eYFP WPRE pA 3'
mPlCoA
MeA
NAc
470nm stimulation
MeA or NAc terminals
plCoA projection neurons
ChR2-mCherry
DAPI
mPlCoA AP: -1.70
MeA AP: -1.34
NAc AP: +0.74
B
plCoA-MeA eYFP (n = 11)
plCoA-MeA ChR2 (n = 13)
plCoA-NAc eYFP (n = 12)
plCoA-NAc ChR2 (n = 10)
Max
Min
Relative time
plCoA-MeA terminal stimulation
C
D
plCoA-NAc terminal stimulation
E
F
Performance Index
Δ Performance Index [ON – OFF]
Mean Port Distance (cm)
Δ Mean Port Distance (cm) [ON – OFF]
OFF ON
eYFP
ChR2
eYFP ChR2
G
5' hSyn EBFP Cre pA 3' AAVretro and
5' hSyn mCherry WPRE pA 3' or
5' hSyn hM4D(Gi) mCherry WPRE pA 3'
hM4DGi/CNO-dependent chemogenetic inhibition
retrograde AAV-Cre into MeA or NAc terminals
plCoA projection neurons
H
bilateral mPlCoA
bilateral MeA
bilateral NAc
2PE
TMT
plCoA-NAc
plCoA-MeA
hM4D(Gi) (n = 8)
mCherry (n = 10)
hM4D(Gi) (n = 10)
hM4D(Gi) (n = 9)
mCherry (n = 11)
Δ Performance Index
Δ Mean Port Distance (cm)
SAL CNO
mCherry
hM4D(Gi)

EBFP-Cre construct into MeA or NAc, along with an AAV in plCoA bearing a Cre-dependent hM4D(Gi)-mCherry construct (Figure 3.6I). We then exposed these animals to 2PE or TMT in the four-quadrant task following administration of CNO or a vehicle control, as before. Here, we found inhibition of plCoA-MeA projection neurons has no effect on innate 2PE attraction, but upon exposure to TMT, the aversive phenotype dramatically decreases in magnitude (Figure 3.6J-M). Conversely, inhibition of plCoA-NAc projection neurons entirely ablates innate 2PE attraction without having any effect on TMT's aversive phenotype (Figure 6N-Q). When these neurons are silenced during the EPM and OFT assays, we again did not observe any behavioral effects unrelated to olfactory valence, including anxiety, exploration, and motility, confirming the effects of silencing these neurons are likely limited to valence and/or olfaction alone (Figure S3.6M-X). From this data, we can thus conclude that plCoA-MeA projection neurons are sufficient and necessary for innate olfactory aversion, while plCoA-NAc projection neurons are themselves sufficient and necessary for innate olfactory attraction, and such phenomena can explain the effect of plCoA manipulation in other modalities on innate olfactory valence.

3.4. Discussion

3.4.1. Topographic organization of valence in plCoA

The neural circuits mediating innate valence responses to odor have not been fully defined. Here, we have advanced our knowledge of the circuitry underlying innate olfactory behaviors by defining its activity and organization within plCoA, and further extending the innate pathway deeper beyond the plCoA. We have identified a novel functional axis for valence with the plCoA that is defined by histologically and functionally distinct domains along the anteroposterior axis. We have also determined the composition of molecular cell types in plCoA and identified

spatially biased populations enriched within each domain, which we find sufficient to drive their respective domain-specific behaviors, though only partially necessary for their functions in olfaction. To resolve this discrepancy, we identified the outputs of plCoA, and quantitatively characterized the relative strength of each, as well as how it relates to plCoA topography and domain-specific molecular cell types, demonstrating that neurons projecting to the MeA and NAc are topographically and molecularly biased. Finally, we demonstrate that neurons projecting to the to the NAc and MeA are capable of driving approach and avoidance responses, and olfactory loss of function experiments demonstrate that the neurons projecting to the NAc or MeA are selectively involved in innate olfactory attraction and avoidance, respectively. Thus, plCoA is composed of dissociable, spatially segregated ensembles for divergent valence, defined by their downstream projection target.

Spatial organization for features of sensory stimuli is common in sensory cortex and has been previously proposed as fundamental to sensory processing (Kaas, 1997). Visual cortex is topographical organized by retinotopic locations in space, somatosensory cortex contains a map of the body, auditory cortex has a crude tonotopic organization by frequency, and gustatory cortex is segregated by taste qualities (Kaas et al., 1979; Schreiner and Winer, 2007; Chen et al., 2011; Garrett et al., 2014; Wang et al., 2018). However, topographic organization by perceptual feature has not been observed in the olfactory system, which has been attributed to the high dimensional nature of olfactory information (Imai et al., 2010; Auffarth, 2013). Our findings identify a topographical motif organizing valence in plCoA, where neural activity in the anterior field evokes aversive behavioral responses, while activity in the posterior field evokes attractive behavioral responses, with a graded transition between the two domains. This is consistent with prior studies implicating a spatial organization to inputs from the OB to plCoA. Glomerulus-

specific anterograde tracing from OB shows specific glomeruli send fibers to invariant, densely clustered, anatomically distinct locations within plCoA, and retrograde tracing from plCoA shows that upstream glomeruli are spatially biased within OB and closer examination reveals that OB input varies depending on the origin's anteroposterior position (Miyamichi et al., 2011; Sosulski et al., 2011). Interestingly, spatial segregation of divergent features is present elsewhere in olfaction as well, although not by perceptual feature. Olfactory sensory receptors display highly stereotyped spatial organization even within the olfactory epithelium, with a corresponding spatially stereotyped glomerular topography in OB (Russell et al., 1993; Soucy et al., 2009; Pacifico et al., 2012; Zapiec and Mombaerts, 2020; Wang et al., 2022). However, the piriform cortex lacks any such spatial organization, and and there is no apparent spatial patterning for odor reponses (Stettler and Axel, 2009). To our knowledge, the topographical organization observed here in plCoA represents the first such description of these spatial patterns occurring in non-peripheral olfactory areas.

Topographic gradients for valence have been observed in other limbic regions, including the basolateral amygdala (BLA) for overall valence, the gustatory cortex for taste valence, the medial amygdala for innate social behaviors, and Drosophila dopaminergic mushroom body neurons for general innate valence (Choi et al., 2005; Chen et al., 2011; Cohn et al., 2015; Kim et al., 2016; Wang et al., 2018). Our results extend this phenomenon into a new region and a new olfactory modality and suggest that spatial segregation could serve as a potential common motif within the limbic system to organize motivational information, especially for innate behaviors, which are heavily overrepresented within this set and require stereotyped neurocircuitry. We believe a model where aplCoA and pplCoA are parts of the same region with similar underlying composition, but with a gradual change in the factor that defines the valence output for a given

part of the gradient, would best explain the underlying gradient-like effect on positive and negative valence. This underlying factor is likely some change in the types of neurons as the gradient progresses, most likely defined by cell type or by projection target. Given the results of following experiments, we determined the underlying decisive factor changing being enrichment for the projection target of the neurons composing the population, instead of the molecular cell type.

3.4.2. Molecular cell types in plCoA segregate topographically and evoke divergent valence behaviors

While examining the cell types composing plCoA, we noticed numerous notable, novel features. First, despite its small area (~1.04 mm^3 and ~170,000 cells), plCoA displays remarkable diversity, hosting dozens of distinct, robustly separable cell types (Erö et al., 2018). The plCoA appears to have multiple domains positioned at the transition between highly dissimilar brain tissue types. Interestingly, the high-dimensional structure of molecular variation differs between glutamatergic and GABAergic neurons. Glutamatergic molecular variation within plCoA is continuous, with two broadly nested groups generally marked by either *Slc17a6* or *Slc17a7* along with one or more additional marker gene(s), though it should be noted that expression of the two broad glutamatergic markers is not necessarily mutually exclusive and a few low abundance "transition" cell types can express either one. In contrast, molecular variation in GABAergic neurons is far more discretized, with ensembles expressing one of a few well-characterized interneuron markers found throughout the brain, such as *Sst*, *Vip*, and *Pvalb*, among others. This is consistent with other studies in neocortex, hippocampus, and subiculum that find similar patterns of variation, where variation within glutamatergic neurons is far more continuous than in GABAergic neurons (Cembrowski et al., 2018; Tasic et al., 2018). In this way, we find the

continuous gradient-like structure of valence in plCoA is recapitulated with gradient-like variation in glutamatergic neuron gene expression in plCoA.

In these molecular datasets, we further observed highly specific differences in cell type enrichment within aplCoA and pplCoA within glutamatergic neurons, but not GABAergic neurons or glia. Within plCoA, *Slc17a6*+ neurons are enriched in aplCoA, *Slc17a7*+ neurons are enriched in pplCoA, though there is gradient-like intermingling of populations, especially toward the middle of plCoA, and all glutamatergic neuron types are present, albeit to an extremely variable degree, along the anteroposterior axis. This molecularly defined order suggests a programmed organization, rather than stochastically distributed populations within the region, especially given that its boundaries match the domains previously identified based on behavior and histology (Cembrowski and Spruston, 2018). This phenomenon also broadly matches observations in the neocortex, hippocampus, and subiculum, where glutamatergic neurons across subdivisions molecularly diverge to a far greater degree than GABAergic neurons or glia, albeit across a far greater area than within plCoA, which is generally accompanied by distinct morphological and electrophysiological phenotypes broadly corresponding to these transcriptomic differences (Cembrowski et al., 2018a,b; Tasic et al., 2018; Ding et al., 2020). Spatial segregation of molecular cell types is also observed within deeper brain regions including BLA, thalamus and habenula, and these molecular differences are also accompanied by extended phenotypic differences as well (Kim et al., 2016; Mandelbaum et al., 2019; Phillips et al., 2019; O'Leary et al., 2020; Calvigioni et al., 2023). Investigation of such properties held in common and diverging within and between *Slc17a6*+ and *Slc17a7*+ glutamatergic neuron types could also serve to further illustrate the local neurocircuitry and information processing dynamics within plCoA and along its anteroposterior axis.

Interestingly, few if any populations within plCoA are clearly separable from most of the regions surrounding it (e.g. piriform cortex, basomedial amygdala, and MeA) based on primary marker gene identity. Instead, plCoA ensembles seem to be defined by the interplay of all three regions within the same tissue. The predominance of populations resembling different regions does appear related to this anteroposterior organization, though, where Slc17a6+ neurons predominate in both aplCoA and MeA, and more specific marker genes, such as Meis2 and Baiap3 are expressed in both regions as well. Conversely, *Slc17a7*+ neurons predominate in both pplCoA and piriform cortex, and the major marker genes *Satb2* and *Reln* are similarly expressed in both regions. It would be misleading to characterize plCoA populations as mere extensions of surrounding populations into an adjacent region, though. *Slc17a7*+ neurons from the cortex-amygdala transition zone are also present in the dataset and are continuously separable from *Slc17a7*+ plCoA neurons, as well as based on Ccbe1 expression, while *Slc17a6*+ neurons from MeA are also present and separable from *Slc17a6*+ neurons in plCoA. Instead, plCoA may itself be a transition region, given that such a relationship with its neighboring regions is very similar to that of the amygdalostriatal transition area, one of the only transition regions to undergo high-resolution molecular profiling (Mills et al., in revision). Given such commonalities between these two putatively dissimilar regions, molecular characterization of additional transition regions could potentially uncover similar organizational motifs, especially if compared with adjacent regions of interest, and allow for a much more in-depth exploration and characterization of the boundaries and transitions between proximally located, distantly related brain regions.

These broad molecular groups of glutamatergic cell types themselves may not completely explain the role of plCoA in innate olfactory valence. While aplCoA-enriched Slc17a6+ neurons are sufficient to induce aversion and pplCoA-enriched *Slc17a7*+ neurons are sufficient to

induces attraction, as would be predicted from the valence responses evoked from each field each group is enriched within. It might be expected that these populations would also be necessary for the respective odor-evoked valence, However, only *Slc17a7*+ neurons are necessary for 2PE attraction, whereas the *Slc17a6*+ neurons were not required aversion to TMT. Given that the plCoA is necessary for TMT aversion, it is unlikely that such a difference is due to additional redundant function within other regions for TMT aversion (Root et al., 2014). Instead, it is far more likely that though *Slc17a6*+ neurons likely contribute to the valence behavior, other populations within the region not expressing the marker gene also likely contribute to the behavioral response, compensating for the loss of *Slc17a6*+ neuron activity. Thus, though these two broad glutamatergic groups can drive innate responses of valence, the *Slc17a6*+ population doesn't fully represent the population that control aversive responses, which is supported by other findings presented here showing that both *Slc17a6*+ and *Slc17a7*+ neurons project to MeA, while the projection to NAc is almost entirely composed of *Slc17a7*+ neurons. Regarding more specific molecular cell types, it could be possible that only a subset of *Slc17a7*+ neurons are required for 2PE attraction, instead of the entirety of the broad group. Similarly, the neurons required for TMT aversion could be marked by a gene orthogonal to the observed *Slc17a6/Slc17a7* gradient, and genetic access to olfactory aversion could potentially be established by investigating these more sparsely expressed marker genes. In both cases, though, further investigation into these more specific cell types and their associated phenotypes would be likely to enhance our understanding of both plCoA and innate olfactory valence and permit far more precise manipulations in the future.

3.4.3. Identified plCoA downstream projection targets separately control innate olfactory valence

In this work, we perform the first characterization of plCoA's downstream outputs. These outputs are dominated by regions generally involved in valence and emotion, such as the NAc, BNST, MeA, BLA, and other amygdalar nuclei, or those involved in olfaction, such as the pmCoA, OT, and PIR. These outputs generally support plCoA's role as a region mediating innate olfactory valence, near-exclusively participating in circuits relating to either functionality. Surprisingly, the plCoA also forms numerous intra-regional connections, where a significant proportion of synapses formed with other neurons are within the region itself. This raises the possibility that plCoA does not simply do feedforward processing, but recurrent processing as well. This raises a number of interesting questions regarding information processing within plCoA, especially given that recurrent networks in other sensory systems will expand the dimensionality of its encoding and incorporate more features to give rise to mixed, continuously updating representations of relevant information (Singer, 2021). Further explorations of information transformation and encoding within plCoA will certainly enrich our understanding of the region's processing dynamics as well as how representations of innately valenced olfactory stimuli are transformed as they undergo both feedforward and recurrent processing within plCoA.

NAc and MeA are interesting downstream targets given their pre-existing known relationships to attraction and aversion, respectively. NAc has historically been critical to the manifestation and processing of reward and motivated behaviors, though this view has been expanded and made more subtle with a recent focus on action selection in general (Floresco, 2015). On the other hand, MeA has been strongly linked to defensive and stress-related behaviors at baseline and in response to aversive stimuli, as well as chemosensation in general

(Petrulis, 2020). MeA has also been specifically linked to olfactory aversion in past studies, as TMT has previously been shown to activate the MeA, which itself is directly necessary for TMT-induced defensive behaviors, though the upstream circuits and processing were not yet investigated (Day et al, 2004; Müller and Fendt, 2006; Saito et al., 2017). These circuits are also notable regarding other features of plCoA spatiomolecular organization, as the projections to the downstream regions of interest are the two that diverge to by far the greatest extent between aplCoA and pplCoA, and between plCoA$^{Slc17a6+}$ and plCoA$^{Slc17a7+}$ glutamatergic neurons, whereas the strength of the projections to most other downstream targets are fairly similar between the divisions of both spatiomolecular organizational axes. Given the relationship between spatiomolecular patterning and the simple wiring and organizational rules used to structure innate circuits across the genetic bottleneck, it could be possible that these highly specific circuit differences are a result of such bottlenecking practices; these two circuits could then potentially be investigated and understood via future studies of innate olfactory valence and the plCoA through the lenses of development and genetic variation, among others.

Given knowledge of inputs, outputs, and collateralization, we can model the motifs used in downstream projections for innate olfactory valence processing. Of the four best-described motifs in valence processing, we can initially rule out one easily. First, plCoA projections for attraction and aversion have no evidence supporting that they to be subject to neuromodulatory gain, because no significant neuromodulatory input to plCoA has yet been identified (Tye, 2018). Second, input properties make labeled-lines motifs far more likely than opposing components motifs given the anatomical segregation of inputs to plCoA and the physical separation of the neurons for each projection within plCoA. Recurrent connections within plCoA could allow it to sidestep the low flexibility and plasticity implied in labeled lines motifs, retaining the ability to

pass information between the circuits laterally within plCoA, even if long range projections are themselves segregated. At first glance, divergent paths would also appear not to be present, due to the anatomical segregation of their respective downstream targets controlling attraction and aversion (Tye, 2018). However, plCoA$^{Slc17a7+}$ glutamatergic neurons (but not their *Slc17a6*-expressing counterparts) project to both MeA and NAc, forming a redundant circuit to MeA that allows continued manifestation of aversion to TMT even when plCoA$^{Slc17a6+}$ glutamatergic neurons are silenced. Further investigation into this molecularly defined circuit is certainly warranted, and could point to more specific manipulable populations within plCoA$^{Slc17a7+}$ glutamatergic neurons that permits isolation of these two circuits.

3.4.4 Conclusion

Our findings identify and characterize the circuits responsible for innate olfactory valence, providing the first account of how the olfactory system links odor sensation to specific valence behaviors. Further, our present study also provides a complete accounting of the topographical, molecular, and connectomic organization of plCoA, showing how the olfactory system can route specific olfactory content in a hardwired manner.

3.5. Methods

3.5.1. Experimental model and subject details

All procedures at the University of California, San Diego, and Columbia University were performed in accordance with Institutional Animal Care and Use Committee protocols in

accordance with NIH guidelines. All mice were provided food and water ad libitum and maintained on a regular 12-hour reverse light/dark cycle at room temperature, with weight, health, and immune status monitored daily and verified to be within normal ranges. Mouse cages were changed regularly based on degree of soiling. All mice were group-housed with randomly assigned littermates prior to surgery, and single-housed after surgery. All animals were used in a single experiment each, except for a subset of mice who underwent 4-quad, EPM, and OFT experiments, who performed each test in no specific order.

3.5.1.1. Subject details for single-nucleus sequencing

All mice for snRNA-seq in the study were males on the wild-type C57BL/6J background (RRID:IMSR_JAX:000664) and received directly from Jackson Laboratories at 6 weeks of age and acclimated to the colony prior to experiments. Animals were single-housed and placed into sensory deprivation 24 hours prior to sacrifice to reduce artifactual immediate early gene expression. Sacrifice was performed at P60 ± 3 days (n = 5-10 mice per pool). Sample size was determined based on number of expected nuclei per region per mouse: estimates of expected nuclei were determined empirically, though nuclear recovery was approximately 20% of total based on cellular density estimates from the Blue Brain Cell Atlas.87 20,000 nuclei were targeted per combination of assay, condition, and region, which was determined using SCOPIT v1.1.4, allowing potential detection of at least 10 nuclei from 10 rare subpopulations at 0.1% frequency with 95% probability.109 A total of 50 mice were used for this purpose.

3.5.1.2. Subject details for spatial transcriptomics

In the separate study for spatial transcriptomics, APP23 (B6.Cg-Tg(Thy1-APP)3Somm/J; C57BL/6J background, RRID:IMSR_JAX:030504) non-transgenic (NTG) littermates control mice were housed in light-tight enclosures (Sturchler-Pierrat et al., 1997). The mice were given ad libitum food and water access. This study used a total of 17 mice almost equally distributed across sex, of which sections from 11 sagitally bisected the plCoA and were used in downstream analysis. No analysis of sex differences was performed due to inaccessibility of that information on a per-section basis. However, no such differences were apparent from per-section gene expression correlations reported in supplementary information.

3.5.1.3. Subject details for wild-type tracing and activity experiments

All mice for topographic and projection-defined manipulation and tracing experiments, as well as calcium imaging, were males on the wild-type C57BL/6J background and received directly from Jackson laboratories before 12 weeks of age. After surgery, mice incubated for at least 21 days if injected with virus or at least 7 days if injected with a retrograde tracer (e.g. retrobeads, cholera toxin B) to allow virus to express and tracers to travel in retrograde, respectively. All surgeries and downstream experiments were performed on mice at least 8 weeks of age.

3.5.1.4. Subject details for transgenic tracing, and activity experiments

We used VGlut2-IRES-Cre (Slc17a6tm2(cre)Lowl; C57BL/6J background, JAX no. 028863; Slc17a6::Cre) and VGlut1-IRES2-Cre-D (Slc17a7tm1.1(cre)Hze; C57BL/6J background, JAX no. 023527; Slc17a7::Cre) strain mice for molecularly defined optogenetic

stimulation experiments (Vong et al., 2011; Harris et al., 2014). These mice were bred on-site at the University of California, San Diego, and were genotyped using genomic DNA from ear tissue amplified with the default primer sets listed by Jackson Laboratories. All mice used for experiments had a heterozygous genotype for the transgenic construct of interest. After surgery, mice incubated for at least 21 days to allow virus to express.

3.5.2. Surgery

All surgeries were performed under aseptic conditions using a digital small animal stereotaxic instrument (VetFlo, Kent Scientific Corporation). Mice were initially anesthetized in a sealed box containing 5% gaseous isoflurane, and then deeply anesthetized using isoflurane (2.5% in 1L/min of O2) during surgeries. We immobilized and leveled the head in a stereotaxic apparatus (Kopf Instruments), removed fur from the scalp by shaving, applied eye lubricant (Optixcare), peeled off connective tissue, and dried the surface of the skull prior to craniotomy before proceeding with injections and implantations specific to certain experiments. All virus injections were performed at 2 nL/sec using a pulled glass pipette (Drummond) and a Nanoject III pressure injector (Drummond). To prevent backflow, the pipette was left in the brain for 15 minutes after injection.

3.5.2.1. Surgeries for optogenetic stimulation experiments

For optogenetic topographic- or projection-specific stimulation experiments, we injected wild-type C57BL/6J mice between 2-4 months of age with 100 (if topographic) or 150 (if projection-specific) nL of either AAV5-hSyn-eYFP (3.3×10^{12} gc/ml, UNC Vector Core) or

AAV5-hSyn-ChR2-mCherry-WPRE-PA (4.1×10^{12} gc/ml, UNC Vector Core). For Cre-dependent molecularly defined optogenetic stimulation, we injected 200 nl AAV5-EF1A-DIO-hChR2(H134R)-eYFP (5.5×10^{12} gc/ml, UNC Vector Core) or AAV5-EF1A-DIO-eYFP (4.0×10^{12} gc/ml, UNC Vector Core) All such injections were left unilateral, into either aplCoA or pplCoA for topographic photostimulation, and into middle plCoA for projection- or genotype-specific photostimulation. For topographic and genotype-specific photostimulation animals, we implanted the fiber 300 um (+0.3 DV) directly above the injection site with all other coordinates remaining constant. Anterior-posterior axis positioning arose from stochastic variation in virus and fiber placement. For projection-specific photostimulation animals, we implanted the fiber 300 um (+0.3 DV) directly above either the MeA or NAc, holding all other coordinates for the two regions constant as described above. For all optogenetic stimulation experiments, we implanted a fiber optic cannula (2.5 mm ferrule outer diameter, 200 um core, 0.39 numerical aperture; RWD) 300 um above the targeted stimulation site. These fibers were affixed onto the skull using OptiBond XTR (Kerr) and stably secured with Tetric Evoflow (Ivoclar Vivadent) coated with cyanoacrylate (Toagosei). After surgery, we injected all mice with 0.04 mL Buprenorphine SR (Ethiqa XR, Fidelis) for pain management. All mice were given their own cage immediately after surgery and returned to the colony once ambulatory.

3.5.2.2. Surgeries for chemogenetic inhibition

For all plCoA inhibition experiments, we bilaterally injected C57BL/6J mice between 2-4 months of age with 250 nL of either AAV2-hSyn-DIO-hM4D(Gi)-mCherry (7.1×10^{12} gc/ml, Addgene) or AAV2-hSyn-mCherry (1.8×10^{13} gc/ml, Addgene) virus. For projection-specific inhibition experiments, wild-type C57BL6/J mice were used, and AAVretro-hSyn-EBFP-Cre

(1.5×10^{12} gc/ml, Addgene) either 50 µL were injected into MeA or 300 µL were injected into NAc. For genotype specific inhibition experiments, *Slc17a6::Cre* or *Slc17a7::Cre* mice were used. All injections were bilateral and targeted to middle plCoA.

3.5.2.3. Surgeries for fluorescent tracing

For non-topographic anterograde tracing experiments, we bilaterally co-injected of mixed 50 nl AAVDJ-hSyn-FLEX-mRuby-T2A-SynEGFP (4.0×10^{12} gc/ml, Addgene, a gift from Byungkook Lim) and AAV5-EF1A-mCherry-IRES-Cre-WPRE (1.9×10^{12} gc/ml, UNC Vector Core) into middle plCoA (-1.8 AP, +/-2.9 ML, -5.95 DV) (Knowland et al., 2017). For topographic anterograde tracing experiments, we unilaterally injected 20 nl AAV8-hSyn-hChR2(H134R)-mCherry (2.1×10^{13} gc/ml, Salk GT3 Viral Vector Core) and AAV8-hSyn-hChR2(H134R)-eYFP (3.2×10^{13} gc/ml, Salk GT3 Viral Vector Core) into aplCoA (-1.4 AP, -2.8 ML, -5.95 DV) and pplCoA (-2.1 AP, -3.0 ML, -5.95 DV), counterbalancing region by fluorophore. For retrograde topographic tracing experiments, we unilaterally injected Red Retrobeads IX (Lumafluor) into either MeA (50 nl, -1.2 AP, -2.0 ML, -5.5 DV) or NAc (+1.1 AP, -1.35 ML, -4.5 DV), at volumes of 50 nl or 300 nl, respectively. For anterograde collateralization experiments, AAVretro-EF1A-IRES-Cre (1.3×10^{13} gc/ml, Addgene) into either MeA or NAc, and AAVDJ-EF1A-DIO-hChR2(H134R)-eYFP-WPRE-pA (4.03×10^{13} gc/ml, Salk GT3 Viral Vector Core) was injected into middle plCoA. For genotype-specific anterograde tracing experiments we injected 50 µl AAVDJ-Ef1a-DIO-ChR2(H134R)-eYFP-WPRE-pA into middle plCoA in Slc17a6::Cre or Slc17a7::Cre mice.

3.5.3. Behavioral assays

Mice had been handled for 5 days prior to experiments and acclimated to the room for an hour prior to testing. All behavioral experiments were performed during the dark period of the light/dark cycle at least an hour away from the switch between the two photoperiods. For all mice, Mice performed behavioral assays in the order: four-quadrant open field assay, open field test, elevated plus maze test. Not all mice were run in all assays, as elevated plus maze and open field tests were added after a significant proportion of four-quadrant data was collected at targeted sample sizes and mice had already been sacrificed.

For all optogenetic experiments, optical fibers (200 mm, 0.39 numerical aperture, Thorlabs) were epoxied to 2.5 mm stainless steel ferrules (Precision Fibre Products), and polished with a fiber optic polishing kit (Thorlabs) to achieve a minimum of 80% transmission. After surgical implantation, the ferrules protruding from the mouse's head were coupled to an ADR-800A 100 mW 473 nm laser (LaserCentury) via custom-made patch cables with a single rotary joint (Doric Lenses) between the mouse and laser. Laser intensity was set to 5-8 mW at the end of the patch cable. For inhibition experiments, all mice were injected intraperitoneally 60 minutes prior to the beginning of the behavioral trial with either sterile PBS vehicle or with clozapine-N-oxide (CNO) dihydrochloride (Hello Bio) dissolved in sterile PBS for a dosage of 2 mg/kg.

3.5.3.1. Four quadrant open field assay

The four-quadrant open-field task was performed as previously described (Root et al., 2014). In short, all behavioral assays took place in a four-quadrant open field chamber. Airflow was pumped into each quadrant via gas-mass flow controllers 150 mL/min (Cole-Parmer).

Airflow exited the chamber via a 1-inch outlet in the center of the chamber's floor covered by steel mesh, and the outlet was connected a vacuum line with a gas-mass controller set to 750 ml/min. The chamber was housed in the dark and illuminated from below by infrared lighting. A Basler A601FM camera (Edmund Optics) mounted above the chamber recorded videos of behavioral trials at 4 Hz, and custom software written in Labview (National Instruments) tracked the position of the mouse in real time for each frame. The symmetrical four-quadrant open field chamber was contained in a lightproof structure (0-10 lux) and illuminated by infrared lights, removing any potential spatial cues available to the animals with respect to the room or its surroundings. In optogenetic experiments, an additional 5 cm spacer was added to the chamber flush with the walls to raise their height for more naturalistic behavior, and an acrylic ceiling with a top with a circular opening 30.5 cm in diameter was added to prevent escape while allowing the fiber optic cable to move freely.

Mice were placed in the chamber for 25 min experiments and tested no more than once per day. The first 10 min served as a baseline test for spatial or temporal bias within the chamber during the trial, and no stimulus of any sort was provided. To ensure effects did not arise from ceiling or floor effects in the baseline or from a nonstandard baseline internal state, the mouse had to remain within the stimulus quadrant during the baseline test between ~20-30% of the time without significant immobility, thigmotaxis, or other signs of distress, or else the experiment was terminated, and the mouse was tested again on another day. The first 2 minutes of data after the stimulus was introduced were excluded from the analysis to reduce variance and account for novelty of the stimulus without affecting the overall valence of the behavioral response.

In optogenetic experiments, the laser was pulsed with 50 ms bins at 10 Hz, and there was a steep gradient from 1 to 10 Hz along the perimeter of the quadrant, increasing as proximity to

the corner of the quadrant decreased. Preliminary experiments in topographical stimulation animals identified no clear behavioral effects from the location of the stimulus quadrant itself (data not shown), and all other downstream stimulation experiments exclusively used the lower right quadrant for stimulation to simplify data analysis. The lasers were controlled by TTL modulation from custom Labview software synchronized to the video capture system.

For inhibition experiments, odor was applied by solenoid valves redirecting airflow through 100 mL glass bottles containing 1 μL of a pure odorant on a small piece of Kimwipes. Odorants used were either the previously-validated innately aversive 2,5-dihydro-2,4,5-trimethylthiazoline (BioSRQ) or the innately appetitive 2-phenylethanol (Sigma-Aldrich) on a small piece of Kimwipe (Root et al., 2014). All odors were presented in the lower-right quadrant, and all trials were spaced out with an hour between runs, during which vacuum was applied to the chamber. Odors and injection treatments were given in random, independent order within experimental groups.

3.5.3.2. Open field test

The open field is a square arena illuminated to 100-150 lux by ambient lighting. Mice were habituated to the room for at least an hour prior to testing, but otherwise had no prior experience in the arena prior to exposure. Mice were placed in the center of a square arena (27.3 × 27.3 × 20.3 cm, Med Associates) with four transparent plexiglass walls. Overall locomotion, immobility, and time spent in corners and center regions of arena during each epoch was analyzed for each mouse. Immobility was defined as movement under 0.5 cm/s for a period of at least 1 s, while the center was defined as the middle 13.7 × 13.7 cm square in the center of the arena and the corners as the corner regions that do not overlap with the center square in either

direction (25% of arena area for each region). For optogenetic experiments, mice were allowed to move freely throughout the arena for 25 min total, with 5-8 mW 473 nm light stimulation pulsed with 50 ms bins at 20 Hz, alternately delivered during the 5-10 min and 15-20 min epochs (OFF, ON, OFF, ON, OFF). For chemogenetic experiments, mice were allowed to freely move through the area for 10 min total.

3.5.3.3. Elevated plus maze

The arms of the elevated plus maze were 30.5 × 5.5 cm. The height of the closed arm walls was 15 cm. The maze was elevated 40 cm from the floor and was placed in the center of the behavior room away from other stimuli. Arms were illuminated to 0-10 lux, with infrared illumination. Mice were placed in the center of maze at the beginning of each trial. For optogenetic experiments, mice were allowed to move freely throughout the maze for 15 min total, with 5-8 mW 473 nm light stimulation pulsed with 50 ms bins at 20 Hz delivered during the 5-10 min epoch (OFF, ON, OFF). For chemogenetic experiments, mice were allowed to freely move through the area for 10 min total.

3.5.4. Histology

3.5.4.1. Non-RNAscope section preparation

All sacrifices were performed during the dark period of the light cycle. Animals were anesthetized prior to sacrifice via combined intraperitoneal injection of 150 mg/kg ketamine

(Zetamine, Vet One) and 15 mg/kg xylazine (AnaSed, AMRI Rensselaer). With the exception of animals used for single-cell sequencing studies, animals were subject to transcardial perfusion with 10 mL of sterile phosphate-buffered saline (PBS), followed by 10 mL 4% paraformaldehyde (PFA) solution. The brain was then extracted from the animal and placed into a 4% (PFA) solution in PBS for at least 36 hours until it was sectioned on a VT1000S vibratome (Leica). For tissue extracted for non-RNAscope histology, mice were transcardially perfused with 20 ml phosphate buffered saline (PBS) followed by 20 ml 4% paraformaldehyde (PFA) in PBS. All brains were extracted and post-fixed for at least 24 hours in 4% PFA. For tissue extracted for RNAscope, mice under 6 months of age were decapitated once unconscious and their brains were extracted into a square Peel-A-Way embedding mold (Polysciences) and embedded in OCT (Fisher), and then snap-frozen a dry-ice/isopentane slurry and stored at -80˚C until cryosectioning within a month of sacrifice.

Tissue was mounted in 5% agarose and sectioned sagittally on a vibratome for retrograde experiments, or sectioned coronally without mounting for all other non-RNAscope experiments. These sections were cut at 50 μm and stored in PBS before processing. All connectomic quantitation was performed on samples using epifluorescence without immunolabeling to avoid potential bias due to non-stoichiometric antibody binding, while all others were immunolabeled for visualization of viral targeting accuracy and collection of representative images. Immunolabeling of eYFP and other GFP-derived fluorophores was performed using goat anti-GFP primary antibodies (Abcam) and Alexa Fluor 488-conjugated anti-goat secondary antibodies (Invitrogen), while immunolabeling of mCherry and other DsRed-derived fluorophores used rabbit anti-DsRed primary antibodies (Takara) and Alexa Fluor 588-conjugated anti-rabbit antibodies (Invitrogen), all diluted 1:1000 in PBS-T. All non-RNAscope

sections were mounted on Superfrost Plus microscope slides (Fisher) and counterstained with Fluoromount-G containing DAPI (SouthernBiotech). Sections were stored long-term at 4˚C.

3.5.4.2. RNAscope fluorescence *in situ* hybridization

RNAscope sections were cut at 15 µm on a CM 1950 cryostat (Leica) and mounted on Superfrost Plus slides and stored at -80˚C until processing via RNAscope within a month of mounting. RNAscope was performed in an RNA-free environment according to manufacturer instructions using the Multiplex Fluorescent Reagent Kit v2 (Advanced Cell Diagnostics) (Wang et al., 2012). RNAscope was performed using the probes mm-Slc17a7 in the C2 channel, and mm-Slc17a6 in the C3 channel, dyed with Opal 520 and Opal 690 in a counterbalanced manner at 1:15,000 concentration to reduce background fluorescence and allow quantitation of unsaturated, clearly distinguishable puncta (Pratelli et al., 2022). Processed RNAscope sections were then mounted with Prolong Antifade Diamond (ThermoFisher) and stored long-term at 4˚C.

3.5.4.3. Fluorescence image acquisition

Non-RNAscope Images were acquired at 10X magnification with an VS120 slide scanner (Olympus), with settings held constant within experiments. Confocal fluorescence images for RNAscope were acquired on an SP8 (Leica) confocal laser scanning microscope using a 40x/1.30NA oil immersion objective. Serial Z-stack images were acquired using the LASX software at a thickness of 1 µm per Z stack, with 14-21 planes taken per image. Images were acquired with identical settings for laser power, detector gain, and amplifier offset for each set of counterbalanced probe-fluorophore combinations.

3.5.5. Sequencing data acquisition

3.5.5.1 Tissue extraction and sample preparation for single-cell sequencing

Once unconscious, mice animals were transcardially perfused with ice-cold, carbogen-bubbled (95% O2, 5% CO2), nuclease-free, 0.22 μm sterile-filtered artificial cerebrospinal fluid (ACSF) with a composition of 93 mM N-methyl-D-glucamine, 2.5 mM KCl, 1.2 mM NaH2PO4, 30 mM NaHCO3, 20 mM HEPES, 25 mM glucose, 5 mM sodium ascorbate, 2 mM thiourea, 3 mM sodium pyruvate, 13.2 mM trehalose, 12 mM N-acetyl-cysteine, 0.5 mM CaCl2, 10 mM MgSO4, and 93 mM HCl, at pH 7.3-7.4 (Tasic et al., 2018; Ting et al., 2014). Following transcardial perfusion, brains were immediately extracted and submerged into ice-cold carbogen-bubbled ACSF, with less than 5 minutes between the beginning of perfusion and final submersion after extraction. Brains were serially sectioned in ice-cold, carbogen-bubbled ACSF on a VT1000S vibratome (Leica) with polytetrafluoroethane-coated razor blades (Ted Pella) at 0.15 mm/sec and 100 Hz, dividing the whole cerebrum into 400 μm coronal slices. Target regions were microdissected from these slices under a stereomicroscope using a sterile blunt-end needle (22 gauge for CeA, ASt, and tail of striatum, 16 gauge for dorsal striatum). All regions were targeted using Paxinos & Franklin, 5th Edition, as reference.42 Extracted tissue samples were recovered in ice-cold, nuclease-free, 0.22 μm sterile-filtered cryoprotective nuclear storage buffer, composed of 0.32 M sucrose, 5 mM CaCl2, 3 mM magnesium acetate, 10 mM Trizma hydrochloride buffer (pH 8.0), 1 mM dithiothreitol, 0.02 U/μl SUPERase•In RNAse Inhibitor (Invitrogen), and 1X cOmplete Protease Inhibitor Cocktail with EDTA (Roche). Tissue was then snap frozen using a metal CoolRack M90 (Biocision) pre-chilled to -80˚C and stored at -80˚C until nuclear isolation. Following extraction of tissue regions of interest, remaining portions of sections were fixed in 4% paraformaldehyde and 4′,6-diamidino-2-phenylindole (DAPI) was

applied to sections at 1 µg/ml. After fixation and staining, sections were mounted and imaged on an VS120 slide scanner (Olympus). From these images, dissection accuracy was assessed for each region, and individual samples were only selected for downstream nuclear isolation if the extracted tissue fell entirely within the defined target regions.

Nuclear isolation procedures were adapted from multiple methods described previously (Krishnaswamy et al., 2016; Preissl et al., 2018) All procedures were performed on ice, and all solutions were ice-cold, nuclease-free, and 0.22 µm sterile-filtered. Cryopreserved tissue pieces were slow thawed by incubation at 4˚C for 1 hour prior to isolation. Tissue pieces were then pooled and resuspended in nuclear isolation medium composed of 0.25 M sucrose, 25 mM KCl, 5 mM MgCl2, 10 mM Trizma hydrochloride buffer (pH 7.4), 1 mM dithiothreitol, 0.04 U/µl RNasin Plus RNAse Inhibitor (Promega), 1X cOmplete Protease Inhibitor Cocktail with EDTA (Roche), and 0.1% Triton-X. The pooled tissue pieces in nuclear isolation medium were transferred to a 2 mL Dounce tissue grinder. Tissue was homogenized by 5 strokes from the loose pestle and 15 followed by the tight pestle, and the resulting homogenate was filtered through a 40 µm Flowmi cell strainer (Bel-Art) into a 1.5 ml Lo-Bind tube (Eppendorf). The homogenate was then centrifuged with a swinging bucket rotor at 4˚C and 1000 x g for 8 minutes. Nuclei were then washed with nuclear flow buffer composed of DPBS with 1% bovine serum albumin, 1 mM dithiothreitol, and 0.04 U/µl RNasin Plus RNAse Inhibitor (Promega) and centrifuged at 4˚C and 500 x g for 5 minutes, which was subsequently repeated. Nuclei were finally resuspended in nuclear flow buffer containing 3 µm DRAQ7 (Cell Signaling Technology) and again filtered through a 40 µm Flowmi cell strainer into a 5 ml round-bottom polystyrene tube. Each isolation took under 45 minutes to perform, from homogenization to final suspension.

3.5.5.2. Fluorescence-activated nuclei sorting (FANS)

Fluorescence-activated nuclei sorting (FANS) was carried out on a FACSAria II SORP (BD Biosciences) using a 70 μm nozzle at 52 PSI sheath pressure. For FANS, debris was first excluded by gating on forward and side scatter pulse area parameters (FSC-A and SSC-A), followed by exclusion of aggregates (FSC-W and SSC-W), and finally gating for nuclei based on DRAQ7 fluorescence (APC-Cy7). Nuclei were successively sorted into 1.5 ml LoBind tubes (Eppendorf) under the purity sort mode. The tube contained 10X RT master mix without RT Buffer C. 16,000 total nuclei were targeted for downstream processing, and to account for cytometer errors and subsequent loss of nuclei, 21,000 were sorted into the tube. Nuclei were then immediately processed for snRNA-seq. FANS conditions were optimized for isolation of debris-free nuclei using the LIVE/DEAD Viability/Cytotoxicity Kit for Mammalian Cells (Molecular Probes), adding to the final suspension according to manufacturer instructions and examining on a hemocytometer using an EVOS FL Cell Imaging System (Thermo Fisher) for enrichment of ethidium homodimer-1-positive nuclei and the absence of Calcein AM-labeled cellular debris.

3.5.5.3. Tissue extraction and sample preparation for spatial transcriptomics

Mice were euthanized with CO2 followed by decapitation, either in the dark or in the light. Brain hemispheres were collected and placed in OCT and then flash frozen in isopentane in liquid nitrogen. One hemibrain from each mouse was cryosectioned at -18°C sagittally to a

thickness of 10 mm (~2.8 mm from the midline) using a standard Leica CM1860 cryostat and processed according to the recommended protocols (Tissue optimization: CG000240 Visium 10X Genomics; Gene expression: CG000239). The tissue was immediately mounted on a Visium spatially barcoded slide (10X Genomics). The tissue was covered with OCT and kept at -80 degrees C until it was cryosectioned again starting at the same position to a thickness of 10mm and mounted onto a Superfrost plus microscope slide (Fisherbrand) for staining. Each section covered approximately 80% of the 5,000 total spots within their fiducial frame. Slides were stored at -80˚C until use.

3.5.6. Library preparation

3.5.6.1. Library preparation for single nucleus sequencing

Nuclear suspensions were converted into barcoded snRNA-seq libraries using the Chromium Next GEM Single Cell 3' v3.1 Reagent Kits v3.1 Single Index (10X Genomics). Library preparation for both assays was performed in accordance with the manufacturer's instructions. 10,000 nuclei were targeted during each snRNA-seq library preparation run. 10X libraries were first sequenced at low depth on a NextSeq 550 Sequencing System (Illumina) to estimate quality and number of nuclei for each library, followed by deep sequencing on a NovaSeq 6000 Sequencing System. All runs were performed using 2 x 100-bp paired-end reads, outputting data in 28/8/91-bp read format for snRNA-seq runs. All sequences were demultiplexed using bcl2fastq.

3.5.6.2. Library preparation for Visium spatial transcriptomics

Visium spatial gene expression slides and reagents were used according to the manufacturer instructions (10X Genomics). Each capture area was 6.5mm x 6.5 mm and contained 5,000 barcoded spots that were 55 μm in diameter (100 μm center to center between spots) provide an average resolution of about 1 to 10 cells per spot. Optimal permeabilization time was measured at 24 min. Libraries were prepared according to the Visium protocol (10X Genomics) and sequenced on a NovaSeq4 (Illumina) at a sequencing depth of 182 million read pairs. Sequencing was performed with the recommended protocol in a 28/10/10/100-bp read format. H&E (Hematoxylin, Thermo; Dako bluing buffer, Dako; Eosin Y, Sigma) staining and image preparation was performed according to the Visium protocol. H&E-stained sections were imaged using a Nanozoomer slide scanner (Hamamatsu) Spatial gene expression assay was performed according to the protocol CG000239.

3.5.7. Statistical Analysis

All statistical details can be found in the figure legends. Sample sizes for behavioral studies were chosen based on past optogenetic studies for each behavior, which had used 6-15 animals per group. Blinding experimenters was not possible for behavioral, imaging, or sequencing experiments, given familiarity with subjects, but manual quantitation for connectivity experiments was performed blinded to group with random assignment. All statistical tests were performed in R (v4.2.3) unless otherwise specified. All statistical tests were performed with two tails. Group comparisons were made using two-way analysis of variance (ANOVA) followed by Bonferroni post hoc tests, except where otherwise specified. All behavioral experiments were

performed by multiple experimenters across multiple cohorts each composed of multiple litters, with littermates distributed across control and treatment groups, with all such cohorts yielding similar results (data not shown), and topography stimulation experiments were performed across multiple facilities and institutions. Numbers of mice used for all non-sequencing experiments are reported within the relevant figures, figure legends, and the text.

3.5.8. Behavioral data analysis

Behavioral metrics (i.e. performance index, port distance, center distance, open field time, and total distance) were calculated on sets of coordinates created by identifying the centroid of the mouse in real time at 4 Hz using custom Labview code and outputting the centroid's coordinates for each frame. The mouse was automatically identified by taking a background greyscale image of the behavioral assay's environment at the beginning of each trial and detecting shapes of a minimum size deviating from the background image by a specific threshold. The centroid was then determined by automated generation of a bounding box for the mouse in each frame in real time, and recording the coordinate of the centroid of this rectangle.

3.5.8.1. Four-quadrant task data analysis

Mice were tested as previously described.[8] Mice were placed in the chamber for 25 min experiments and tested no more than once per day. The first 10 min served as a baseline test for spatial or temporal bias within the chamber during the trial, and no stimulus of any sort was provided, while the last 15 min were the test of the manipulation. 15 minutes was chosen to

balance time courses of odor responses observed in previous experiments, where appetitive odors tend to yield initial responses that decay, while aversive odors tend to yield responses that grow in magnitude over time. To ensure effects did not arise from ceiling or floor effects in the baseline or from a nonstandard baseline internal state, the mouse had to remain within the stimulus quadrant during the baseline test between ~20-30% of the time or else the experiment was terminated, and the mouse was tested again later. The first 2 minutes of data after the stimulus was introduced were excluded from the analysis to reduce variance and account for novelty of the stimulus without affecting the overall valence of the behavioral response, and the last minute of data was excluded to ensure no minor differences in frames captured could affect analysis. For chemogenetic odor response silencing experiments, animals with vehicle odor responses below an absolute value of 0.1 were excluded from experiments to avoid false negatives from attempting to silence a response that was not observed at baseline, which applied to less than a quarter of overall animals tested across experimental conditions. Performance index represents the percent difference from chance occupancy in the manipulation quadrant, calculated as PI = (P - 25) / 0.25*;* where P is the percentage of time the animal spends in the manipulation quadrant. Mean port distance represents the mean distance of each point to the deepest point into the manipulation quadrant observed at baseline.

3.5.8.2. Open field test data analysis

For elevated plus maze analysis, all chemogenetic inhibition trials used the entirely of the 10 min test length as a single period, while optogenetic stimulation trials used the mean of the three "OFF" periods to compare to the mean of the two "ON" periods. Three metrics of interest were

calculated. Center time was calculated as the proportion of time spent in the middle square of the open field comprising 50% of its total area. Corner time was calculated as the proportion of time spent in the corner squares bounded by the walls and the lines bounding the center region. Time immobile was calculated as the proportion of time when the animal moved less than 1 cm/s for at least a one-second period. Location of the open field and bounding regions was kept constant from trial to trial by registering the apparatus to a bounding box with the same top-down dimensions, and every measured centroid outside of the registered region resulting from shadows cast and other artifacts was interpolated between the closest points before and after within the region.

3.5.8.3. Elevated plus maze data analysis

For elevated plus maze analysis, all chemogenetic inhibition trials used the entirely of the 10 min test length as a single period, while optogenetic stimulation trials used the mean of the two "OFF" periods to compare to the "ON" period. Three metrics of interest were calculated. Time in the open arms was calculated as the proportion of time spent in the open arms compared to the whole period of interest and did not include time in the center between the two arms. Open arm entries measures number of episodes where the centroid is observed outside of the bounds of the closed arms or the center region, without any minimum time or distance out onto the open arms. Finally, distance was simply calculated as the distance traveled during each period of interest. Location of open and closed arms was kept constant from trial to trial by registering the apparatus to a cross-shaped bounding box with the same top-down dimensions, and every measured centroid outside of the registered region due to factors like the mouse leaning over the edge of the open arms, among others, was interpolated between the closest points before and after within the region.

3.5.9. snRNA-seq data analysis

3.5.9.1. Sequence alignment

All samples were processed using Cell Ranger (v5.0.0) (Zheng et al., 2017). All processing was done by using Cell Ranger's implementation of STAR to align sample sequence reads to their pre-built mm10 vm23/Ens98 reference transcriptome index 2020-A, with predicted and non-validated transcripts removed. All sequencing reads were aligned to both the exons and the introns present in the index. Samples were demultiplexed to produce a pair of FASTQ files for each sample. FASTQ files containing raw read sequence information were aligned to the Cell Ranger index using the cellranger count command with --chemistry SC3Pv3 and --include-introns flags enabled. Cell Ranger corrected sequencing errors in cell barcodes to pre-defined sequences in the 10X v3 single-index whitelist within Hamming distance 1. PCR duplicates were removed by selecting unique combinations of corrected cell barcodes, unique molecular identifiers, gene names, and location within the transcript. Raw unfiltered count data was read into R (v4.2.1) using the Seurat package (v4.2.0) (Satija et al., 2015; Butler et al., 2018; Stuart et al., 2019; Hao et al., 2021). The final result of the pipeline was a barcode x gene expression matrix for further analysis downstream.

3.5.9.2. Quality control

We used the raw, unfiltered matrix output from CellRanger as the input to the beginning of the pipeline. However, to apply a more stringent filter, the emptyDrops dirichlet-multinomial model from the DropletUtils package (v1.10.2) was applied to each library individually (Griffiths

et al., 2018; Lun et al., 2019). Droplets with less than 100 total counts were used to construct the ambient RNA profile and an FDR threshold below 0.001 was used to select putatively occupied droplets. All barcodes with greater than 1000 UMIs were further assumed non-empty. Most quality filtration choices were heavily influenced by the recommendations presented in pipeComp (Germain et al., 2020). All quality control was performed on each library individually prior to merging. Minimal quality filtering for each barcode was performed by setting a floor of 1000 features per barcode for downstream inclusion to ensure the dataset is entirely composed of high-quality nuclei. Next, to remove highly likely multiplet barcodes, barcodes were filtered out if their count depth was more than 5 median absolute deviations above the median count depth. Barcodes were then removed if their proportion of ribosomal or mitochondrial reads was more than 5 interquartile ranges above the 75th percentile (median absolute deviations cannot be used, because in many cases the median absolute deviation is 0). Heterotypic doublets were identified by creating simulated artificial doublets in scDblFinder (v1.4.1), which uses a DoubletFinder-like model to remove barcodes similar to simulated doublets, with an assumed doublet rate of 1% per 1000 nuclei in the library (McGinnis et al., 2019; Germain et al., 2021). Scater (v1.18.3) was used to produce initial diagnostic tSNE and UMAP plots for visually checking the influence of each above metric on the structure of the data (McCarthy et al., 2017).

3.5.9.3. Data processing/transformation

All datasets (initially for all nuclei and again for selected subclusters) were formatted into Seurat objects (v4.0.0), merged, and then normalized and transformed individually using the SCTransform (v2) variance stabilizing transform, which performs best according to prior

comparisons in pipeComp (Germain et al., 2020; Hafemeister and Satija, 2019; Choudhary and Satija, 2022). Following the merge, all genes expressed in 3 or fewer nuclei of interest were removed from analysis. SCTransform was run returning Pearson residuals regressing out mitochondrial gene expression, retaining the top 5000 highly variable features. Dimensionality of the dataset was first reduced using principal component analysis, as implemented in Seurat's RunPCA function, retaining the top 50 principal components (Jolliffe and Cadima, 2016). Principal components were selected for downstream use by using the lower value of either the number of principal components where the lowest contributes 5% of standard deviation and all cumulatively contribute 90% of the standard deviation, or the number of principal components where the percent change in variation between the consecutive components is lower than 0.1%. These principal components were used as input to the non-linear tSNE and UMAP dimensionality reduction methods as implemented by Seurat's RunTSNE and/or RunUMAP functions with 1000 epochs at 0.5 minimum distance, with otherwise default settings (van der Maaten and Hinton, 2008; McInnes et al., 2018; Becht et al., 2019).

Clusters were identified via Leiden clustering in latent space using the previously selected principal components as input (Traag et al., 2019). Optimal clustering resolution was identified in a supervised manner using clustree, finding the highest resolution for each dataset where clustering remains stable (Zappia and Oshlack, 2018). Cluster annotation was performed in a semi-hierarchical semi-supervised manner, where known marker genes were first used to separate all nuclei into neuronal and non-neuronal cell types, and then these cells were re-analyzed and neurons were respectively separated into glutamatergic and GABAergic neurons, while non-neuronal cells were separated into astrocytes, microglia, macrophages, oligodendrocytes and their precursors/lineage, mural cells, endothelia, and vascular

leptomeningeal cells. This lower level of cells was then reanalyzed, and novel cell types were then identified within these more-granular known cell types. For identification of known cell types, clusters expressing the same marker genes were manually merged to ensure all cells of a known type were analyzed together, which did not occur for novel cell type identification. Clusters resulting from specific difference in nuclei quality instead of true changes in gene expression (i.e. markedly lower mean UMI/features per nucleus, increased ribosomal/mitochondrial gene expression proportion) were removed prior to final clustering. Relationships between cell type proportion and plCoA zone were quantitated using propeller, treating each library as an independent replicate (Phipson et al., 2022).

3.9.5.4. Differential expression

Marker genes were identified using Wilcoxon rank-sum test as implemented by the FindConservedMarkers function in Seurat, using the region as a grouping variable. Genes were accepted as differentially expressed with a minimum proportion cutoff at 0.1 and minimum fold change at 1.5-fold (log2-fold change of 0.585), with a p-value cutoff of 0.01 after Bonferroni correction. To identify genes differentially expressed by region, single-cell values were converted to pseudo-bulk by batch using the run_de function as implemented in the Libra package (v1.0.0) using default settings with a minimum proportion cutoff at 0.1, and tested for differential expression using edgeR's likelihood ratio test (Squair et al., 2021). Zone-specific gene expression was identified by comparing batches from the two isolated zones.

3.5.10. Analysis of Spatial Transcriptomics Data

3.5.10.1. Sequence and image alignment

All samples were processed using Space Ranger (v1.3.0). All processing was done by using Space Ranger's implementation of STAR to align sample sequence reads to their pre-built mm10 vm23/Ens98 reference transcriptome index 2020-A, with predicted and non-validated transcripts removed, as in snRNA-seq data alignment. Samples were demultiplexed to produce a pair of FASTQ files for each sample. FASTQ files containing raw read sequence information were aligned to the index using the spaceranger count command. Space Ranger corrected sequencing errors in cell barcodes to pre-defined sequences in the single-index whitelist within Hamming distance 1. PCR duplicates were removed by selecting unique combinations of corrected cell barcodes, unique molecular identifiers, gene names, and location within the transcript. Imaging data was processed using automatic fiducial alignment and tissue detection on a brightfield input.

3.5.10.2. Data processing/transformation

We used the image-filtered matrix output from Space Ranger as the input to the beginning of the pipeline. In a similar manner to snRNA-seq data, all datasets were formatted into Seurat objects (v5.0.0), merged, and then normalized and transformed using the SCTransform (v2) variance stabilizing transform (Hafemeister et al., 2019). SCTransform was run returning Pearson residuals regressing out mitochondrial gene expression, retaining the top 5000 highly variable features. Dimensionality of the dataset was first reduced using principal component analysis, as implemented in Seurat's RunPCA function, retaining the top 50 principal

components, all of which were used in downstream processing. These principal components were used as input to the non-linear tSNE and UMAP dimensionality reduction methods as implemented by Seurat's RunTSNE and/or RunUMAP functions with 1000 epochs at 0.2 minimum distance, with otherwise default settings. Clusters were identified via Leiden clustering in latent space using all 50 principal components as input. Optimal clustering resolution was identified in a supervised manner using clustree, finding the highest resolution for each dataset where clustering remains stable, choosing a resolution of 0.7. Cluster annotation was performed in a semi-supervised manner, observing where in captured plCoA regions each cluster's spots localized to. For clusters that could not be annotated from spatial location alone (e.g. OLG), marker genes were examined to determine the molecular identity of relevant spots. Spatial data was projected onto neuronal molecular cell types from snRNA-seq data and cell type likelihood was predicted using Seurat's FindTransferAnchors and TransferData functions using snRNA-seq data as a reference and plCoA spatial data as the query, using all 50 PCs. Prediction of a minority of subtypes failed, likely due to low abundance in tissue and/or due to mediolateral spatial differences, alluded to in a separate study, causing the section not to intersect with the part of the tissue containing the relevant neuronal subtypes (Costantini et al., 2020). Glutamatergic and GABAergic molecular subtype likelihoods were predicted separately to remove noise and increase modeled prediction confidence.

3.5.11. Imaging fluorescence analysis

3.5.11.1. Registration and localization

Histology for all animals and samples was examined prior to inclusion. Localization within the coronal plane was determined by registering the coronal slice to the Allen Brain Atlas via the ABBA plugin, using elastix to sequentially perform affine and spline registration of the DAPI channel of the slice to the Nissl channel of the atlas (Klein et al., 2010; Shamonin et al., 2013). The region of interest was then compared to the Paxinos and Franklin atlas to confirm localization, and find the region's anteroposterior distance from bregma (Paxinos and Franklin, 2008). This combined method was used because sections cannot be accurately registered to the Paxinos and Franklin atlas due to low Z-resolution, while the Allen Brain Atlas lacks information about anteroposterior distance from bregma. Exclusion based on histology would occur when the majority of the intervention fell outside of the region of interest. Due to these differences, individual representative images use the individually registered Allen Reference Atlas schematics with the comparable Paxinos and Franklin anteroposterior coordinates noted, while consolidated targeting schematics use the Paxinos and Franklin atlas for visualization.

3.5.11.2. Quantification of histological fluorescence

In anterograde tracing experiments, output quantification was performed based on background-corrected total fluorescence. For all non-collateralization anterograde experiments, fluorescence intensities were quantified using FIJI (v2.9.0) throughout the whole brain in a series of evenly-space 50 µm coronal sections, manually segmenting by region with all settings held constant within experiments (Scheindelin et al., 2012). For collateralization experiments, we exclusively examined fluorescence in the MeA and NAc. We calculated background-corrected total fluorescence using the equation $F_{total} = ID - (Area \times F_{background})$, where F_{total} is the

background-corrected total fluorescence, ID is the integrated density, and $F_{background}$ is the mean background fluorescence measured from four randomly selected areas per section not receiving input from plCoA. Overall proportion was calculated by taking the sum of background-corrected fluorescence values across all sections for a given region and dividing it by the sum of all background-corrected values. For retrograde experiments, we quantified number of cells using the Cell Counter plugin (v3.0.0) in FIJI. The sagittal brain slices containing the plCoA were then compared to Paxinos and Franklin, 5th Edition to count the number of cells found per distance away from bregma from -1.3 to -2.5 mm in increments of 100 μm (Paxinos and Franklin, 2008). At least two sections per region per animal were analyzed. Representative images were produced from slide scanner image output, with background subtraction and uniform brightness and contrast thresholds applied equally to all fluorescent channels in FIJI to avoid potential distortion of visible fluorescence levels.

3.5.11.3. Quantification and analysis of RNAscope images

RNAscope images were analyzed as previously described (Mills et al., 2024). Images were opened in FIJI and individual Z-planes encompassing the entire ROI were selected from each image for further image processing. Background was subtracted from all channels in all images using the subtract background feature. Masks of each region were drawn based on the mouse brain atlas, and images were then saved as 8bit TIFFs for further cell and puncta identification in CellProfiler (v4.2.4) (Paxinos and Franklin, 2008; Carpenter et al., 2006). Image TIFFs were run through CellProfiler using an optimized version of the CellProfiler Colocalization pipeline. The pipeline was optimized to identify DAPI labelled cells (15-45 pixels

in diameter) and then subsequently identify mRNA puncta (4-10 pixels in diameter). DAPI cell detection was further restricted by shrinking DAPI ROIs by 1 pixel. Puncta overlapping with DAPI-identified cells (using the relate objects module) were considered for analysis to assess the level of mRNA expression per cell. To determine if cells were expressing mRNA, a threshold of 5 or more puncta within twice the diameter of nucleus centered over the nucleus was used (McCullough et al., 2018). Total number and density of *Slc17a6*+ and *Slc17a7*+ cells in each region of interest were calculated from CellProfiler .csv outputs using custom R scripts.

3.6. Acknowledgments

We thank the entire Root lab for helpful discussion and support. We thank B. Lim for provision of the Slc17a6-IRES-Cre mouse strain and AAVDJ-hSyn-Flex-mRuby-T2A-SynEGFP virus. We thank G. Pekkurnaz, N. Spitzer, and M. Pratelli for reagents and facilities support. We also thank C. O'Connor and L. Boggeman at the Salk flow cytometry core, and N. Hah at the Salk next-generation sequencing core. We thank D. Jimenez for assistance with histology and colony management. This publication includes data generated at the UC San Diego IGM Genomics Center utilizing an Illumina NovaSeq 6000 that was purchased with funding from a National Institutes of Health SIG grant (#S10 OD026929). J.R.H. is a National Defense Science and Engineering Fellow supported by the Department of Defense, K.M.T. is an HHMI Investigator and the Wylie Vale chair at the Salk Institute for Biological Studies, and C.M.R. is a Hellman Fellow. This work was generously supported by the National Defense Science and Engineering Fellowship (J.R.H.), CIHR Postdoctoral Fellowship (F.M.), JPB Foundation, the PIIF, PNDRF, JFDP, New York Stem Cell Foundation, Klingenstein Foundation, McKnight Foundation, Salk Institute, Howard Hughes Medical Institute, Clayton Foundation, Kavli

Foundation, Dolby Family Fund (K.M.T.), the Hellman Fellowship (C.M.R.), and the National Institutions of Health, via grants through the NIA (RF1AG061831-01S1, P.A.D.), NIMH (K99MH121563-02, F.M.; R01MH115920-03 and R37MH102441, K.M.T.), NIDDK (DP2DK102256-01S1, K.M.T.), and NCCIH (DP1AT009925-04, K.M.T.), and the NIDCD (R00DC014516-05 and R01DC018313-01A1, C.M.R.).

Chapter 3, in full, is a reprint of the material as it was prepared for simultaneous submission to Cell and Neuron. Howe, J.R., Chan, C.L., Blanquart, M., Lemieux, M.E., Mills, F., Tye, K.M., Root, C.M. Control of innate olfactory valence by segregated cortical amygdala circuits. In preparation. The dissertation author was the primary investigator and the first author on the paper.

3.7. Appendix

Figure S3.1. Targeting of plCoA neurons for optogenetic stimulation.

(A) Histologically verified placements for optic fiber implants (bars) and viral injection sites (circles) in wild type animals infected with AAV-hSyn-ChR2-mCherry (blue) or AAV-hSyn-eYFP (green) in topographic optogenetic cell body stimulation experiments.

(B) Same as (A), but for cell-type specific optogenetic cell body stimulation experiments for *Slc17a7::Cre* (top) and *Slc17a6::Cre* (bottom) animals infected with AAV-DIO-EF1A-ChR2-eYFP (blue) or AAV-EF1A-DIO-eYFP (green).

(C) Respective placements for fiber implants (bars) and injection sites (plCoA-NAc, circles; plCoA-MeA, diamonds) in wild-type animals infected with AAV-hSyn-ChR2-mCherry (blue) or AAV-hSyn-eYFP (green) in projection-specific optogenetic axon terminal stimulation experiments.

n denotes number of mice per group batched across 4-quad, elevated plus maze, and open field test experiments, exceeding n values for individual experiments due to behavioral cohort design (see STAR Methods). Relevant regions are highlighted in grey and outlined: plCoA (red), NAc (purple, only in C), and MeA (pink, only in C). All mouse brain sections reproduced from Paxinos and Franklin, 5th Edition, and numbers below all images denote its anterior-posterior distance from bregma in this atlas (Paxinos and Franklin, 2008). All scale bars, 500 μm.

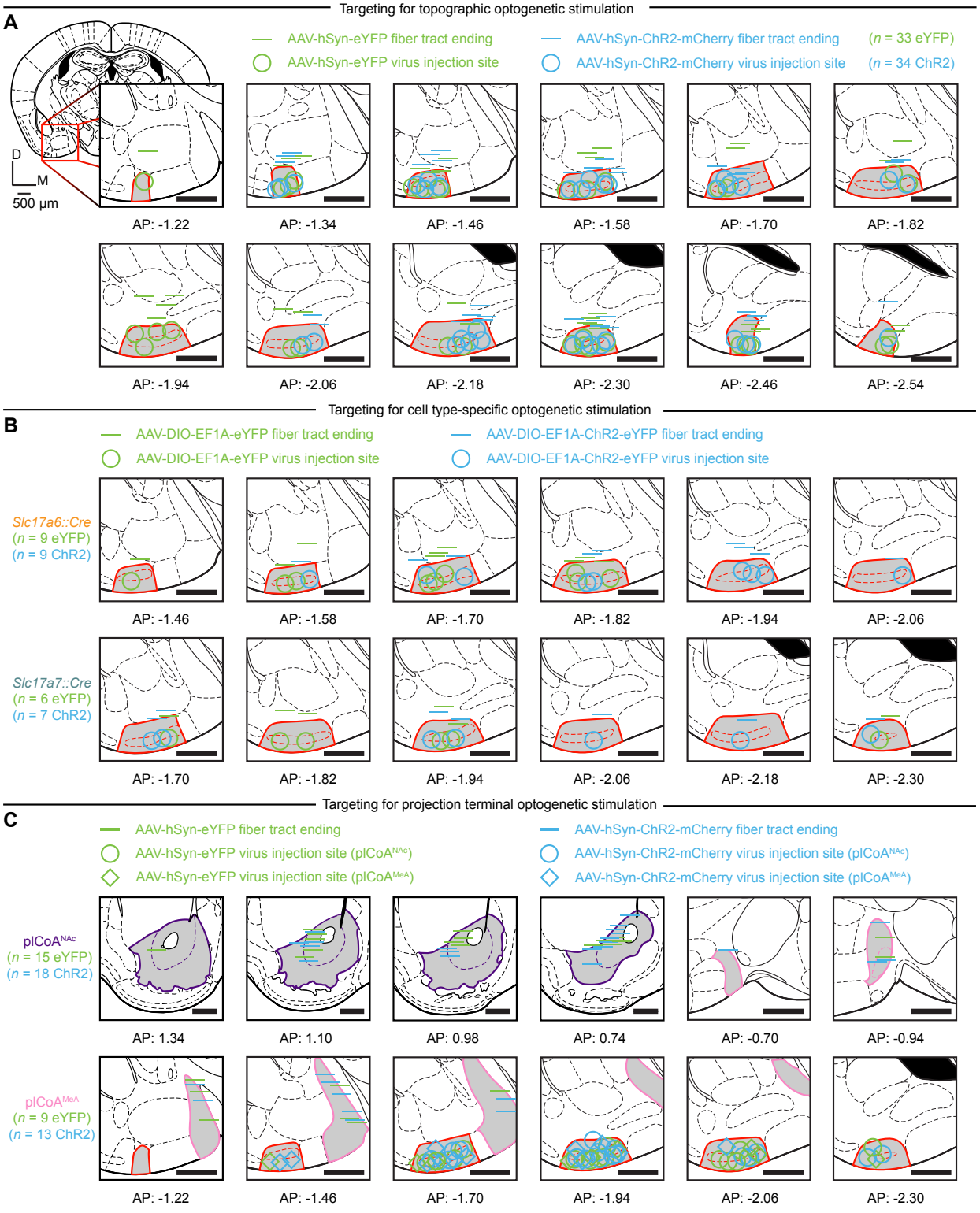
Targeting for topographic optogenetic stimulation
A
AAV-hSyn-eYFP fiber tract ending
AAV-hSyn-eYFP virus injection site
AAV-hSyn-ChR2-mCherry fiber tract ending
AAV-hSyn-ChR2-mCherry virus injection site
(n = 33 eYFP)
(n = 34 ChR2)
D
M
500 μm
AP: -1.22
AP: -1.34
AP: -1.46
AP: -1.58
AP: -1.70
AP: -1.82
AP: -1.94
AP: -2.06
AP: -2.18
AP: -2.30
AP: -2.46
AP: -2.54
Targeting for cell type-specific optogenetic stimulation
B
AAV-DIO-EF1A-eYFP fiber tract ending
AAV-DIO-EF1A-eYFP virus injection site
AAV-DIO-EF1A-ChR2-eYFP fiber tract ending
AAV-DIO-EF1A-ChR2-eYFP virus injection site
Slc17a6::Cre
(n = 9 eYFP)
(n = 9 ChR2)
AP: -1.46
AP: -1.58
AP: -1.70
AP: -1.82
AP: -1.94
AP: -2.06
Slc17a7::Cre
(n = 6 eYFP)
(n = 7 ChR2)
AP: -1.70
AP: -1.82
AP: -1.94
AP: -2.06
AP: -2.18
AP: -2.30
Targeting for projection terminal optogenetic stimulation
C
AAV-hSyn-eYFP fiber tract ending
AAV-hSyn-eYFP virus injection site (plCoA^NAc)
AAV-hSyn-eYFP virus injection site (plCoA^MeA)
AAV-hSyn-ChR2-mCherry fiber tract ending
AAV-hSyn-ChR2-mCherry virus injection site (plCoA^NAc)
AAV-hSyn-ChR2-mCherry virus injection site (plCoA^MeA)
plCoA^NAc
(n = 15 eYFP)
(n = 18 ChR2)
AP: 1.34
AP: 1.10
AP: 0.98
AP: 0.74
AP: -0.70
AP: -0.94
plCoA^MeA
(n = 9 eYFP)
(n = 13 ChR2)
AP: -1.22
AP: -1.46
AP: -1.70
AP: -1.94
AP: -2.06
AP: -2.30

Figure S3.2. Behavioral effects of topographic plCoA stimulation are limited to valence alone.

(A) Behavioral paradigm for optogenetic stimulation in the open field test.

(B-D) Optogenetic stimulation-induced change in time spent (B) and number of entries (C) into the open arms, as well as distance traveled (D) in the elevated plus maze is not correlated to anteroposterior axis position in plCoA.

(E-G) Time series (left) and overall period (right) effects for optogenetic stimulation of aplCoA neurons in the elevated plus maze. Photostimulation of aplCoA neurons does not induce a significant change in time spent (E) and number of entries (F) into the open arms, as well as distance traveled (G) in the elevated plus maze.

(H-J) Time series (left) and overall period (right) effects for optogenetic stimulation of pplCoA neurons in the elevated plus maze. Photostimulation of pplCoA neurons does not induce a significant change in time spent (H) and number of entries (I) into the open arms, as well as distance traveled (J) in the elevated plus maze.

(K) Behavioral paradigm for optogenetic stimulation in the open field test.

(L-N) Optogenetic stimulation-induced change in time spent in the center (L) and corners (M), as well as distance traveled (N) in the open field test is not correlated to anteroposterior axis position in plCoA.

(O-Q) Time series (left) and overall period (right) effects for optogenetic stimulation of aplCoA neurons in the open field test. Photostimulation of aplCoA neurons does not induce a significant change time spent in the center (O) and corners (P), as well as distance traveled (Q) in the open field test.

(R-T) Time series (left) and overall period (right) effects for optogenetic stimulation of pplCoA neurons in the open field test. Photostimulation of pplCoA neurons does not induce a significant change time spent in the center (R) and corners (S), as well as distance traveled (T) in the open field test.

All “ON” and “OFF” comparisons in bar graphs and linear regressions are on a per 5-minute basis. (B-D, L-M) Least-squares linear regression +/- 95% confidence interval. (E-J, O-T) Mean +/- s.e.m. Abbreviations: ns, not significant.

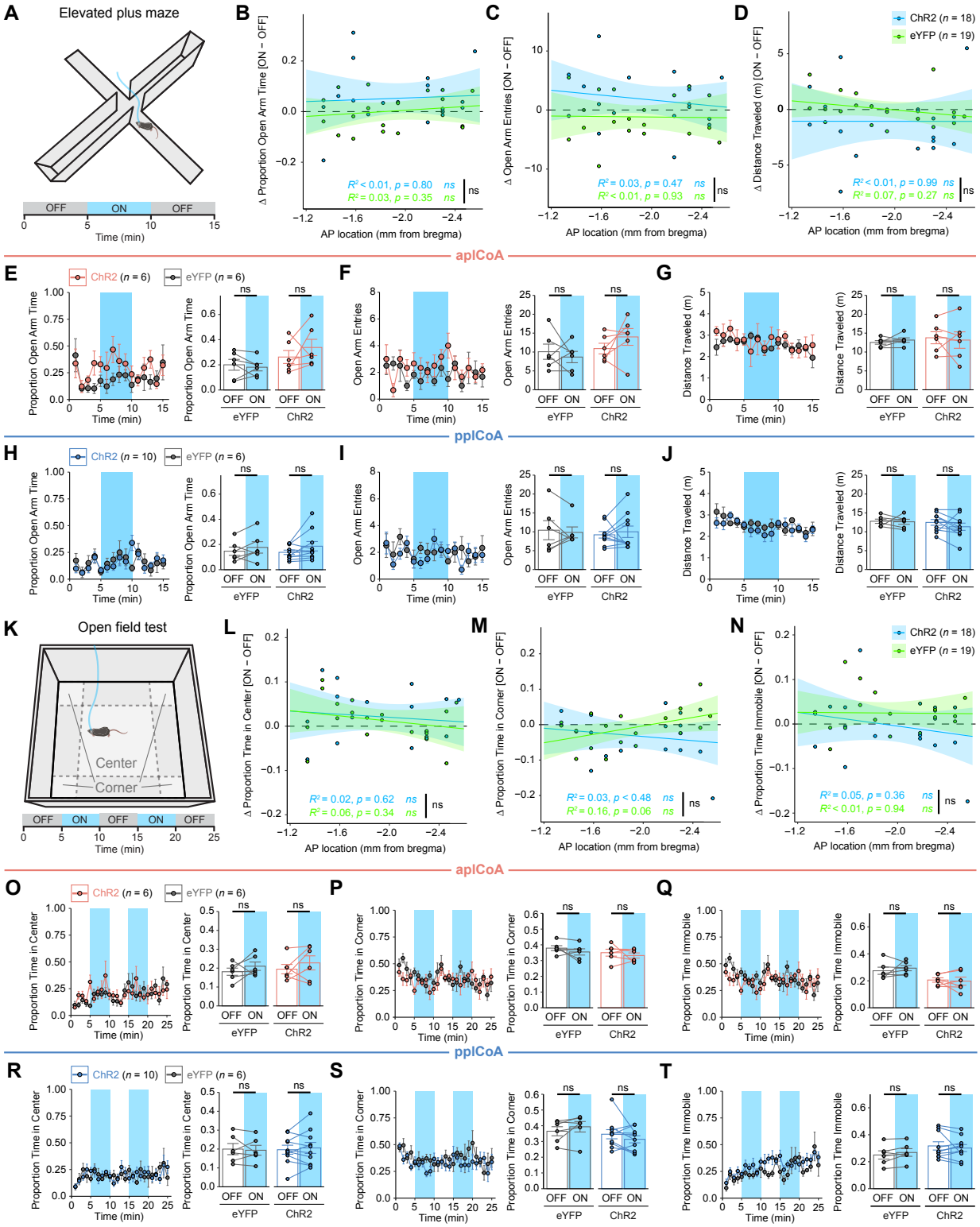
A
Elevated plus maze
OFF
ON
OFF
Time (min)
B
Δ Proportion Open Arm Time [ON − OFF]
AP location (mm from bregma)
C
Δ Open Arm Entries [ON − OFF]
AP location (mm from bregma)
D
ChR2 (n = 18)
eYFP (n = 19)
Δ Distance Traveled (m) [ON − OFF]
AP location (mm from bregma)
apICoA
E
ChR2 (n = 6)
eYFP (n = 6)
Proportion Open Arm Time
Time (min)
eYFP
ChR2
F
Open Arm Entries
G
Distance Traveled (m)
pplCoA
H
ChR2 (n = 10)
eYFP (n = 6)
I
J
K
Open field test
Center
Corner
L
Δ Proportion Time in Center [ON − OFF]
M
Δ Proportion Time in Corner [ON − OFF]
N
Δ Proportion Time Immobile [ON − OFF]
O
Proportion Time in Center
P
Proportion Time in Corner
Q
Proportion Time Immobile
R
S
T

Figure S3.3. Additional information and quality-control for single-nucleus sequencing experiments.

(A) Representative images of tissue microdissection sites from aplCoA and pplCoA following extraction and DAPI staining (blue). Scale bars, 500 μm.

(B) Location of all tissue sample sites for used for snRNA-seq or snATAC-seq, color coded by plCoA zone (n = 3 pools per zone for snRNA-seq, 2 per zone for snATAC-seq, 4-11 sections per pool). Scale bars, 500 μm.

(C) Common gating strategy for FANS sorts for snRNA-seq in a representative sample.89 Far left, morphology gate on forward and side scatter area excludes likely debris. Middle left, forward scatter gate excludes nuclear doublets with high forward scatter width. Middle right, side scatter gate excludes nuclear multiplets with high side scatter width. Far right, stoichiometric DRAQ7+ fluorescence allows enrichment of single nuclei and exclusion of debris and multiplets.

(D) Validation of nuclear enrichment after FANS. Ethidium homodimer-1 (EthD-1, red) labels nuclei on a hemocytometer after sorting, with an absence of non-nuclear, EthD-1-negative debris. Scale bar, 100 μm.

(E) Absolute number and proportion of snRNA-seq nuclei passing quality control filters from each replicate in each plCoA zone (n = 27,726 in aplCoA, 19,406 in pplCoA, 3 libraries/batches each).

(F) Violin plot of UMIs detected per snRNA-seq nucleus for each replicate, filtered at the median per library + five times the median absolute deviation within each library (median 6081 UMIs/nucleus).

(G) Violin plot of genes detected per nucleus from each replicate, filtered at a minimum of 1000 features per nucleus (median 2547 genes/nucleus).

(H) Percent mitochondrial gene UMIs per snRNA-seq nucleus, filtered at median + five times the median absolute deviation per library (median 0.02% mitochondrial UMIs/nucleus).

(I) Percent ribosomal gene UMIs per snRNA-seq nucleus, filtered at median + five times the median absolute deviation per library (median 0.17% ribosomal UMIs/nucleus).

(J) Principal component analysis of pseudobulk snRNA-seq samples created from each batch, colored based on their combination of zone and batch identity.

(K) Evaluation of transcriptomic homology between batches, where the distance matrix is based on Spearman correlation between median expression of highly variable features for the whole dataset, and the dendrogram was created via hierarchical clustering of batches on this correlation matrix.

(L) UMAP of all snRNA-seq nuclei colored by both target region and batch identity.

(M) Relative proportion of nuclei of each type for all snRNA-seq batches.

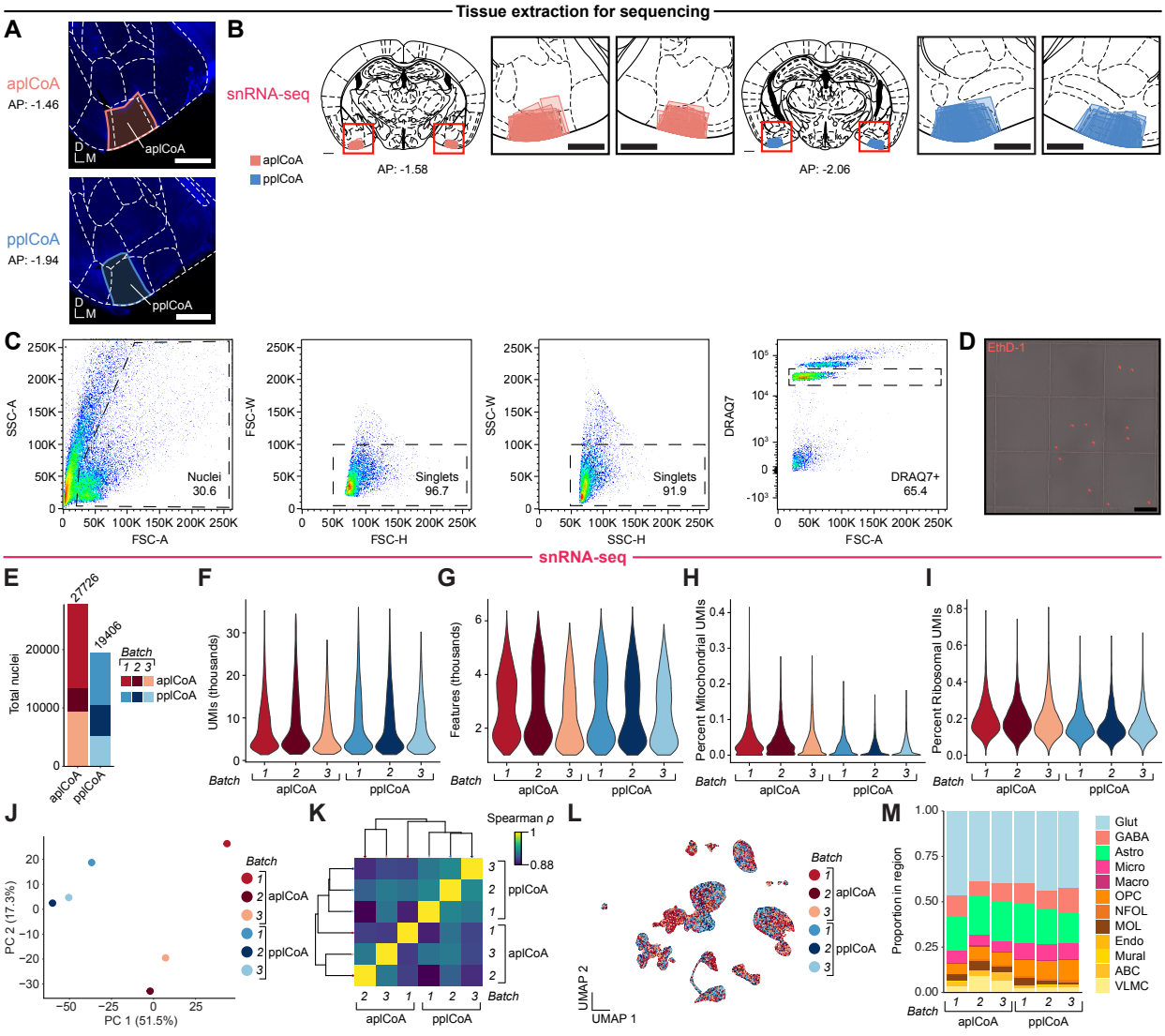
Tissue extraction for sequencing
A
aplCoA
AP: -1.46
pplCoA
AP: -1.94
B
snRNA-seq
aplCoA
pplCoA
AP: -1.58
AP: -2.06
C
SSC-A
FSC-A
Nuclei
30.6
FSC-W
FSC-H
Singlets
96.7
SSC-W
SSC-H
Singlets
91.9
DRAQ7
DRAQ7+
65.4
D
EthD-1
snRNA-seq
E
Total nuclei
27726
19406
Batch
F
UMIs (thousands)
G
Features (thousands)
H
Percent Mitochondrial UMIs
I
Percent Ribosomal UMIs
J
PC 2 (17.3%)
PC 1 (51.5%)
K
Spearman ρ
L
UMAP 2
UMAP 1
M
Proportion in region
Glut
GABA
Astro
Micro
Macro
OPC
NFOL
MOL
Endo
Mural
ABC
VLMC

Figure S3.4. Additional information about spatial gene expression.

(A-C) Allen ISH data for marker genes from molecular cell types likely adjacent to, but not within plCoA. *Sim1* (**A**) marks cells in the NLOT, *Etv1* (**B**) marks cells in the BLA and posterior basomedial amygdala, and *Fign* (**C**) marks cells in the CxA, but none of these mark cells in the plCoA.

(D) UMAP of all plCoA GABAergic neurons, colored by domain of origin.

(E) Relative proportion of molecular subtype nuclei from each domain within GABAergic neurons. Dotted line indicates chance level for plCoA GABAergic neuron nuclei.

(F) UMAP of all plCoA OPCs, colored by domain of origin.

(G) UMAP of astrocytes, colored by molecular cell type.

(H) Heatmap of astrocyte subtype marker genes.

(I) UMAP of all plCoA astrocytes, colored by domain of origin.

(J) Left, relative proportion of molecular subtype nuclei from each domain within astrocytes. Dotted line indicates chance level for plCoA astrocyte nuclei. Right, relative abundance of each astrocyte subtype within plCoA.

(K) UMAP of immune cells, colored by molecular cell type.

(L) Heatmap of immune cell subtype marker genes.

(M) UMAP of all plCoA immune cells, colored by domain of origin.

(N) Left, relative proportion of molecular subtype nuclei from each domain within immune cells. Dotted line indicates chance level for plCoA immune cell nuclei. Right, relative abundance of each immune cell type within plCoA.

(O) UMAP of VLMC nuclei, colored by molecular cell type.

(P) Heatmap of VLMC subtype marker genes.

(Q) UMAP of all plCoA VLMC nuclei, colored by domain of origin.

(R) Left, relative proportion of molecular subtype nuclei from each domain within VLMCs. Dotted line indicates chance level for plCoA VLMC nuclei. Right, relative abundance of each VLMC subtype within plCoA.

(S) Left, H&E image of a representative section on a Visium slide capture area. Right, representative section with capture spots overlaid (grey) and plCoA-overlapping spots highlighted (red).

(T) Violin plots of quality metrics for individual Visium sections on a per-spot basis in plCoA-overlapping spots (N = 21 sections). Upper left, UMIs per spot; upper right, features per spot; lower left, proportion mitochondrial UMIs per spot; lower right, proportion ribosomal UMIs per spot.

(U) Number of plCoA-overlapping capture spots per section (n = 3,616 total spots).

(V) UMAP of all plCoA-overlapping capture spots, colored by section of origin.

(W) Evaluation of transcriptomic homology between sections, where the distance matrix is based on Spearman correlation between median expression of highly variable features for the whole dataset, and the dendrogram was created via hierarchical clustering of sections on this correlation matrix.

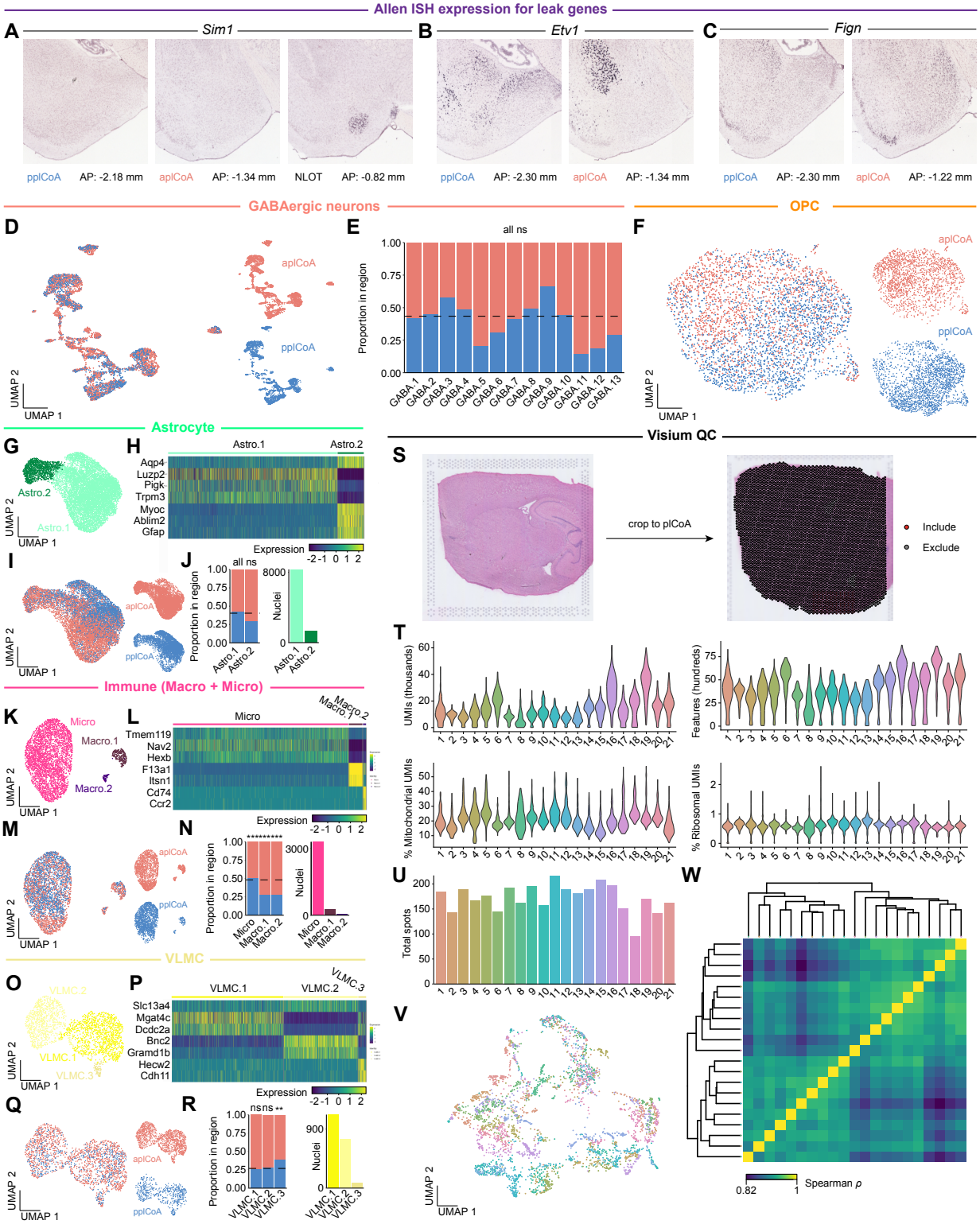
Allen ISH expression for leak genes
A
Sim1
pplCoA
AP: -2.18 mm
aplCoA
AP: -1.34 mm
NLOT
AP: -0.82 mm
B
Etv1
pplCoA
AP: -2.30 mm
aplCoA
AP: -1.34 mm
C
Fign
pplCoA
AP: -2.30 mm
aplCoA
AP: -1.22 mm
GABAergic neurons
OPC
D
aplCoA
pplCoA
UMAP 2
UMAP 1
E
all ns
Proportion in region
GABA.1
GABA.2
GABA.3
GABA.4
GABA.5
GABA.6
GABA.7
GABA.8
GABA.9
GABA.10
GABA.11
GABA.12
GABA.13
F
aplCoA
pplCoA
Astrocyte
G
Astro.2
Astro.1
H
Astro.1
Astro.2
Aqp4
Luzp2
Pigk
Trpm3
Myoc
Ablim2
Gfap
Expression
I
J
all ns
Nuclei
Immune (Macro + Micro)
K
Micro
Macro.1
Macro.2
L
Micro
Macro.1
Macro.2
Tmem119
Nav2
Hexb
F13a1
Itsn1
Cd74
Ccr2
M
N
VLMC
O
VLMC.1
VLMC.2
VLMC.3
P
Slc13a4
Mgat4c
Dcdc2a
Bnc2
Gramd1b
Hecw2
Cdh11
Q
R
Visium QC
S
crop to plCoA
Include
Exclude
T
UMIs (thousands)
Features (hundreds)
% Mitochondrial UMIs
% Ribosomal UMIs
U
Total spots
V
W
Spearman ρ

Figure S3.5. Additional information for Cre-dependent molecularly targeted chemogenetic inhibition experiments.

(A) Representative histology for inhibition experiments for AAV-hM4D(Gi)-mCherry-infected *Slc17a6::Cre* (left) or *Slc17a7::Cre* (right) animals.

(B) Strategy for chemogenetic inhibition in the open field test and elevated plus maze.

(C-E) Effect of chemogenetic inhibition of plCoA$^{Slc17a6+}$ neurons in the elevated plus maze. Inhibition does not induce a significant change in time spent (C) and number of entries (D) into the open arms, as well as distance traveled (E) in the elevated plus maze.

(F-H) Effect of chemogenetic inhibition of plCoA$^{Slc17a6+}$ neurons in the open field test. Inhibition does not induce a significant change in time spent in the center (F) and corners (G), as well as distance traveled (H) in the open field test.

(I-K) Effect of chemogenetic inhibition of plCoA$^{Slc17a7+}$ neurons in the elevated plus maze. Inhibition does not induce a significant change in time spent (I) and number of entries (J) into the open arms, as well as distance traveled (K) in the elevated plus maze.

(L-N) Effect of chemogenetic inhibition of plCoA$^{Slc17a7+}$ neurons in the open field test. Inhibition does not induce a significant change in time spent in the center (L) and corners (M), as well as distance traveled (N) in the open field test.

(O) Histologically verified placements for viral injection sites in *Slc17a6::Cre* animals infected with AAV-DIO-hSyn-mCherry (red) or AAV-DIO-hSyn-hM4D(Gi) (light orange) in molecularly targeted chemogenetic inhibition experiments.

(P) Same as (O), but in *Slc17a7::Cre* animals.

n denotes number of mice per group batched across 4-quad, elevated plus maze, and open field test experiments, exceeding n values for individual experiments due to behavioral cohort design (see STAR Methods). All mouse brain sections reproduced from Paxinos and Franklin, 5th Edition, with plCoA highlighted in grey and outlined in purple, and numbers below all images denote its anterior-posterior distance from bregma in this atlas (Paxinos and Franklin, 2008). All scale bars, 500 μm.

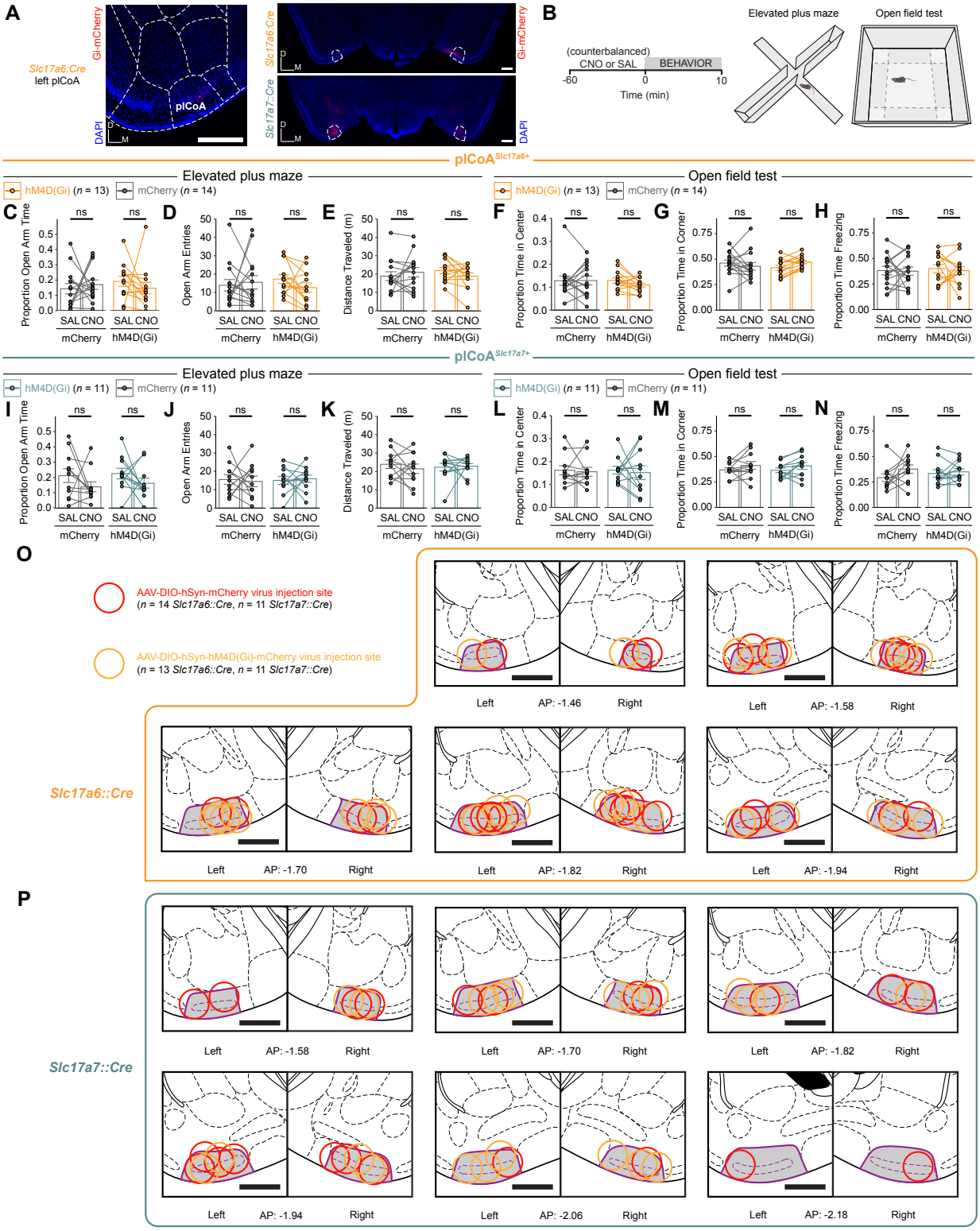
A
Slc17a6:Cre
left plCoA
Gi-mCherry
DAPI
plCoA
Slc17a6::Cre
Slc17a7::Cre
B
(counterbalanced)
CNO or SAL
BEHAVIOR
-60
0
10
Time (min)
Elevated plus maze
Open field test
plCoA Slc17a6+
plCoA Slc17a7+
hM4D(Gi) (n = 13)
mCherry (n = 14)
hM4D(Gi) (n = 11)
mCherry (n = 11)
C
D
E
F
G
H
I
J
K
L
M
N
Proportion Open Arm Time
Open Arm Entries
Distance Traveled (m)
Proportion Time in Center
Proportion Time in Corner
Proportion Time Freezing
ns
SAL CNO
mCherry
hM4D(Gi)
O
AAV-DIO-hSyn-mCherry virus injection site
(n = 14 Slc17a6::Cre, n = 11 Slc17a7::Cre)
AAV-DIO-hSyn-hM4D(Gi)-mCherry virus injection site
(n = 13 Slc17a6::Cre, n = 11 Slc17a7::Cre)
Slc17a6::Cre
Left
Right
AP: -1.46
AP: -1.58
AP: -1.70
AP: -1.82
AP: -1.94
P
Slc17a7::Cre
AP: -1.58
AP: -1.70
AP: -1.82
AP: -1.94
AP: -2.06
AP: -2.18

Figure S3.6. Manipulation of plCoA projections to MeA or NAc in either direction does not change features of behavior unrelated to innate valence.

(A-C) Time series (left) and overall period (right) effects for optogenetic stimulation of plCoA terminals in MeA in the elevated plus maze. Photostimulation does not induce a significant change in time spent (A) and number of entries (B) into the open arms, as well as distance traveled (C) in the elevated plus maze.

(D-F) Time series (left) and overall period (right) effects for optogenetic stimulation of plCoA terminals in NAc in the elevated plus maze. Photostimulation does not induce a significant change in time spent (H) and number of entries (I) into the open arms, as well as distance traveled (J) in the elevated plus maze.

(G-I) Time series (left) and overall period (right) effects for optogenetic stimulation of plCoA terminals in MeA in the open field test. Photostimulation does not induce a significant change time spent in the center (G) and corners (H), as well as distance traveled (I) in the open field test.

(J-L) Time series (left) and overall period (right) effects for optogenetic stimulation of plCoA terminals in NAc in the open field test. Photostimulation does not induce a significant change time spent in the center (G) and corners (H), as well as distance traveled (I) in the open field test.

(M-O) Effect of chemogenetic inhibition of plCoA-MeA projection neurons in the elevated plus maze. Inhibition does not induce a significant change in time spent (M) and number of entries (N) into the open arms, as well as distance traveled (O) in the elevated plus maze.

(P-R) Effect of chemogenetic inhibition of plCoA-MeA projection neurons in the open field test. Inhibition does not induce a significant change in time spent in the center (P) and corners (Q), as well as distance traveled (R) in the open field test.

(S-U) Effect of chemogenetic inhibition of plCoA-NAc projection neurons in the elevated plus maze. Inhibition does not induce a significant change in time spent (S) and number of entries (T) into the open arms, as well as distance traveled (U) in the elevated plus maze.

(V-X) Effect of chemogenetic inhibition of plCoA-NAc projection neurons in the open field test. Inhibition does not induce a significant change in time spent in the center (V) and corners (W), as well as distance traveled (X) in the open field test.

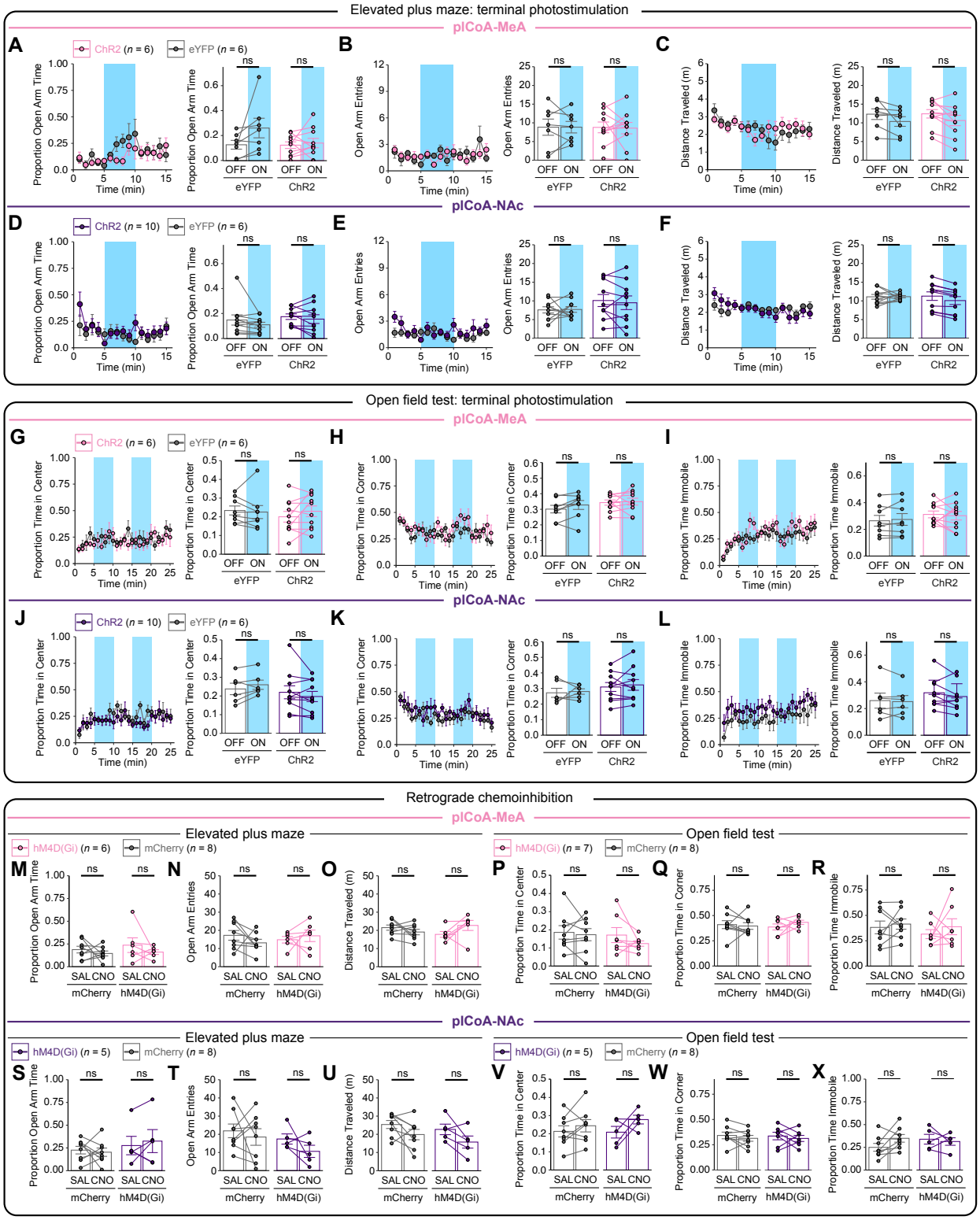
Elevated plus maze: terminal photostimulation
plCoA-MeA
A
ChR2 (n = 6)
eYFP (n = 6)
Proportion Open Arm Time
Time (min)
ns
OFF ON
eYFP
ChR2
B
Open Arm Entries
C
Distance Traveled (m)
plCoA-NAc
D
ChR2 (n = 10)
eYFP (n = 6)
E
F
Open field test: terminal photostimulation
plCoA-MeA
G
Proportion Time in Center
H
Proportion Time in Corner
I
Proportion Time Immobile
plCoA-NAc
J
K
L
Retrograde chemoinhibition
plCoA-MeA
Elevated plus maze
hM4D(Gi) (n = 6)
mCherry (n = 8)
M
N
O
Open field test
hM4D(Gi) (n = 7)
P
Q
R
SAL CNO
mCherry
hM4D(Gi)
plCoA-NAc
hM4D(Gi) (n = 5)
S
T
U
V
W
X

3.8. References

Abraira, V.E., and Ginty, D.D. (2013). The Sensory Neurons of Touch. Neuron *79*.

Arshamian, A., Gerkin, R.C., Kruspe, N., Wnuk, E., Floyd, S., O'Meara, C., Garrido Rodriguez, G., Lundström, J.N., Mainland, J.D., Majid, A. (2022). The perception of odor pleasantness is shared across cultures. Curr. Biol. *32*, 2061-2066.e3.

Auffarth, B. (2013). Understanding smell--the olfactory stimulus problem. Neurosci. Biobehav. Rev. *37*, 1667-1679.

Barabási, D.L., Beynon, T., Katona, Á., Perez-Nieves, N. (2023). Complex computation from developmental priors. Nat. Commun. *14*, 2226.

Becht, E., McInnes, L., Healy, J., Dutertre, C.-A., Kwok, I.W.H., Ng, L.G., Ginhoux, F., Newell, E.W. (2019). Dimensionality reduction for visualizing single-cell data using UMAP. Nat. Biotechnol. *37*, 38-44.

Beyeler, A., Namburi, P., Glober, G.F., Simonnet, C., Calhoon, G.G., Conyers, G.F., Luck, R., Wildes, C.P., Tye, K.M. (2016). Divergent routing of positive and negative information from the amygdala during memory retrieval. Neuron *90*, 348-361.

Beyeler, A., Chang, C.-J., Silvestre, M., Lévêque, C., Namburi, P., Wildes, C.P., Tye, K.M. (2018). Organization of valence-encoding and projection-defined neurons in the basolateral amygdala. Cell Rep., 905-918.

Butler, A., Hoffman, P., Smibert, P., Papalexi, E., Satija, R. (2018). Integrating single-cell transcriptomic data across different conditions, technologies, and species. Nat. Biotechnol. *36*, 411-420.

Calvigioni, D., Fuzik, J., Le Merre, P., Slashcheva, M., Jung, F., Ortiz, C., Lentini, A., Csillag, V., Graziano, M., Nikolakopoulou, I., Weglage, M., Lazaridis, I., Kim, H., Lenzi, I., Park, H., Reinius, B., Carlén, M., Meletis, K. (2023). Esr1+ hypothalamic-habenula neurons shape aversive states. Nat. Neurosci. *26*, 1245-1255.

Carpenter, A.E., Jones, T.R., Lamprecht, M.R., Clarke, C., Kang, I.H., Friman, O., Guertin, D.A., Chang, J.H., Lindquist, R.A., Moffat, J., Golland, P., Sabatini, D.M. (2006). CellProfiler: image analysis software for identifying and quantifying cell phenotypes. Genome Biol. *7*, R100.

Cembrowski, M.S., Phillips, M.G., DiLisio, S.F., Shields, B.C., Winnubst, J., Chandrashekar, J., Bas, E., Spruston, N. (2018). Dissociable structural and functional hippocampal outputs via distinct subiculum cell classes. Cell *173*, 1280-1292.e18.

Cembrowski, M.S., Spruston, N. (2019). Heterogeneity within classical cell types is the rule: lessons from hippocampal pyramidal neurons. Nat. Rev. Neurosci. *20*, 193–204.

Cembrowski, M.S., Wang, L., Lemire, A.L., Copeland, M., DiLisio, S.F., Clements, J., Spruston, N. (2018). The subiculum is a patchwork of discrete subregions. eLife *7*, e37701.

Chen, X., Gabito, M., Peng, Y., Ryba, N.J.P., Zuker, C.S. (2011). A Gustotopic Map of Taste Qualities in the Mammalian Brain. Science *333*, 1262–1266.

Chen, Y., Chen, X., Baserdem, B., Zhan, H., Li, Y., Davis, M.B., Kebschull, J.M., Zador, A.M., Koulakov, A.A., Albeanu, D.F. (2022). High-throughput sequencing of single neuron projections reveals spatial organization in the olfactory cortex. Cell *185*, 4117-4134.e28.

Chae, H., Kepple, D.R., Bast, W.G., Murthy, V.N., Koulakov, A.A., Albeanu, D.F. (2019). Mosaic representations of odors in the input and output layers of the mouse olfactory bulb. Nat. Neurosci. *22*, 1306-1317.

Choi, G.B., Dong, H., Murphy, A.J., Valenzuela, D.M., Yancopoulos, G.D., Swanson, L.W., Anderson, D.J. (2005). Lhx6 Delineates a Pathway Mediating Innate Reproductive Behaviors from the Amygdala to the Hypothalamus. Neuron *46*, 647-660.

Choudhary, S., Satija, R. (2022). Comparison and evaluation of statistical error models for scRNA-seq. Genome Biol. *23*, 27.

Cohn, R., Morantte, I., Ruta, V. (2015). Coordinated and Compartmentalized Neuromodulation Shapes Sensory Processing in Drosophila. Cell *163*, 1742-1755.

Costantini, D. (2020). Neuronal topography in a cortical circuit for innate odor valence. Columbia University.

Cousens, G.A. (2020). Characterization of odor-evoked neural activity in the olfactory peduncle. IBRO Rep. *9*, 157-163.

Daviu, N., Bruchas, M.R., Moghaddam, B., Sandi, C., Beyeler, A. (2019). Neurobiological links between stress and anxiety. Neurobiol. Stress *11*, 100191.

Davis, A., Gao, R., Navin, N.E. (2019). SCOPIT: Sample size calculations for single-cell sequencing experiments. BMC Bioinformatics *20*, 566.

Day, H.E.W., Masini, C.V., Campeau, S. (2004). The pattern of brain c-fos mRNA induced by a component of fox odor, 2,5-dihydro-2,4,5-trimethylthiazoline (TMT), in rats, suggests both systemic and processive stress characteristics. Brain Res. *1025*, 139-151.

Ding, S.-L., Yao, Z., Hirokawa, K.E., Nguyen, T.N., Graybuck, L.T., Fong, O., Bohn, P., Ngo, K., Smith, K.A., Koch, C., Philips, J.W., Lein, E.S., Harris, J.A., Tasic, B., Zeng, H. (2020). Distinct transcriptomic cell types and neural circuits of the subiculum and prosubiculum along the dorsal-ventral axis. Cell Rep. *31*, 107648.

Elias, L.J., Succi, I.K., Schaffler, M.D., Foster, W., Gradwell, M.A., Bohic, M., Fushiki, A., Upadhyay, A., Ejoh, L.L., Schwark, R., Frazer, R., Bistis, B., Burke, J.E., Saltz, V., Boyce, J.E., Jhumka, A., Costa, R.M., Abraira, V.E., Abdus-Saboor, I. (2023). Touch neurons underlying dopaminergic pleasurable touch and sexual receptivity. Cell *186*, 577-590.e16.

Erö, C., Gewaltig, M.-O., Keller, D., Markram, H. (2018). A cell atlas for the mouse brain. Front. Neuroinformatics *12*.

Floresco, S.B. (2015). The nucleus accumbens: An interface between cognition, emotion, and action. Annu. Rev. Psychol. *66*, 25-52.

Garrett, M.E., Nauhaus, I., Marshel, J.H., Callaway, E.M. (2014). Topography and areal organization of mouse visual cortex. J. Neurosci. *34*, 12587-12600.

Garcia, R. (2017). Neurobiology of fear and specific phobias. Learn. Mem. *24*, 462-471.

Gruters, K., and Groh, J. (2012). Sounds and beyond: multisensory and other non-auditory signals in the inferior colliculus. Front. Neural Circuits *6*.

Griffiths, J.A., Richard, A.C., Bach, K., Lun, A.T.L., and Marioni, J.C. (2018). Detection and removal of barcode swapping in single-cell RNA-seq data. Nat. Commun. *9*.

Germain, P.-L., and Lun, A. (2021). scDblFinder. Version 1.4.0 (Bioconductor version: Release (3.12)).

Hafemeister, C., and Satija, R. (2019). Normalization and variance stabilization of single-cell RNA-seq data using regularized negative binomial regression. Genome Biol. *20*, 296.

Harris, J.A., Hirokawa, K.E., Sorensen, S.A., Gu, H., Mills, M., Ng, L.L., Bohn, P., Mortrud, M., Ouellette, B., Kidney, J., Smith, K.A., Dang, C., Sunkin, S., Bernard, A., Oh, S.W., Madisen, L., Zeng, H. (2014). Anatomical characterization of Cre driver mice for neural circuit mapping and manipulation. Front. Neural Circuits *8*, 76.

Hayden, S., Bekaert, M., Crider, T.A., Mariani, S., Murphy, W.J., Teeling, E.C. (2010). Ecological adaptation determines functional mammalian olfactory subgenomes. Genome Res. *20*, 1–9.

Hao, Y., Hao, S., Andersen-Nissen, E., Mauck, W.M., Zheng, S., Butler, A., Lee, M.J., Wilk, A.J., Darby, C., Zager, M., Hoffman, P., Stoeckius, M., Papalexi, E., Mimitou, E.P., Jain, J., Srivastava, A., Stuart, T., Fleming, L.M., Yeung, B., Rogers, A.J., McElrath, J.M., Blish, C.A., Gottardo, R., Smibert, P., Satija, R. (2021). Integrated analysis of multimodal single-cell data. Cell *184*, 3573-3587.e29.

Ibarra-Soria, X., Nakahara, T.S., Lilue, J., Jiang, Y., Trimmer, C., Souza, M.A., Netto, P.H., Ikegami, K., Murphy, N.R., Kusma, M., Kirton, A., Saraiva, L.R., Keane, T.M., Matsunami, H.,

Mainland, J., Papes, F., Logan, D.W. (2017). Variation in olfactory neuron repertoires is genetically controlled and environmentally modulated. eLife *6*, e21476.

Ikemoto, S. (2007). Dopamine reward circuitry: two projection systems from the ventral midbrain to the nucleus accumbens-olfactory tubercle complex. Brain Res. Rev. *56*, 27–78.

Imai, T., Sakano, H., and Vosshall, L.B. (2010). Topographic mapping—The olfactory system. Cold Spring Harb. Perspect. Biol. *2*, a001776.

Iurilli, G., and Datta, S.R. (2017). Population coding in an innately relevant olfactory area. Neuron *93*, 1180-1197.e7.

Ito, S., and Feldheim, D.A. (2018). The mouse superior colliculus: An emerging model for studying circuit formation and function. Front. Neural Circuits *12*, 10.

Jaeger, S.R., McRae, J.F., Bava, C.M., Beresford, M.K., Hunter, D., Jia, Y., Chheang, S.L., Jin, D., Peng, M., Gamble, J.C., Atkinson, K.R., Axten, L.G., Paisley, A.G., Tooman, L., Pineau, B., Rouse, S.A., Newcomb, R.D. (2013). A mendelian trait for olfactory sensitivity affects odor experience and food selection. Curr. Biol. *23*, 1601-1605.

Jolliffe, I.T., and Cadima, J. (2016). Principal component analysis: a review and recent developments. Philos. Trans. R. Soc. Math. Phys. Eng. Sci. *374*, 20150202.

Kaas, J.H. (1997). Topographic maps are fundamental to sensory processing. Brain Res. Bull. *44*, 107–112.

Kaas, J.H., Nelson, R.J., Sur, M., Lin, C.-S., and Merzenich, M.M. (1979). Multiple Representations of the Body Within the Primary Somatosensory Cortex of Primates. Science *204*, 521–523. 10.1126/science.107591.

Keller, A., Zhuang, H., Chi, Q., Vosshall, L.B., and Matsunami, H. (2007). Genetic variation in a human odorant receptor alters odour perception. Nature *449*, 468-472.

Keller, A., Gerkin, R.C., Guan, Y., Dhurandhar, A., Turu, G., Szalai, B., Mainland, J.D., Ihara, Y., Yu, C.W., Wolfinger, R., Vens, C., Scheitgat, L., de Grave, K., Norel, R., DREAM Olfaction Prediction Consortium, Stolovitzky, G., Cecchi, G., Vosshall, L.B., Meyer, P. (2017). Predicting human olfactory perception from chemical features of odor molecules. Science *355*, 820-826.

Kim, J., Pignatelli, M., Xu, S., Itohara, S., Tonegawa, S. (2016). Antagonistic negative and positive neurons of the basolateral amygdala. Nat. Neurosci. *19*, 1636-1646.

Klein, S., Staring, M., Murphy, K., Viergever, M.A., Pluim, J.P.W. (2010). elastix: a toolbox for intensity-based medical image registration. IEEE Trans. Med. Imaging *29*, 196-205.

Knowland, D., Lilascharoen, V., Pacia, C.P., Shin, S., Wang, E.H.-J.,Lim, B.K. (2017). Distinct ventral pallidal neural populations mediate separate symptoms of depression. Cell *170*, 284-297.e18.

Koulakov, A., Shuvaev, S., Lachi, D., Zador, A. (2022). Encoding innate ability through a genomic bottleneck. Preprint at bioRxiv.

Krashes, M.J., Koda, S., Ye, C., Rogan, S.C., Adams, A.C., Cusher, D.S., Maratos-Flier, E., Roth, B.L., Lowell, B.B. (2011). Rapid, reversible activation of AgRP neurons drives feeding behavior in mice. J. Clin. Invest. 121, 1424-1428.

Krishnaswami, S.R., Grindberg, R.V., Novotny, M., Venepally, P., Lacar, B., Bhutani, K., Linker, S.B., Pham, S., Erwin, J.A., Miller, J.A., Hodge, R., McCarthy, J.K., Kelder, M., McCorrison, J., Aevermann, B.D., Fuertes, F.D., Scheuermann, R.H., Lee, J., Lein, E.S., Schork, N., McConnell, M.J., Gage, F.H., Lasken, R.S. (2016). Using single nuclei for RNA-seq to capture the transcriptome of postmortem neurons. Nat. Protoc. *11*, 499-524.

Lebow, M.A., Chen, A. (2016). Overshadowed by the amygdala: the bed nucleus of the stria terminalis emerges as key to psychiatric disorders. Mol. Psychiatry *21*, 450-463.

Lee, B.K., Mayhew, E.J., Sanchez-Lengeling, B., Wei, J.N., Qian, W.W., Little, K.A., Andres, M., Nguyen, B.B., Moloy, T., Yasonik, J., Parker, J.K., Gerken, R.C., Mainland, J.D., Wiltschko, A.B. (2023). A principal odor map unifies diverse tasks in olfactory perception. Science *381*, 999-1006.

Lee, D., Liu, L., Root, C.M. (2023). Transformation of value signaling in a striatopallidal circuit. eLife *12*.

Li, B., Kamarck, M.L., Peng, Q., Lim, F.-L., Keller, A., Smeets, M.A.M., Mainland, J.D., Wang, S. (2022). From musk to body odor: Decoding olfaction through genetic variation. PLoS Genet. *18*, e1009564.

Li, Q., Liberles, S.D. (2015). Aversion and attraction through olfaction. Curr. Biol. *25*, R120–R129.

Lun, A.T.L., Riesenfeld, S., Andrews, T., Dao, T.P., Gomes, T., Marioni, J.C., participants in the 1st Human Cell Atlas Jamboree (2019). EmptyDrops: distinguishing cells from empty droplets in droplet-based single-cell RNA sequencing data. Genome Biol. *20*, 63.

Ma, L., Qiu, Q., Gradwohl, S., Scott, A., Yu, E.Q., Alexander, R., Wiegraebe, W., Yu, C.R. (2012). Distributed representation of chemical features and tunotopic organization of glomeruli in the mouse olfactory bulb. Proc. Natl. Acad. Sci. U.S.A. *109*, 5481–5486.

Mainland, J.D., Keller, A., Li, Y.R., Zhou, T., Trimmer, C., Snyder, L.L., Moberly, A.H., Adipietro, K.A., Liu, W.L.L., Zhuang, H., Zhan, S., Lee, S.S., Lin, A., Matsunami, H. (2014).

The missense of smell: Functional variability in the human odorant receptor repertoire. Nat. Neurosci. *17*, 114–120.

Malnic, B., Hirono, J., Sato, T., Buck, L.B. (1999). Combinatorial receptor codes for odors. Cell *96*, 713–723.

Mandelbaum, G., Taranda, J., Haynes, T.M., Hochbaum, D.R., Huang, K.W., Hyun, M., Venkataraju, K.U., Straub, C., Wang, W., Robertson, K., Osten, B., Sabatini, B.L. (2019). Distinct cortical-thalamic-striatal circuits through the parafascicular nucleus. Neuron *102*, 636-652.e7. 10.1016/j.neuron.2019.02.035.

Marques, S., Zeisel, A., Codeluppi, S., van Bruggen, D., Mendanha Falcão, A., Xiao, L., Li, H., Häring, M., Hochgerner, H., Romanov, R.A., Gyllborg, D., Manchado, A.M., La Manno, G., Lönnerberg, P., Floriddia, E., Rezayee, F., Ernfors, P., Arenas, E., Hjerling-Leffler, J., Harkany, T., Richardson, W.D., Linnarsson, S., Castelo-Branco, G. (2016). Oligodendrocyte heterogeneity in the mouse juvenile and adult central nervous system. Science *352*, 1326-1329.

McCarthy, D.J., Campbell, K.R., Lun, A.T.L., Wills, Q.F., and Hofacker, I. (2017). Scater: pre-processing, quality control, normalization and visualization of single-cell RNA-seq data in R. Bioinformatics *33*, btw777.

McCullough, K.M., Morrison, F.G., Hartmann, J., Carlezon, W.A., Ressler, K.J. (2018). Quantified coexpression analysis of central amygdala subpopulations. eNeuro *5*.

McGinnis, C.S., Murrow, L.M., Gartner, Z.J. (2019). DoubletFinder: Doublet detection in single-cell RNA sequencing data using artificial nearest neighbors. Cell Syst. *8*, 329-337.e4.

McInnes, L., Healy, J., Melville, J., (2018). UMAP: Uniform Manifold Approximation and Projection for dimension reduction. arXiv:1802.03426 [cs, stat].

Mills, F., Lee, C.R., Howe, J.R., Li, H., Shao, S., Keisler, M.N., Lemieux, M.E., Taschbach, F.H., Keyes, L.R., Borio, M., Chen, H.S., Patel, R.R., Gross, A.L., Delahanty, J., Cazares, C., Maree, L., Wichmann, R., Pereira, T.D., Benna, M.K., Root, C.M., Tye, K.M. (2024). Amygdalostriatal transition zone neurons encode sustained valence to direct conditioned behaviors. Preprint at bioRxiv.

Miyamichi, K., Amat, F., Moussavi, F., Wang, C., Wickersham, I., Wall, N.R., Taniguchi, H., Tasic, B., Huang, Z.J., He, Z., Callaway, E.M., Horowitz, M.A., Luo, L. (2011). Cortical representations of olfactory input by trans-synaptic tracing. Nature *472*, 191-199.

McRae, J.F., Mainland, J.D., Jaeger, S.R., Adipietro, K.A., Matsunami, H., Newcomb, R.D. (2012). Genetic variation in the odorant receptor OR2J3 is associated with the ability to detect the “grassy” smelling odor, cis-3-hexen-1-ol. Chem. Senses *37*, 585–593.

Menashe, I., Abaffy, T., Hasin, Y., Goshen, S., Yahalom, V., Luetje, C.W., Lancet, D. (2007). Genetic Elucidation of Human Hyperosmia to Isovaleric Acid. PLOS Biol. *5*, e284.

Müller, M., Fendt, M. (2006). Temporary inactivation of the medial and basolateral amygdala differentially affects TMT-induced fear behavior in rats. Behav. Brain Res. *167*, 57–62.

O'Leary, T.P., Sullivan, K.E., Wang, L., Clements, J., Lemire, A.L., Cembrowski, M.S. (2020). Extensive and spatially variable within-cell-type heterogeneity across the basolateral amygdala. eLife *9*, e59003.

Ohla, K., Yoshida, R., Roper, S.D., Di Lorenzo, P.M., Victor, J.D., Boughter, J.D., Fletcher, M., Katz, D.B., Chaudhari, N. (2019). Recognizing Taste: Coding patterns along the neural axis in mammals. Chem. Senses *44*, 237–247.

Pacifico, R., Dewan, A., Cawley, D., Guo, C., and Bozza, T. (2012). An olfactory subsystem that mediates high-sensitivity detection of volatile amines. Cell Rep. *2*, 76–88.

Pardo-Bellver, C., Vila-Martin, M.E., Martínez-Bellver, S., Villafranca-Faus, M., Teruel-Sanchis, A., Savarelli-Balsamo, C.A., Drabik, S.M., Martínez-Ricós, J., Cervera-Ferri, A., Martínez-García, F., Lanuza, E., Teruel-Marti, V. (2022). Neural activity patterns in the chemosensory network encoding vomeronasal and olfactory information in mice. Front. Neuroanat. *16*.

Payton, C.A., Wilson, D.A., Wesson, D.W. (2012). Parallel odor processing by two anatomically distinct olfactory bulb target structures. PloS One *7*, e34926.

Petrulis, A. (2020). Chapter 2 - Structure and function of the medial amygdala. In Handbook of Behavioral Neuroscience: Handbook of Amygdala Structure and Function., J. H. Urban and J. A. Rosenkranz, eds. (Elsevier), pp. 39-61.

Phillips, J.W., Schulmann, A., Hara, E., Winnubst, J., Liu, C., Valakh, V., Wang, L., Shields, B.C., Korff, W., Chandrashekar, J., Lemire, A.L., Mensh, B., Dudman, J.T., Nelson, S.B.. Hantman, A.W. (2019). A repeated molecular architecture across thalamic pathways. Nat. Neurosci. *22*, 1925.

Phipson, B., Sim, C.B., Porrello, E.R., Hewitt, A.W., Powell, J., Oshlack, A. (2022). propeller: testing for differences in cell type proportions in single cell data. Bioinformatics *38*, 4720-4726.

Pratelli, M., Thaker, A., Li, H., Godavarthi, S., Spitzer, N.C. (2022). Phencyclidine and methamphetamine cause cognitive deficits by changing pyramidal neuron transmitter identity in the prefrontal cortex. Preprint at bioRxiv.

Preissl, S., Fang, R., Huang, H., Zhao, Y., Raviram, R., Gorkin, D.U., Zhang, Y., Sos, B.C., Afzal, V., Dickel, D.E., Kuan, S., Visel, A., Pennacchio, L.A., Zhang, K., Ren, B. (2018). Single-nucleus analysis of accessible chromatin in developing mouse forebrain reveals cell-type-specific transcriptional regulation. Nat. Neurosci. *21*, 432-439.

Recanzone, G.H., and Sutter, M.L. (2008). The Biological Basis of Audition. Annu. Rev. Psychol. *59*.

Ressler, K.J., Sullivan, S.L., Buck, L.B. (1993). A zonal organization of odorant receptor gene expression in the olfactory epithelium. Cell *73*, 597–609.

Roland, B., Deneux, T., Franks, K.M., Bathellier, B., Fleischmann, A. (2017). Odor identity coding by distributed ensembles of neurons in the mouse olfactory cortex. eLife *6*, e26337.

Root, C.M., Denny, C.A., Hen, R., Axel, R. (2014). The participation of cortical amygdala in innate, odour-driven behaviour. Nature *515*, 269–273.

Saito, H., Nishizumi, H., Suzuki, S., Matsumoto, H., Ieki, N., Abe, T., Kiyonari, H., Morita, M., Yokota, H., Hirayama, N., Yamazaki, T., Kikusui, T., Mori, K., Sakano, H. (2017). Immobility responses are induced by photoactivation of single glomerular species responsive to fox odour TMT. Nat. Commun. *8*: 16011.

Saraiva, L.R., Riveros-McKay, F., Mezzavilla, M., Abou-Moussa, E.H., Arayata, C.J., Makhlouf, M., Trimmer, C., Ibarra-Soria, X., Khan, M., Van Gerven, L., Jorissen, M., Gibbs, M., O'Flynn, C., McGrane, S., Mombaerts, P., Marioni, J.C., Mainland, J.D., Logan, D.W. (2019). A transcriptomic atlas of mammalian olfactory mucosae reveals an evolutionary influence on food odor detection in humans. Sci. Adv. *5*, eaax0396.

Satija, R., Farrell, J.A., Gennert, D., Schier, A.F., Regev, A. (2015). Spatial reconstruction of single-cell gene expression data. Nat. Biotechnol. *33*, 495–502.

Schindelin, J., Arganda-Carreras, I., Frise, E., Kaynig, V., Longair, M., Pietzsch, T., Preibisch, S., Rueden, C., Saalfeld, S., Schmid, B., Tinevez, J.-Y., White, D.J., Hartenstein, V., Elicieri, K., Tomancek, P., Cardona, A. (2012). Fiji: an open-source platform for biological-image analysis. Nat. Methods *9*, 676–682.

Schreiner, C.E., Winer, J.A. (2007). Auditory Cortex Mapmaking: Principles, Projections, and Plasticity. Neuron *56*, 356–365.

Sedwick, V.M., Autry, A.E. (2022). Anatomical and molecular features of the amygdalohippocampal transition area and its role in social and emotional behavior processes. Neurosci. Biobehav. Rev. *142*, 104893.

Shamonin, D.P., Bron, E.E., Lelieveldt, B.P.F., Smits, M., Klein, S., Staring, M., Alzheimer's Disease Neuroimaging Initiative (2013). Fast parallel image registration on CPU and GPU for diagnostic classification of Alzheimer's disease. Front. Neuroinformatics *7*, 50.

Singer, W. (2021). Recurrent dynamics in the cerebral cortex: Integration of sensory evidence with stored knowledge. Proc. Natl. Acad. Sci. U.S.A. *118*, 10.

Sosulski, D.L., Lissitsyna Bloom, M., Cutforth, T., Axel, R., Datta, S.R. (2011). Distinct representations of olfactory information in different cortical centres. Nature *472*, 213–219.

Soucy, E.R., Albeanu, D.F., Fantana, A.L., Murthy, V.N., Meister, M. (2009). Precision and diversity in an odor map on the olfactory bulb. Nat. Neurosci. *12*, 210–220.

Squair, J.W., Gautier, M., Kathe, C., Anderson, M.A., James, N.D., Hutson, T.H., Hudelle, R., Qaiser, T., Matson, K.J.E., Barraud, Q., et al. (2021). Confronting false discoveries in single-cell differential expression. Nat. Commun. *12*, 5692. 10.1038/s41467-021-25960-2.

Stettler, D.D., and Axel, R. (2009). Representations of odor in the piriform cortex. Neuron *63*, 854–864.

Sturchler-Pierrat, C., Abramowski, D., Duke, M., Wiederhold, K.-H., Mistl, C., Rothacher, S., Ledermann, B., Bürki, K., Frey, P., Paganetti, P.A., Waridiel, C., Calhoun, M.E., Jucker, M., Probst, A., Staufenbiel, M., Sommer, B. (1997). Two amyloid precursor protein transgenic mouse models with Alzheimer disease-like pathology. Proc. Natl. Acad. Sci. U.S.A. *94*, 13287-13292.

Stowers, L., Cameron, P., Keller, J.A. (2013). Ominous Odors: olfactory control of instinctive fear and aggression in mice. Curr. Opin. Neurobiol. *23*, 339-345.

Stowers, L., Kuo, T.-H. (2015). Mammalian pheromones; emerging properties and mechanisms of detection. Curr. Opin. Neurobiol. *34*, 103-109.

Stuart, T., Butler, A., Hoffman, P., Hafemeister, C., Papalexi, E., Mauck, W.M., Hao, Y., Stoeckius, M., Smibert, P., Satija, R. (2019). Comprehensive Integration of Single-Cell Data. Cell *177*, 1888-1902.e21.

Tanabe, S. (2013). Population codes in the visual cortex. Neurosci. Res. *76*, 101–105. 10.1016/j.neures.2013.03.010.

Tasic, B., Yao, Z., Graybuck, L.T., Smith, K.A., Nguyen, T.N., Bertagnolli, D., Goldy, J., Garren, E., Economo, M.N., Viswanathan, S., Penn, O., Bakken, T., Menon, V., Miller, J., Fong, O., Hirokawa, K.E., Lathia, K., Rimorin, C., Tieu, M., Larsen, R., Casper, T., Barkan, E., Kroll, M., Parry, S., Shapovalova, N.V., Hirschstein, D., Pendergraft, J., Sullivan, H.A., Kim, T.K., Szafer, A., Dee, N., Groblewski, P., Wickersham, I., Cetin, A., Harris, J.A., Levi, B.P., Sunkin, S.M., Madisen, L., Daigle, T.L., Looger, L., Bernard, A., Phillips, J., Lein, E., Hawrylycz, M., Svoboda, K., Jones, A.R., Koch, C., Zeng, H. (2018). Shared and distinct transcriptomic cell types across neocortical areas. Nature *563*, 72-78.

Tierney, A.J. (1986). The evolution of learned and innate behavior: Contributions from genetics and neurobiology to a theory of behavioral evolution. Anim. Learn. Behav. *14*, 339–348.

Ting, J.T., Daigle, T.L., Chen, Q., Feng, G. (2014). Acute Brain Slice Methods for Adult and Aging Animals: Application of Targeted Patch Clamp Analysis and Optogenetics. In (Humana Press, New York, NY), pp. 221–242.

Todd, A.J. (2010). Neuronal circuitry for pain processing in the dorsal horn. Nat. Rev. Neurosci. *11*, 823–836.

Traag, V.A., Waltman, L., van Eck, N.J. (2019). From Louvain to Leiden: guaranteeing well-connected communities. Sci. Rep. *9*, 5233.

Trimmer, C., Keller, A., Murphy, N.R., Snyder, L.L., Willer, J.R., Nagai, M.H., Katsanis, N., Vosshall, L.B., Matsunami, H., Mainland, J.D. (2019). Genetic variation across the human olfactory receptor repertoire alters odor perception. Proc. Natl. Acad. Sci. U.S.A. *116*, 9475–9480.

Tsuji, T., Tsuji, C., Lozic, M., Ludwig, M., Leng, G. (2019). Coding of odors in the anterior olfactory nucleus. Physiol. Rep. *7*, e14284.

Tye, K.M. (2018). Neural circuit motifs in valence processing. Neuron *100*, 436–452.

Vong, L., Ye, C., Yang, Z., Choi, B., Chua, S., and Lowell, B.B. (2011). Leptin action on GABAergic neurons prevents obesity and reduces inhibitory tone to POMC neurons. Neuron *71*, 142–154.

Van der Maaten, L., and Hinton, G. (2008). Visualizing Data using t-SNE. J. Mach. Learn. Res. *9*, 2579–2605.

Wang, F., Flanagan, J., Su, N., Wang, L.C., Bui, S., Nielson, A., Wu, X., Vo, H.T., Ma, X.J., Luo, Y. (2012). RNAscope: A novel in situ RNA analysis platform for formalin-fixed, paraffin-embedded tissues. J. Mol. Diagn. *14*, 22–29.

Wang, I.-H., Murray, E., Andrews, G., Jiang, H.-C., Park, S.J., Donnard, E., Durán-Laforet, V., Bear, D.M., Faust, T.E., Garber, M., Baer, C.E., Schafer, D.P., Weng, Z., Chen, F., Macosko, E.Z. (2022). Spatial transcriptomic reconstruction of the mouse olfactory glomerular map suggests principles of odor processing. Nat. Neurosci. *25*, 484-492.

Wang, L., Gillis-Smith, S., Peng, Y., Zhang, J., Chen, X., Salzman, C.D., Ryba, N.J.P., Zuker, C.S. (2018). The coding of valence and identity in the mammalian taste system. Nature *558*, 127-131.

Yarmolinsky, D.A., Zuker, C.S., and Ryba, N.J.P. (2009). Common sense about taste: From mammals to insects. Cell *139*, 234–244.

Yasuda, K., Cline, C., Vogel, P., Onciu, M., Fatima, S., Sorrentino, B.P., Thirumaran, R.K., Ekins, S., Urade, Y., Fujimori, K., Schuetz, E.G. (2013). Drug transporters on arachnoid barrier cells contribute to the blood–cerebrospinal fluid barrier. Drug Metab. Dispos. *41*, 923–931.

Zador, A.M. (2019). A critique of pure learning and what artificial neural networks can learn from animal brains. Nat. Commun. *10*, 3770.

Zapiec, B., Mombaerts, P. (2020). The zonal organization of odorant receptor gene choice in the main olfactory epithelium of the mouse. Cell Rep. *30*, 4220-4234.e5.

Zappia, L., and Oshlack, A. (2018). Clustering trees: a visualization for evaluating clusterings at multiple resolutions. GigaScience *7*, giy083.

Zheng, G.X.Y., Terry, J.M., Belgrader, P., Ryvkin, P., Bent, Z.W., Wilson, R., Ziraldo, S.B., Wheeler, T.D., McDermott, G.P., Zhu, J., Gregory, M.T., Shuga, J., Montesclaros, L., Underwood, J.G., Masquelier, D.A., Nishimura, S.Y., Schnall-Levin, M., Wyatt, P.W., Hindson, C.M., Bharadwaj, R., Wong, A., Ness, K.D., Beppu, L.W., Deeg, H.J., McFarland, C., Loeb, K.R., Valente, W.J., Ericson, N.G., Stevens, E.A., Radich, J.P., Mikkelsen, T.S., Hindson, B.J., Bielas, J.H. (2017). Massively parallel digital transcriptional profiling of single cells. Nat. Commun. *8*, 14049.